Exploiting Extrinsic Passivation on Thin Film Dielectrics for High Efficiency Solar Cells

By

Isabel Rose Al-Dhahir

A thesis presented for the degree of

Doctor of Philosophy

October 2021

Supervised by Prof. Ruy Sebastian Bonilla and Prof. Peter Wilshaw

University of Oxford

Department of Materials

Acknowledgements

During the course of my DPhil, I was fortunate to have been part of a talented team at the Department of Materials Science at the University of Oxford, and to have had the valuable support of my family. I would like to begin by extending my gratitude to EPSRC for funding my doctoral studies. Of the many people that have been instrumental to the success of my DPhil, foremost I thank Sebastian Bonilla for being a truly excellent supervisor, and for helping me to develop such an engaging and and stimulating thesis. I would also like to thank my co-supervisor, Peter Wilshaw, for welcoming me to the group three years ago. I want to take this opportunity to show my appreciation of the team members; to Shona McNab, Eleanor Shaw, Mingzhe Yu, Donghao Liu, and Yifu Shi who have been fantastic peers, and have always been ready to give constructive advice and share their knowledge; to Mohsen Goodarzi, who has many a time indulged me in my hesitancy to use HF, and very kindly performed innumerable etches for me; and lastly to Radka Chakalova for her immense help in the clean room and for making sure my specimens always came out perfectly.

Above all, I want to thank the many generations of Al-Dhahirs and Djamaranis who long ago made the pursuit of education of utmost importance, and without whose commitment my accomplishments may not have been possible.

The soul in darkness sins, but the real sinner is he who created the darkness

Victor Hugo, Les Misérables

Abstract

The development of high efficiency solar cells is critical for the expansion of solar power capacity across the world. A major limitation to achieving high efficiency is the recombination of electrons and holes at the silicon surface. A common method to reduce recombination is to deposit a dielectric thin film, such as SiO_2 or SiN_x, upon the silicon surface. This serves to chemically passivate the surface, while the dielectric's intrinsic charge provides a surface electric field to control the charge carrier population. The passivation performance of such dielectrics can be further improved by extrinsic methods that modify the film properties after deposition. This thesis explores how the intrinsic properties of dielectrics can be supplemented by extrinsic methods to provide enhanced surface passivation.

Dielectric thin films are a fundamental part of solid-state devices providing the means for advanced structures and enhanced operation. Ion-charged dielectrics are a particular kind of thin film in which ions are embedded to create a static electric field. Such charge can add functionality and improve the performance of electronic devices. To date, the electric field has been primarily demonstrated using embedded potassium and sodium cations. While the field effect provided by such ions have shown promising results in surface passivation, it is possible that alternative ions can provide greater long-term durability while enabling fine tailoring of the electric fields. Alongside potassium ions, this work demonstrates the migration kinetics, passivation performance, and stability of two new alkali ions, rubidium and caesium, inside of a SiO_2 thin film. A comprehensive model of ion injection and transport has been developed, and a detailed investigation of the kinetics of potassium, rubidium and caesium ions is presented. It is shown that the concentration of charged ions within the film can be tuned by controlling the embedding process, leading to charge densities between 0.1-10 x 10^{12} q cm^{-2}. Through the use of ion-charged SiO_2, this thesis demonstrates that the effective surface recombination velocities can be reduced from $\sim$100 cm s^{-1} to as a low as 2.23 cm s^{-1} on 1 Ω cm n-type FZ silicon. The role of dielectric charge in producing high efficiency solar cells is

demonstrated through Sentaurus TCAD modelling of PERC, IBC, TOPCon cell architectures. It is shown that by optimising the charge concentration within the dielectric, the recombination activity at defect-heavy interfaces can be successfully mitigated by field effect passivation. The exploitation of dielectric charge is predicted to achieve efficiencies >24% in PERC and TOPCon cells, and >25 % in IBC cells.

Additionally, this thesis demonstrates that surface electric fields can influence the chemical passivation provided by a SiO_2 + SiN_x dielectric stack. It is shown that an electric field present within a dielectric not only modifies the charge carrier concentrations at the silicon surface, but also induces a chemical change in the interface properties upon annealing. By tailoring the surface electric field in the dielectric stack prior to annealing, it is shown that the capture rates at the Si-SiO_2 interface can be modified depending on the field polarity and magnitude. Understanding the effect of surface electric fields on chemical passivation can lead to novel and unexplored methods of surface passivation.

Preface

This thesis is an account of the work I have carried out as a postgraduate student at the Department of Materials, University of Oxford. I have not previously submitted any part of this thesis for a degree at this University or elsewhere. The work of other authors is duly acknowledged in the text, and appropriate references are given.

During the course of this thesis, I have written or contributed towards the following publications:

I. Al-Dhahir, R.Kealy, S. Kelly, M. Yu, S. McNab, K. Collett, J. Liu, P. Wilshaw, C. Grovenor, and R.S. Bonilla, "Electrostatic Tuning of Ionic Charge in Dielectric Thin Films", *Electrochemical Society - Journal of Solid State Science and Technology*, (2022), 11, 063010.

I. Al-Dhahir, S. McNab, M. Yu, E. Shaw, P. Hamer, and R.S. Bonilla, "The Influence of Surface Electric Fields on the Chemical Passivation of Si-SiO_2 Interfaces After Firing", *in Proceedings of the 11th International Conference on Silicon Photovoltaics*, American Institute of Physics, 2021. *In Press*

M. Yu, S. McNab, **I. Al-Dhahir**, C. E. Patrick, P. P. Altermatt, and R. S. Bonilla, “Extracting Band-Tail Interface State Densities from Measurements and Modelling of Space Charge Layer Resistance”, *Solar Energy Materials and Solar Cells*, (2021), 231, 111307.

M. Yu, Y. Shi, J. Deru, **I. Al-Dhahir**, S. McNab, D. Chen, M. Voss, E. Hwu, A. Ciesla, B. Hallam, P. Hamer, P. Altermatt, P. Wilshaw, and R. S. Bonilla, "Assessing the Potential of Inversion Layer Solar Cells Based on Highly Charged Dielectric Nanolayers", *physica status solidi - RRL*, (2021), 15, 2100129.

R. S. Bonilla, **I. Al-Dhahir**, M. Yu, P. Hamer, and P. P. Altermatt, “Charge Fluctuations at the Si—SiO_2 Interface and its Effect on Surface Recombination in Solar Cells”, *Solar Energy Materials and Solar Cells*, (2020), 215, 110649.

Table of Contents

List of Figures

List of Tables

List of Acronyms

ALD	Atomic Layer Deposition
CV	Capacitance-Voltage
CZ	Czochralski
FEP	Field Effect Passivation
FGA	Forming Gas Anneal
FZ	Float Zone
IBC	Interdigitated Back Contact
MIS	Metal-Insulator-Semiconductor
PECVD	Plasma Enhanced Chemical Vapour Deposition
PERC	Passivated Emitter and Rear Cell
QSS	Quasi Steady State
SIMS	Secondary Ion Mass Spectrometry
SRH	Shockley-Read-Hall
SRV	Surface Recombination Velocity
TOPCon	Tunnelling Oxide Passivated Contact

List of Symbols

ε_r	Relative permittivity
D_{it}	Density of interface states ($cm^{-2}eV^{-1}$)
η	Efficiency (%)
ΔE_{ao}	Activation energy at the air-oxide interface (eV)
ΔE_{os}	Activation energy at the oxide-silicon interface (eV)
ΔE_d	Activation energy of diffusion (eV)
E_{ions}	Electric field from ions ($V\ cm^{-1}$)
E_{corona}	Electric field from surface corona charge ($V\ cm^{-1}$)
G	Generation rate (s^{-1})
J_{0s}	Surface saturation current density ($A\ cm^{-2}$)
J_{0e}	Emitter saturation current density ($A\ cm^{-2}$)
J_{sc}	Short circuit current density ($A\ cm^{-2}$)
μ_0	Mobility pre-factor ($cm^{-2}\ V^{-1}\ s^{-1}$)
μ	Mobility ($cm^{-2}\ V^{-1}\ s^{-1}$)
n_0, p_0	Electron (hole) concentration at thermal equilibrium (cm^{-3})
n_i	Intrinsic carrier concentration (cm^{-3})
Δn**,**Δp	Excess electron (hole) concentration (cm^{-3})
Q_{eff}	Effective interface charge concentration ($q\ cm^{-2}$)
Q_f	Fixed dielectric charge concentration ($q\ cm^{-2}$)
Q_{it}	Interface trapped charge concentration ($q\ cm^{-2}$)
Q_m	Mobile charge concentration ($q\ cm^{-2}$)
Q_{surf}	Surface charge concentration ($q\ cm^{-2}$)
R	Recombination rate (s^{-1})
R_{trap}	Capture rate of ions ($cm^{-2}\ s^{-1}$)
s	Attempt frequency (s^{-1})

S_{eff}	Effective surface recombination velocity (cm s^{-1})
S_{n0}, S_{p0}	Capture rate of electron (hole) (cm s^{-1})
σ_n, σ_p	Electron (hole) capture cross section (cm^2)
μ_n, μ_p	Electron (hole) mobility (cm^2 $V^{-1}s^{-1}$)
τ_{eff}	Effective minority carrier lifetime (s)
V_{FB}	Flat band voltage (V)
V_{oc}	Open circuit voltage (V)

1 | INTRODUCTION

1.1 Climate Change and Renewable Energy

The threat of climate change is considered unequivocal and imminent. The dangers of climate change are already observable as extreme weather patterns become increasingly frequent [1]. Climate change is reported to be strongly linked to the increasing global production of greenhouse gases generated from burning fossil fuels [2, 3]. Due to continuously growing energy demands, half of the cumulative greenhouse gas emissions produced between the years 1750 and 2010 occurred in the last 40 years [2]. As a result of these emissions, the global mean temperature has been rising steadily. Figure 1.1 shows how the global mean temperature has changed between the years 1880 and 2020, relative to the global mean temperature of the 20th century [4]. According to these historical records, the global mean temperature has increased at a rate of 0.18 °C per decade since 1981. As temperatures continue to rise, the likelihood of extreme weather increases. Events such as floods, droughts and wildfires pose a substantial risk to health, transportation, water, and power supplies [2, 5]. To mitigate the impact of climate change, dependency on fossil fuels as an energy source must reduce.

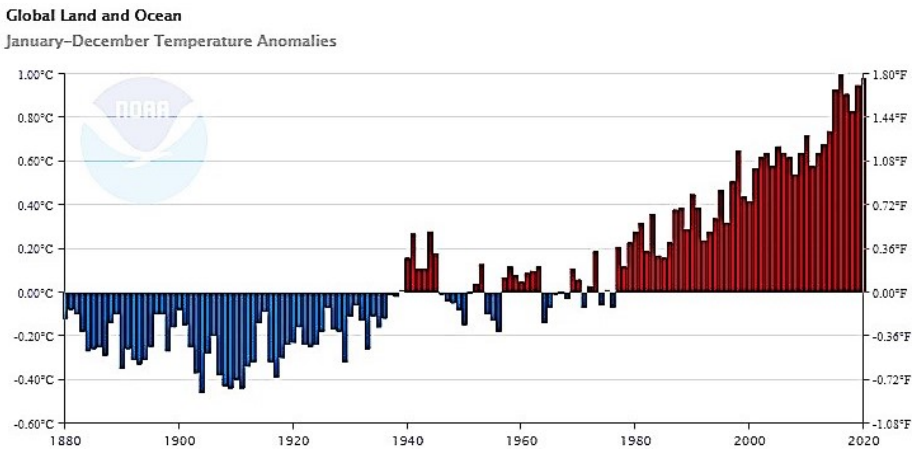

Figure 1.1: Changes in global mean temperature between 1880 and 2020 relative to the global mean for the 20th century. *Source: National Centers for Environmental Information* [4].

Renewable energy sources are being researched as an alternative to fossil fuels [2, 6–9]. Figure 1.2 tracks the expansion of nuclear, wind and solar energy technology across 67 countries from 1965 to 2016 [6]. Nuclear energy has plateaued at 40 % over the last two decades. The interest in nuclear energy has stagnated due to concerns over public safety and the high expense of building nuclear power plants. In contrast, wind and solar energy have continued to grow, with solar exhibiting the most rapid rate of expansion. Currently, renewable energy sources make up almost 30 % of global electricity generation and 18.1 % of total energy consumption [10, 11]. Global renewable energy capacity is predicted to expand by 50 % between 2019 and 2024, and is anticipated to be predominantly led by solar energy [8]. To meet these predictions, continued research is crucial to advance the current understanding of renewable technologies.

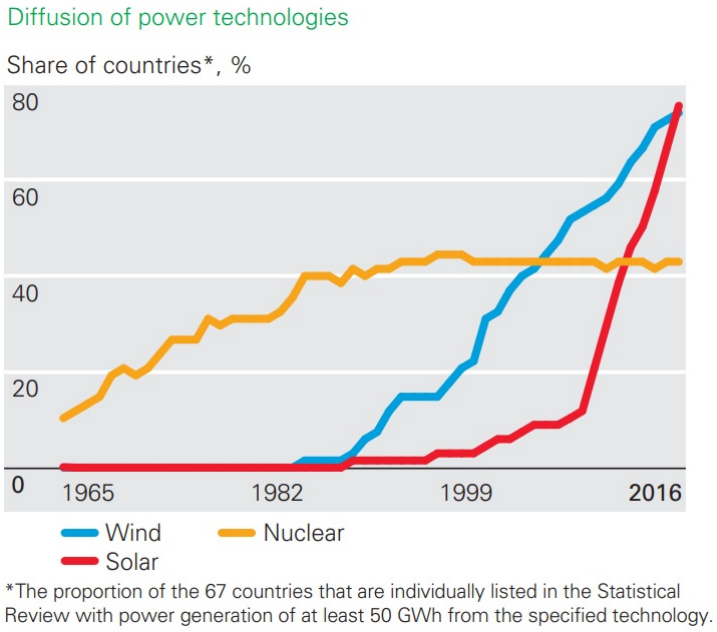

Figure 1.2: Expansion of nuclear, wind and solar technologies from 1965 to 2016. *Source: British Petroleum* [6].

Solar powered photovoltaics (PV) are a fast-developing renewable technology. Figure 1.3 depicts the predicted global cumulative installed solar capacity up to the year 2050. Between 2000 and 2018 there was a compound annual growth rate of 43 %. Such rapid

increase in capacity has been made possible by extensive research into PV technology to improve manufacturing processes [9, 12, 13]. By 2030, the capacity is predicted to increase sixfold relative to the historical values of 2018 [9]. To expedite the expansion of renewable technologies, it is essential that renewable energy sources generate power at low costs equal to or cheaper than the price of power provided by the electricity grid - an objective known as "grid parity". Whilst widespread grid parity has not yet been achieved, renewable energy sources are fast approaching it. Figure 1.4 shows the rapid reduction in costs per kW for residential solar panels between 2010 and 2018 across eight nations, during which time costs dropped by an average of 76% [9]. Within the very near future, there is potential for solar technology to become economically competitive with conventional energy sources like fossil fuels.

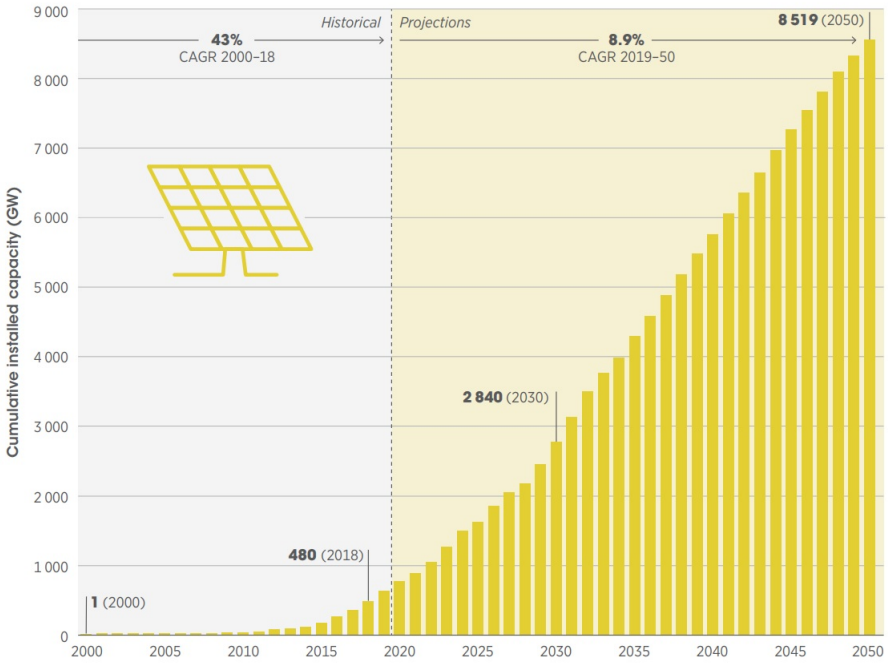

Figure 1.3: Historical and projected global installed solar PV capacity. *Source: IRENA* [9].

Silicon is the leading raw material for manufacture of commercial solar cell technology. In 2019, silicon PV accounted for 95% of all fabricated solar modules [7]. This is because solar cells made of silicon exhibit high efficiency and longevity, and can be

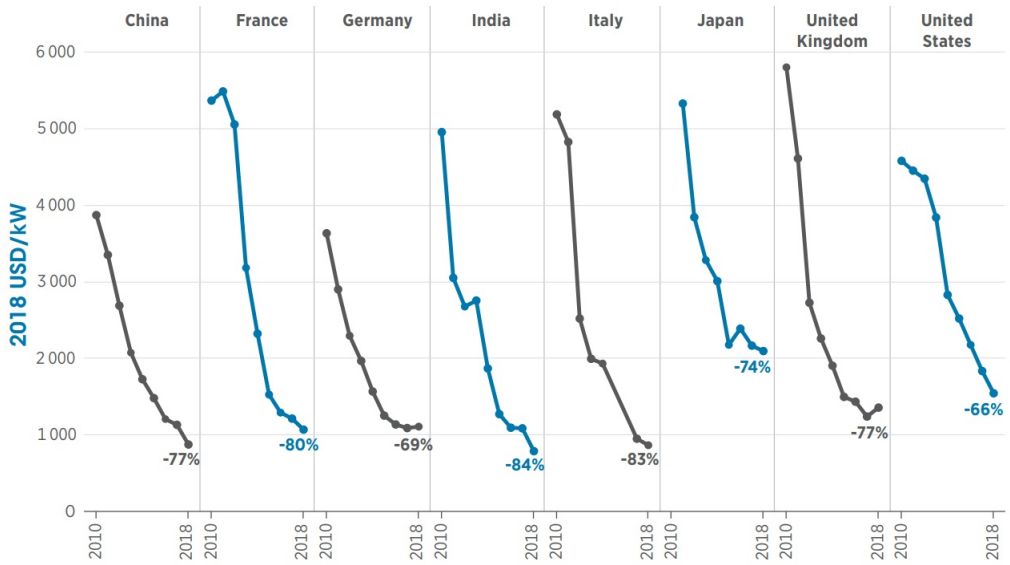

Figure 1.4: The average installed cost of residential solar PV systems by country. *Source: IRENA* [9].

manufactured at low cost. As a consequence of improvements in silicon technology, the energy payback time of installed PV modules has decreased over the years. Recently, the lowest reported energy payback times of installed multi crystalline and mono crystalline silicon modules are 1.5 and 1.3 years, respectively [14]. This translates into net clean electricity for approximately 94% of a projected module lifespan of 25 years. In view of the projections for PV capacity, silicon technology is a crucial area of research to continue increasing module efficiencies, reducing installation costs, and improving manufacturing processes.

1.2 Silicon Photovoltaics

1.2.1 Fundamentals of Solar Cells

A solar cell converts light into an electrical current via the photovoltaic effect. This conversion takes place within a semiconductor material. When light is absorbed by the semiconductor, its energy is transferred to electrons, which are freed from their

molecular orbitals. These electrons are termed "excited" and can move freely around the semiconductor thus generating a current. When an electron is excited, it makes the transition from the valence band of the semiconductor to the conduction band. The difference between these two energy bands is called the band gap.

The band gap is an important characteristic that determines the semiconductor's electrical conductivity. A large band gap means excited charge carriers have more energy, which produces a greater cell voltage. However, a large band gap also means a smaller percentage of incident photons will have the enough energy to be absorbed. Therefore, fewer electrons will be excited to the conduction band. The ideal semiconductor band gap for a solar cell is $\sim$1.32 eV, calculated to give the maximum theoretical efficiency of 33.7% following the Shockley-Queisser limit [15, 16]. Silicon possesses a band gap of 1.14 eV and therefore makes for a nearly ideal semiconductor [17, 18]. Since sunlight is composed of photons of varying energies corresponding to different wavelengths of the solar spectrum, only photons with energy equal to or greater than the band gap will be able to free a bound electron and excite it to the conduction band.

When an electron is excited to the conduction band, it leaves behind a positively charged counterpart called a *hole* in the valence band. Similarly to free electrons, holes are able to move around the lattice. To contribute to the output power of the cell, the electron and hole currents must be separated and collected at their respective metal contacts. The separation of electrons and holes within silicon is achieved through the use of a *p-n junction*. Through the introduction of dopant atoms, such as phosphorus or boron, silicon can be made n-type (electron rich) or p-type (hole rich). Creating a junction between these two types generates an in-built electric field that aids carrier separation. The region where the electric field exists is referred to as the depletion region, and it exhibits a variation in the available energies of electrons known as band bending. The operation of a p-n junction is shown in Figure 1.5. Electrons and holes can be generated in any region of the silicon, however, the minority charge carrier in each type must be

drifted across the junction where it becomes a majority carrier, and subsequently can be extracted from the cell.

When an excited electron loses its energy, it drops to a lower energy band where its charge is neutralised by a hole. The elimination of both charge carriers is called *recombination*, and results in the unwanted loss of electrical energy. The theory and different mechanisms by which an electron and hole can recombine are explained next.

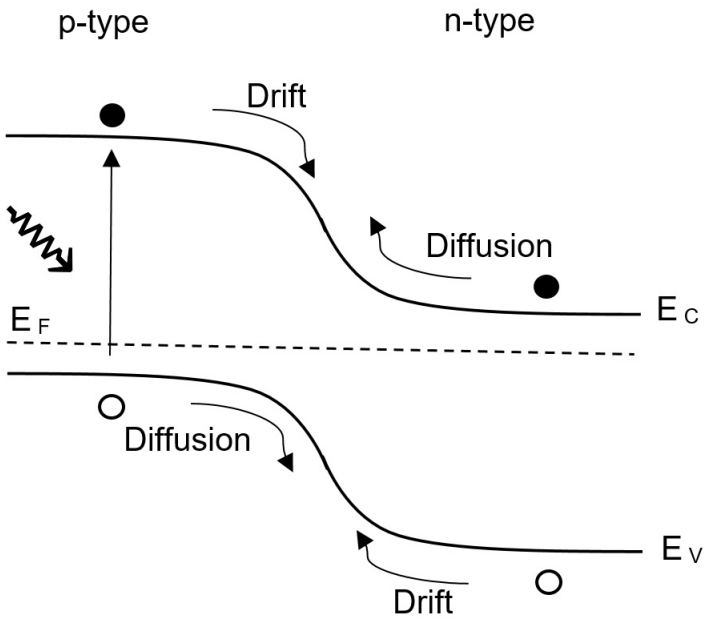

Figure 1.5: Schematic depicting the energy band bending of a p-n junction and the migration of electrons and holes across the junction. E_C is the conduction band, E_V is the valence band and E_F is the Fermi level. The arrow represents an incoming photon.

1.2.2 Recombination Theory

In a semiconductor, generation defines the process by which a bound electron in the valence band gains enough energy to be excited to the conduction band. Recombination describes the process where an excited electron loses its energy and re-occupies the energy state of a hole. When a semiconductor is at thermal equilibrium, charge carriers within a semiconductor have a generation rate (G) equal to their recombination rate (R), such that the net recombination rate (U) equals 0. Under this condition, the law of mass

action states that the concentration of majority and minority carriers is constant, such that

$$n_0 p_0 = n_i^2 \tag{1.1}$$

where n_0 and p_0 are respectively the electron and hole carrier concentration at thermal equilibrium. The intrinsic carrier concentration (n_i) is the number of electrons in the conduction band, and is a fundamental property of an undoped semiconductor. In the case of an extrinsic (doped) semiconductor, there can be a difference of several orders of magnitude between n_0 and p_0 if the concentration of dopants greatly exceeds n_i. Under the assumption that all dopant atoms are ionised at thermal equilibrium, n_0 and p_0 can be calculated in n-type and p-type silicon as:

$$\begin{aligned} n_0 &= N_D, \quad p_0 = \frac{n_i^2}{n_0} \qquad \text{(n-type)} \\ p_0 &= N_A, \quad n_0 = \frac{n_i^2}{p_0} \qquad \text{(p-type)} \end{aligned} \tag{1.2}$$

where N_D is the concentration of donor dopant atoms, and N_A is the concentration of acceptor dopant atoms. Upon illumination the system is no longer in thermal equilibrium. Excess carriers are created such that the total carrier concentration is defined as $n = n_0 + \Delta n$ and $p = p_0 + \Delta p$. Here n and p represent the total electron and hole concentrations in steady state. Relative to the majority carriers, the minority carrier concentration at thermal equilibrium is often negligible. Thus, under illumination the minority carrier concentration is approximately equal to the excess carrier concentration.

Each absorbed photon is assumed to create one electron-hole pair such that $\Delta n = \Delta p$. Once the illumination is turned off, Δn and Δp will decay with time due to either recombination, or to the extraction of carriers at metal-semiconductor contacts. In the

absence of such contacts, equilibrium is restored only once all excess carriers have recombined. The average time taken for the excess carriers to recombine is known as the carrier lifetime (τ), defined in Equation 1.3 for an n-type semiconductor. In an extrinsic semiconductor, the lifetime of minority carriers is used to evaluate the net recombination since they are the limiting factor due to their smaller concentration.

$$\tau = \frac{\Delta p}{U} \tag{1.3}$$

The minority carrier lifetime at the surface of the semiconductor is typically different to that within the bulk due to different recombination losses within each region. An *effective* minority carrier lifetime (τ_{eff}) can be calculated from both the bulk lifetime (τ_B) and the surface lifetime (τ_S) as:

$$\frac{1}{\tau_{eff}} = \frac{1}{\tau_B} + \frac{1}{\tau_S} \tag{1.4}$$

The different types of recombination mechanisms within the semiconductor bulk and at the surface are now discussed.

1.2.3 Bulk Recombination

Recombination within the bulk occurs due to a combination of intrinsic and extrinsic processes. Intrinsic recombination processes are inherent to the semiconductor and are therefore inevitable. Extrinsic processes require the presence of defects such as impurities, crystallographic imperfections, and surface damage. These are created during silicon casting and processing methods.

The total bulk lifetime consists of three recombination processes: radiative, Auger, and defect-assisted (also known as Shockley-Read-Hall). The mechanism by which an electron and hole recombine in each process is depicted in Figure 1.6. Radiative and

Auger recombination are intrinsic processes through which an electron's energy can either be emitted as a photon or transferred to another charge carrier. Defect-assisted recombination is an extrinsic process that occurs due to the presence of energy states within the band gap by lattice imperfections and impurities. The total bulk lifetime is the sum of the three independent recombination rates and can therefore be expressed as:

$$\frac{1}{\tau_B} = \frac{1}{\tau_{rad}} + \frac{1}{\tau_{Aug}} + \frac{1}{\tau_{SRH}} \tag{1.5}$$

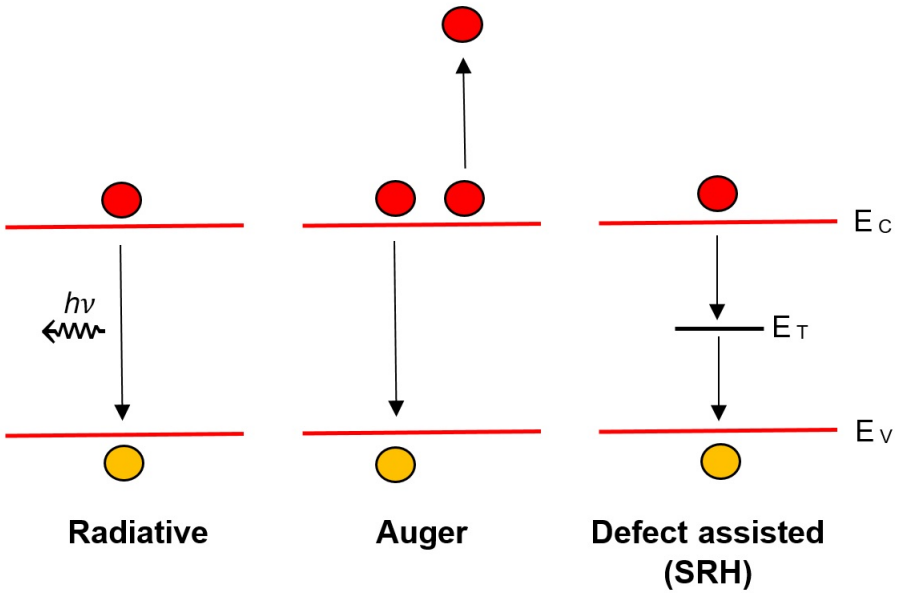

Figure 1.6: Schematic diagram of the three different types of recombination; radiative where a photon is released, non-radiative through defect level at energy E_T, and Auger. E_C is the conduction band and E_V is the valence band. Red circles represent electrons and yellow circles represent holes.

1.2.3.1 Radiative Recombination

Radiative recombination occurs when an electron recombines with a hole in the valence band to release energy in the form of a photon. The net radiative recombination rate is given as [16]:

$$U_{rad} = B(np - n_i^2) \tag{1.6}$$

where B is the radiative recombination probability and is specific to the semiconductor. The lifetime of a minority carrier before it is lost through radiative recombination is given by:

$$\tau_{rad} = \frac{1}{B(n_0 + p_0 + \Delta p)} \tag{1.7}$$

In indirect band gap semiconductors, like silicon, radiative recombination is the least dominant of the three mechanisms [16, 18]. This is because electrons in the conduction band have a momentum different to that of holes in the valence band. For radiative recombination to take place in an indirect semiconductor, a phonon with momentum equal to the difference in momentum between the electron and hole is required for the electron to make the transition. As the number of elements required for radiative recombination increases, the likelihood of occurrence decreases [18]. In crystalline silicon at 300 K, the probability B has a value of 10^{-14} cm^3s^{-1} [19].

1.2.3.2 Auger Recombination

During Auger recombination, an electron recombines with a hole and, instead of releasing its excess energy as a photon, it transmits its energy to either an electron in the conduction band or a hole in the valence band. This third carrier thermalises back to the band edge shortly after excitation and releases its own excess energy as phonons. If the third carrier is an electron, the process is labelled *eeh* and if it is a hole the process is labelled *ehh*. The recombination rate for each process is proportional to the carrier densities, and is given by:

$$\begin{aligned} R_{eeh} &= C_n(n^2p - n_0^2p_0) \\ R_{ehh} &= C_p(np^2 - n_0p_0^2) \end{aligned} \tag{1.8}$$

where C_n and C_p are respectively the Auger capture probability coefficients for *eeh* and *ehh* processes. The net Auger recombination rate (U_{Aug}) is expressed in Equation 1.9 as the sum of the two rates.

$$U_{Aug} = C_n(n^2p - n_0^2p_0) + C_p(np^2 - n_0p_0^2) \tag{1.9}$$

The Auger recombination rate is proportional to the product of electrons and holes, and as a result depends strongly upon the carrier density. The Auger lifetime therefore decreases with increasing doping concentration (injection level). At doping concentrations above 10^{17} cm^{-3}, Auger recombination is hence reported to be the dominant recombination mechanism in mono-crystalline silicon [18].

The coefficients, C_n and C_p, were originally calculated for only high injection and high doping conditions [20]. Experimental results showed that under low injection and low doping conditions Auger lifetimes were significantly lower than predicted [21, 22]. The reason was that the traditional Auger theory used to attain Equation 1.9 assumed non-interacting charge carriers. Hangleiter and Häcker explained the discrepancy in experimental and predicted recombination rates by considering Coulombic interactions between charge carriers at low injection levels [23]. In low injection conditions, the electron density increases in the proximity of a hole and, as a result, the Auger recombination rate also increases. To take these interactions into account, the Auger coefficients are multiplied by Coulombic interaction enhancement factors g_{eeh} and g_{ehh} so that the net recombination rate becomes

$$U_{Aug,LLI} = g_{eeh}C_n(n^2p - n_0^2p_0) + g_{ehh}C_p(np^2 - n_0p_0^2) \tag{1.10}$$

where LLI denotes low injection conditions. Enhancement factors g_{eeh} and g_{ehh} are calculated as functions of electron and hole densities as shown in Figure 1.7, as per Altermatt's parametrisations [24]. As the doping level increases to approximately 10^{18} cm^{-3} the enhancement factors approach 1, at which point the traditional Auger theory of non-interacting carriers becomes valid [21]. At such high doping densities, the large number of majority carriers screens any electron-hole interactions. The most complete and widely accepted model of Auger recombination today is that by Richter et al [25], which includes Altermatt's parametrisation of the enhancement factors. It calculates the Auger lifetime as

$$\tau_{Aug} = \frac{\Delta p}{(np - n_{ieff}^2)(2.5 \times 10^{-31} g_{eeh} n_0 + 8.5 \times 10^{-32} g_{ehh} p_0 + 3 \times 10^{-29} \Delta p^{0.92})} \tag{1.11}$$

where

$$\begin{aligned} g_{eeh} &= 1 + 13\left\{1 - \tanh\left[\left(\frac{n_0}{N_{0,eeh}}\right)^{0.66}\right]\right\} \\ g_{ehh} &= 1 + 7.5\left\{1 - \tanh\left[\left(\frac{p_0}{N_{0,ehh}}\right)^{0.63}\right]\right\} \\ N_{0,eeh} = 3.3 \times 10^{17} cm^{-3} \quad &\text{and} \quad N_{0,ehh} = 7 \times 10^{17} cm^{-3} \end{aligned} \tag{1.12}$$

1.2.3.3 Defect-Assisted Recombination

Defect-assisted recombination refers to a two-step process where an electron from the conduction band passes through a trap state in the band gap before recombining with a

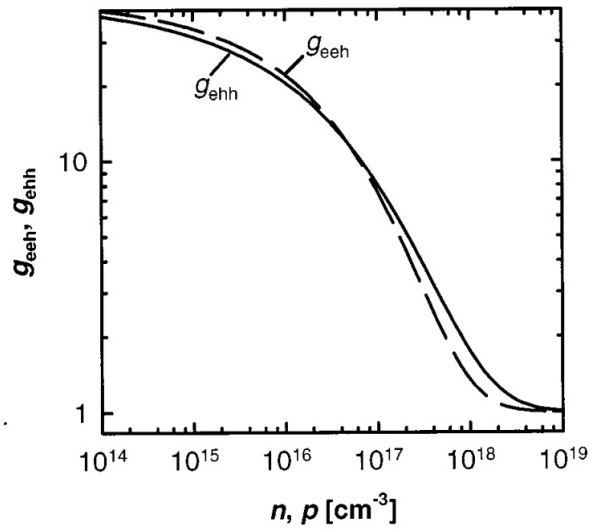

Figure 1.7: Low injection enhancement factors, g_{eeh} and g_{ehh}, at 300 K as a function of electron and hole carrier densities respectively, after [21].

hole in the valence band. Such trap states are called recombination centres and originate from extrinsic defects that occur during material processing. Figure 1.8 depicts the four possible defect-assisted transitions. Depending on the occupation of the trap state, it can be neutral, positively charged or negatively charged. Based on the four types of possible transitions, a statistical model for the rate of defect-assisted recombination was first calculated by Shockley and Read [26], and further developed by Hall [27]. Hence this process is also frequently known as Shockley-Read-Hall (SRH) recombination. Equation 1.13 defines the net SRH recombination rate as a function of recombination centre density (N_t), the capture cross section of electrons and holes ($\sigma_{n,p}$), and the energy level of a single recombination centre (E_T).

$$U_{SRH} = \frac{np - n_i^2}{\frac{p+p_1}{N_T \sigma_n \nu_{th}} + \frac{n+n_1}{N_T \sigma_p \nu_{th}}} \tag{1.13}$$

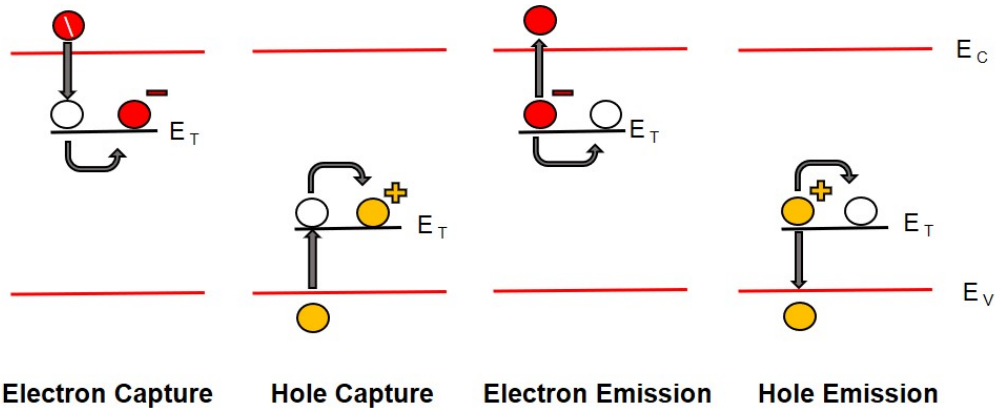

Figure 1.8: The four types of transitions between trap states and the conduction and valence bands. Red circles represent electrons, yellow circles represent holes and blank circles represent neutral trap states.

The capture cross section is defined as the area surrounding a defect that a carrier must pass through to be trapped. Here ν_{th} is the thermal velocity, and p_1 and n_1 are the SRH trap occupancy factors [28] expressed as:

$$\begin{aligned} p_1 &= p_0 e^{(E_T - E_F)/k_B T} \\ n_1 &= n_0 e^{(E_F - E_T)/k_B T} \end{aligned} \tag{1.14}$$

Substituting Equation 1.13 into Equation 1.3 yields the SRH lifetime as:

$$\tau_{SRH} = \frac{\tau_{p_0}(n_0 + n_1 + \Delta p) + \tau_{n_0}(p_0 + p_1 + \Delta p)}{p_0 + n_0 + \Delta p} \tag{1.15}$$

where τ_{n_0} and τ_{p_0} are respectively the capture rates of electrons and holes, defined as:

$$\begin{aligned} \tau_{n0} &= (N_t \sigma_n \nu_{th})^{-1} \\ \tau_{p0} &= (N_t \sigma_p \nu_{th})^{-1} \end{aligned} \tag{1.16}$$

The uniform periodicity of the semiconductor lattice can be disrupted by the presence of dislocations, vacancies, grain boundaries, and impurities. As a result, the likelihood of defect-assisted recombination is dependent upon the material quality. For example, the formation of oxygen precipitates is highly detrimental to solar cell performance, and has been reported to be responsible for decreasing solar cell efficiency from 17.5 % to 12.7 % [29–31]. Oxygen precipitates can be dissolved by thermal processing, or passivated by hydrogen [30, 32]. Another prevalent defect in boron doped silicon is the boron-oxygen defect. These arise from the interaction of boron dopant atoms with oxygen impurities. The recombination activity of boron-oxygen defects can be reduced by high temperature annealing and hydrogen passivation [33, 34].

1.2.4 Surface Recombination

The sudden termination of the crystal periodicity at the silicon surface results in many unsaturated bonds, termed *dangling bonds* [35, 36]. These dangling bonds create surface states of varying energy levels throughout the band gap. Owing to these surface states the predominant recombination mechanism at the surface is defect-assisted and follows SRH theory. Equation 1.13 can therefore be rewritten for surface recombination as:

$$U_S = \frac{n_s p_s - n_i^2}{\frac{p_s + p_1}{N_{st}\sigma_n \nu_{th}} + \frac{n_s + n_1}{N_{st}\sigma_p \nu_{th}}} \tag{1.17}$$

where n_s and p_s are the electron and hole concentrations at the surface. N_{st} is the density of surface states per unit area (cm^{-2}), as opposed to unit volume (cm^{-3}) in bulk recombination. The resulting units of U_{Surf} are $cm^{-2}s^{-1}$. At a real surface there is a continuous distribution of energy states. Therefore, the density of surface states is often referred to as D_{it}, and is a function of energy. The net surface recombination must be integrated across the entirety of the band gap. The resulting SRH surface recombination rate for a real surface is defined as:

$$U_S = \int_{E_v}^{E_c} \frac{n_s p_s - n_i^2}{\frac{p_s + p_1}{D_{it}\sigma_n \nu_{th}} + \frac{n_s + n_1}{D_{it}\sigma_p \nu_{th}}} \quad dE \tag{1.18}$$

Here, the terms $D_{it}\sigma_n\nu_{th}$ and $D_{it}\sigma_p\nu_{th}$ are velocities as opposed to time constants. These are labelled the electron and hole capture velocities, respectively, and are denoted as S_{n0} and S_{p0}. The surface recombination velocity (SRV) is a measure of the total recombination activity at the surface due to the capture of both carriers; the lower the SRV, the lower the recombination. It is defined as:

$$SRV = \frac{U_s}{\Delta p} \tag{1.19}$$

The SRV calculated above is applicable to charge neutral surfaces, where the concentration of carriers is the same across the depth of the semiconductor, and the energy bands are hence flat from bulk to surface. In reality, at the surface of the semiconductor there exists an area called the space charge region (SCR) where the energy bands bend due to the accumulation of electrical charges at the surface [18]. A schematic illustration of the SCR at the semiconductor surface is given in Figure 1.9. A modified concentration of charge carriers exists within this region since they drift away due to the surface potential (Ψ_s) generated by the surface charges. The length of the SCR is defined as the distance into the silicon until the bands are flat. Recombination that takes place within this region is also included in the surface recombination. Therefore an *effective* SRV (S_{eff}) must be defined that accounts not only for the recombination velocity at the immediate silicon surface, but also the contribution due to the SCR [18]. The effective surface recombination velocity cannot be measured directly, and it is therefore calculated from τ_{eff}, as explained next.

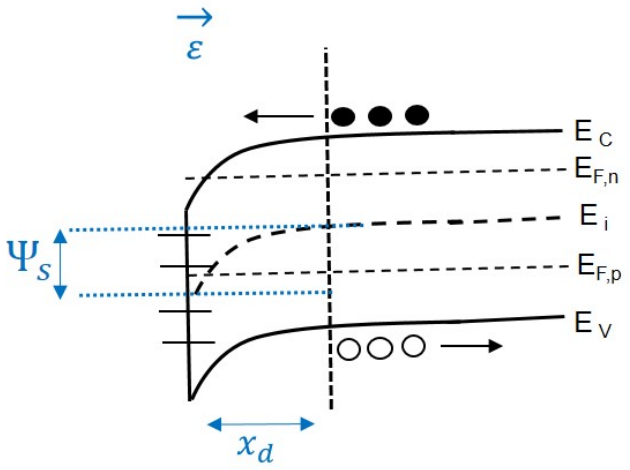

Figure 1.9: Schematic representation of the SCR at the semiconductor surface in the presence of a positive surface electric field. The vertical dotted line indicates the end of the SCR, and the horizontal lines represent defects at the semiconductor surface. Filled circles represent electrons and blank circles represent holes.

1.2.5 Obtaining the Effective Surface Recombination Velocity

In this section, it will be explained how τ_{eff} is calculated in order to determine S_{eff}. For an explanation of the experimental measurement of τ_{eff}, please refer to Section 2.8.1. τ_{eff} is given by the sum of the bulk and surface components as expressed in Equation 1.4. The semiconductor bulk lifetime (τ_B) is calculated from the radiative lifetime, Richter's parametrisation for Auger recombination, and the SRH lifetime given in Equations 1.7,1.11, and 1.15, respectively. The calculation of the surface lifetime then follows a formalism proposed by Luke and Cheng that considers the distribution of excess charge carriers as a function of time and spatial depth [37]. Here, τ_{eff} is calculated as a function of the sum of all the exponential decay terms. Each decay term n has its own decay constant (λ_n) given by:

$$\lambda_n = \frac{1}{\tau_B} + {\alpha_n}^2 D \tag{1.20}$$

where the second term on the right represents surface recombination as a function of the

absorption coefficient (α) and the diffusivity (D). The first decay term is dominant, and subsequent decay terms considered negligible. Therefore, the decay can be represented by a single exponential term, λ_1. Here, the absorption coefficient can be found by solving Equation 1.21 [18, 37]:

$$\tan\left(\frac{\alpha W}{2}\right) = \frac{S_{eff}}{\alpha D} \tag{1.21}$$

Inserting the solution for α from Equation 1.20 into Equation 1.21 results in:

$$S_{eff} = \sqrt{D\left(\frac{1}{\tau_{eff}} - \frac{1}{\tau_B}\right)} \tan\left[\frac{W}{2}\sqrt{\frac{1}{D_{it}}\left(\frac{1}{\tau_{eff}} - \frac{1}{\tau_B}\right)}\right] \tag{1.22}$$

where W is the wafer thickness.

If the value of S_{eff} is low, the tan function in Equation 1.21 can be approximated as a linear function such that $\tan\left(\frac{\alpha W}{2}\right) \rightarrow \frac{\alpha W}{2}$ [18, 38]. Solving again for α and inserting into Equation 1.20 results a simple and commonly used expression for the effective lifetime:

$$\frac{1}{\tau_{eff}} = \frac{1}{\tau_B} + \frac{2S_{eff}}{W} \tag{1.23}$$

Sproul calculated that this simplified approximation has an accuracy of within 4 % under the condition that recombination is equal at both surfaces of the silicon, and $\frac{S_{eff}W}{D} < 0.25$ [38]. The parameter S_{eff} was reported by McIntosh and Black to be dependent upon injection level [39]. Therefore S_{eff} should always be quoted alongside an indication of the doping concentration.

Surface recombination is often further characterised by the *surface saturation current density*, J_{0s}. Where an emitter is present at the front of the solar cell, this term is synonymous with the *emitter saturation current density* (J_{0e}), and it includes both surface and emitter recombination. This parameter is defined as the current produced due

to the flow of carriers recombining at thermal equilibrium within the SCR, or emitter, and represents the sum of all the recombination mechanisms therein. Following reference [39], it is calculated as:

$$J_{0s} = \frac{qn_i^2 S_{eff}}{N_d} \tag{1.24}$$

Over a large range of surface charge conditions, as specified in reference [39], J_{0s} is independent of injection level. For this reason, J_{0s} is sometimes considered preferable to S_{eff} when comparing surface passivation results. For the specimens used in this thesis, injection-independent J_{0s} conditions hold true.

The saturation current density is related to the cumulative flow of charge carriers recombining at the surface (J_{rec}) under forward bias by the traditional diode equation:

$$J_{rec} = J_{0s}[e^{\frac{V_s}{V_t}} - 1] \tag{1.25}$$

where V_t is the thermal potential.

1.3 Silicon Surface Passivation

Modifications to a silicon surface to reduce the recombination rate are called *surface passivation*. Figure 1.10 illustrates how the passivation of the silicon surface can be improved. At a bare surface, as depicted in Figure 1.10a, there is a high density of defects due to the abrupt discontinuity of the silicon structure. As a result, SRH recombination dominates at the silicon surface. Since SRH recombination requires the presence of three elements - an electron, a hole, and a defect state - recombination can be reduced by minimising the presence of either the charge carrier or the defect. There exist two methods to accomplish this. The first, as shown in Figure 1.10b, is to reduce the concentration of defects through *chemical passivation*. This is achieved by depositing a

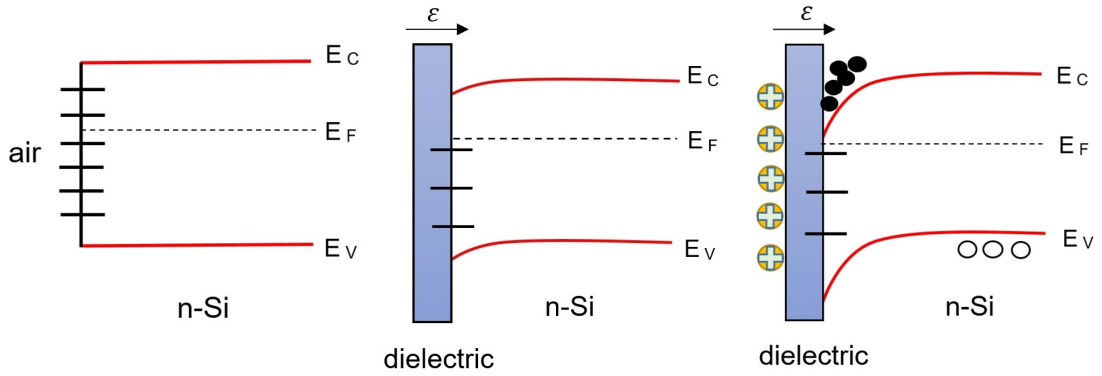

Figure 1.10: Schematic diagram of n-type silicon depicting (a) a bare silicon surface (b) effect of chemical passivation on interface states and (c) the combined effect of chemical and field effect passivation. Filled circles represent electrons and hollow circles represent holes. Black horizontal lines represent surface states.

dielectric layer onto the surface to bind to the non-co-ordinated silicon bonds [17, 35, 40]. This method can be further improved via thermal processing of the dielectric layers to drive hydrogen atoms towards the silicon-dielectric interface to further passivate remaining silicon dangling bonds [41]. The second method is shown in Figure 1.10c. Here, an electric field is imposed at the silicon surface to modulate the SCR, control the surface carrier concentrations, and limit the availability of one type of charge carrier. This is called *field effect passivation* (FEP). The accumulation of one type of charge carrier in response to the polarity of the electric field creates an SCR that bends the energy bands. If the accumulated charge consists primarily of majority carriers, the surface of the silicon is termed an *accumulation layer*. If enough minority carriers are attracted to the surface to exceed the concentration of majority carriers, this region is called an *inversion layer*. The following sections discuss methods of surface passivation through the use of surface doping, dielectric film deposition, and extrinsic dielectric charging.

1.3.1 Surface Doping

The conductivity of the silicon surface can be modified by the introduction of dopant atoms to create electron-rich or hole-rich regions. The resulting internal electric field repels one type of charge carrier from the surface. This technique is ubiquitously exploited in commercial cell architectures to reduce surface recombination [42–44]. When applied to the front of a cell, the doping region is termed *front surface field* (FSF), and when applied to the rear of the cell it is termed *back surface field* (BSF). There are various reported methods of creating these surface fields. For example, an Al-BSF is created by depositing aluminium on p-type silicon, and driving aluminium atoms into the silicon under high temperatures of ∼800 - 900 °C [45, 46]. This process creates a p^+p junction with low surface recombination. Alternative methods of creating p^+ regions involve the in-diffusion of boron atoms, typically performed by exposing silicon to BBr_3 gas in a tube furnace [47, 48]. An n^+ region at the silicon surface can be produced through the in-diffusion of phosphorus atoms. Here, the silicon wafer is exposed to high temperatures of ∼800 - 900 °C in the presence of $POCl_3$ gas within a tube furnace [42, 49].

The depth variation in dopant concentration within these regions is known as a dopant profile. Control of the dopant profile is important to produce the optimal surface field. As explained in Section 1.2.3.2, Auger recombination increases at heavily doped surfaces leading to low lifetimes [18, 50]. If such doped regions are additionally too deep, the photo-generated electrons and holes will recombine before being separated by the p-n junction. Due to increased recombination activity, heavily doped FSFs tend to decrease the conversion efficiency of blue light energy, which is primarily absorbed near the front surface of the silicon wafer due to its shorter wavelength.

1.3.2 Dielectric Films

Methods of improving the surface passivation of silicon using dielectric films are discussed here. While numerous different dielectrics exist, this section will focus on

silicon oxide (SiO_2) and silicon nitride (SiN_x) as these feature extensively in this thesis. For completeness, a brief discussion of aluminium oxide (AlO_x) is also presented due to its relevance in PV manufacturing. All three dielectrics are widespread within the solar industry due to the passivation properties that are presented in this section [35, 51–53].

1.3.2.1 Thermal Silicon Oxide

Thermal silicon oxide is one of the most employed dielectrics due to its well-established performance in producing the lowest D_{it} at the silicon surface out of all passivation techniques [18, 40]. D_{it} values at the (100) plane of the Si-SiO_2 interface can be on the order of 10^{10} cm^{-2} eV^{-1} or less [54–56]. A thermal SiO_2 film grows by consuming the surface of the silicon during oxidation such that the final interface is displaced to a cleaner and more organised region of the semiconductor. This provides superior passivation at the thermal Si-SiO_2 interface [18].

Thermal SiO_2 can be grown via dry or wet oxidation and follows the chemical reactions provided in Equations 1.26a and 1.26b:

$$Si + O_2 \rightarrow SiO_2 \qquad \text{(dry oxidation)} \tag{1.26a}$$

$$Si + 2H_2O \rightarrow SiO_2 + 2H_2 \quad \text{(wet oxidation)} \tag{1.26b}$$

The growth rate of wet oxidation is much faster than that of dry oxidation and as a result is often the more practical technique for growing thick oxides [18]. As a frame of reference, where 100 nm dry oxide would take over an hour, wet oxidation would take a matter of minutes [18, 57]. However, wet oxidation produces lower density films that leave more silicon dangling bonds unsatisfied. Furthermore, due to the presence of water vapour, wet oxides have a lower dielectric strength and are more pervious to impurities [58]. High quality SiO_2 films are therefore typically grown using the dry approach.

Figure 1.11 exhibits an energy band diagram of a typical Si-SiO_2 interface. An inherent

fixed positive charge (Q_f) exists within the oxide. These charges arise from interfacial dangling silicon bonds located within 2 nm of the Si-SiO_2 interface [18]. These dangling bonds produce donor states that lie in the upper half of the oxide band gap, above the conduction band of the silicon [17]. Electrons do not interact with these donor states as electrons are more likely to fall down to the valence band than be excited above the conduction band. The density of Q_f does not depend upon oxide thickness, but upon oxidation and annealing conditions, and is typically between 5 x 10^{10} and 2 x 10^{11} q cm^{-2} [18, 59]. The charge due to the interface states within the band gap (Q_{it}) is accounted for separately, and is strongly dependent upon the position of the Fermi level; donor states are neutral when occupied by an electron, and acceptor states are neutral when unoccupied [18]. Typically, in the case of well-passivated interfaces, Q_{it} is much smaller than Q_f, and for this reason is often considered negligible.

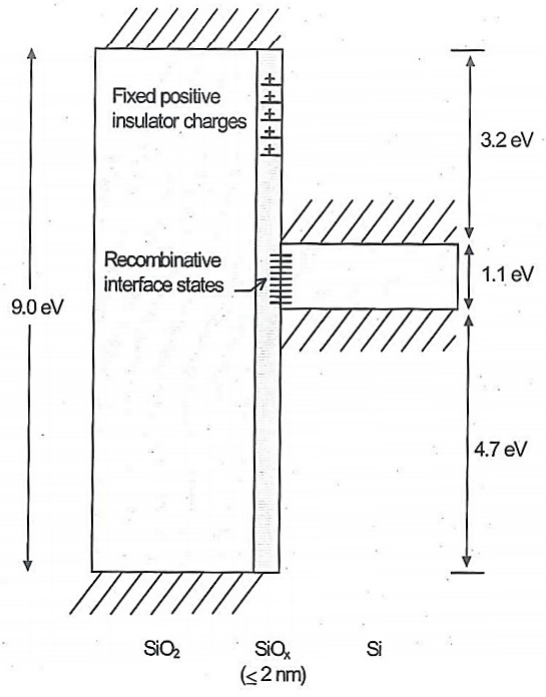

Figure 1.11: Schematic energy diagram of the Si-SiO_2 interface under zero electric field. After [18].

The passivation of the Si-SiO_2 interface can be improved by the presence of hydrogen.

One of the most effective methods of introducing hydrogen to the dielectric is through a process known as the *alneal* [60–62]. Here, a layer of aluminium is deposited onto the surface of the SiO_2 film, and annealed in a forming gas (5 % H_2, 95 % N_2) atmosphere at $\sim$400 °C. It is postulated that during the alneal, hydrogen enters the dielectric via a reaction between aluminium and water, or hydroxyl ions, adsorbed to the SiO_2 surface [60, 61, 63]. Following the alneal, D_{it} values as low as 10^{10} $cm^{-2}eV^{-1}$ have been reported [64]. Photo conductance decay measurements performed by Kerr and Cuevas demonstrated τ_{eff} of 6 ms on 1.5 Ω cm n-type silicon, equivalent to S_{eff} of 2.40 cm s^{-1} [40, 65]. This is in comparison to typical S_{eff} of 50 – 150 cm s^{-1} reported after oxidation of low resistivity n-type silicon [66, 67]. Recently, the *enhanced alneal* method by Collett et al. demonstrated that the passivation of the silicon surface can be further improved by the inclusion of extrinsic charges within SiO_2. Here, potassium ions are deposited on the surface of SiO_2 prior to aluminium deposition [68]. The ions are introduced to the oxide film during the subsequent anneal to combine the hydrogen passivation of the standard alneal with field effect. This method has produced an S_{eff} < 0.4 cm s^{-1} on 1 Ω cm n-type silicon [68].

1.3.2.2 Silicon Nitride

Silicon nitride is a frequently used dielectric in industrial solar cell manufacturing [43, 69]. Due to its tuneable refractive index, it is often deposited on the surface of other dielectrics to serve an anti-reflective coating [35, 41, 70]. The chemical and optical properies of SiN_x strongly depend upon the deposition methods [18, 41, 70, 71]. The film is typically deposited via plasma enhanced chemical vapour deposition (PECVD) where ammonia and silane serve as the precursor gases [18, 72, 73]. This technique uses relatively low temperatures of $\sim$350 °C to grow SiN_x films in a matter of minutes. By controlling the ratio of gases supplied during deposition, non-stoichiometric films of varying refractive indices can be produced. The optimal refractive index is a compromise between minimising reflectivity and preventing light absorption by the dielectric itself.

For example, higher refractive index (silicon-rich) films have increased blue light absorption [71]. A study by Soppe et al. found that the transmittance of SiN_x was maximised at refractive indices between 2.1 and 2.2 [71].

In addition to its anti-reflective properties, SiN_x is also reported to provide effective surface passivation [18, 69–71, 74]. During PECVD deposition, a substantial concentration of hydrogen is incorporated due to the use of hydrogen-containing precursor gases. The hydrogen atoms are reported to migrate to the silicon surface and passivate interfacial dangling bonds [18, 69, 71, 74]. In addition, SiN_x films have a positive Q_f on the order of 10^{12} q cm^{-2} that contributes to FEP on n-type silicon. Fixed positive charges arise in SiN_x from what are known as K-centres [18, 75]. K-centres are dangling silicon bonds back-bonded to 3 nitrogen atoms. Silicon-rich films typically have a lower Q_f due to increased Si-Si bond co-ordination [18, 76].

The passivation performance of SiN_x is well reported. An S_{eff} as low as 1.6 cm s^{-1} was reported for SiN_x deposited directly on 1 Ω cm n-type silicon [25]. The exploitation of a double layer SiO_2 + SiN_x stack is expected to further improve surface passivation. An S_{eff} < 2.4 cm s^{-1} and < 3.5 cm s^{-1} has been reported for such double layer stacks on 2.5 and 1 Ω cm n-type silicon, respectively. In this thesis, all SiN_x films are deposited upon SiO_2 to maximise the surface passivation.

1.3.2.3 Aluminium Oxide

Aluminium oxide (AlO_x) is unique amongst dielectrics as it contains a high concentration of negative charges as opposed to positive. The charge is reported to be on the scale of $\sim$-3 x 10^{12} q cm^{-2} [75, 77, 78]. The origin of the negative charge is still under debate. Previously, it has been suggested that it arises from negatively charged vacancies and interstitials present in non-stoichiometric AlO_x films [75, 79]. More recent reports postulate that the negative charge arises from point defects located at the interface between AlO_x and the ultra-thin SiO_2 layer than grows on the silicon surface as a by product during deposition [80–82]. Owing to its' negative charge, AlO_x is

particularly useful in passivating p-type silicon [75]. The negative charge minimises the concentration of electrons at the surface via FEP. However, the charge density is also sufficient to passivate n-type emitters through the creation of an inversion layer [25].

Aluminium oxide can be deposited via numerous methods; thermal atomic layer deposition (ALD), plasma ALD, atmospheric pressure chemical vapour deposition (APCVD), sputtering and PECVD. Advantageously, AlO_x deposition requires relatively low temperatures between 250 °C and 400 °C [83–85]. Irrespective of deposition method, the passivation effect of AlO_x is reported to be maximised after a moderate temperature anneal at ∼400 °C [83, 85–87]. Additionally, all deposition methods are reported to introduce hydrogen to the dielectric due to the use of hydrogen-containing precursors such as trimethylaluminium (TMA) and triethyldialuminium tri-(*sec*-butoxide) (TEDA-TSB) [40, 83, 85–88]. The hydrogen within the dielectric is reported to contribute significantly towards chemical passivation [25, 40, 83, 85–87].

Very low effective surface recombination velocities < 5 cm s^{-1} have been reported for AlO_x films on low resistivity p-type and n-type silicon [40, 83, 86]. Richter et al. reported S_{eff} < 1.3 and < 4.0 cm s^{-1} on 1 Ω cm n-type and p-type silicon, respectively, using plasma ALD [25]. Using PECVD, Dingemans et al. demonstrated S_{eff} < 1 cm s^{-1} on 3.5 Ω cm n-type silicon [89]. To the author's knowledge, other work by Dingemans demonstrated the record lowest S_{eff} < 0.8 cm s^{-1} on the same silicon type using plasma ALD [86].

1.3.3 Extrinsic Field Effect Passivation

The dielectric films discussed in Section 1.3.2 have been shown to possess an intrinsic concentration of fixed charge (Q_f), which is incorporated during synthesis [41, 51, 77, 90–92]. Typically, the intrinsic Q_f is not large enough to contribute significantly to FEP, and is limited by the synthesis process [18, 59, 76]. The intrinsic Q_f can be supplemented by the addition of extrinsic charge after deposition [66, 67, 93, 94]. The ability to add charge extrinsically to dielectric films means that the film properties do not

have to be compromised in order to achieve high charge concentrations during synthesis. This section discusses the use of corona charging and ion-charged dielectrics to provide extrinsic FEP.

1.3.3.1 Corona Charging

Corona discharge is a method used to cover the surface of the dielectric layer in positive or negative charges, thus allowing to tailor the field effect passivation mechanism. Figure 1.12 illustrates a typical corona discharge set-up. Corona charges are generated by applying a high voltage, >10 kV, to a pin-like electrode placed at a distance above a grounded plane electrode where the sample sits. The strong electric field formed near the sharp electrode ionises surrounding air molecules that come into contact with it, producing positively charged molecular ions and free electrons [95]. Through a process known as *electron avalanche*, the free electrons energised by the electrode's electric field ionise more air molecules producing more free electrons, and so on. Outside of a certain distance of the electrode, the electric field is too weak to maintain this electron avalanche and no further ions are produced. When a positive voltage is applied to the electrode the electrons are attracted towards the source and the positive ions repelled towards the sample. Negative charging results in the positive ions being attracted to the source electrode whilst the free electrons collide with ambient air molecules and create negative ions that are repelled towards the sample [96, 97]. Mass spectroscopic studies have shown that positive charging mostly comprises of hydrated hydrogen atoms ($(H_2O)_nH^+$), whilst negative charging results in primarily CO_3^- ions [98, 99].

Corona charging has been well-reported to provide extrinsic FEP [66, 95, 100–103]. Exceptionally high levels of passivation are reported in references [101] and [102] on 1 Ω cm n-type Si. An S_{eff} < 0.65 cm s^{-1} and < 0.15 cm s^{-1} was reported for corona-charged SiO_2 and SiO_2 + SiN_x dielectric coatings, respectively. Nevertheless, corona charges are unstable over time due to the absorption of water molecules, which increases lateral surface conductivity [101, 104]. Corona-charged samples are often

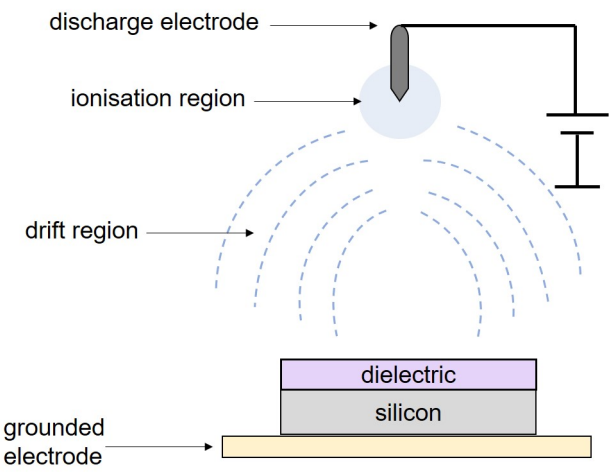

Figure 1.12: Schematic diagram of a corona discharge set-up.

treated with hexamethyldisilazane (HMDS) to provide a hydrophobic protective coating. The stability provided by HMDS is reported to last ∼3 years, which is not durable enough for industrial application. Furthermore, the resistance of HMDS to the elements under harsh environmental conditions such as humidity and high temperature is unreported [101]. Another method of utilising corona charge is to perform a rapid thermal anneal (RTA) to drive the corona charges into the dielectric and embed them within [66, 105]. This technique has been used to embed a charge of 5 x 10^{12} q cm^{-2} in SiO_2, resulting in SRV < 20 cm s^{-1} on 1 Ω cm n-type Si [66].

More recently, Kho et al. demonstrated the outstanding potential a surface electric field has on surface passivation via corona charging [94]. Figure 1.13 shows the J_{0e} that is produced for different SiO_2 + SiN_x + SiO_x (ONO) stacks, when the refractive index is varied, on 100 Ω cm n-type silicon with either boron or phosphorus front diffusions. The effective interface charge concentration (Q_{eff}) of the dielectric stack is reported here to be dependent upon the sample's refractive index (n) and front diffusion type. Here it is demonstrated that in the case of a boron emitter, prior to corona charging (blank circles), J_{0e} reduces from ∼600 to ∼40 fA cm^{-2} with increasing refractive index, and reduced dielectric charge. The surface passivation improvement at low dielectric charge is due to minimising electron density in the hole-rich emitter. Upon negative corona charging

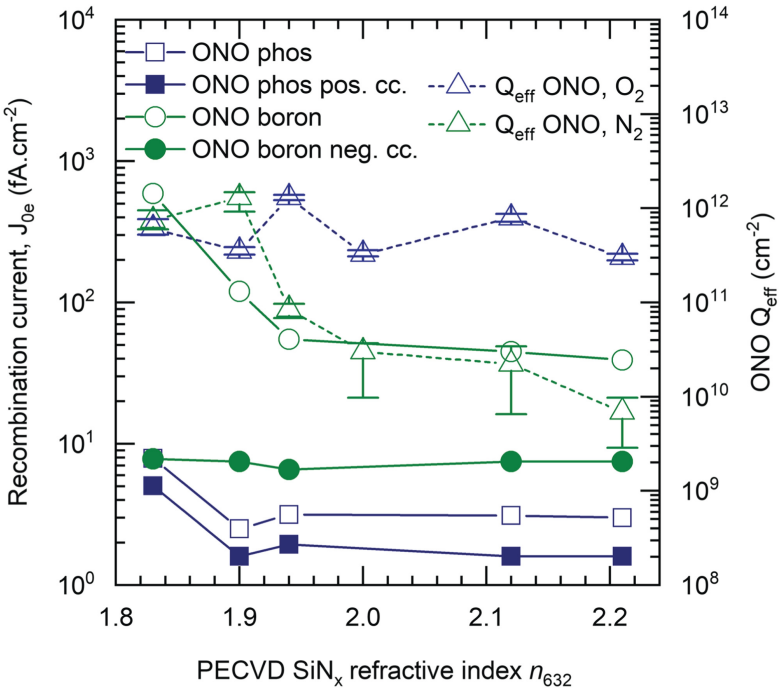

Figure 1.13: Effect of positive and negative corona fields on recombination currents of boron and phosphorus diffused silicon passivated by ONO stacks. After [94].

(filled circles), J_{0e} is reduced to ~8 fA cm^{-2}, irrespective of n. Following Equation 1.24, this is equivalent to an S_{eff} ~0.02 cm s^{-1}. For a phosphorus emitter, prior to corona charging (blank squares), there is a lower dependency of J_{0e} on the dielectric properties. Here, J_{0e} remains ~3 fA cm^{-2} for n between 1.9 and 2.2. Applying positive corona charge (filled squares) results in J_{0e} ~2fA cm^{-2}. This is equivalent to S_{eff} ~0.006 cm s^{-1}, and is consistent for 1.9 < n < 2.2. Such high levels of passivation are required to last approximately 30 years, as this is the lifespan of a solar panel. Since corona discharge has been widely reported to be an unstable method of producing the surface electric field [101, 102, 104], other methods of providing a fixed concentration of charge inside of a dielectric should be explored. These are discussed in the following section.

1.3.3.2 Ion-Charged Dielectrics

Ion-charged dielectrics are a class of thin film dielectric materials that hold a quasi permanent charge [106]. The charge storage capability of such materials makes them effective for a wide range of applications. From telecommunications to air filters and biomedical instruments, charged dielectrics are useful for a variety of devices where high charge density films with stable polarisation are required [106–109]. In this thesis, ion charged dielectrics are applied to silicon surface passivation.

Methods of incorporating ions into dielectrics include ion implantation and *in situ* delivery during oxidation [110–112]. Recently, a novel method of introducing ions to dielectrics after deposition was proposed by Bonilla [113]. Here, aqueous potassium salt precursors were thermally evaporated onto the SiO_2 surface followed by high temperature annealing to drive the ions to the Si-SiO_2 interface [93, 113]. This was adapted from a technique used in a study by Eldridge and Kerr to study the drift of sodium (Na^+) ions through phosphosilicate glass [114]. Relying on pure diffusion kinetics, Bonilla found that the transport time of K^+ ions across SiO_2 varied from several minutes at 500 °C to over an hour at 400 °C. Later work by Collett evaluated the transport time of K^+ ions in the presence of a surface electric field generated by corona discharge [67, 115]. It was found that at 450 °C, K^+ ions arrived at the Si-SiO_2 interface within just a few seconds. In this thesis, the deposition and delivery methods of K^+, Rb^+ and Cs^+ ions into SiO_2 have been adapted from Bonilla and Collett.

Surface passivation studies of SiO_2 dielectrics embedded with K^+ ions on 1 Ω cm n-type silicon have demonstrated S_{eff} < 3.3 cm s^{-1} can be achieved compared with S_{eff} ∼100 cm s^{-1} of SiO_2 alone [67]. For such high performance passivation to be practical in commercial manufacturing it must be durable for ∼30 years under operational conditions [7, 101]. Recent work has shown that K^+ ions remain quenched at the Si-SiO_2 interface for up to 8 years held at a temperature of 65 °C [112]. Ageing studies conducted on K^+ embedded dielectrics have so far only concentrated on laboratory conditions and have

shown that 63 % of the initial passivation performance is retained after a projected 45 years [93].

1.3.4 State of the Art in Surface Passivation

Numerous different methods of surface passivation have been researched in recent years. A selection of methods most relevant to this thesis have been discussed in Section 1.3. Of these methods, Table 1.1 provides a summary of the best passivation performances on low resistivity n-type silicon. Techniques such as the alneal and the enhanced alneal demonstrate outstanding surface passivation results. However, at present these techniques are not compatible with scalable industrial production due to the requirement for the deposition and subsequent removal of a metal contact to passivate the surface. Techniques focused on exploiting the chemical passivation and charge storage capabilities of dielectrics are expected to be more compatible with industry production. Bonilla et al [102] demonstrated an exceptionally low S_{eff} < 0.15 cm s^{-1} by combining the intrinsic properties of a SiO_2 + SiN_x dielectric stack with an extrinsic electric surface field provided by corona charging. This is in comparison to an S_{eff} $\sim$3.5 cm s^{-1} for a SiO_2 + SiN_x stack alone [102]. Given the instability of corona charges, it is necessary to find alternative methods to maintain such low surface recombination for many years. This thesis explores the use of ion-charged dielectrics to provide long-term effective passivation.

PASSIVATION METHOD	DIELECTRIC	SILICON TYPE	S_{eff} (cm s^{-1})
Standard Alneal Kerr & Cuevas [65]	SiO_2	1.5 Ωcm 285 μm	2.4
Enhanced Alneal Collett [68]	SiO_2	1 Ωcm 200 μm	0.4
Extrinsic FEP (corona charging) Bonilla et al. [101]	SiO_2	1 Ωcm 200 μm	0.65
Extrinsic FEP (corona charging) Bonilla et al. [102]	SiO_2 + SiN_x	1 Ωcm 200 μm	0.15
Extrinsic FEP (K^+ ion SiO_2) Collett et al. [67]	SiO_2	1 Ωcm 200 μm	3.3
PECVD SiN_x Richter et al. [25]	SiN_x	1 Ωcm 200 μm	1.6
PECVD SiN_x Bonilla et al. [102]	SiO_2 + SiN_x	1 Ωcm 200 μm	3.5
PECVD SiN_x Larionova et al. [116]	SiO_2 + SiN_x	2.5 Ωcm 155 μm	2.4
Plasma ALD AlO_x Richter et al. [25]	AlO_x	1 Ωcm 200 μm	1.3
Plasma ALD AlO_x Dingemans et al. [86]	AlO_x	3.5 Ωcm 275 μm	0.8
PECVD AlO_x Dingemans et al. [89]	AlO_x	3.5 Ωcm 275 μm	1.0

Table 1.1: Summary of best passivation methods on low resistivity n-type silicon at the time of writing.

1.4 Role of Surface Passivation in Solar Cell Architectures

A complete solar cell architecture comprises the silicon wafer, its dielectric coatings and selective metal contacts to extract the holes and electrons. The design of a solar cell is crucial to maximise the photo-conversion efficiency. An overview of the three most relevant cell architectures and their performance is presented in this section. In this thesis, cell efficiencies of these three architectures are modelled based on the novel surface passivation techniques that are explored in this work.

One of the most common cell architectures is the *passivated emitter and rear cell* (PERC). A typical bifacial PERC design is depicted in Figure 1.14a. In a typical PERC structure, p-type silicon is used as the base material. The rear of the cell is passivated by an AlO_x + SiN_x stack. In addition to chemical passivation, the negative charge within the AlO_x film creates an accumulation layer at the rear surface. The SiN_x capping layer enhances the hydrogen passivation provided by AlO_x alone, and minimises rear side reflectivity [117, 118]. It is common for the rear contacts to have localised p^{++} regions to reduce resistance losses between the silicon and the metal. The front surface of the PERC is doped with phosphorus to create an n^+ emitter region that leads to the accumulation of electrons. Lightly doped emitters are often favoured to maximise the absorption of short wavelengths at the front surface. Therefore, some PERC designs use localised n^{++} regions directly under the metal contacts to reduce contact resistance, analogously to the rear. Passivation of the contact interface is very important for maximising light absorption. Well-passivated contacts allow for greater carrier extraction, and therefore the width and number of them can be reduced in order to increase light exposure. To the author's knowledge, the highest recorded efficiency of an industrial PERC is 24.06 % [LONGI Solar, 2019]. The record effiency was demonstrated on a mono-crystalline p-type bifacial cell of commercial size [119]. At research scale,

the highest performing PERC was produced by UNSW in 1999, reaching an efficiency of 25 % [120, 121].

Figure 1.14b depicts the architecture of a contending cell design called *interdigitated back contact* (IBC). The IBC design places all the contacts on the rear of the cell so that the surface is maximally exposed to light. The base silicon is typically n-type. Despite higher associated processing costs [43], there are numerous advantages to n-type silicon, such as the avoidance of boron-oxygen defects and a lower susceptibility to metal impurities compared to p-type silicon [122, 123]. For these reasons, n-type silicon is gaining more attention in new commercial cell designs. A further discussion of p-type versus n-type silicon is provided in Section 2.1. To reduce recombination at contact interfaces, rear p^{++} and n^{++} localised diffusions are used. The silicon surface is typically passivated by a SiO_2 layer to provide chemical passivation, and a SiN_x capping layer to provide hydrogen passivation and to maximise light absorption. At the time of writing, the IBC cell holds the record efficiency for any solar cell at 26.7 % [124, 125]. This record cell uses a very thin amorphous silicon layer to create exceptionally well-passivated contacts. Despite such high performance, mass production of IBC cells has been slow to take off. This is due to the complexity of creating a consecutive series of dopant profiles of opposing polarities and selective contacts on the rear side [43].

The last cell architecture to be discussed here is the *tunnelling oxide and passivated contact* (TOPCon). Despite being a very recent technology, it has achieved a record industrial efficiency of 25.25 % [Jinko Solar, 2021], and a research efficiency of 26.0 % [126]. As depicted in Figure 1.14c, the TOPCon architecture uses n-type base silicon that is passivated at the rear by an ultra-thin SiO_x layer of $\sim$2 nm. The SiO_x layer is thin enough for the electrons to tunnel through. The combination with a phosphorus doped poly-silicon capping layer leads to well-passivated electron-selective contacts at the rear. At the surface of the cell, a p^+ emitter is formed by boron diffusion [127]. The emitter is further passivated by an AlO_x + SiN_x double layer. The TOPCon cell architecture is considered to be more attractive to industry than the IBC cell given its simpler design

and closer similarity to the already existing PERC production line [43].

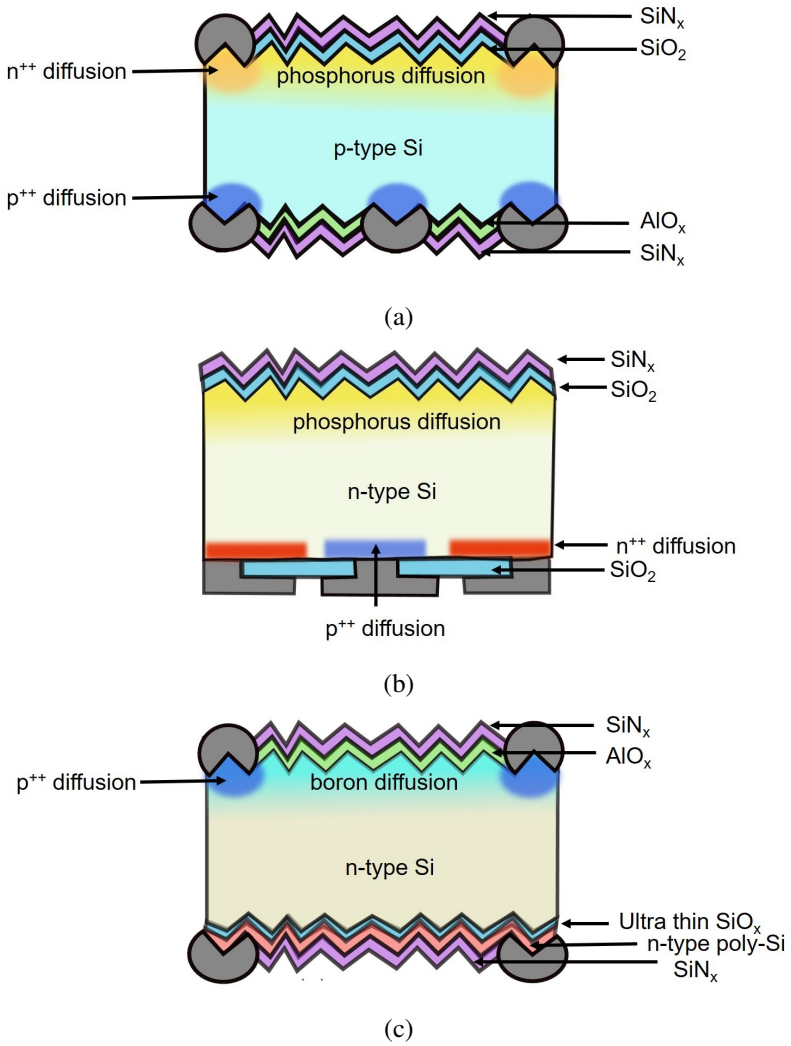

Figure 1.14: Schematic illustration of a standard (a) PERC (b) IBC and (c) TOPCon architecture.

1.5 Aim of this Thesis

The exploitation of dielectrics for surface passivation is ubiquitous in the solar cell industry. In order to optimise the optical, chemical, and field effect properties of the dielectrics, it is common to employ double or triple layer stacks. In particular, it is becoming increasingly common to deposit a thin oxide layer on the silicon surface to provide effective chemical passivation, while benefitting from the intrinsic charge of the capping layers to provide FEP. As will be discussed further in Section 4.1, extrinsic methods of supplementing the intrinsic charge have not become widespread due to the lack of long-term stability or industrial compatibility. This thesis aims to address both of these problems by proposing the use of ion-embedded oxide films. As will be demonstrated, these films can be created rapidly and uniformly using versatile techniques. The passivation performance and stability of three different ions – potassium, rubidium, and caesium – is explored and compared. Contrary to literature expectations, this thesis provides evidence for the first time that rubidium and caesium can be introduced to an oxide film through a kinetic approach. Additionally, this work aims to further the understanding of ion kinetics within dielectrics by proposing a model that simulates the injection of ions into the thin film and the transport to the Si-SiO_2 interface in the presence of a variable electric field and at elevated temperatures. The dependence of solar cell efficiency on dielectric charge concentration is subsequently studied for PERC, IBC, and TOPCon structures via finite element modelling.

Lastly, this thesis explores the relationship between surface electric fields and the chemical passivation provided by a SiO_2+SiN_x dielectric stack. Here, the dependency of the fundamental Si-SiO_2 interface properties on surface electric field strength and polarity is studied. The ability to tailor the chemical passivation through the use of surface electric fields could present new approaches to enhance extrinsic surface passivation.

1.6 Structure of this Thesis

The chapters of this thesis are as follows:

- **Chapter 2:** A detailed description of the experimental and characterisation methods used in this work is presented.
- **Chapter 3:** This chapter demonstrates that, contrary to findings in the literature, alkali ions larger than potassium are able to be migrated across a SiO_2 thin film. It is shown that the concentration of K^+, Rb^+, and Cs^+ charge at a Si-SiO_2 interface can be finely tuned by controlling the ion embedding process. A comprehensive model of the kinetics of potassium, rubidium, and caesium ions within a SiO_2 thin film is presented here.
- **Chapter 4:** The use of ionic aqueous precursors and deposition techniques is discussed here. The versatility and dependability of various deposition methods such as thermal evaporation, spin coating and *in situ* delivery of ions during oxidation is explored. SIMS evidence of the incorporation of rubidium and caesium ions is presented.
- **Chapter 5:** Substantial improvements in the surface passivation of oxidised silicon is demonstrated following the embedding of K^+, Rb^+, and Cs^+ ions at the Si-SiO_2 interface. The durability of the passivation performance and the physical resistance of alkali ions to harsh conditions, such as heat, UV radiation, and bias stress is evaluated.
- **Chapter 6:** It is demonstrated here that surface electric fields do not only influence the surface carrier concentration, but also affect the chemical passivation of the Si-SiO_2 interface. To explain this observation, this chapter explores the connection between surface electric fields, dielectric film properties, and hydrogenation.
- **Chapter 7:** The impact of the extrinsic surface passivation methods presented in

this work are examined in the context of producing high efficiency solar cells. Using Sentaurus TCAD finite element modelling, cell efficiency as a function of dielectric charge is simulated for three types of cell architectures; PERC, IBC, and TOPCon.

- **Chapter 8:** The important findings of this thesis are reviewed and a discussion of future research directions is presented.

2 | EXPERIMENTAL METHODS

2.1 Base Silicon

In industry, p-type silicon has been the base silicon substrate of choice [43]. This is due to two primary reasons. The first is that p-type silicon is cheaper to manufacture [43, 122, 123]. The second is because the minority carrier generated within the bulk has to travel the furthest distance to reach the p-n junction towards the silicon surface. The mobility of electrons is reported to be three times higher than that of electrons in p-type silicon [128]. Excited electrons have a greater mobility than holes since they are not subject to atomic forces in the same way holes are in the valence band. Therefore, for the same τ_{eff}, electrons have a longer diffusion length. Despite this, n-type silicon has been gaining attention in industry in recent years. N-type silicon has been demonstrated to show better resistance to impurities, metal contaminants and dislocations, particularly within the bulk [122, 129]. Additionally, given that silicon wafers are becoming so thin that the diffusion length equals or exceeds the thickness, minority carrier mobility is less of a compromising factor [129]. As surface passivation is the emphasis of this thesis, only mono-crystalline n-type silicon wafers are used so that the τ_{eff} is primarily limited by surface recombination.

There are two methods to grow mono-crystalline silicon: Czochralski (CZ) and Float Zone (FZ). A description of the CZ growth method can be found in reference [130], and the FZ method in references [131] and [132]. The majority of mono-crystalline wafers are grown via the CZ method due to its lower cost and faster throughput of production. Additionally, CZ silicon is reported to have a greater resistance to thermal stress [133]. The primary disadvantage of this method is that a substantial concentration of oxygen ($\sim 10^{18}$ cm^{-3}) and carbon ($\sim 10^{17}$ cm^{-3}) is introduced to the silicon [134, 135]. The presence of these impurities lowers the carrier lifetimes due to the generation of defects.

FZ silicon is of superior purity and for this reason is typically used to produce very high efficiency solar cells. However, thus far the higher production costs per wafer has prevented FZ silicon from becoming commonplace in commercial manufacture [131, 132]. Both CZ and FZ wafers are used in this work, a summary of which is provided in the next section.

2.1.1 Wafer Substrates

Table 2.1 provides a summary of the wafers used in this thesis. All substrates were n-type silicon wafers as-received with thermal SiO_2 grown on both sides. A subset of wafers received from Trina Solar also had SiN_x deposited on both sides, on top of the oxide. Wafers received from Fraunhofer ISE and MEMC were 4 inch wafers, and those from Trina Solar were full size 6 inch wafers. Throughout this thesis, the type of silicon used will be denoted by Set A, Set B, and Set C, with a description of the subsequent processing described in the relevant sections.

IDENTIFIER	TYPE	RESISTIVITY (Ωcm)	THICKNESS (μm)	SURFACE	SOURCE
Set A	n-type FZ Si	1	200	Planar	Fraunhofer ISE
Set B	n-type CZ Si	30-60	675	Planar	MEMC
Set C	n-type CZ Si	5-10	135	Textured	Trina Solar

Table 2.1: Summary of the silicon wafers used in this work.

2.1.2 Planar and Textured Finish

Texturing of the silicon surface is conventional in industrial manufacture. Compared to a smooth planar finish, rough surfaces benefit from increased light trapping due to the pyramidal arrangement that causes reflected photons to rebound back onto the surface. Texturing of samples used in this work was carried out at the source facility using a potassium hydroxide (KOH) and isopropanol (IPA) etch. The pyramidal surface structure is produced because of the faster etching rate of the (100) plane compared to

the (111) plane of the silicon [136]. The IPA solvent increases the wettability of the silicon surface to increase uniformity of the etchant [137]. Additionally, IPA is often used as an additive to reduce the etching rate of KOH to create well defined pyramid peaks [138–141]. Although textured wafers have the advantage of increased light absorption, they suffer from increased surface recombination due to both increased surface area and a higher density of defect states on the (111) face exposed by the alkaline etch.

In this thesis, only Set C wafers had pyramidal texturing. Texturing was carried out at Trina Solar using an undisclosed process. The majority of analysis was implemented on planar wafers as they are more compatible with characterisation techniques. Data pertaining to textured wafers were collected where possible to demonstrate the potential in industrial application.

2.2 Dielectrics

2.2.1 Thermal Oxide Growth

Set A wafers were thermally oxidised at Fraunhofer ISE. A dry thermal SiO_2 was grown at 1050 °C in an oxygen and dichloroethylene atmosphere. Dichloroethylene is used in small concentrations to serve as a chlorine source, which helps to remove metal contaminants. Set B wafers received from MEMC were oxidised in the Begbroke clean room at the University of Oxford. A 100 nm thermal SiO_2 was grown at 950 °C in a dry oxygen atmosphere for 4 hours. It is essential that oxidation is carried out in a clean environment to minimise the concentration of impurities entering the oxide film. Oxidation performed at Trina Solar on Set C wafers was carried out at 900 °C for 15 minutes following a proprietary process.

2.2.2 Chemical Vapour Deposition

SiN_x films were deposited via PECVD either at the Begbroke cleanroom in Oxford using an Oxford Instruments PlasmaLab 80+ system, or at Trina Solar's facilities using a tube processed PECVD. All SiN_x films were deposited on the surface of SiO_2 to create double layer stacks. The depositions carried out at the Begbroke cleanroom were performed at 350 °C. The parameters listed in Table 2.2 were used to deposit films of ∼65 nm thickness with a refractive index of 1.9, as measured on a FilmSense FS1 ellipsometer.

DEPOSITION PARAMETERS		
Power	W	20
Plate Temperature	°C	350
Chamber Pressure	mTorr	650
Ammmonia	sccm	20
Nitrogen	sccm	600
5% Silane / 95% Nitrogen	sccm	400

Table 2.2: Parameters for the silicon nitride recipe performed at Begbroke cleanroom, Oxford.

Silicon nitride deposition at Trina Solar was carried out at 450 °C. A subset of samples had a double layer deposited where the first layer on the oxide surface was 5 nm with a refractive index of 2.2, and the second layer was 60 nm with a refractive index of 1.95. Another subset of wafers had single layer films of 60 nm thickness deposited on the oxide surface. The refractive index of these films was tuned to 1.95, 2.1 and 2.4. The parameters for SiN_x deposition at Trina Solar are not disclosed.

2.3 Ellipsometry

Ellipsometry is an optical technique used to characterise dielectric properties such as thickness, refractive index, and optical constants by means of reflected light rays. In this work, an FS-1 Film Sense ellipsometer is used. Figure 2.1 illustrates the typical set-up of an ellipsometry measurement. When a source beam of non-polarised light enters the

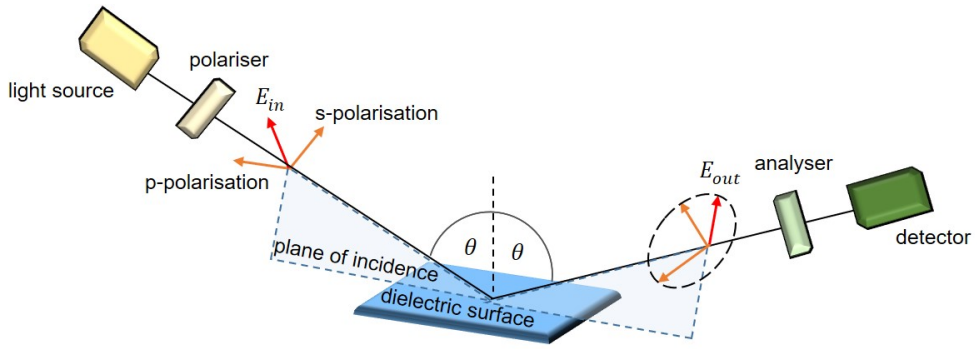

Figure 2.1: Experimental set-up of an ellipsometry measurement.

polariser, it becomes linearly polarised such that the incident electric field wave vector (E_{in}) is decomposed into two orthogonal components that oscillate in phase with each other. The component parallel to the plane of incidence is termed *p-polarisation*, and the component perpendicular is termed *s-polarisation*. The polarised light is directed at the sample surface at an angle of incidence θ. Upon reflection off the dielectric surface, the phase, amplitude, and polarisation of the light are altered such that the reflected wave vector (E_{out}) moves in an ellipse. The shape and orientation of the ellipse are dependent upon the polarisation of the incident light, the angle of incidence, and the dielectric properties. The ellipsometer does not measure the film properties directly, but measures the parameters Ψ and Δ, which describe the form of the reflected electromagnetic wave's ellipse. These parameters are related to the complex ratio of the reflection coefficients, r_s and r_p, of the s and p components, respectively, as given in Equation 2.1.

$$\frac{r_p}{r_s} = \tan(\Psi)e^{i\Delta} \tag{2.1}$$

where $\tan(\Psi)$ is the magnitude of the amplitude ratio of the two components, and Δ is the phase difference between the parallel and perpendicular components. To compute the film properties, Ψ and Δ are first simulated based on known optical properties of the sample film and substrate. The simulated Ψ and Δ are subsequently fit to the values that were experimentally acquired. The dielectric properties can be varied in the model as

adjustable parameters to minimise the difference between the experimental and simulated Ψ and Δ. There are numerous existing models to compute the film properties for a given sample structure. In this thesis, the Sellmeier model was used to calculate the thickness of the dielectrics, and the Cauchy model is used to calculate the refractive index. The models are simplified by the FS1 software, which inputs pre-derived optical constants from Jellison and Palik [142, 143]. A detailed explanation of these models is beyond the scope of this thesis, however, a summary of these models can be found in references [144] and [145].

2.4 Ion Deposition

The deposition of ionic charges is a central component of this thesis. Ionic charges have been shown to be successfully introduced to a dielectric via thermal evaporation, spin coating and spray coating, followed by post-deposition processing [67, 93, 115, 146]. In this work, K^+, Rb^+ and Cs^+ ions were deposited directly onto the SiO_2 surface by either spin coating or thermal evaporation. All ionic precursors are deposited as aqueous solutions, as described in the following sections.

2.4.1 Spin Coating

Spin coating is well known technique to both rapidly and uniformly deposit thin films. Here, a solution is pipetted onto the surface of a substrate while it rotates at a high angular velocity. The centrifugal force produces an even distribution of the solution across the surface area of the substrate. In this work, all ionic precursors were deposited in the form of chloride salts dissolved in a mixture of 25% deionised (DI) water and 75% IPA. While all these salts used present excellent solubility in water, IPA is added as it improves the wettability of the dielectric surface and evaporates quickly at room temperature. The chuck of the spin coater was programmed to rotate at 2000 rpm for 30 seconds. During the first 15 to 20 seconds, 2 mL $\pm$ 0.1 mL of ionic solution was deposited incrementally

via pipette. The remaining spinning time was used to allow the solution to dry.

In general, the film thickness is proportional to the inverse of the spin speed squared. The exact film thickness depends upon a combination of factors such as solvent viscosity, solute concentration, temperature, and humidity. Numerous models exist to approximate the film thickness [147–149]. In this work, sub monolayer concentrations were deposited on the dielectric surface. It was deemed unnecessary to estimate the film thickness as the ionic surface concentration per unit area after spin coating is of greater significance. This value was determined by depleting the surface of ions during the migration process described in Section 2.6, and measuring the resulting charge within the dielectric.

2.4.2 Thermal Evaporation

During thermal evaporation, a source material is subjected to high temperature within a vacuum to make it evaporate. Placed directly above the source material is a target substrate held at a cooler temperature to allow the source material to condense on the surface. This technique is used frequently in the semiconductor industry [150, 151]. In this thesis, only KCl solution was deposited using thermal evaporation to avoid cross contamination of different ionic species within the evaporating chamber. Depositions were carried out using the thermal evaporator in the Begbroke cleanroom in Oxford. The precursor was prepared by dissolving the KCl salt in 100 % DI water. 50 μL of KCl solution was dropped via pipette into a tungsten boat. The boat was placed directly into the evaporator and a current of 30 amps was applied for 1 minute, by which point the deposition was complete and the current was turned off.

The molarity of the 50 μL droplet was determined by the mass of KCl required to deposit an ionic surface charge concentration of $\sim 10^{13}$ ions cm^{-2}. Here the mass of the salt (M_{salt}) is calculated as:

$$M_{salt} = \frac{V_{sol}}{V_{boat}} \frac{\rho_{salt}}{N_{AVG}} \Sigma \tag{2.2}$$

where V_{sol} is the total volume of the prepared solution, V_{boat} is the amount placed in the tungsten boat, ρ_{salt} is the density of the salt and N_{AVG} is Avogadro's constant. The number of molecules, Σ, is related to the desired ionic surface concentration, σ:

$$\Sigma = \sigma(2\pi r^2) \tag{2.3}$$

where r is the distance from the tungsten boat to the flat substrate held directly above, here 15 cm. Similarly to spin coated samples, the deposited ionic surface concentration was verified by depleting the surface of ions and measuring the dielectric charge.

2.5 Corona Discharge

Corona discharge is used to create a surface electric field without the need of a metal contact. Corona discharge consists of ionised air molecules that are drifted down to the surface of the target substrate. A description of the corona discharge mechanism is provided in Section 1.3.3.1. Figure 2.2 provides a schematic of the experimental set-up used in this work. This set-up is called "tip to plane" where the substrate is placed on the grounded platform at a distance d directly under the electrode. Charge uniformity across the specimen is essential for producing a uniform distribution of charge at the interface. The current density (j) of the deposited corona charge can be used as measure of uniformity. In traditional tip-to-plane setups, j can be defined at any point on the plane by Warburg's law as [152, 153]:

$$\begin{aligned} j &= j_0 cos^5\theta \\ j_0 &\approx I/2d^2 \end{aligned} \tag{2.4}$$

where j_0 is the peak current density, I is the total corona current, d is the distance from

the tip to the plane and θ is the angle relative to the normal as shown in Figure 2.2. Therefore, increasing d reduces the displacement in θ and increases the uniformity of corona current across the plane. The plane current drops with increased height so a higher source electrode current would need to be applied to compensate this loss.

In this work the centre of a standard 4 x 4 cm sample was placed 20 cm below the tip of the source electrode held at $\pm$30 kV. Following Warburg's law, this distance is expected to give charge uniformity with a variation of less than 1% [102, 154].

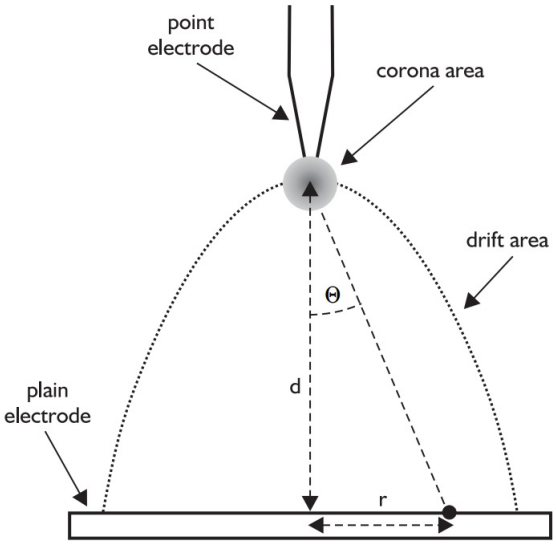

Figure 2.2: Schematic diagram of a tip-to-plane corona discharge, after [152].

2.6 Ion Migration

Set A wafers (n-type 1 Ωcm FZ) were exclusively used for ion migration studies. These had 100 nm thermal SiO_2 grown on both surfaces at Fraunhofer ISE. A flow chart of the subsequent processing sequence is shown in Figure 2.3. Ionic precursors were deposited directly on the front and rear oxide surfaces by either spin coating or thermal evaporation, as described in Section 2.4.1 and 2.4.2. Both faces were subsequently corona charged for varying amounts of time, and immediately placed on a hotplate and annealed at a temperature between 250 - 600 °C. Annealing is required to provide enough energy to overcome the barrier for ion injection while the positive surface electric field drifts the ions across the oxide film. To prevent contamination from the hotplate surface, a dummy wafer was placed underneath the specimen. Separate dummy wafers were used for each ion. The hotplates in the laboratory were able to reach a maximum temperature of 500 °C. In order to raise the hotplate temperature further to 600 °C, a clean glass lid was placed on the surface of the hotplate. The temperature of the surface underneath the lid was verified using an RS PRO Type K thermocouple. Using a heat-proof glove, the lid was raised for 3-4 seconds to slide the specimen onto the dummy wafer. The lid was immediately replaced. Removal of the specimen from the hotplate after annealing required approximately 10-12 seconds. Here, the lid was removed once again with heat-proof gloves. Given the lack of dexterity, the gloves were first taken off before removing the specimen from the hotplate with metal tweezers.

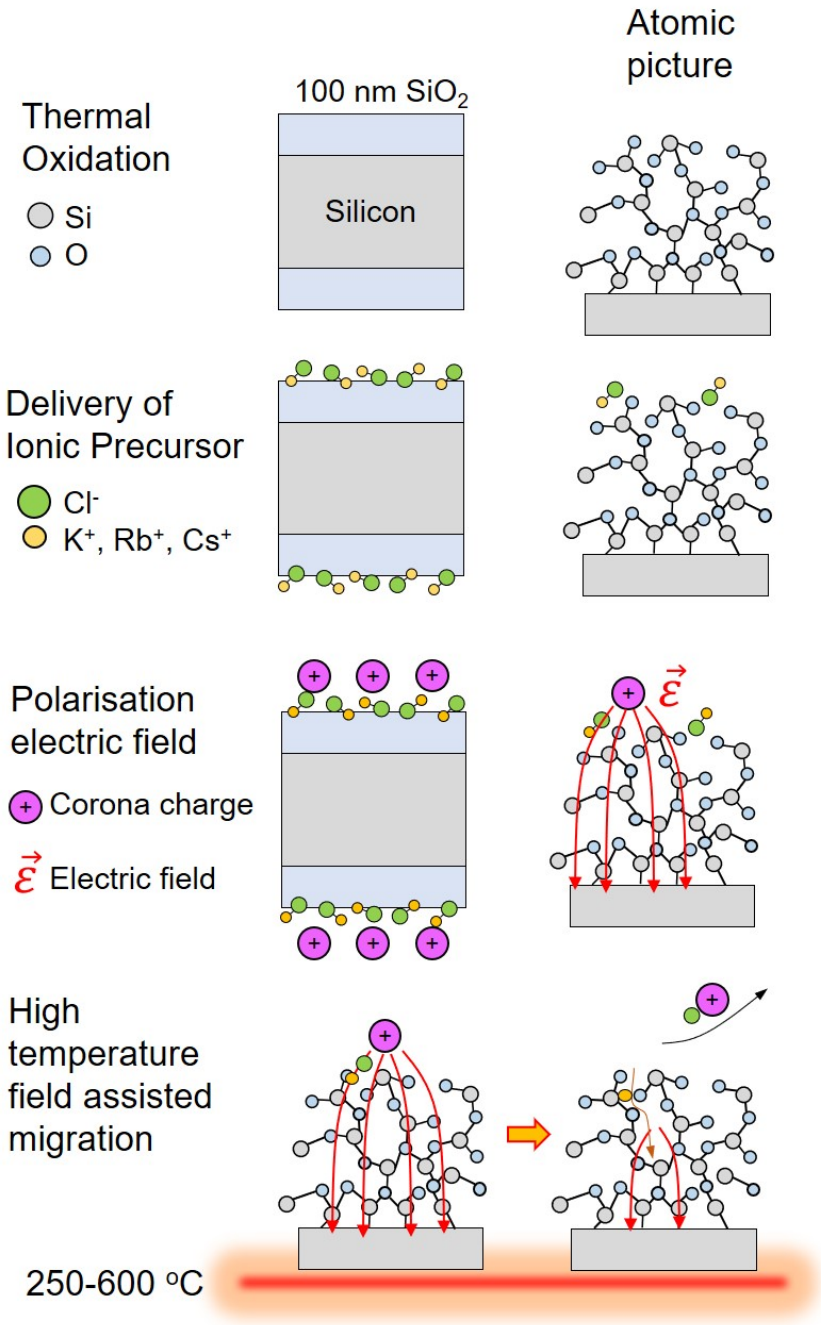

Figure 2.3: Flow chart of the ion migration procedure used in this work.

2.7 Ultraviolet Radiation

Ultraviolet (UV) radiation was used to perform accelerated ageing experiments on specimens passivated by ion-charged oxides. An in-house UV exposure chamber was constructed using four Osram UVA lamps to achieve a total optical irradiance of ~5 mW cm^{-2} with the spectrum and configuration shown in Figure 2.4. Within the chamber, only one side of the specimen could be exposed to UV radiation.

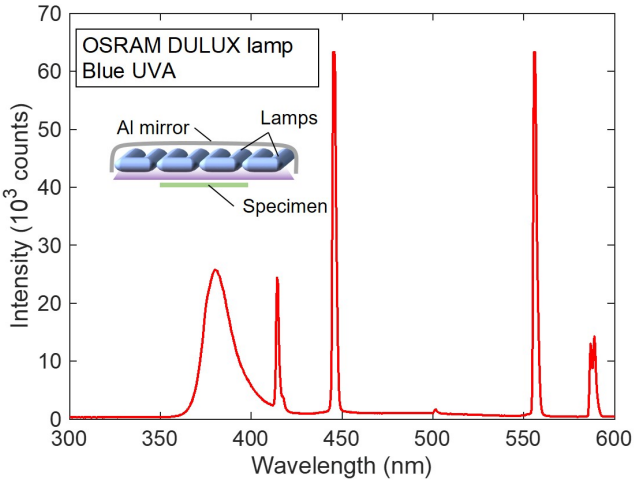

Figure 2.4: Ultraviolet spectral irradiance and configuration.

2.8 Electrical Characterisation

2.8.1 Photoconductance Decay

The effective lifetime of minority carriers was evaluated by measuring the photoconductance decay on a Sinton WCT-120 Lifetime Tester. Figure 2.5 depicts the set-up of the Sinton tester. Within the stage there is an inductive coil that creates a magnetic field within the specimen sitting above. A high intensity flash of light generates electron-hole pairs within the silicon. The impedance of the inductive coil changes, which is used to measure the change in conductivity of the specimen as the

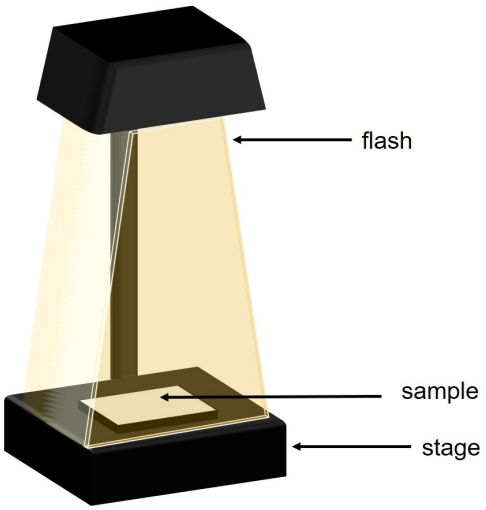

Figure 2.5: Schematic of the Sinton Lifetime Tester.

flash decays. The change in conductivity of a specimen, $\Delta\sigma$, is directly related to the minority carrier concentration, Δp, in n-type Si, as:

$$\Delta\sigma = q\Delta p(\mu_n + \mu_p) \tag{2.5}$$

where q is the electron charge and μ_n and μ_p are electron and hole mobilities, respectively. Solving for Δp, τ_{eff} can be calculated as a function of time:

$$\tau_{eff} = \frac{\Delta p}{G - \frac{d\Delta p}{dt}} \tag{2.6}$$

where G is the rate of electron-hole pair generation.

Two types of measurements exist depending on the lifetime of the sample; transient and quasi steady state (QSS). The transient measurement is used on wafers with lifetimes of 100 μs or longer. Under transient conditions, the sample is illuminated by a short pulse of light that excites charge carriers. The actual measurement begins once the flash has ended during which the decay of excited carriers is measured over time. Since the measurement begins after the pulse of light has ended, G is not calculated. Therefore under transient

conditions, τ_{eff} is expressed as:

$$\tau_{eff} = -\frac{\Delta p}{\frac{d\Delta P}{dt}} \tag{2.7}$$

QSS mode is used when wafers have a lifetime below 100 μs. The sample is illuminated for approximately 10 times longer than its lifetime so that steady state conditions are created. Since carriers are continually generated at a constant rate, the term $d\Delta p/dt$ = 0. The lifetime under QSS conditions is expressed in equation 2.8. G is calculated by measuring the incident number of photons per cm^2 per second and correcting for the Si absorption coefficient and wafer thickness.

$$\tau_{eff} = \frac{\Delta p}{G} \tag{2.8}$$

2.8.2 Transparent Gate Electrode

To estimate the fundamental interface recombination parameters, surface recombination at the Si-SiO_2 interface was varied by regulating the carrier density using a biased transparent gate. The method recently developed by Bonilla [155] was used to record effective lifetime as a function of gate bias. In this procedure, a semi-transparent gate electrode is produced on top of the dielectric to simultaneously control surface potential and measure effective lifetime on the Sinton Lifetime Tester. Undiluted poly(3,4-ethylenedioxythiophene) polystyrene sulfonate (PEDOT:PSS) was coated over both sides of all finished samples with a standard paintbrush to form a nearly transparent thin film. After coating, the film was annealed for 20 seconds at 120 °C in air to evaporate the solvent to allow the polymer to bind, and increase the conductivity [156, 157]. The PEDOT:PSS solution was 3.0 - 4.0 wt. % in H_2O from Sigma Aldrich.

In the experimental set-up shown in Figure 2.6, the coated specimen is placed on the Sinton Lifetime Tester. Two spring loaded probes connect a source meter to the front and

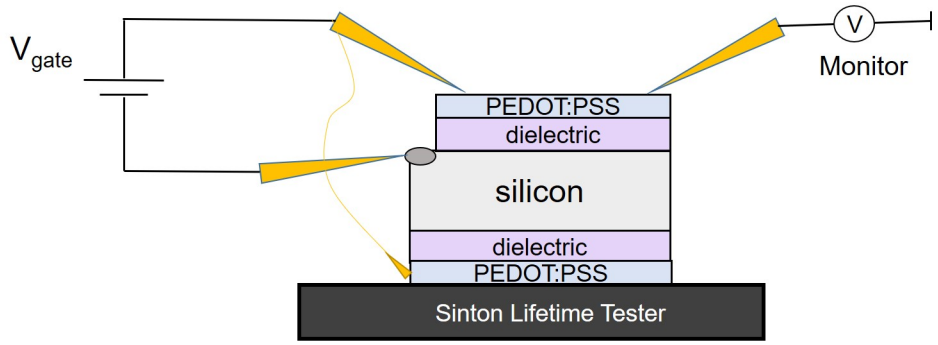

Figure 2.6: Schematic diagram of the electrically connected transparent electrode upon the Sinton Lifetime Tester.

rear gates. Another set of probes is positioned laterally across the specimen from the first set and is connected to a multimeter to ensure the applied voltage from the source meter is constant across the polymer. As the gate voltage is incrementally changed, lifetime measurements can be recorded to construct a plot of τ_{eff} vs gate voltage.

This technique can only be used on planar wafers as the valleys and peaks of textured wafers make it difficult to apply a smooth and continuous layer of PEDOT:PSS across the dielectric. Therefore, for textured specimens incremental additions of corona charge served as the gate electrode where the concentration of corona charge was quantified using Kelvin Probe. The Kelvin Probe technique will be explained in Section 2.8.4.

2.8.3 Capacitance-Voltage Measurements

Capacitance-voltage (CV) measurements were used to calculate the effective concentration of charge at the dielectric-silicon interface. CV was performed on metal-insulator-semiconductor (MIS) structures using a Keysight 4980A LCR meter. MIS structures were prepared in two ways. In the first, the rear dielectric was etched with hydrofluoric acid to remove the dielectric on one side of the substrate prior to thermally evaporating $\sim$100 nm of aluminium in an Edwards 306 evaporator. Front contacts 1 mm in diameter were made by evaporating aluminium through a shadow contact mask directly onto the dielectric. The second method is known as mercury probe

CV. Here, a temporary front contact is made with mercury, as shown in Figure 2.7. The rear contact is made by manually etching the dielectric and painting gallium indium eutectic followed by silver DAG directly onto the silicon. As the more rapid technique, mercury probe CV was used when many samples needed to be tested in succession.

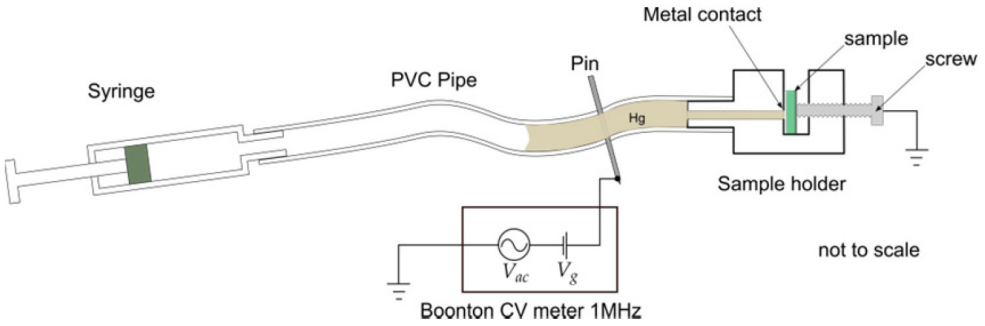

Figure 2.7: Schematic diagram of mercury probe CV, after [100].

During a CV measurement, the capacitance is recorded as the gate bias is varied. The change in gate bias influences the carrier concentration at the silicon surface and modifies the band bending as shown in Figure 2.8. Biasing the gate more positively or negatively results respectively in accumulation and inversion of majority carriers at the silicon surface. The flat band voltage is where the semiconductor surface transitions from accumulation to depletion. At this voltage the electric field in the silicon, and therefore the charge, is zero.

The combination of three sources make up the total capacitance of the MIS structure. Within the semiconductor, the capacitance of the space charge region (C_{SCR}) is in parallel to that of the interface traps (C_{it}). Together these are in series with the capacitance of the dielectric (C_i). The equivalent measured capacitance is therefore given as:

$$C_{meas} = \frac{(C_{SCR} + C_{it})C_i}{C_{SCR} + C_{it} + C_i} \tag{2.9}$$

The capacitance of the dielectric at strong accumulation is calculated as:

$$C_i = \frac{\varepsilon_r A}{d} \tag{2.10}$$

where ε_r is the relative permittivity. The insulator thickness, d, is the thickness of the oxide layer or the *effective* oxide thickness where a second dielectric is deposited. A is the area of the metal contact on the MIS device. As the area of the contact is often difficult to measure precisely, it is common to assume that C_i is equal to C_{meas} in accumulation.

Origin of Charges

An ideal MIS capacitor assumes no charge in the insulator. In reality, charges are introduced during the various stages of processing. Charges arise from three separate sources; mobile ions, interface traps and fixed charges. Mobile charge, Q_m, is predominantly composed of sodium contaminants and heavy metals, and possibly H^+ atoms [158–160]. Interface trapped charge, Q_{it}, can be positive or negative and arises from structural defects and broken bonds. Interface traps respond to the DC gate voltage during a CV measurement and can become charged or uncharged depending on the surface potential. Q_{it} can be reduced via annealing and in the case of a well passivated thermal Si-SiO_2 interface it is usually very low in the range of 10^9-10^{10} $cm^{-2}eV^{-1}$ [161–163]. Fixed positive charges, Q_f, are also located close to the interface. Unlike interface trapped charges, Q_f does not respond to changes in gate voltage. Figure 2.8 depicts the changes in charge within the MIS structure under accumulation, flat band, depletion and inversion conditions.

The total concentration of charge can be calculated from the flat band characteristics of the capacitor. Under ideal conditions, the flat band voltage (V_{FB}) is calculated simply as the difference between the work function of the metal, Φ_m, and the work function of the silicon, Φ_{Si}. The presence of Q_f causes a shift in V_{FB} as a more negative gate bias is required to flatten the energy bands in the silicon. The effect of charge is shown in Figure 2.9a and b. V_{FB} for non-ideal conditions is then calculated as:

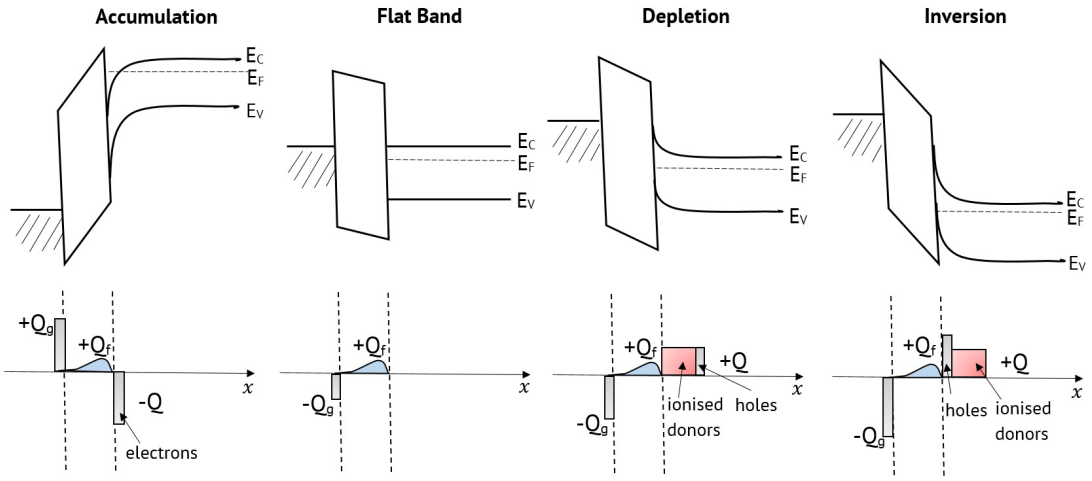

Figure 2.8: Energy and charge diagrams for non-ideal n-type MIS devices in accumulation, at flat band, in depletion, and in inversion.

$$V_{FB} = \frac{\Phi_m - \Phi_{Si}}{q} - \frac{Q_{it}d}{\varepsilon_r} - \frac{1}{\varepsilon_r}\int_0^d x\rho_i(x) \quad dx \tag{2.11}$$

where $\rho_i(x)$ is the volumetric charge distribution within the insulator, and d is the length of the dielectric. Since it is not possible to know the exact distribution of charge within the dielectric film, it is simpler to represent it as an *effective* sheet of charge with its centroid x_c at position $x = d$ [161]. This is termed the effective interface charge concentration Q_{eff}. Therefore, ρ_x can be expressed as a delta Dirac function $\rho_x = Q_{eff}\delta(x - [d - x_c])$. V_{FB} can then be expressed as:

$$V_{FB} = \frac{\Phi_m - \Phi_{Si}}{q} - \frac{Q_{it}d}{\varepsilon_r} - \frac{Q_{eff}(d - x_c)}{\varepsilon_r} \tag{2.12}$$

Once V_{FB} has been calculated from the CV measurement, Q_{eff} can be determined as:

$$Q_{eff} = \frac{\varepsilon_r}{d - x_c}\left(\frac{\Phi_m - \Phi_{Si}}{q} - V_{FB} - \frac{Q_{it}d}{\varepsilon_r}\right) \tag{2.13}$$

From Equation 2.13, it is clear that the closer the position of the charge to the Si-SiO_2

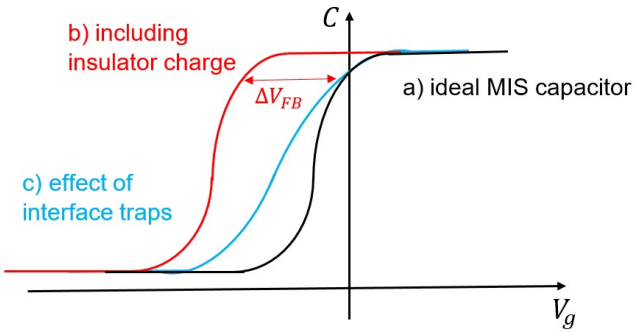

Figure 2.9: Capacitance-voltage curves for a) an ideal n-type capacitor b) the effect of charge in the insulator and c) the stretching effect due to interface states.

interface, the more sensitive the CV measurement.

Density of Interface States

The density of interface states (D_{it}) is often used as a quantitative measure of the chemical passivation of the interface. As the voltage is varied during a CV measurement, the position of the donor and acceptor states changes relative to the Fermi level. Starting from inversion, as the voltage becomes more positive the Fermi level rises relative to the mid-gap and more acceptor states become negatively charged. This increases the capacitance at any given voltage. The "stretching" effect of D_{it} on a CV curve of an n-type semiconductor is shown in Figure 2.9c. Q_{it} is therefore a function of the Fermi energy expressed as:

$$Q_{it} = q \int_{E_V}^{E_C} D_{it} \quad dE \tag{2.14}$$

In this thesis, D_{it} is obtained from experimental data using a model adapted from the Terman method [164]. Here, the total capacitance is measured at high frequencies of 1 MHz. Interface traps are slow to charge or discharge at high AC perturbation frequencies and so at 1 MHz they do not respond to the AC signal [165]. This ensures that the interface traps only respond to the position of the Fermi level as the DC voltage is swept. The D_{it}

can be related to the capacitance that arises from the interface traps:

$$C_{it} = \frac{dQ_{it}}{d\Psi_s} = q^2 D_{it} \tag{2.15}$$

where Ψ_s is the semiconductor surface potential. The ratio of Ψ_s to the applied gate potential, V_g, is a measure of the stretching effect and is given by:

$$\frac{d\Psi_s}{dV_g} = \frac{C_i}{C_i + C_{it} + C_{SCR}} \tag{2.16}$$

Substituting equation 2.15 into 2.16 and solving for D_{it} gives the following:

$$D_{it} = \frac{C_i}{q^2}\left[\left(\frac{d\Psi_s}{dV_g}\right)^{-1} - 1\right] - \frac{C_{SCR}}{q^2} \tag{2.17}$$

The stretching effect, $\frac{d\Psi_s}{dV_g}$, is quantified by comparing the experimental curve to an ideal theoretical CV curve. As D_{it} depends upon the energy level in the band gap [18], it is the norm to quote D_{it} at the mid-gap where the deepest and therefore most effective recombination traps lie.

2.8.4 Kelvin Probe Measurements

Kelvin Probe (KP) characterisation is a non-contact technique to measure the difference in surface potential between a metal probe and the dielectric surface. During a KP measurement the metal probe with a known work function (Φ_m) is contacted to the silicon wafer, and brought to close proximity of the dielectric surface. Figure 2.10a shows the relative differences in energy of the probe and silicon before they are connected. When the two materials are electrically connected, as shown in Figure 2.10b, a capacitor is created where the silicon wafer and metal probe act as electrodes. As the electrons travel from the lower work function material to the higher, the Fermi levels equalise and a contact potential difference, equal to the work function difference, is

created between the two surfaces.

The metal probe is oscillated up and down directly above the sample surface. The oscillation varies the capacitance and generates an AC backing current, i_b:

$$i_b = \frac{dC}{dt}V \tag{2.18}$$

Baikie's method is used to determine the work function difference [166]. Here a counter potential, also known as a backing potential (V_b), is applied to the probe (Figure 2.10c) and i_b is recorded. V_b is slowly increased until there is no oscillating current. The voltage at which V_b nullifies the contact potential difference occurs when the current equals 0.

In this thesis, the KP technique is used to calculate the surface charge concentration of the dielectric (Q_{surf}). The backing potential is required to counterbalance both the potential of the pin and the dielectric-silicon system. V_b is therefore calculated as

$$V_b = -\left[\frac{\Phi_m - \Phi_s}{q} - V_{SCR} - V_i\right] \tag{2.19}$$

where V_{SCR} is the voltage of the space charge region and V_i is the voltage across the dielectric. The precise calculation of V_{SCR} is a laborious task that follows an iterative algorithm by Girish et al [167]. Previous work in reference [113] has determined that the contribution from the space charge region is < 0.25 V where the surface charge density is below 10^{13} q cm^{-2}. Given that the contribution from V_{SCR} is expected to be negligible, it can be omitted from equation 2.19. V_i is calculated assuming a uniform charge density (ρ_i) across the length of the dielectric and is expressed as the integral

$$V_i = \frac{1}{\varepsilon_r}\int_0^d x\rho_i(x) \quad dx \tag{2.20}$$

Therefore, omitting V_{SCR} and substituting equation 2.20 into equation 2.19, we arrive at

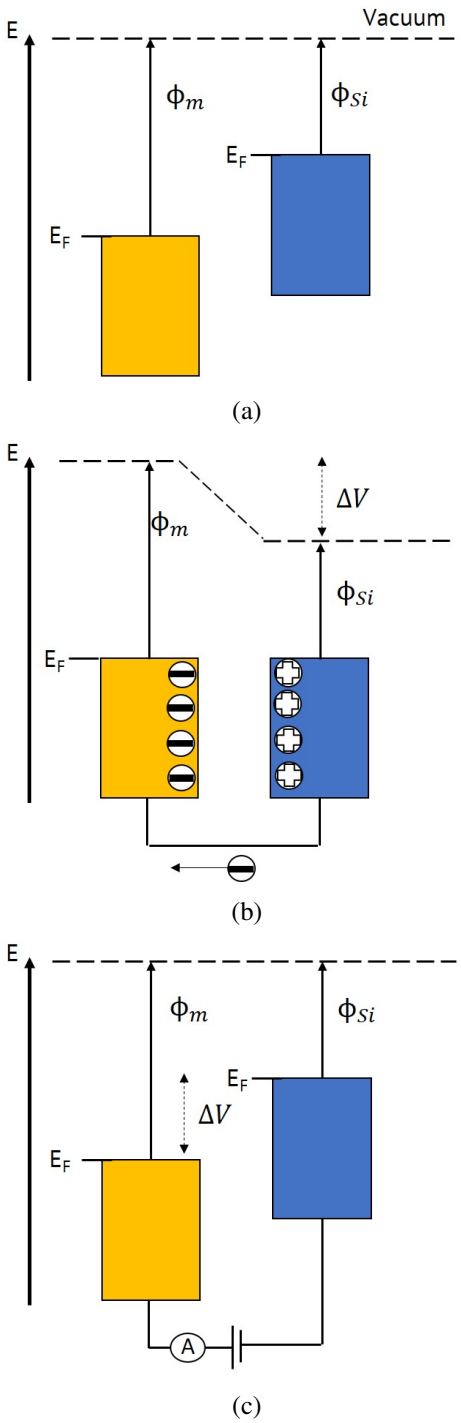

Figure 2.10: Energy diagrams of (a) two unconnected surfaces (b) the band alignment when metal probe and silicon surface are connected and in proximity and (c) the effect of applying a counter potential.

the same equation for calculating V_{FB} in equation 2.11.

$$V_b = \frac{\Phi_m - \Phi_s}{q} - \frac{1}{\varepsilon_r}\int_0^d x\rho_i(x) \quad dx \tag{2.21}$$

Similarly to a CV measurement, ρ_i can be assumed to reside as a plane of charge at a distance x_d from the dielectric-silicon interface. The relationship can be expressed as $\rho_i = Q_f\delta(x - x_d)$. V_b is then calculated as:

$$V_b = \frac{\Phi_m - \Phi_s}{q} - \frac{x_d Q_f}{\varepsilon_r} \tag{2.22}$$

Rearranging, the effective surface charge is then calculated as:

$$Q_{surf} = \frac{\varepsilon_r}{x_d}\left(\frac{\Phi_m - \Phi_s}{q} - V_b\right) \tag{2.23}$$

In this work, KP is used to measure Q_{surf} at the very surface of the dielectric, ie. the air-dielectric interface, and so x_d equals the dielectric thickness in all cases.

2.9 Secondary Ion Mass Spectrometry

Secondary Ion Mass Spectrometry (SIMS) is a technique used to determine elemental, isotopic, and molecular composition of solids. It is one of the most sensitive surface analysis techniques available. Here, under vacuum the surface of the specimen is sputtered using a focused ion beam under vacuum. The ejected secondary ions are transferred to a mass spectrometer under a strong electric field. The mass to charge ratio of these collected ions is used to identify the elemental or molecular composition.

In this work, SIMS characterisation was used to confirm the presence of K^+, Rb^+ and Cs^+ ions within SiO_2. A Thermo Scientific Helios G4 Plasma FIB DualBeam (PFIB) system combined with a Hiden Analytical EQS quadrupole SIMS detector was used. In

preparation, samples were contacted to a metal stub and had 15 nm of platinum deposited on the surface to prevent charging of the insulating dielectric. During the measurement, an area of 50 μm x 50 μm (100 x 100 pixels) was scanned using a focused beam of Xe^+ at 5 kV and 100 pA. Selected secondary ions were collected by the quadrupole detector. This scanning process was repeated throughout the depth of the oxide film to create stacks of images showing the distribution of each element. The Hiden SIMS Mapper was then used to create elemental depth profiles.

Due to access restrictions in the electron microscopy facility, all SIMS measurements were performed by Junliang Liu at the University of Oxford.

3 | Electrostatic Tuning of Ionic Charge in Silicon Dioxide

The incorporation of solid-state ions within dielectric films is a key method to generate permanent electric fields in electronic devices. Potassium ion-charged dielectrics, for example, have been used in a range of applications. Recently, they have been reported in vibrational energy harvesters, pressure sensors, and actuators, as well as in silicon surface passivation [67, 93, 111, 112, 168]. To the authors knowledge, no reports exist on Rb^+ charged dielectrics. However, research dating from the 1980s studied the use of Cs^+ ions in creating inversion layers in p-type silicon [78, 169–173]. In these reports, ions were introduced to the silicon-dielectric interface either by dipping bare silicon in an ionic solution before dielectric deposition, or via ion implantation directly within the dielectric [78, 169–173]. It has long been presumed that owing to their large ionic radius these ions were immobile within SiO_2 [174, 175]. In the last 30 years since these reports, little research has been conducted to examine further the use of ions larger than K^+.

In this chapter it is demonstrated that all three alkali ions are mobile within SiO_2. It is demonstrated that the measured Q_{eff} of K^+, Rb^+, and Cs^+ ions within SiO_2 can be acutely controlled by regulating the surface electric field strength as well as the temperature and duration of the anneal during migration. Following the methodology described in Section 2.6, the ions were driven to the Si-SiO_2 interface during a high temperature anneal assisted by a variable corona-induced surface electric field. By employing this methodology, acute control over Q_{eff} ranging from 0.5 x 10^{11} q cm^{-2} to 1 x 10^{13} q cm^{-2} is demonstrated here. The ability to tune the embedded charge is beneficial not just to the field of surface passivation, but to a variety of applications where the performance of dielectric-based devices is strongly dependent upon the charge concentration. For example, in the field of electrostatic energy harvesters, the power output is proportional to the square of the charge concentration within the dielectric [176, 177]. Dielectric devices with substantial

in-built electric fields eliminate the need for DC biasing, thus benefitting from low voltage and reduced power consumption [178, 179].

Following a review of previously reported work on K^+ ion kinetics in SiO_2, this chapter presents a novel and comprehensive model of the migration process. The model explores the dependency of K^+, Rb^+, and Cs^+ ion kinetics within SiO_2 on temperature and surface electric field. It describes the first complete model that accounts for the injection of ions at the air-SiO_2 interface, the transport of ions under a temporary surface electric field provided by corona charging, and the trapping of ions at the Si-SiO_2 interface.

3.1 Literature Review of K^+ Ion Kinetics

To the author's knowledge, the first study on the kinetics of ions within dielectrics was the work of Yamin in 1965 [180]. Yamin examined the diffusion of ions across SiO_2 in metal-oxide-semiconductor (MOS) structures and their response to a surface bias at elevated temperatures. These ions were found to be Na^+ contaminants and were determined to be a key source of instability in silicon devices due to their high mobility even at low temperatures [114, 181]. In further studies, the larger K^+ ion was also shown to respond to a surface bias, however, with stronger charge trapping at the Si-SiO_2 interface. As a result, K^+ exhibited greater stability than Na^+. Nauta and Hillen explained the behavioural difference between the two ions by studying their activation energies [182]. They showed that under a bias of +2.5 V and temperature ranging between 50 - 350 °C, the activation energy of Na^+ and K^+ ions at an Al-SiO_2 interface is 1.10 eV and 1.65 eV, respectively. Under the same thermal stress and equivalent reverse bias, the activation energy of the ions trapped at the Si-SiO_2 interface was reported to be 1.01 eV and 1.65 eV, respectively [182]. The higher activation energy of K^+ ions at both interfaces in comparison to that of Na^+ ions lowers the probability of de-trapping from the interface, which improves the stability of the ions inside of the thin film.

The mobility of K^+ ions within SiO_2 has also been previously reported [174, 183, 184].

Mobility values have been determined on MOS structures by measuring the transit times of K^+ ions from the metal-SiO_2 interface to the Si-SiO_2 interface at a range of temperatures. From the relationship between mobility and temperature, the activation energy of diffusion can be determined. Within the literature, there is close agreement that the activation energy of diffusion lies between 1.01 eV and 1.09 eV [174, 183, 184].

Traditional methods of drifting charge through the oxide film require the deposition of a metal contact to apply a surface bias. This technique is not adaptable to solar cell production, and limits further characterisation such as photoconductance decay measurements. The recent method reported by Bonilla addresses this problem by using corona charge to serve as a temporary and transparent electrode [93]. It was found that by applying corona charge prior to annealing, a substantial concentration of K^+ ions >2 x 10^{12} q cm^{-2} can be migrated to the Si-SiO_2 interface within 2 minutes at temperatures of 400 - 450 °C. This is in comparison to a transit time of 15 - 90 minutes relying on diffusion alone, without electric field enhancement, at elevated temperatures [93, 113]. A model of K^+ ion diffusion dynamics in the absence of a metal contact is reported in reference [93]. This simplified model does not consider the effect of surface electric field, nor the electric field arising from the ions within the oxide itself. An updated model that takes into account all electric field components, including the time and temperature dependent decay of corona charge is presented next.

3.2 Physical Model of Ion Injection, Transport and Trapping

A model of ion injection at the surface and transport through the dielectric has been developed and is described in this section. Due to its relevance and ubiquity in electronic devices, the model has been optimised for the case of alkali ionic charge in a SiO_2 thin film. Contrary to prior work, this model accounts fully for both injection and migration processes, while also considering the electrostatic interaction of ions in the presence of a

variable electric field. The kinetics of K^+, Rb^+, and Cs^+ ions in SiO_2 are studied experimentally and used to find the kinetic parameters via the proposed model.

The model uses finite element analysis to simulate ion migration into and across the dielectric. Here, the SiO_2 film of thickness d is discretised into n number of equal elements. As SiO_2 is known to possess a small native concentration of positive charge, a concentration of 8 x 10^{15} q cm^{-3} was assumed to exist uniformly within each element prior to the introduction of extrinsic charge [18]. This is equivalent to Q_{eff} = 4 x 10^{10} q cm^{-2}, which has been corroborated using capacitance-voltage (CV) measurements.

A schematic diagram of the air-oxide-silicon system is depicted in Figure 3.1. On the surface of the dielectric, the ions are bound to Cl^- since a chloride salt is used as a precursor. In the bound state, the alkali ions face a considerable energy barrier to enter the SiO_2. The energy required to overcome the barrier at the air-SiO_2 interface is referred to as the activation energy of injection (ΔE_{ao}). The distribution of activation energies has previously been approximated most typically using either a single energy value [185], or Gaussian distributions [158, 182, 186, 187]. In this work, a single activation energy is used for simplicity. Ions are thermally excited over the injection barrier during high temperature anneals. Upon injection into the SiO_2, the ions exist in a free state and contribute to the positive charge within the SiO_2. As the concentration of ions within the SiO_2 increases, negative mirror charge accumulates at the silicon surface resulting in an electric field. This field can be further augmented by the presence of positive corona charges on the SiO_2 surface. The field provided by corona charges is not stable throughout the anneal and decays with time and increasing temperature [93, 103]. The effect of the corona charge concentration over various annealing times and temperatures is investigated in this work. The ions arriving at the Si-SiO_2 interface are assumed to be similarly trapped at a single energy level, ΔE_{os}. The accumulation of ions at the Si-SiO_2 interface generates a field that reduces the corona-induced field, and thus limits further ionic migration. Each kinetic process in this system is described next.

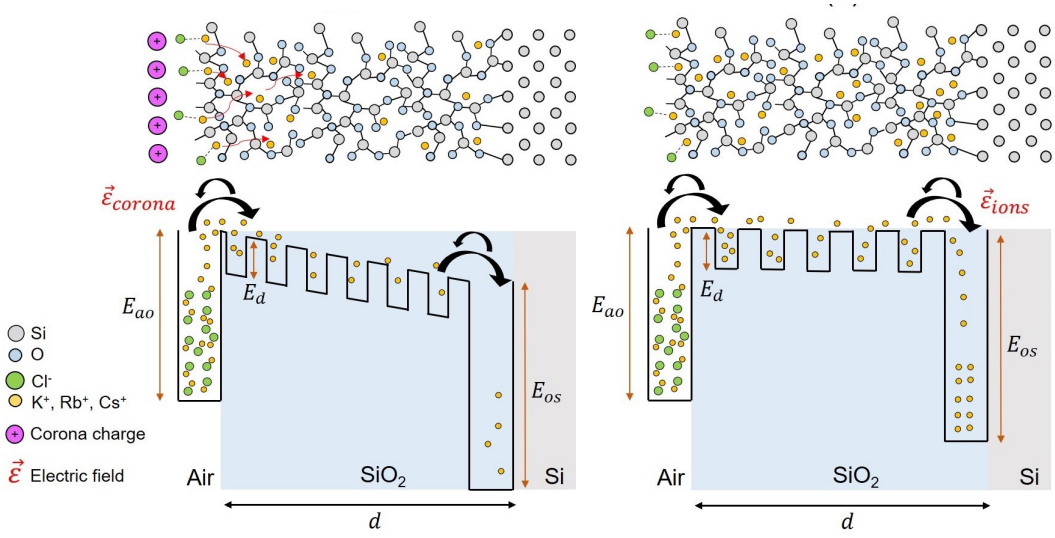

Figure 3.1: Schematic illustration of the ion kinetics in the dielectric thin film system (a) shortly after inital ion injection and (b) after the electric field of the ions compensates the corona-induced field.

3.2.1 Ion Injection at the Air-SiO_2 and Trapping at the Si-SiO_2 Interfaces

The rate determining step of ion migration is the de-trapping and trapping of ions at the air-oxide and oxide-silicon interfaces, respectively [185, 187]. Since these rates are directly proportional to the concentration of ions, either trapped at interfaces or de-trapped in the oxide bulk, a first-order kinetic approach is used to model ion injection at the air-oxide interface and ion trapping at the oxide-silicon interface. Firstly, the concentration of ions trapped at the SiO_2 surface (C_{ao}) is calculated using Equation 3.1 [93]:

$$\frac{dC_{ao}}{dt} = C_1 \times (N_{trap}(E,t)R_{trap}(E)) - C_{ao}(E,t) \times s \times e^{\frac{-\Delta E_{ao}}{kT}} \tag{3.1}$$

where the first term represents increases in ion concentration due to trapping and the second term represents decreases in concentration due to injection into the SiO_2, mediated by a barrier with energy ΔE_{ao}. As ions are released into the SiO_2, the number of trap

states (N_{trap}) available at the air-oxide interface increases. The total number of trap states is set to 10^{13} cm^{-2} following references [158] and [188], and the capture rate (R_{trap}) set to 10^{11} $cm^{-2}s^{-1}$ [93]. The ion concentration within the first segment of the oxide film (C_1) has a re-trapping probability at the SiO_2 surface equal to $N_{trap}(E,t)R_{trap}(E)$. The escape frequency (s) defines the dynamics of ion release. Following reference [158], a value well within physical constraints of 5 x 10^{11} s^{-1} was used for s, while the activation energy at the air-oxide interface (ΔE_{ao}) was left as a fitting parameter.

Ion trapping/de-trapping at the Si-SiO_2 interface is expressed similarly in Equation 3.2. Here, C_n is the concentration of ions in the last element of the SiO_2, and ΔE_{os} is the activation energy at the Si-SiO_2 interface. N_{trap}, R_{trap}, and s are the same as previous. It is assumed that there is no trapped charge at the interface at time $t = 0$.

$$\frac{dC_{os}}{dt} = C_n \times (N_{trap}(E,t)R_{trap}(E)) - C_{os}(E,t) \times s \times e^{\frac{-\Delta E_{os}}{kT}} \tag{3.2}$$

The effective interface charge concentration (Q_{eff}) at the Si-SiO_2 interface at time t is calculated as a function of the ionic concentration C_x at position x, following Equation 3.3.

$$Q_{eff} = q_e \Sigma_0^{x=d} C_x \times \frac{x}{d} \tag{3.3}$$

Q_{eff} represents the measurable ionic charge when using, for example, capacitance voltage technique [100], and assuming that the charge centroid lies at the Si-SiO_2 interface such that $x = d$. This is chosen due to the use of CV characterisation as described in Section 2.8.3.

3.2.2 Ion Transport Through SiO_2

The SiO_2 matrix allows ions to diffuse through large interstitial sites created by the continuous interconnected network of tetrahedral SiO_4 molecules [189, 190]. The energy required to allow ion transport through the dielectric is called the diffusion activation energy (ΔE_d). The Anderson-Stuart model of diffusion defines ΔE_d as the sum of the electrostatic binding energy of the ion and the strain energy required to dilate the oxide structure to permit movement of the ion [191]. The model delivers a parabolic dependence of activation energy on ionic radius. Despite inducing minimal distortion of the oxide, ions of a smaller ionic radius than Na^+ have a high ΔE_d due to their greater binding force to O^{2-} ions of the oxide. On the other hand, ions larger than Na^+ possess a smaller binding force but have increasingly higher ΔE_d caused by greater network strain energy. The mobility (μ) of the ions through the dielectric as a function of temperature is defined as [174, 183, 184]:

$$\mu = \mu_0 e^{\frac{-\Delta E_d}{kT}} \tag{3.4}$$

Table 3.1 lists a range of mobility pre-factors (μ_0) that have been reported in the literature for K^+ ions within SiO_2. These values differ by up to 1 order of magnitude. Previously reported mobility data are plotted as a function of temperature in Figure 3.2. Stagg's results were determined from thermally stimulated ionic conductance (TSIC) measurements performed on MOS structures between 227 - 297 °C [183]. Hillen et al. used triangular voltage sweep (TVS) measurements between the temperature range 300 - 450 °C, and found very close correspondance to Stagg's data [184]. Hillen et al. additionally determined an expression for μ_0 as a function of temperature (provided in Table 3.1) and found that within the temperature range studied, μ_0 has negligible influence. Greeuw and Verwey similarly used TVS measurements, however, their results do no correlate well with the other authors' [174]. No explanation is given for the discrepancy in results, however, it is reported that μ_0 could vary depending on oxidation

conditions and temperature [174, 184]. Despite the discrepancy in μ_0, the corresponding values of ΔE_d are in excellent agreement with each other. Given such uncertainty in μ_0, the pre-factor was adjusted in this work as a parameter to ensure the value of ΔE_d is in good agreement with the literature. Here, μ_0 was set to 0.05 $cm^{-2}V^{-1}s^{-1}$, which is within the range calculated by Stagg, and just outside the range calculated by Hillen et al. It is noted that their calculations of mobility include both the de-trapping and migration of K^+ ions across the oxide, so these values could be altered when obtained by a more fitting experiment. To the author's knowledge, no mobility data exist for Rb^+ and Cs^+ ions. Therefore this pre-factor was kept constant for all three ions.

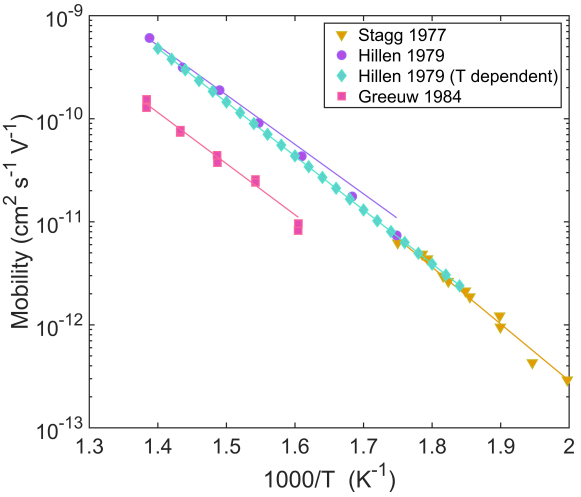

Figure 3.2: K^+ ion mobility as a function of temperature as reported in the literature.

AUTHORS	μ_0 **($cm^{-2}V^{-1}s^{-1}$)**	ΔE_d **(eV)**
Stagg, 1977 [183]	0.026 (within a factor of 4)	1.09 ±0.06
Hillen et al, 1979, [184]	0.016 (within a factor of 2.5)	1.04 ±0.03
Hillen et al, 1979 (T dependent) [184]	$\frac{17.46}{T}$	1.09
Greeuw and Verwey, 1984 [174]	0.0025 (within a factor of 8)	1.04 ±0.10

Table 3.1: Summary of K^+ mobility pre-factors and activation energies of diffusion from the literature.

Following the Einstein relation, the diffusivity (D) can be calculated as:

$$D = \frac{kT\mu}{q} \tag{3.5}$$

The migration of ions across the dielectric is governed by Fick's laws of diffusion. At elevated temperatures, alkali ions injected into the SiO_2 are driven across the film with the driving force provided by the concentration gradient. The concentration gradient is supplemented by an external surface bias and the Coulombic attraction between the ions and the mirror charges that appear at the Si surface. The total flux within the system is therefore the sum of the diffusive and drift flux. Following Fick's first law, the diffusive flux is given as:

$$J_{diff} = -D\frac{dC}{dx} \tag{3.6}$$

where C is the ionic concentration per unit volume. The flux arising from drift is expressed as:

$$J_{drift} = \mu EC \tag{3.7}$$

where E is the electric field present within each element.

There are three sources of electric field. The first is the field from surface corona charges (E_{corona}), purposefully applied to enhance migration. This electric field source is not constant as the instability of corona charge increases with temperature. Experimental data recording the decay of surface charge over time was taken in 50 °C increments between 200 °C and 500 °C to parametrise this field. The field from the corona charge experienced in every element of the SiO_2 is reduced by the amount of injected ionic charge as Cl^- anions left behind after K^+ injection effectively neutralise the corona surface charge. Consequently, the field experienced within each element as a function of

time is calculated from Gauss' Law as:

$$E_{corona} = \frac{qC_{corona}(t) - q\Sigma_0^{x=d}C(x,t)}{\varepsilon_r} \tag{3.8}$$

where C_{corona} is the surface concentration of corona charge per unit area.

The second contribution to the electric field arises from the ionic charge within each element (E_{ions}). The electric field is the sum of all the ion contributions at position x, with greater contribution the closer to the Si-SiO_2 interface, as described by the calculation for the *effective* interface charge concentration in Equation 2.13. Therefore, the field within each element is calculated at time t by performing a cumulative integration at time t with respect to position x, following Gauss' Law, as:

$$E_{ions} = \int_0^{x=d} \frac{qC_{ions}(x,t)}{\varepsilon_r} \qquad dx \tag{3.9}$$

The third contribution is from ions that are re-trapped at the SiO_2 surface, which is to say ions that are ejected to the air-oxide interface. Before injection, ions are assumed to be bound to Cl^- and therefore not contribute to the electric field. After injection into the SiO_2, the alkali ions are free ions that contribute to the electric field. Re-trapped ions therefore contribute to the electric field similar to any remaining corona ions, as follows:

$$E_{retrapped,ao} = \frac{qC_{retrapped}}{\varepsilon_r} \tag{3.10}$$

3.2.3 Stability of the Model

The model of ion kinetics follows the iterative sequence illustrated in Figure 3.3. The model is divided into the three segments: ion injection at the SiO_2 surface, transport across the film, and trapping at the Si-SiO_2 interface. A fixed amount of time is allowed for each segment to complete. As ion kinetics are limited by the rate of release from

trap sites [93, 181, 182, 185], a longer amount of time is required for surface injection and interface trapping than for diffusion across the SiO_2. Here, 10 ms was allocated for segments 1 and 3, and 2 ms was allocated for segment 2. Reducing these time increments to simulate a more continuous process resulted in no further change to the results.

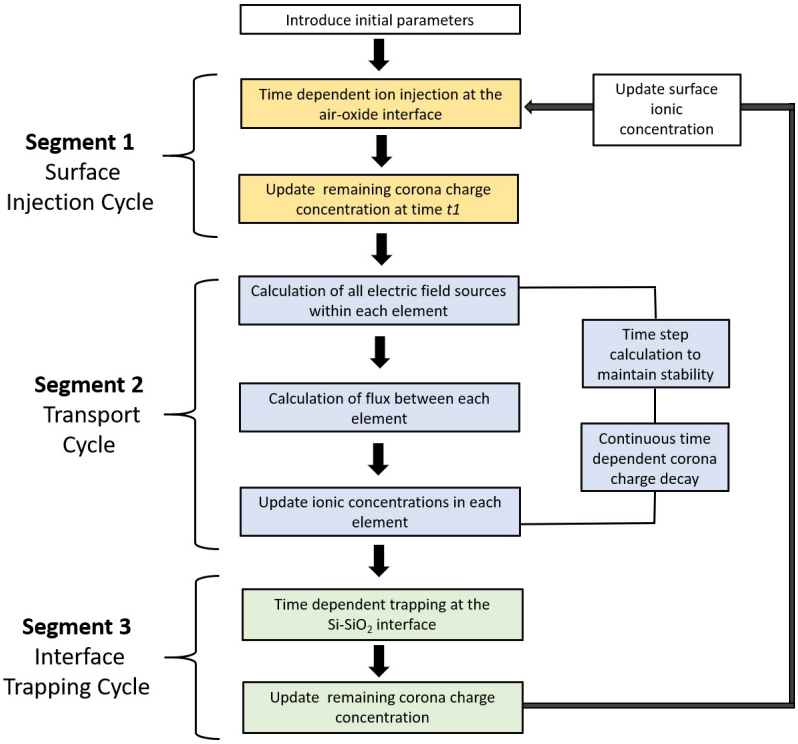

Figure 3.3: Flow chart of code execution.

The finite difference method was used to simulate the transport of ions within segment 2. The oxide film of thickness d = 100 nm was discretised into n number of equal elements, each of thickness dx. During segment 2, the change in ionic charge concentration (dC) within each element is updated every time step (dt). Therefore the new charge concentration is calculated as:

$$C(t + dt) = C(t) + dC \tag{3.11}$$

Where following Fick's second law of diffusion, dC is given as:

$$dC = \frac{dJ_{tot}}{dx}dt \tag{3.12}$$

This iterative sequence is known as the Forward Euler Method [192]. Provided dt is kept small, the approximation of the new charge concentration is expected to be very accurate. The time step is therefore important to ensure the model runs stably. Following an initial time step of 1 ns for the first iteration within segment 2, the model self-regulates by placing a limit of 0.01 % on the maximum allowable change in ionic concentration within each element. If dC exceeds this limit, the step is retracted and the previous concentrations re-instated. The time step is subsequently reduced by 5 % until dC is within 0.01 %. A maximum tolerated time step is determined following the Von Neumann Stability Analysis and is expressed in Equation 3.13. The derivation can be found in reference [193]. If the variable time step is below dt_{max}, the time step is increased by 15 %. The stability section of the code was largely based on previous work by a Part II student, Rachel Kealy.

$$dt_{max} = \frac{dx^2}{2D} \tag{3.13}$$

3.2.4 Simulating Corona Charge Decay

Corona charge decay data was taken experimentally to account for the time and temperature dependent electric field induced by corona charges. Kelvin Probe surface charge measurements were taken immediately following corona charging and subsequently every 15 seconds of annealing, with the first 3 measurements taken every 5 seconds. A range of initial charge concentrations between 10^{12} – 10^{13} q cm^{-2} were deposited and the decay of each was recorded at 300 °C, 450 °C and 500 °C. The same charge decay data taken at 500 °C was also used for 600 °C as the time taken to remove the sample from the hotplate at 600 °C increases the error in time significantly. Additionally, the charge decay at 500 °C is so rapid that it is unlikely the data at 600 °C

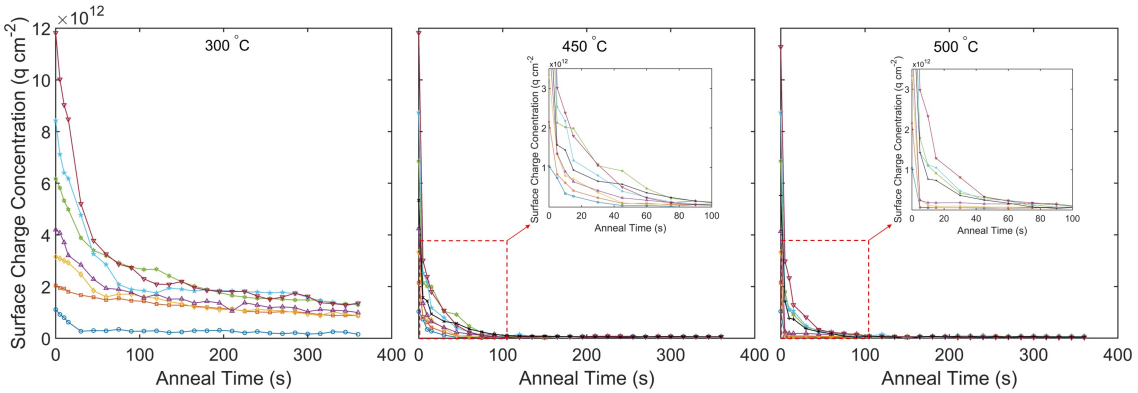

(a) (b) (c)

Figure 3.4: Corona charge decay data at (a) 300 °C (b) 450°C and (c) 500 °C. The data taken at 500 °C was also used to simulate charge decay at 600 °C. Each coloured line represents a different starting concentration of corona charge varying from 1 x 10^{12} q cm^{-2} to 1.2 x 10^{13} q cm^{-2}.

would differ significantly. The experimental data are shown in Figure 3.4. At 300 °C, the a more gradual charge decay was observed compared to the higher temperatures of 450 °C and 500 °C. At 450 °C and 500 °C, the charge decays to negligible values of ∼5 x 10^{10} q cm^{-2} within the first 100 seconds of annealing. This is equivalent to the surface charge of an untreated SiO_2, and therefore indicates that all corona charge is lost. To incorporate these measurements into the simulation, the experimental data were smoothed and subsequently fitted to a 2D function using MATLAB Curve Fitting Toolbox. This function was used to extract the remaining corona surface charge at any given time at a specified temperature, and was required to calculate Equation 3.8. This function was used to model the dependency of Q_{eff} on initial corona charge charge concentration observed in Figure 3.8.

Charge decay measurements were also recorded between 250°C and 500 °C in 50 °C increments to monitor how a fixed surface charge concentration of 2 x 10^{12} q cm^{-2} decays at each temperature. The experimental data are shown in Figure 3.5. The charge decay measurements show that at up to a temperature of 200 °C, the corona charge is very stable. As the temperature is increased, the rate of corona charge decay becomes faster. At 500 °C, almost all the corona charge is lost within the first 5 seconds of annealing. A 2D fit

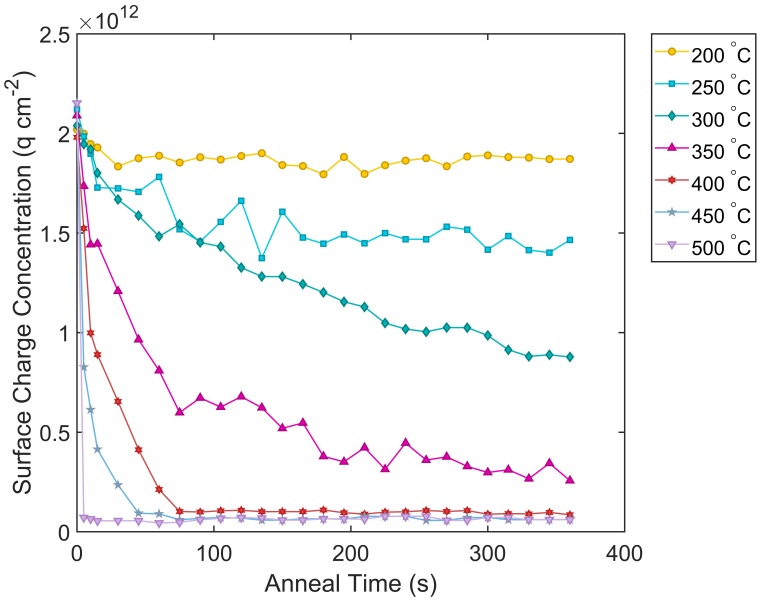

Figure 3.5: Charge decay measurements after an initial corona charge deposition of 2 x 10^{12} q cm^{-2} and subsequently annealed between 200 °C and 500 °C. The data taken at 500 °C was also used to simulate charge decay at 600 °C. The tip was held at a voltage of +30 kV for 30 s.

function was produced from the smoothed data and was used to model the results of Q_{eff} as a function of annealing time observed in Figure 3.6.

3.3 Alkali Ion Dynamics in SiO_2

In this chapter, Set A wafers (n-type 1 Ω cm FZ) were exclusively used. These had 100 nm thermal oxide grown on both sides at Fraunhofer ISE. Initial experiments were carried out to evaluate the kinetic response of the K^+, Rb^+, and Cs^+ ions deposited on the dielectric surface to both electric field strength and annealing temperature. First, the effect of annealing time and temperature was studied on all three ions separately. Samples were spin coated with either KCl, RbCl, or CsCl solution. Since many samples were to be tested, the spin coated specimens were cut into small pieces of approximately 2 cm x 1 cm. A corona discharge time of 30 s, equivalent to ∼2 x 10^{12} q cm^{-2}, was applied to the surface of all samples to ensure the same initial surface electric field strength prior to annealing. As shown in Figure 3.6, Q_{eff} of all three ions was measured at intervals

over the course of 6 minutes annealing at a range of temperatures. The results for K^+ ions are shown in Figure 3.6a. K^+ ions were migrated at 250 °C, 300 °C and 350 °C. At 250 °C, a gradual increase in Q_{eff} with time was recorded. A maximum value of 0.8 x 10^{12} q cm^{-2} was obtained within 6 minutes of annealing. At 300 °C and 350 °C the K^+ ions saturated at the same Q_{eff} of 1.8 x 10^{12} q cm^{-2} irrespective of temperature within just 60 s of annealing. In the case of Rb^+ ions, a minimum temperature of 375 °C was required to detect any migration across the oxide, as shown in Figure 3.6b. The effective interface charge gradually reaches saturation at ∼1.3 x 10^{-2} q cm^{-2} after 4 minutes at 450 °C. The results for the largest of the 3 ions, Cs^+, are shown in Figure 3.6c. A minimum of 500 °C was required to detect a small amount of charge migration. After 6 minutes of annealing, Q_{eff} increased from ∼4 x 10^{10} q cm^{-2} to ∼2 x 10^{11} q cm^{-2}. A higher temperature of 600 °C showed a more substantial increase as Q_{eff} saturates at ∼10^{12} q cm^{-2} within 60 s of annealing.

The model described in Section 3.2 was used to simulate Q_{eff} as a function of time, temperature and corona charge decay for all three ions. The modelling results are represented as solid curves in Figure 3.6, and the parameters are provided in Table 3.2. A value of 1.0 eV and 1.34 eV was chosen as ΔE_d for K^+ and Rb^+, respectively. These values are in very good agreement with those proposed by Anderson, Stagg, Hillen and Greeuw [174, 183, 184, 191]. For Cs^+, a value of 1.65 eV was determined as ΔE_d. This value is lower than the predicted value of 1.83 eV by the Anderson-Stuart model, and significantly lower than the value of 2.9 eV proposed by Fishbein et al. [194].

The injection of K^+ ions at the SiO_2 surface has predominantly been studied on MOS structures and values of ∼1.65 eV have been determined as the activation barrier at the metal-SiO_2 interface [93, 158, 174, 182, 183, 195]. In this work, ions are trapped at an air-SiO_2 interface. Previous work showed that there is a significant difference in activation energy at the oxide surface depending on the presence of a metal contact [93, 146]. If K^+ ions are trapped at an Al-SiO_2 interface they behave differently than at an air-SiO_2 interface. A possible reason for this difference could be due to the difference in interface

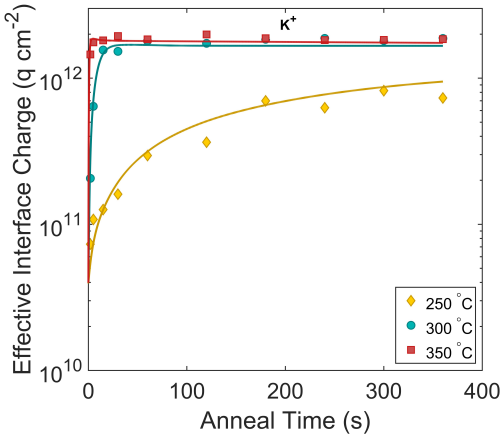

(a)

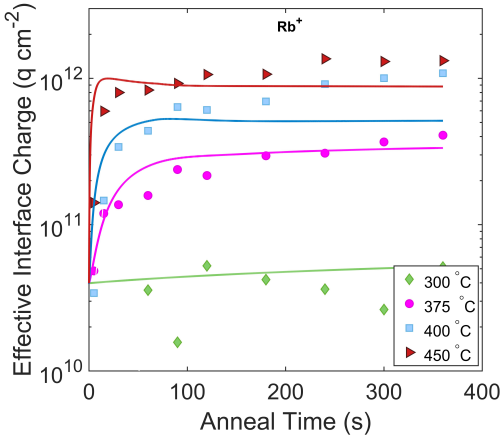

(b)

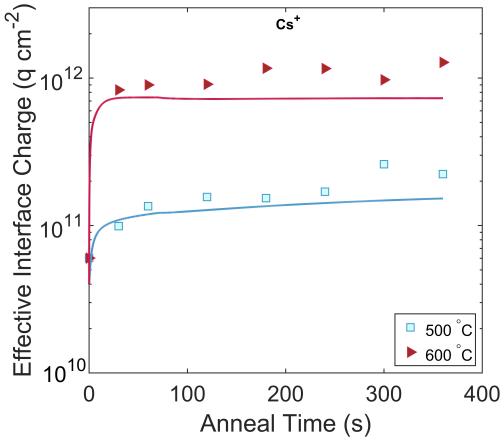

(c)

Figure 3.6: The influence of annealing time and temperature on migrated (a) K^+ (b) Rb^+ and (c) Cs^+ ions at the Si-SiO_2 interface. Solid lines are model fittings using the parameters in Table 3.2.

	K^+	Rb^+	Cs^+
$C_{ao}(t=0)$ (x10^{12} q cm^{-2})	4 [a)]	4	10
	10 [b)]		
$C_{os}(t=0)$ (x10^{12} q cm^{-2})	0	0	0
ΔE_{ao} (eV)	1.44	1.57	1.80
ΔE_d (eV)	1.00	1.34	1.65
ΔE_{os} (eV)	1.90	2.10	2.25

[a)]spin coated [b)]evaporated

Table 3.2: Modelling parameters for the results in Figure 3.6.

trap concentration at a metal-SiO_2 and air-SiO_2 interface. Here, the parameter ΔE_{ao} was varied empirically to establish an accurate fitting. In the case of K^+, a value of 1.44 eV was determined. For Rb^+ and Cs^+ ions, activation energies of 1.57 eV and 1.80 eV were found. The parameter ΔE_{os} was similarly varied and a value of 1.90 eV, 2.10 eV, and 2.25 eV were determined for K^+, Rb^+ and Cs^+, respectively. The depth of the energy well at the Si-SiO_2 interface was chosen as to prevent de-trapping. A more precise value of ΔE_{os} should be determined in future work by analysing the de-trapping and migration of ions at the Si-SiO_2 interface under reverse bias. To the author's knowledge, no reported values of ΔE_{ao} and ΔE_{os} exist in the literature for alkali ions larger than K^+.

Figure 3.7 depicts the modelled volumetric distribution of K^+, Rb^+, and Cs^+ ions throughout the depth of the 100 nm SiO_2 film after six minutes of annealing, using the same experimental and modelling parameters as in Figure 3.6. The results for K^+ are shown in Figure 3.7a. For all three temperatures, the K^+ ions accumulate in the final element of the oxide film, within 0.5 nm of the Si-SiO_2 interface. Depending on the anneal temperature, the peak interface concentration is 3 to 7 orders of magnitude greater than the bulk concentration. This indicates that the experimental Q_{eff} measured is approximately equivalent to the interface charge. This is in good agreement with SIMS results presented in the literature that show the the peak concentration of K^+ ions located within a few nanometres from the Si-SiO_2 interface is at least 1-2 orders of magnitude greater than the concentration within the bulk [111, 115, 178, 196]. The results for Rb^+

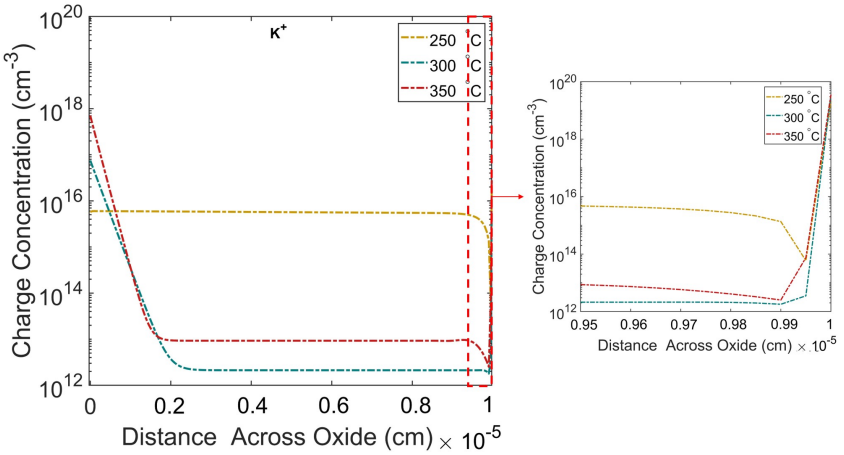

(a)

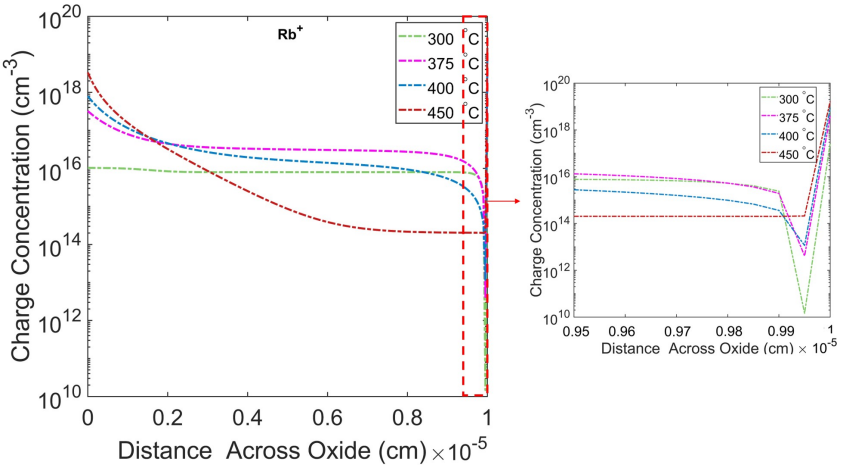

(b)

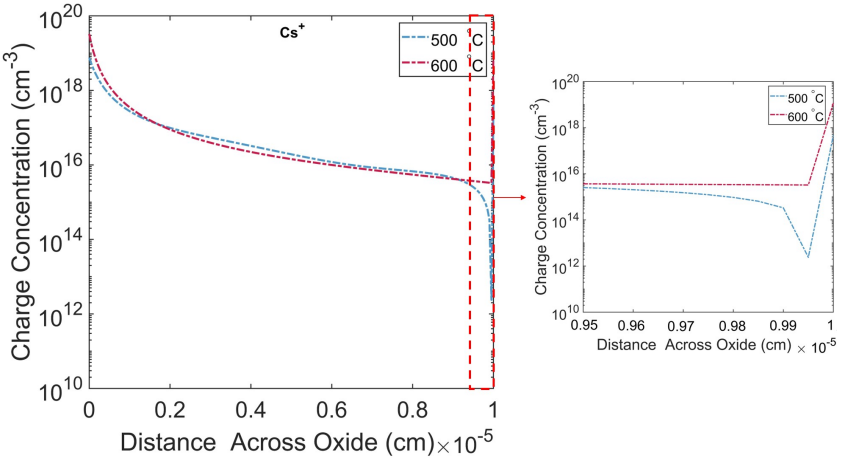

(c)

Figure 3.7: Simulated volumetric distribution of (a) K^+ (b) Rb^+ and (c) Cs^+ ions throughout the depth of the SiO_2 film after 6 minutes of annealing.

ions are shown in Figure 3.7b. Similarly to K^+, the peak concentration of Rb^+ ions migrated at temperatures $\geq$ 375 °C is located within the final element of the SiO_2, at its interface with silicon. With increased temperature, the Rb^+ concentration at the air-SiO_2 interface increases. This is due to the faster decay of corona charge at high temperatures, which results in negligible surface electric field. The untrapped Rb^+ ions within the oxide film are drifted back towards the air-SiO_2 under the field generated by the trapped charge at the Si-SiO_2 interface. The distribution of Cs^+ ions is exhibited in Figure 3.7c The peak concentration of Cs^+ is greater at the air-SiO_2 interface than the Si-SiO_2 interface after annealing at both 500 °C and 600 °C. This can similarly be explained by the reverse drift of untrapped Cs^+ ions due to the accumulated interface charge, once the corona charge has fully decayed.

Figure 3.8 explores the relationship between the concentration of corona charge deposited on the oxide surface prior to annealing, and the saturated Q_{eff} after annealing. The relationship for K^+ ions is shown in Figure 3.8a. Specimens had KCl solution either spin coated or evaporated onto the oxide surface. As before, specimens were cut into 2 cm x 1 cm pieces. Different amounts of corona charge were deposited onto the surface of the specimens. The surface charge concentration was verified used Kelvin Probe before the specimen was annealed for 3 minutes at 300 °C to ensure a maximum Q_{eff}. A linear correlation between the corona-induced surface bias and final interface charge is evident, where the ratio of ionic charge to corona charge observed at 300 °C is nearly 1:1. For spin coated samples where the initial ionic concentration is less, Q_{eff} saturates at $\sim$4 x 10^{12} q cm^{-2}, at which point the surface is presumably depleted of K^+ ions. Until this saturation point is reached, the difference in ionic surface concentration does not affect the relationship observed. The relationship for Rb^+ ions is shown in Figure 3.8b. Specimens were prepared by spin coating RbCl solution before apply varying amounts of corona charge and annealing at 450 °C for 5 minutes. On average, a Rb^+ ionic charge to corona charge ratio of 1:2 is observed. In the case of the larger Cs^+ ion, specimens were corona charged and annealed at 600 °C for 60 s. From the results in Figure 3.6c, it

was determined that the ratio of Cs^+ interface ions to corona charges is 2:5. These observations show that the larger the ion, the smaller the rate of injection and migration to the Si-SiO_2 interface, as supported by the modelling parameters obtained in Table 3.2.

It has been previously suggested in the literature that an applied electric field may lower the energy barrier for ionic conduction through an oxide thin film [93, 187, 197, 198]. To determine if ΔE_{ao} does have a dependency on surface fields, the data in Figure 3.8 were modelled. Here it was determined that a single value of ΔE_{ao} could be used to model the results irrespective of surface charge concentration. Values of 1.34 eV, 1.56 eV and 1.85 eV were chosen as ΔE_{ao} for K^+, Rb^+, and Cs^+ ions, respectively. The other parameters were the same as in Table 3.2. The rate of release of ions at the air-SiO_2 interface is thus unaffected by surface field strength, and the changes in the kinetics are purely given by the electrostatic components considered in the model. The weaker response of Rb^+ and Cs^+ to surface fields than K^+ is explained by the lower injection rate and limited drift velocity of larger ions. The values of ΔE_{ao} used to model the results in Figure 3.6 differ by 0.1 eV, 0.01 eV, 0.05 eV from the values for K^+, Rb^+, and Cs^+ ions given in Table 3.2. These values are in close agreement with each other, and may provide an indication of the range of activation energies for each ion at the air-SiO_2 interface.

3.4 Discussion

Section 3.2 presented a comprehensive model of ion injection and migration through a SiO_2 thin film. Corona discharge was used to provide a surface electric field without the need to deposit a destructive metal contact. Figure 3.1 illustrated the physical system being modelled. Initially, the ions are injected into the oxide film and drifted across to the Si-SiO_2 interface at elevated temperatures under the corona-induced field. Once the corona charge has decayed to negligible concentrations, the drift velocity of the ions becomes significantly smaller. It is therefore imperative that the desired concentration of ions arrive at the Si-SiO_2 interface and are trapped before the corona charge has

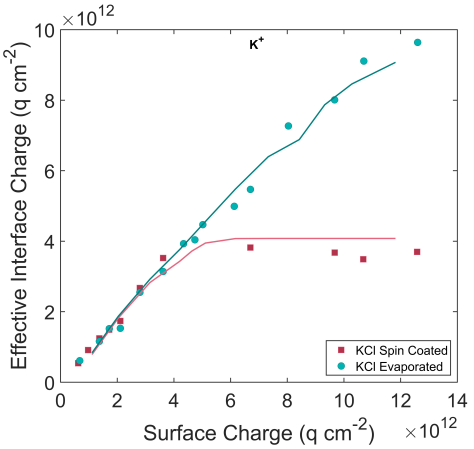

(a)

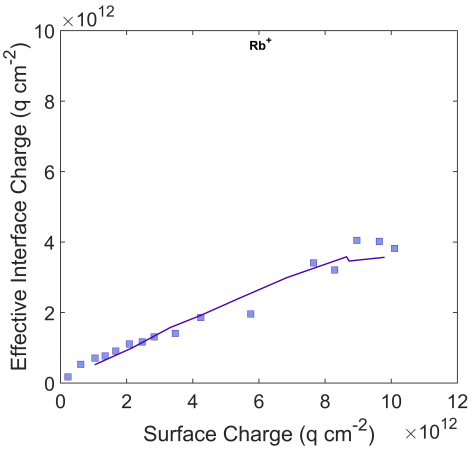

(b)

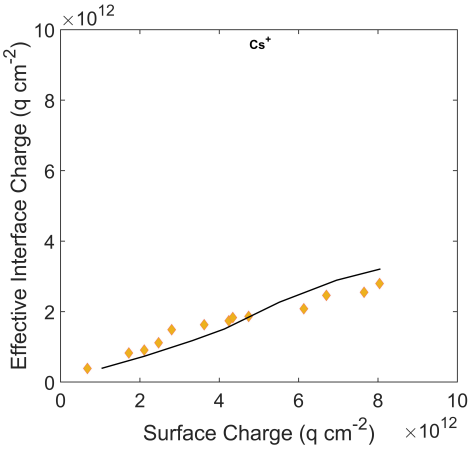

(c)

Figure 3.8: The influence of surface charge concentration pre-anneal on the migrated charge concentration of (a) K^+ (b) Rb^+, and (c) Cs^+ ions. Solid lines are model fittings using a single value for ΔE_{ao} of 1.34 eV, 1.56 eV and 1.85 for K^+, Rb^+, and Cs^+, respectively.

significantly decayed.

Figure 3.6 demonstrated the kinetic response of each ion to the same initial corona charge concentration after annealing at a variety of temperatures. K^+ ions were found to have the greatest mobility owing to their smaller ionic radius. The effective interface charge saturated at $\sim$2 x 10^{12} q cm^{-2} within 60 seconds of annealing at temperatures $\geq$300 °C. To migrate comparable amounts of Rb^+ charge, a 5 minute anneal at a temperature of 450 °C was required. Cs^+ ion samples required a minimum of 1 minute annealing at 600 °C to reach Q_{eff} $\sim$1 x 10^{12} q cm^{-2}. The saturation point for all three ions is reached due to the decay of surface corona charge during annealing. The trapped ionic concentration remains constant after the corona-induced field has decayed due to the depth of the energy well. The electric field generated by the trapped ions at the Si-SiO_2 interface limits further migration, and drifts untrapped ions within the bulk back towards the air-SiO_2 interface. The fit of the model is close to the experimentally acquired data for temperatures below 375 °C. At higher temperatures, the maximum predicted Q_{eff} is below that determined experimentally. This is most likely due to inaccuracies in recording the rapid decay of corona charge at elevated temperatures, which may result in underestimates of the surface electric field in the simulation. This results in a faster reduction of the calculated ionic drift velocity, and the prevention of further charge accumulating due to the compensation of the surface field by the reverse field generated by the trapped ions at the Si-SiO_2 interface.

Figure 3.7 demonstrated the simulated distribution of ions within the SiO_2 film after 6 minutes of annealing at temperatures between 250 °C and 600 °C. It can be seen that as the annealing temperature increases, the greater the accumulation at the air-SiO_2 interface due to the increased mobility at high temperature, and the faster decay rate of the surface electric field. The measured Q_{eff} is not noticeably influenced by the distribution of charge within the bulk. This is due to the significantly greater concentration of ions trapped at the Si-SiO_2 interface relative to the bulk, and because the sensitivity of Q_{eff} decreases with distance away from the interface, as explained in Section 2.8.3.

Given the limit imposed on ion migration by the rate of surface field decay, greater concentrations of corona charge are required to produce high charge density dielectrics. Figure 3.8 demonstrated a dependable linear relationship between the concentration of corona charge concentration deposited prior to annealing and the saturated Q_{eff} after annealing. This is the first time that surface electric fields have been demonstrated to finely tune the ionic interface charge. These findings are relevant to a variety of applications that depend upon charged dielectrics. As will be discussed in Chapter 5, precise control over the ionic interface charge is critical in optimising surface passivation. The capability to tailor dielectric charge is also applicable to the field of electrostatic energy harvesters, where the force factor strongly depends upon dielectric charge [199]. Force factors on the order of 10^{-5} C m^{-1} are considered optimal to produce highly efficient energy harvesters [199]. In previous work, the use of K^+ ion-charged dielectrics produced force factors on the order of 10^{-4} to 10^{-5} C m^{-1} by incorporating $\sim 10^{18}$ ions cm^{-3} within the oxide film [199, 200]. Owing to such high force factors, power conversion efficiencies of 80.7 % have been achieved [200].

The longevity and endurance of ion-charged dielectrics is a crucial factor for industrial compatibility. The values of ΔE_{ao}, ΔE_{os}, and ΔE_d presented in this chapter are indicative of the stability of each ion. Due to their greater energy barriers compared to that of K^+, higher temperatures are required to inject the larger alkali ions, Rb^+ and Cs^+, into the SiO_2 film. Higher temperatures and stronger electric fields are also required to increase the flux of ions within the film. Sugiyama reported that the built-in potential of K^+ charged oxides decreased by 13 % after just one month in ambient conditions. It is expected that the larger alkali ions trapped at the Si-SiO_2 interface will present greater stability than K^+ ions, particularly in response to elevated temperatures and reverse electric fields. The use of Rb^+ or Cs^+ ion-charged dielectrics could allow for the field-effect of high charge density dielectrics to be exploited for long-term use.

3.5 Summary

In this chapter, a comprehensive model of ion migration through SiO_2 has been developed. This model demonstrates for the first time the dependency of ion kinetics on both temperature and surface electric fields. It was determined that surface electric fields affect ionic conduction through a SiO_2 thin film, however, they do not influence the activation energy of injection. As such, a single value of ΔE_{ao} could be used to model the experimental data, irrespective of surface electric field strength. It was found that the value of ΔE_{ao}, ΔE_{os}, and ΔE_d increases with ionic radius. Owing to the deeper energy wells at the air-SiO_2 interface and throughout the oxide film, greater thermal stress and stronger electric fields are required to migrate substantial concentrations of the larger alkali ions, Rb^+ and Cs^+. Larger alkali ions trapped at the Si-SiO_2 interface are expected to present greater durability in comparison to K^+ ions due to the substantial energy barrier, ΔE_{os}. The comparative stability of all three ions is explored further in Chapter 5.

The annealing parameters used in the subsequent chapters of this thesis are based on the results demonstrated here. A summary of these parameters is provided in Table 3.3, and were chosen to ensure that for a given initial corona charge concentration, sufficient heat and time are allowed to saturate the Si-SiO_2 interface with ions. The annealing time was chosen carefully to prevent the transit of ions back towards to the SiO_2 surface at high temperatures after the corona charge has decayed.

	K^+	Rb^+	Cs^+
Annealing Temperature (°C)	300	450	600
Annealing Time (s)	180	300	60
Corona Charge Concentration	Variable		

Table 3.3: Summary of processing parameters used in the following chapters of this thesis.

Versatile techniques of incorporating alkali ions into SiO_2 have been presented in this chapter. Through thermal evaporation or spin coating, ions can be deposited directly onto the dielectric surface. By modulating the surface electric field strength prior to annealing, and the annealing temperature and time, the ionic interface charge can be finely tuned. The exploitation of corona discharge as a non-destructive technique to impose a temporary electric field can be used in a range of applications.

4 | Engineering Ionic Precursors and Delivery Methods

This chapter discusses the development and optimisation of ionic precursors and delivery methods. Here, both research scale techniques, such as thermal evaporation, and industrially compatible techniques, such as spin coating, can be used to deposit ionic precursors with negligible contamination. Ionic contaminants are prevalent in the environment and can be found on most surfaces, including metal contacts. It is essential for device performance that the ionic precursor delivery methods minimise such contamination. Studies dating back to the 1960s researched methods to remove ions from dielectric films [188, 201, 202]. Contaminants such as Na^+, and to a lesser extent K^+, are detrimental to device performance owing to their instability within the dielectric at operational voltages and raised temperatures [181, 182, 203]. Additionally, Na^+ ions have been reported to migrate into stacking faults at the silicon surface and generate new defects [176, 204, 205]. In contrast to Na^+, the stability of larger alkali ions can be harnessed to provide durable electric fields [67, 93, 111, 112].

Industry requires fast, scalable, and reproducible production of solar cells. In Chapter 3, it was shown that within less that a minute at elevated temperatures, substantial ionic charge could be built into a Si-SiO_2 interface. Such rapid migration makes the proposed methodology compatible with industry requirements that demand a high average throughput of at least 1 wafer processed every half a second [43]. Furthermore, the use of spin coating, corona discharge, and annealing is well reported within the semiconductor field, and are suitable for batch and in-line processing [18, 100, 103].

In addition to high throughput, industrial solar cell production requires longevity. Therefore, this thesis explores the use of larger and potentially more stable alkali ions - rubidium and caesium. Other authors have asserted in the past that alkali ions with a

larger ionic radius than K^+ are too big to be mobile within SiO_2 [174, 175]. In experimental studies, Deal reported zero drift of Cs^+ ions in MOS structures under applied fields up to temperatures of 300 °C [175]. To the author's knowledge, the migration of Rb^+ ions within SiO_2 has been reported once [115]. However, the presence of the ionic species was assumed, not proven. In this chapter, it is proven that Rb^+ and Cs^+ ions are indeed mobile within SiO_2, and can be drifted through the oxide matrix. To confirm this, SIMS depth profiling was used to detect the presence of all three ions within the SiO_2 thin film.

This chapter first provides an overview of previously reported methods to embed extrinsic charge within dielectrics, and their relevance and practicality within industry. Subsequently, the development and optimisation of aqueous K^+, Rb^+, and Cs^+ ionic precursors is discussed. To demonstrate the industrial compatibility of both the deposition and the migration procedure for all three ions, the spatial uniformity and reproducibility of Q_{eff} is demonstrated across multiple specimens. This chapter also demonstrates for the first time the *in situ* incorporation of Cs^+ ions during oxidation.

4.1 Review of Extrinsic Charging and Delivery Methods

Previously reported methods of incorporating extrinsic charge within dielectric thin films include electron beam injection [206], x-ray charging [109, 207], ion implantation [110, 208], and corona charging [66, 103, 107]. While little data exist for the stability provided by x-ray charging, charge incorporated within SiO_2 by electron beam and corona charging is reported to be stable for only a few weeks at most under operational conditions [209, 210]. The stability of ion implantation depends on the species. For example, implanted phosphorus and boron atoms are reported to be stable within SiO_2 for 5 months and 1.5 years, respectively [110]. This technique has also been reported to embed Cs^+ ions within SiO_2 [172, 173, 194]. Caesium ions are first implanted into the silicon wafer at energies varying from 20 - 145 keV to produce charge concentrations of

10^{13} - 5 x 10^{14} q cm^{-2} [172, 173, 194]. The ions are embedded as fixed charges within the SiO_2 film during oxidation as the implanted silicon region is consumed. Ion implantation is energy intensive, and the interface charge control depends strongly upon the oxide depth [172, 173, 194]. Additionally, while ion implantation is a doping technique common to semiconductor manufacturing, it is rarely used within the PV industry where the traditional diffusion technique is more prevalent to create doped regions [211–213].

In recent years, an alternative method of incorporating ions *in situ* during oxidation has been developed by Sugiyama [111]. Here, potassium hydroxide (KOH) is heated within a bubbler. The vapour produced is transported by a carrier gas into the oxidation furnace where the ions become embedded within the SiO_2 film as it grows. This technique has been reported to result in very high ionic charge concentrations on the order of 10^{17} - 10^{18} ions cm^{-3} [111, 112]. This technique of embedding ions *in situ* during oxidation is particularly suited to industry since it reduces the number of additional processing steps required to incorporate extrinsic dielectric charge. Additionally, it relies upon conventional equipment used for oxidation, and as such can be readily implemented into a production line. To the author's knowledge only K^+ ions have been introduced during dielectric synthesis using this method [111, 112, 179, 196, 199, 200]. Section 4.5 demonstrates for the first time that Cs^+ ions can also be incorporated *in situ* during oxidation.

It has also been demonstrated that K^+ ions deposited on an oxide surface can be injected into the dielectric and migrated towards the Si-SiO_2 interface at temperatures >300 °C [67, 93]. Early reports of this technique used thermal evaporation to deposit K^+ ions on the oxide surface [93, 113]. KCl salt dissolved in pure DI water served as the aqueous precursor for deposition [93, 113]. Later work by Collett demonstrated the versatility of such precursors by showing that K^+ ions could also be deposited on the oxide surface using spin coating and spray coating techniques [67, 115]. These techniques may be preferable to thermal evaporation owing to their speed and lower energy consumption [151]. Spin coating and spray coating were used in the creation of uniformly ion-charged

oxides [67, 115]. To improve the wettability of the oxide surface and reduce the drying time, KCl salt was dissolved in a mixture of DI water and IPA [67]. For evaporation, spin coating, and spray coating, control of the precursor molarity and the volume deposited allowed for sub-monolayer concentrations of K^+ ions to be uniformly delivered to the SiO_2 surface [93, 113, 115]. The ions are presumed to remain bound to the chloride counterpart upon the surface, and are dissociated upon thermal activation. Due to the sparsity of the ions deposited on the oxide surface, salt crystals do not nucleate through aggregation. Excess ionic concentrations have been reported to result in clustering of crystallised salt, which impedes injection into the dielectric [115].

4.2 Ionic Precursors for K^+, Rb^+ and Cs^+ ions

In Chapter 3, both thermal evaporation and spin coating were used to deposit KCl solution onto the oxide surfaces of Set A (n-type 1 Ω cm FZ) wafers. For thermal evaporation, the precursor was prepared by dissolving KCl salt in pure DI water, following the work of Bonilla and Collett [67, 93, 113]. In this thesis, a calibrated pipette was used to deposit 50 μL of 1 mM KCl solution into a clean tungsten boat prior to evaporation. This was estimated to deliver a surface ionic concentration of $\sim 10^{13}$ ions cm^{-2}. This estimate was made based the maximum amount of ions that could be migrated to the interface in the presence of excess corona charge. Figure 4.1 shows that the K^+ Q_{eff} plateaus at $\sim 10^{13}$ q cm^{-2} after a corona deposition time of 160 s, equivalent to a Q_{surf} $\sim 10^{13}$ q cm^{-2}. Since further corona charging does not migrate any more ionic charge, it is assumed that the oxide surface has been depleted of ions. The x axis is provided in terms of corona deposition time since the Kelvin Probe has a maximum detection limit of 10^{13} q cm^{-2}, and as such greater corona charge concentrations could not be quantified.

For spin coating, the same molarity KCl solution was used. Following reference [115], a mixture of 75 % IPA and 25 % DI water was used to increase the wettability of the

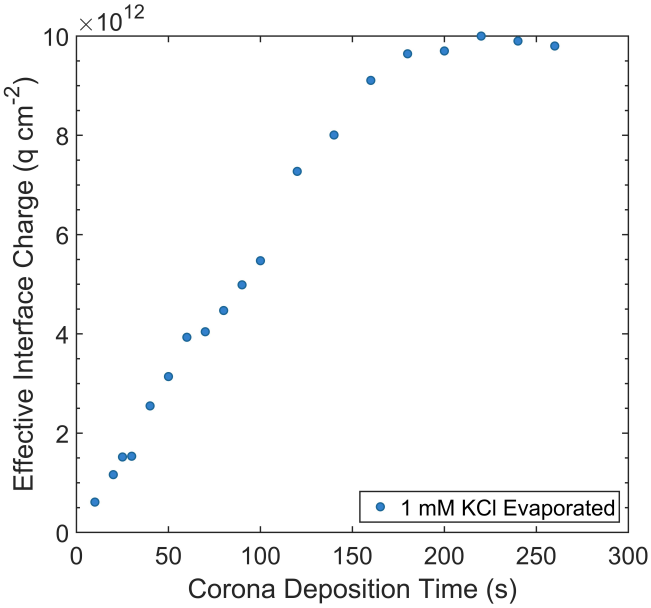

Figure 4.1: Effect of corona deposition time on K^+ ion Q_{eff} for evaporated specimens. Corona charge was deposited at a tip voltage of +30 kV.

spinning substrate and to accelarate the solvent evaporation. This ratio of IPA to DI water was optimal as the oxide surface was found to be completely dry upon removal from the spin coater. Increasing the percentage of DI water to 40 % resulted in the remainder of droplets visible to the naked eye. The droplets evaporated shortly after removal within 10 to 15 seconds. The avoidance of droplets is important to prevent localised areas of variable ionic concentration, or slow drying leading to crystal nucleation. The aqueous precursors for Rb^+ and Cs^+ were prepared similarly to produce 1 mM solutions. Figure 4.2, shows the dependency of the Q_{eff} on corona deposition time for K^+, Rb^+, and Cs^+ charged oxides. Oxidised wafers were spin coated with either 1mM KCl, 1 mM RbCl, or 1 mM CsCl solution. Since many specimens were to be tested, the substrates were cleaved into small pieces of approximately 2 cm x 1 cm. Following corona charging, the specimens were annealed at 300 °C, 450 °C and 600 °C for K^+, Rb^+, and Cs^+, respectively. It was determined that the maximum Q_{eff} for both K^+ and Rb^+ ions saturated at a 4 x 10^{12} q cm^{-2} after 50 s and 120 s of corona charging, respectively. Given that depositing excess corona charge does not migrate any more ions, it can be presumed that the Q_{eff} saturation

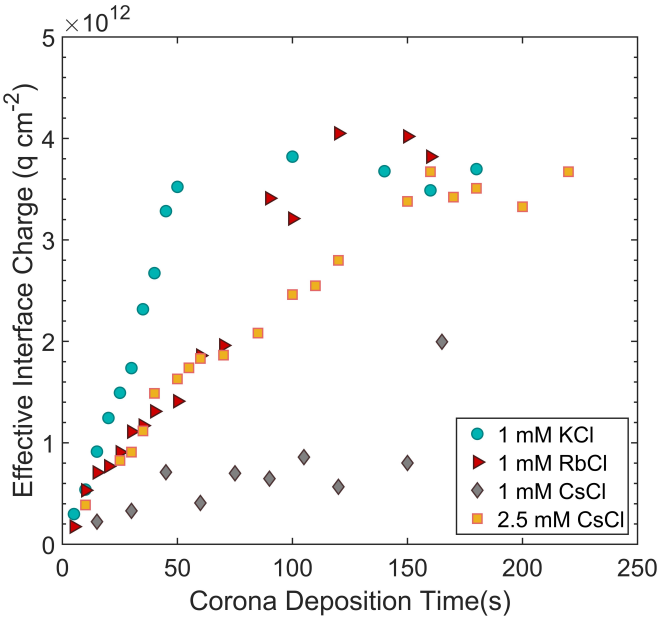

Figure 4.2: Effect of corona deposition time on K^+, Rb^+, and Cs^+ ion Q_{eff} for spin coated specimens. Corona charge was deposited at a tip voltage of +30 kV.

point is equivalent to the ionic surface concentration after deposition. It can be seen that Cs^+ migration is significantly lower in comparison to K^+ and Rb^+, and additionally the data shows irregular dependency on corona charge.

To test if a stronger molarity CsCl solution would introduce more ions to the interface, a 2.5 mM solution was prepared. Samples spin coated with 2.5 mM CsCl solution were similarly corona charged and annealed at 600 °C. The results are also shown in Figure 4.2. The 2.5 mM CsCl solution resulted in greater ion migration and a similar dependency on corona charge as Rb^+ ions. Unexpectedly, the concentration of Cs^+ ions saturated at ~3.5 x 10^{12} q cm^{-2}, despite the greater ionic surface charge concentration. The saturation occurred at ~150 s of corona deposition, which is equivalent to ~10^{13} q cm^{-2}. One possibility could be that at such high temperatures of 600 °C, the corona decays so quickly that once a substantial concentration of trapped charge accumulates at the Si-SiO_2 interface, further migration is limited by coulombic repulsion. Another possibility could be that the SiO_2 film cannot sustain surface electric fields beyond the limit of 10^{13} q cm^{-2} due to the dielectric breakdown strength. To test these hypotheses,

spin coated specimens 5 cm x 5 cm in size had the cycle of corona charging and annealing performed between 1-7 times. For each cycle, 30 s of corona charge was deposited. This is equivalent to $\sim$2 x 10^{12} q cm^{-2}, which is well below the suspected dielectric breakdown limit. Corona charging was followed immediately by a 60 second anneal at 600 °C. After the final cycle, MOS structures were created, and Q_{eff} was recorded at 10 locations per specimen, hence the use of larger substrates. The results are shown in Figure 4.3. It can be seen that the mean Q_{eff} increases from 1.63 x 10^{12} q cm^{-2} after 1 cycle to 3.75 x 10^{12} q cm^{-2} after 5 cycles. Performing more than 5 cycles resulted in a reduction in the mean Q_{eff}. Since the applied corona concentration was equivalent to $\sim$2 x 10^{12} q cm^{-2}, it is likely that the higher trapped charge concentration at the Si-SiO_2 interface counteracts the rapidly decaying surface electric field. Thus, the reverse field drifts untrapped ions near the interface back towards the oxide surface, lowering the measured Q_{eff}. From the data in Figure 4.3 it can also be seen that Q_{eff} can be increased following numerous cycles, however, the distribution of charge is highly variable in specimens that were subjected to more than 1 cycle. Therefore this method of increasing the interface charge is not advised to produce uniformly charged dielectrics. Further analysis of the ionic charge uniformity is presented next.

4.3 Ionic Interface Charge Uniformity

To provide effective surface passivation, a uniform electric field is required to be distributed laterally across the whole silicon surface. Firstly, the lateral uniformity was evaluated for K^+ ion-charged oxides that had been prepared using thermal evaporation and spin coating deposition techniques. Three 5 cm x 5 cm specimens had 1 mM KCl solution either evaporated or spin coated on the SiO_2 surface. The samples were corona charged for 30 seconds and annealed at 300 °C for 3 minutes to produce Q_{eff} $\sim$2 x 10^{12} q cm^{-2}. To evaluate the lateral uniformity of charge within each specimen, MOS structures were created, and Q_{eff} was measured at 10 locations per specimen using CV.

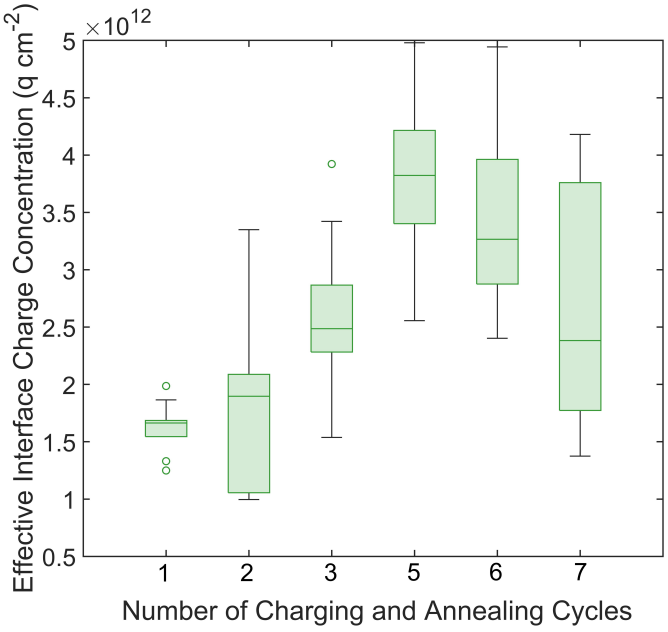

Figure 4.3: Distribution of Cs^+ ion Q_{eff} after multiple cycles of corona charging and annealing. Q_{eff} was recorded at 10 locations per specimen.

Figure 4.4 shows the variation in K^+ ion Q_{eff} for both evaporated and spin coated samples. For the evaporated specimens, all measured values of Q_{eff} fall within 5-7 % of each specimen's mean. For the spin coated specimens, the measured values fall within 10-17 % of each specimen's mean. A summary of the mean and standard deviation of each specimen is provided in Table 4.1. These results show that thermal evaporation produces a more uniform distribution of Q_{eff} in comparison to spin coating. The poorer uniformity in spin coated specimens could be due to the introduction of impurities, which would explain the slightly higher mean Q_{eff} of all three spin coated specimens compared to those that were evaporated. Since thermal evaporation took place within a clean room environment, and under vacuum, the presence of impurities is minimised. Spin coating was performed under normal laboratory conditions. Charge fluctuations within the dielectric can affect device performance by modifying the surface passivation provided by the dielectric's built-in potential. It has been reported that at charge concentrations between 10^{11} q cm^{-2} and 2 x 10^{12} q cm^{-2}, such fluctuations can result in efficiency losses of $\sim$1 % [214].

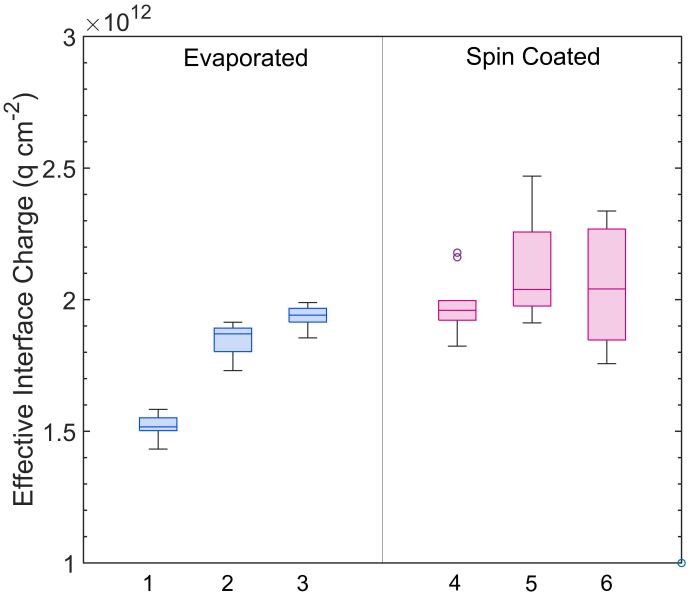

Figure 4.4: Distribution of K^+ ion Q_{eff} of 3 specimens that had KCl evaporated and 3 specimens that were spin coated prior to migration. Q_{eff} was recorded at 10 locations per specimen.

SPECIMEN	MEAN (Q CM^{-2})	STANDARD DEVIATION (Q CM^{-2})
1	1.52 x 10^{12}	4.74 x 10^{10}
2	1.85 x 10^{12}	5.90 x 10^{10}
3	1.93 x 10^{12}	4.50 x 10^{10}
4	1.98 x 10^{12}	1.15 x 10^{11}
5	2.10 x 10^{12}	1.77 x 10^{11}
6	2.05 x 10^{12}	2.17 x 10^{11}

Table 4.1: Summary of charge uniformity data in Figure 4.4.

Figure 4.5 shows the variation in Q_{eff} for three samples that had 1 mM RbCl or 2.5 mM CsCl solution spin coated, followed by corona charging and annealing. Due to the difference in the two ions' dynamics, different corona charging and annealing conditions were used. Rb^+ samples were corona charged for 120 s and annealed at 450 °C. Cs^+

samples were corona charged for 30 s and annealed at 600 °C. MOS structures were created after ion migration, and Q_{eff} was measured at 10 locations on each specimen's surface. A summary of the plotted results is provided in Table 4.2. Here it was found that all Cs^+ samples exhibited better charge uniformity than Rb^+ samples. The standard deviation of the mean for Cs^+ samples is comparable to that of spin coated K^+ samples in Table 4.1. Both K^+ and Cs^+ samples had a mean Q_{eff} of 1.5 - 2 x 10^{12} q cm^{-2}, while the mean Q_{eff} of Rb^+ samples was ~3.2 x 10^{12} q cm^{-2}. It is widely reported in the literature that the charge distribution varies more as Q_{eff} increases [103, 162, 214]. Empirical data in reference [115] demonstrated that increasing K^+ ion Q_{eff} results in greater charge fluctuation within the dielectric. It has been reported that charge fluctuations of 5 x 10^{11} q cm^{-2} have a negligible effect on solar cell efficiency where the dielectric charge is >2 x 10^{12} [214]. The mean Q_{eff} and fluctuations in Rb^+ and Cs^+ charge presented in Figure 4.5 are within a similar range, and are therefore not expected to be detrimental to the surface passivation quality.

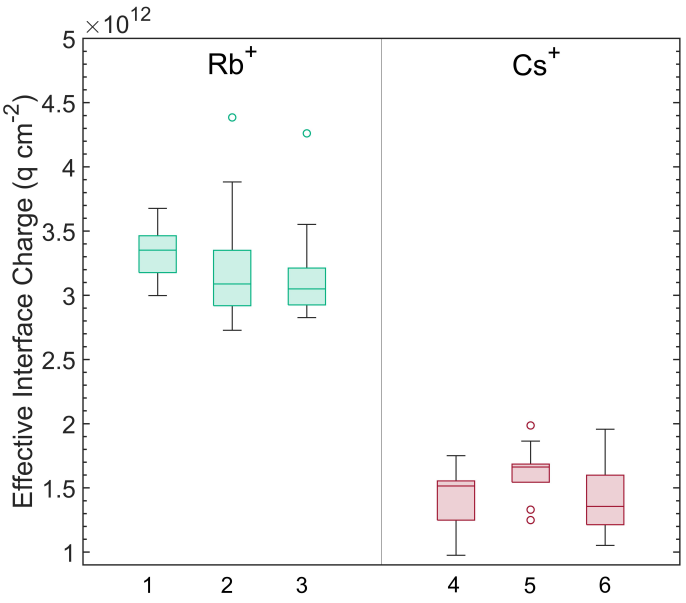

Figure 4.5: Distribution of Q_{eff} within 3 specimens that had RbCl spin coated and 3 specimens that had CsCl spin coated. Q_{eff} was recorded at 10 locations per specimen.

SPECIMEN	MEAN (Q CM^{-2})	STANDARD DEVIATION (Q CM^{-2})
1	3.33 x 10^{12}	2.03 x 10^{11}
2	3.24 x 10^{12}	5.20 x 10^{10}
3	3.18 x 10^{12}	4.32 x 10^{10}
4	1.45 x 10^{12}	2.34 x 10^{11}
5	1.63 x 10^{12}	2.19 x 10^{11}
6	1.41 x 10^{12}	2.80 x 10^{11}

Table 4.2: Summary of charge uniformity data in Figure 4.5.

4.4 SIMS Profiling of Alkali Ions Within SiO_2

Secondary ion mass spectroscopy was used to confirm the presence of K^+, Rb^+, and Cs^+ ions following ion injection and migration. 1 mM KCl was thermally evaporated onto the oxide surface of Set A wafers. On separate samples, 1 mM RbCl and 2.5 mM CsCl solution were spin coated. Following this, all samples were corona charged and annealed to drift the ions to the interface. Before being loaded into the PFIB-SIMS, all samples were coated with 15 nm of platinum to avoid charging from the insulating oxide film. The results are shown in Figure 4.6. The cycle number is an indicator of the depth into the SiO_2, from where atoms are being ablated. The location of the surface of the underlying Si wafer is marked by the abrupt drop in the Si^+ signal due to the well-known dramatic change in ion ablation yield for Si^+ ions at the Si-SiO_2 interface due to the abrupt reduction in oxygen concentration [215, 216]. To ensure Q_{eff} can be predominantly attributed to each of these ions, common contaminants such as Na^+ and, for the Rb^+ and Cs^+ samples, K^+ ions were also profiled. In the KCl sample, Figure 4.6a confirms the majority presence of K^+ ions in the SiO_2 layer. A negligible signal intensity denotes a trace contamination by Na^+ ions. Figure 4.6b shows results from two samples where Rb^+ ions were introduced to the oxide by corona charging for 30 s and 180 s,

respectively, followed by 5 minutes of annealing at 450 °C. The sample with the longer charging time, and therefore stronger surface electric field, shows deeper penetration of Rb^+ ions into the oxide layer, and increased accumulation at the Si-SiO_2 interface. Similar to Figure 4.6a, a negligible concentration of Na^+ and K^+ ions was recorded in the sample with the shorter charging time, thus demonstrating that the methodology of ion introduction used in this work is a very clean process. Figure 4.6c demonstrates the successful incorporation of Cs^+ ions into SiO_2, which is the largest of the three ions studied. The profile shows that Cs^+ ions have not only been introduced into the oxide surface but have also been able to migrate through the film towards the Si-SiO_2 interface.

4.5 *In Situ* Delivery During Oxidation

It is highly desirable to deliver ions to the dielectric film during synthesis. *In situ* delivery eliminates the need for additional processing steps to embed the ionic charge, which is advantageous for high throughput manufacturing of ion-charged dielectrics. In this section, it is demonstrated for the first time this method can be used to embed Cs^+ ions *in situ* during oxidation. For this experiment, Set B wafers (n-type 30 - 60 Ω cm CZ) were used. These were oxidised to 100 nm thickness at the Begbroke clean room at the University of Oxford using the procedure described in Section 2.2.1. The substrates were cut into 2 x 1 cm samples, and the existing SiO_2 film was etched off with hydrofluoric acid to reveal bare silicon. This was followed by an RCA clean to remove organic residues and metal contaminants. The details of RCA clean can be found in Appendix A.1. Immediately following the RCA clean, the substrate was placed into a quartz tube and positioned in the middle of the furnace. Figure 4.7a provides an illustrative schematic of the experimental set-up. The end of the glass tube was closed off and argon (Ar) gas was used to flush out air as the furnace was heated to 950 °C. At the same time a bubbler containing 300 mL of 5 wt. % CsOH in DI water was gradually heated to ∼80 °C. Once the target temperature of the furnace was reached, the Ar gas

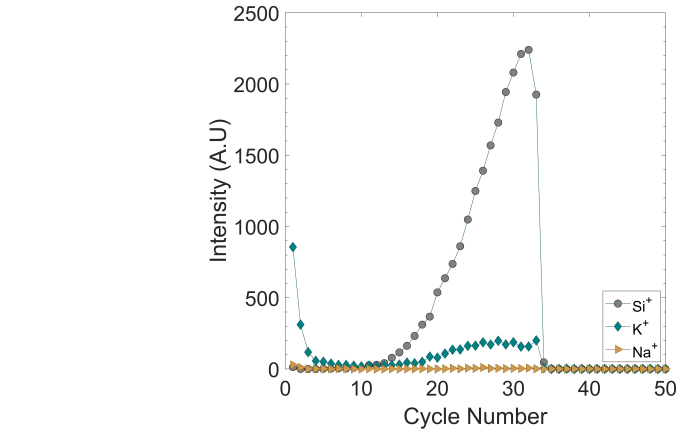

(a)

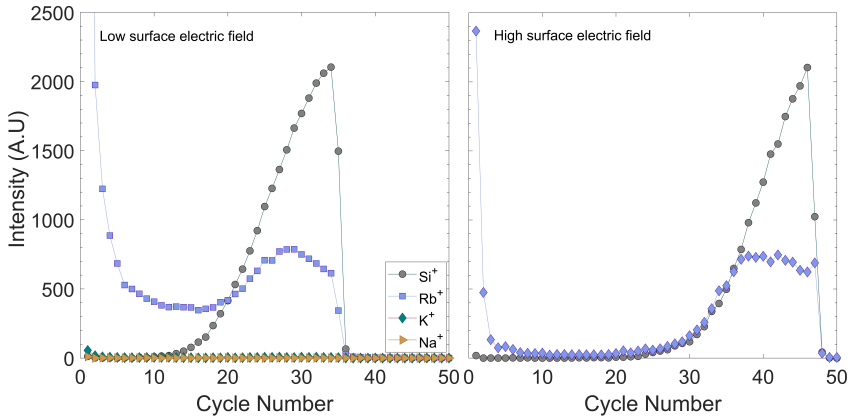

(b)

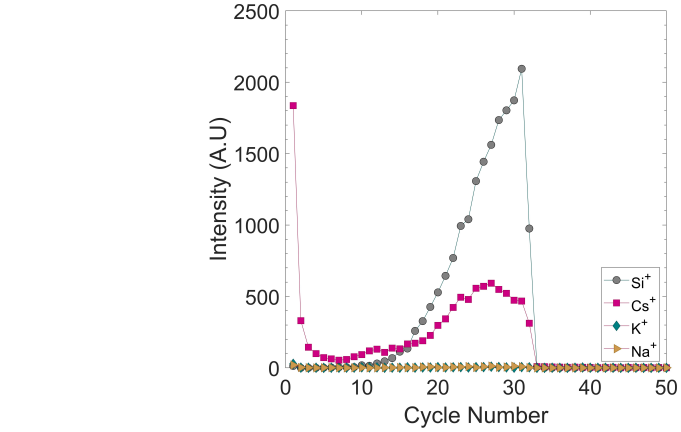

(c)

Figure 4.6: SIMS depth profiling through SiO_2 for (a) K^+ ions (b) Rb^+ ions annealed under 30 s and 180 s corona charge exposure at +30 kV and (c) Cs^+ ions.

valve was closed and O_2 gas was allowed to flow directly into the tube at a rate of 1 L min^{-1}. After 30 minutes of dry oxidation, the Ar valve was re-opened and the flow was directed to the bubbler at a rate of 0.2 L min^{-1}. The inert Ar served as a carrier gas to transport the water vapour containing Cs^+ into the tube furnace as the oxide forms. Both O_2 and Ar were allowed to flow for another 60 minutes. At the end of a total oxidation time of 90 minutes, the furnace was turned off and the gases stopped. The specimen was extracted at 600 °C. Figure 4.7b provides a summary of the oxidation timeline.

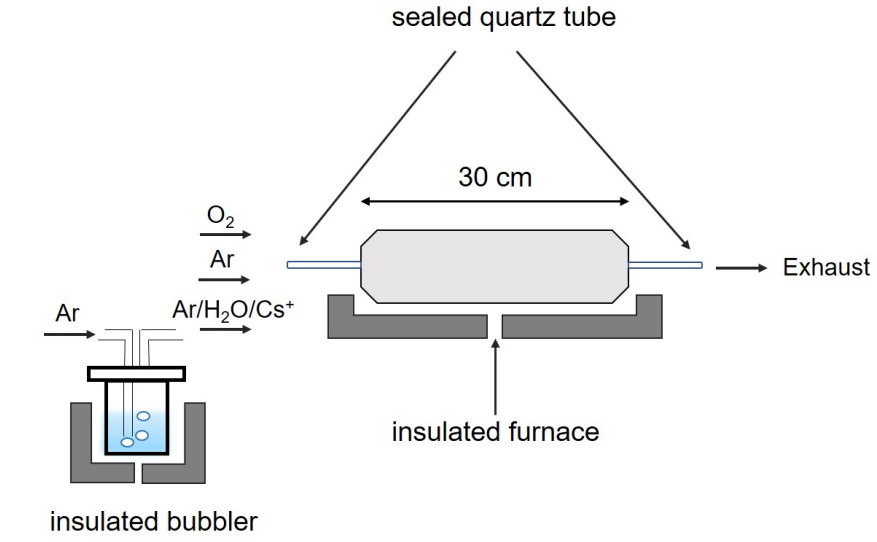

(a)

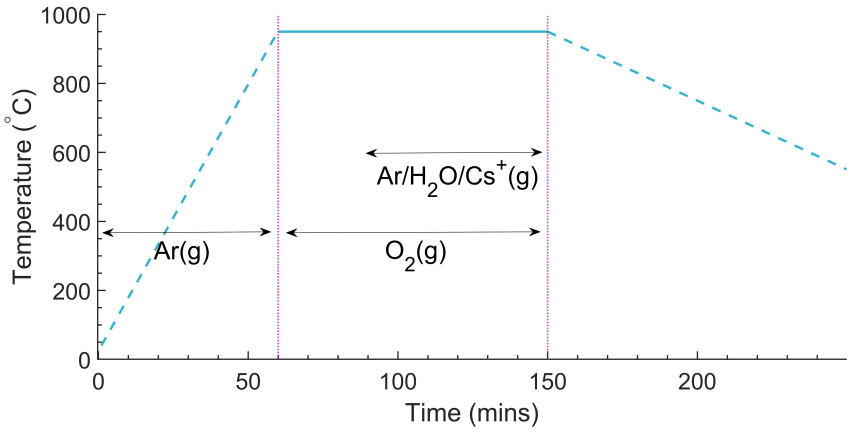

(b)

Figure 4.7: (a) Schematic of the experimental set up to deliver Cs^+ ions during oxidation (b) Summary of the oxidation timeline. Oxidation was performed at a temperature of 950 °C.

Two types of control specimens were produced in addition to the experimental specimen. The first control underwent the same procedure described above, however, only pure DI water was added to the bubbler. To avoid cross-contamination, a separate clean bubbler was used from the one that contained CsOH solution. The second control was oxidised for the full 90 minutes without the introduction of any vapour to produce a dry oxide film. Following the creation of all three sample types, the oxide thickness was measured at five locations per specimen using an ellipsometer. Figure 4.8a plots the recorded oxide thicknesses. The dry oxide had a thickness of 95.5 $\pm$ 0.66 nm. This is higher than the predicted value of $\sim$60 nm by the well-established Deal-Grove model for dry oxidation under similar conditions [217]. It is plausible that the ambient humidity in the laboratory increased the oxidation rate. It is advisable for future work to flood the oxidation tube with nitrogen for a longer duration to produce a dryer environment. The thickness of the wet oxide produced after bubbling pure DI water during oxidation was 131.8 $\pm$ 1.4 nm. A film thickness of 190.4 $\pm$ 4.7 nm was recorded on the wafer exposed to CsOH vapour. The large difference in film thickness between the two wet oxides is due to a lack of control of the vapour pressure leaving the bubbler. Both wet oxides are also considerably thicker than the predicted value of 100 nm by the Deal-Grove model for wet oxidation [217].

Subsequently, MOS structures were created on all three specimens, as described in Section 2.8.3. CV measurements were taken at 5 locations on each to determine the Q_{eff} after the three different oxidation processes. The results are shown in Figure 4.8b. The dry oxide film had Q_{eff} of 3.22 $\pm$ 0.33 x 10^{12} q cm^{-2}. This value is significantly higher than industrial standards of $\sim 10^{10}$ q cm^{-2}, and is due to residual contamination at the silicon surface. Such a high concentration of impurities can be explained given the simple set up, relatively low gas pressures, and the fact the procedure did not take place in a clean room. The measured Q_{eff} increased slightly to 3.63 $\pm$ 0.26 x 10^{12} q cm^{-2} after bubbling pure DI water. The small increase implies that the DI water is very clean and does not introduce a significant amount of impurities. Following the exposure to CsOH

vapour, the third sample showed the largest Q_{eff} of 6.00 $\pm$ 0.21 x 10^{12} q cm^{-2}.

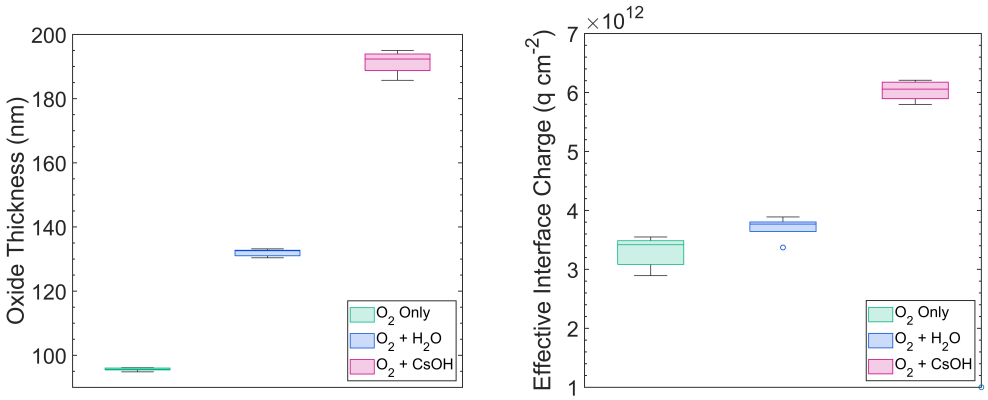

(a) (b)

Figure 4.8: (a) Oxide thickness measured at 5 locations per sample (b) Uniformity of Q_{eff} measured at 5 locations per sample.

Secondary ion mass spectroscopy was used to confirm the presence of Cs^+ within the dielectric. Here, in addition to Cs^+ ions, the expected major contaminants Na^+ and K^+ were also profiled. The MOS structure suspected to contain Cs^+ ions was placed on a hotplate at 450 °C. A strong forward bias was applied to the aluminium dot to drive all the ionic charge to the Si-SiO_2 interface so that its detectability within SIMS would be enhanced. While on the hotplate, an arbitrarily strong electric field of 7.5 x 10^5 V cm^{-1} was chosen, equivalent to a bias of 14.25 V, and held for 20 minutes at a constant temperature. The sample was subsequently coated with 15 nm of platinum before being loaded into the PFIB-SIMS. The SIMS depth profiles of Na^+, K^+, and Cs^+ ions are shown in Figure 4.9. As described in Section 4.4, the Si^+ signal is an indicator of the depth of the oxide film, where the drop in the signal intensity indicates the interface with the silicon wafer. Here, a small signal intensity confirms the presence of Cs^+ ions located close to the Si-SiO_2 interface. Stronger signals were recorded for Na^+ and K^+ ions at a similar depth within the dielectric. The relative intensities indicate that a high concentration of contaminants were present during oxidation, as expected from the lack of clean room conditions. The contaminants most likely settle on the bare silicon during exposure of the surface after

RCA cleaning.

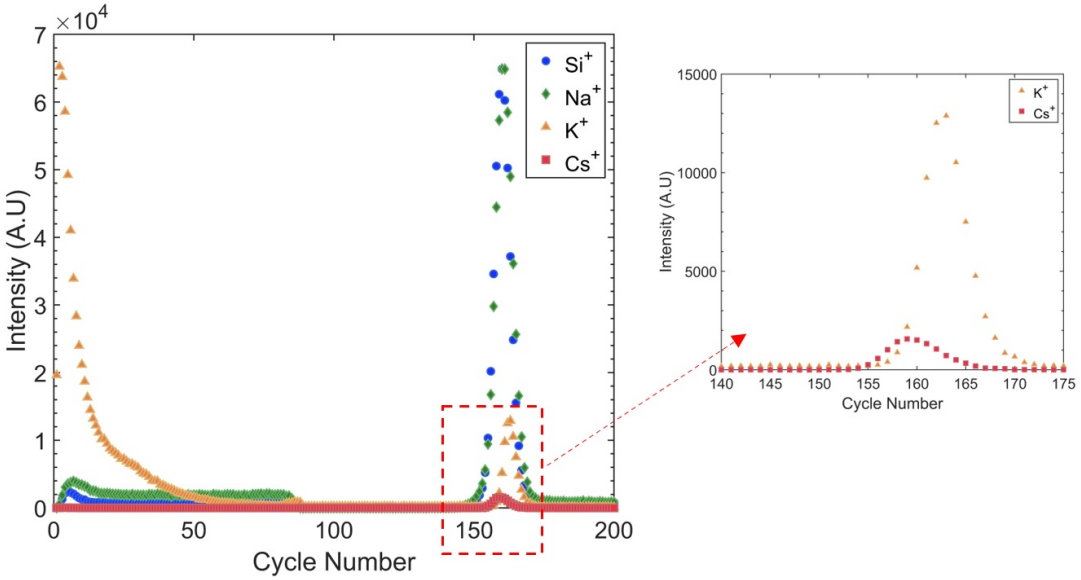

Figure 4.9: SIMS depth profiles of Na^+, K^+, and Cs^+ within SiO_2 after *in situ* oxidation in the presence of CsOH vapour.

4.6 Discussion

In this chapter, the development of ionic precursors and delivery methods was explored. The versatility of ionic deposition was demonstrated through the use of both thermal evaporation and spin coating. Both methods are well-established within the semiconductor and electronics industries [151, 218, 219]. Spin coating was the preferred technique in this thesis since different ions could be deposited in this way without cross-contamination. As discussed in depth in reference [115], thermal evaporation of K^+ ions results in permanent contamination of the evaporation chamber. Additionally, due to the high energy consumption of thermal evaporation, solution based processing such as a spin coating, or spray coating, are more attractive techniques [151]. Spray coating was not studied in this work as a deposition technique due to lack of equipment on-site, however, in previous work by Collett, spray coating was demonstrated to successfully deliver a uniform concentration of K^+ ions [67, 115].

The results for K^+ ions in Figure 4.1 and Figure 4.2 demonstrated that the deposition technique strongly influences the amount of ions deposited on the dielectric surface. For the same 1 mM KCl solution, an estimated ionic surface concentration of 10^{13} ions cm^{-2} was produced after thermal evaporation in comparison to 4 x 10^{12} ions cm^{-2} after spin coating. It was also demonstrated in Figure 4.4 that the resulting uniformity in Q_{eff} was influenced by the deposition technique. All samples that were spin coated prior to ion migration had greater spatial fluctuations in charge compared to those that were evaporated. These results indicate that thermal evaporation may be the more suitable technique where uniform charge densities are required along the interfacial plane. This is particularly important for devices that are sensitive to changes in capacitance, such as electret microphones and actuators [111, 179, 220, 221]. Charge uniformity is also reported to be highly desirable in the design of air filters due to the coulombic attraction between the dielectric and particulate matter [222]. As will be demonstrated in Chapter 5, uniform surface electric fields are necessary to create stable accumulation layers for well passivated silicon surfaces. Although greater fluctuation was recorded in spin coated specimens, it was observed that the reproducibility of the mean was better. The difference between inter-sample reproducibilty of the mean for spin coated and evaporated specimens is small, and may not be of statistical significance given the small sample size. Additionally, small variation in the resulting mean could depend upon other factors such as the precise concentration of corona charge and the small fluctuations in the temperature of the hotplate during annealing.

Figure 4.2 demonstrated that for Cs^+ ions the concentration of ions deposited via spin coating influenced the amount of charge migrated to the Si-SiO_2 interface. The use of a 1 mM solution resulted in < 10^{12} q cm^{-2} after 150 s of corona charging, and annealing at the maximum temperature of 600 °C. The 2.5 mM solution resulted in both better charge control and a greater concentration of ions at the interface under the same migration parameters. For this reason, the 2.5 mM solution was used throughout this thesis. As demonstrated in Section 3.3, different ionic surface concentrations of K^+ ions did not

noticeably influence the kinetic response of the ions. For the larger Cs^+ ion, which faces a greater energy barrier of injection and diffusion, the probability of overcoming the barrier is significantly smaller, and for this reason the dynamics are more sensitive to the ionic surface concentration. This leads to the possibility of tuning the final ion concentration by both the migration process and the molarity of the precursor.

Figure 4.6 demonstrated SIMS measurements of oxide films containing K^+, Rb^+, and Cs^+. This is the first time that conclusive evidence of the presence of Rb^+ and Cs^+ ions has been presented, indicating that these ions are mobile inside of SiO_2 films when provided with enough driving force. The significantly stronger signal intensity arising from each ion relative to the contaminant concentration indicates that the vast majority of Q_{eff} recorded experimentally can confidently be attributed to the purposefully introduced species. The negligible intensity produced by the contaminants shows that spin coating and thermal evaporation are clean processes that introduce few unwanted impurities. The distribution of charge throughout the depth of the oxide confirms that the ions accumulate close to the Si-SiO_2 interface. These findings confirm that the measured Q_{eff} is predominantly influenced by the peak charge concentration at the interface, and that the kinetic parameters used in Chapter 3 to model ion migration towards the interface are accurate. The ability to embed alkali ions larger than K^+ within a dielectric may open up new avenues of exploration for electronic devices that rely upon permanently charged dielectrics.

The SIMS measurement technique was also used to confirm the presence of Cs^+ ions within the SiO_2 film after *in situ* delivery of CsOH vapour during oxidation. The results in Figure 4.9 showed that of the three alkali ions profiled, K^+ and Na^+ ions had the strongest signal intensities. A relatively low intensity was recorded for Cs^+ ions, which shows that although only a small concentration of Cs^+ ions was incorporated, the *in situ* delivery was successful. In work by Sugiyama, a solution of 40 wt. % KOH solution was reported to embed a concentration $\sim 10^{17}$ K^+ ions cm^{-3} within the bulk of the oxide, and a substantial concentration of 10^{19} cm^{-3} at the Si-SiO_2 interface [111]. In this thesis, only 5 wt. %

CsOH solution was used due to the poor resistance of the plastic tubing to strong alkaline vapour. It is therefore expected that by increasing the weight percent of the CsOH solution inside the bubbler, a greater concentration of ions can be introduced during oxidation. This should certainly be explored in future work.

4.7 Summary

This chapter discussed the use of thermal evaporation and spin coating to deposit aqueous alkali chloride precursors, serving as a source of cations. Molarities of 1 mM were prepared to deliver K^+ and Rb^+ ions. A greater concentration of 2.5 mM CsCl solution was required to increase the amount of ions injected into the SiO_2 film. Evidence of the incorporation and migration of all three ions within SiO_2 was demonstrated through SIMS measurements. It was observed that a negligible concentration of contaminants exist within the dielectric, which indicates that the methodology is clean, and that the recorded Q_{eff} can safely be attributed to each ionic species. This is the first time a direct demonstration has been provided of their existence within the dielectric in response to thermal and bias stress, thus confirming the mobility of all three ions within SiO_2.

This chapter also provided direct evidence through SIMS measurements that Cs^+ ions can be introduced to the SiO_2 film during oxidation. To the author's knowledge, this is the first time that the *in situ* delivery method has been used to incorporate Cs^+ ions. The process used in this chapter can be improved by carrying it out under clean room conditions to minimise the presence of contaminants during the RCA clean and within the oxidation set-up. Additionally, increasing the weight percent of the CsOH solution is expected to deliver a more substantial concentration of ionic charge. *In situ* delivery allows for oxidation and ion-charging to be performed simultaneously, thus enabling high throughput production that is highly desirable in solar cell manufacturing. The dielectric film can be polarised at a later stage to manipulate the distribution of ions located within.

This process is therefore well-suited to rapid and scalable industry processes.

5 | Alkali Ion Passivation on Thermal Silicon Dioxide

This chapter explores the role of ion-charged dielectrics in silicon surface passivation. The incorporation of extrinsic positive charge within the dielectric is expected to generate an accumulation layer within n-type silicon that effectively minimises the recombination of electrons and holes. The field effect passivation (FEP) provided by K^+ ion-charged oxides has been previously reported in references [67, 68, 93, 115]. However, little data exist on stability and methods of charge control to optimise FEP. It is plausible that larger alkali ions may permit similarly high charge density dielectrics with improved durability due to their increased size within the amorphous oxide matrix. It was demonstrated in Chapter 3 that the effective interface charge concentration of K^+, Rb^+, and Cs^+ ions within SiO_2 can be finely tuned by varying the strength of the surface electric field prior to annealing, and the annealing temperature. The ability to introduce ions to the dielectric with precision is important since the over-saturation at the Si-SiO_2 interface generates defects, as will be shown in this chapter.

This chapter begins by presenting an analysis of the surface passivation performance of K^+, Rb^+, and Cs^+ charged oxide films on Set A (n-type 1 Ωcm FZ) wafers. An optimal Q_{eff} of ∼1.5 x 10^{12} q cm^{-2} was found to produce the highest τ_{eff} for all three ions. It was found that the maximum τ_{eff} is influenced by the concentration of ionic charge within the dielectric, and is limited due to the creation of interface states. Additionally, this chapter evaluates the longevity of the passivation performance provided by ion-charged oxide films exposed to elevated temperatures and under UV radiation. The physical stability and endurance of the ions at the Si-SiO_2 interface is also studied in response to heat, UV radiation and reverse bias stress.

5.1 Passivation Performance of Ion-Charged Oxides

In this chapter, the passivation performance of ion-charged oxides on Set A (n-type 1 Ωcm FZ) wafers is studied. These wafers were thermally oxidised to 100 nm thickness on both sides at Fraunhofer ISE. Ions were introduced to the oxide and migrated towards the Si-SiO_2 interface using the methodology outlined in Section 2.6. The different migration parameters chosen for each ion were determined from the results in Chapter 3, summarised in Table 3.3.

Figure 5.1a shows the dependence of τ_{eff} on the K^+ Q_{eff} for specimens that used the evaporation technique to deposit KCl solution. As τ_{eff} represents the recombination within the silicon wafer including its surfaces, both sides of the specimen need to be equally passivated. KCl solution was evaporated onto both oxide faces of 5 cm x 5 cm specimens followed by corona charging. The samples were subsequently annealed at 300 °C for 180 s. The interface charge concentration was controlled by varying the concentration of corona charge (Q_{surf}) deposited on the oxide surfaces prior to the anneal. The green bars represent τ_{eff} of the as-received oxidised wafers prior to any treatment, approximately 0.1 ms. The blue bars represent τ_{eff} after the ions have been migrated to the Si-SiO_2 interface. The red bars represent the τ_{eff} after a further 30 s of corona charge, equivalent to Q_{surf} ~2 x 10^{12} q cm^{-2}, was deposited to evaluate if the passivation has been maximised by ions alone. These results are displayed in comparison to an oxidised wafer that had 60 s of corona charge deposited on both faces - equivalent to Q_{surf} ~4 x 10^{12} q cm^{-2}. The measured τ_{eff} of the corona charged control was 3.75 ms (S_{eff} < 1.39 cm s^{-1}). The passivation performance of the corona-charged control was consistently superior to that of the K^+ ion-charged specimens. However, the field provided by corona charging is not permanent. K^+ ion-charged specimens demonstrated a maximum τ_{eff} of 2.40 ms at Q_{eff} = 1.5 x 10^{12} q cm^{-2}. This is achieved by a corona discharge time of 30 s, equivalent to Q_{surf} ~2 x 10^{12} q cm^{-2}, prior to the anneal. Increasing Q_{eff} beyond 1.5 x 10^{12} q cm^{-2} results in a gradual decrease in τ_{eff} to

a low of 1.33 ms at 1 x 10^{13} q cm^{-2}. For specimens with Q_{eff} > 5 x 10^{12}, additional corona charging does not improve the lifetime further. This indicates that FEP has been maximised.

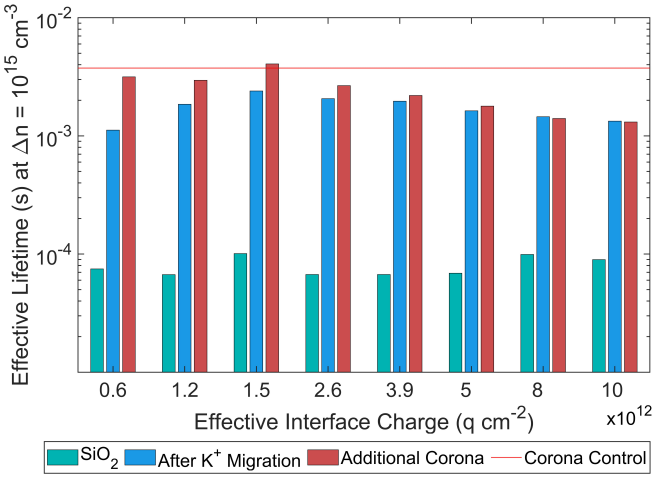

(a)

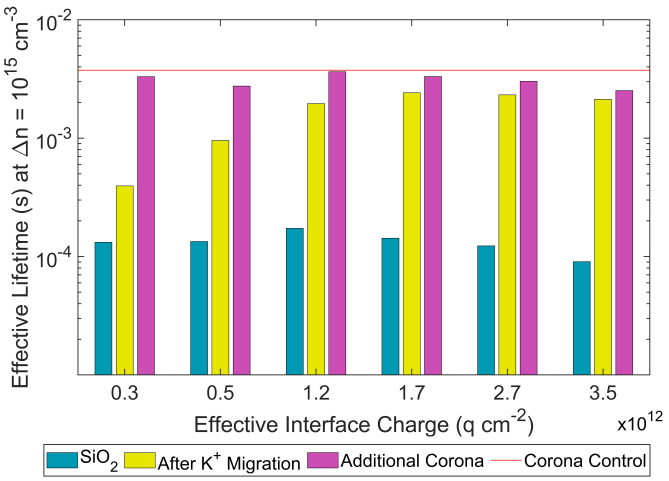

(b)

Figure 5.1: The dependence of effective lifetime on K^+ interface charge concentration for (a) thermally evaporated samples and (b) spin coated samples. The corona control represents the effective lifetime of an as-received oxidised wafer after 60 s corona charge deposition. Corona charge was deposited at a tip voltage of +30 kV.

Figure 5.1b shows the same experiment performed on specimens that had KCl solution spin coated on the surface. Here an almost identical maximum τ_{eff} of 2.42 ms is achieved at a very similar interface charge of 1.7 x 10^{12} q cm^{-2}, thus showing that the two deposition methods result in highly comparable data. Similarly to the evaporated samples, the optimal Q_{eff} was achieved by depositing 30 s of corona prior to the anneal. The maximum τ_{eff} observed in both the evaporated and spin coated samples are equivalent to S_{eff} < 2.80 cm s^{-1}.

Similar experiments were carried out to demonstrate how τ_{eff} is influenced by Rb^+ and Cs^+ ion Q_{eff}. The resulting dependency is shown in Figure 5.2. The results for Rb^+ are given in Figure 5.2a. Both sides of the oxidised wafers were spin coated with RbCl solution. Following corona charging on both surfaces, the samples were annealed for a duration of 5 minutes at 450 °C. As before, the interface charge was controlled by varying the concentration of corona charge deposited prior to the anneal. Following Rb^+ migration, a maximum τ_{eff} of 2.81 ms was recorded at Q_{eff} = 1.4 x 10^{12} q cm^{-2}. This is equivalent to S_{eff} < 2.23 cm s^{-1}. Such a high level of surface passivation was achieved using a corona discharge time of 50 s, equivalent to a $\sim$3.5 x 10^{12} q cm^{-2}, prior to the anneal. Increasing Q_{eff} beyond 1.4 x 10^{12} q cm^{-2} results in a gradual decrease in τ_{eff} to a low of 0.63 ms at 5.2 x 10^{12} q cm^{-2}. Figure 5.2b shows the results for Cs^+ charged specimens. Samples were spin coated with 2.5 mM CsCl solution prior to corona charging on both sides. The specimens were annealed for 60 s at 600 °C. Here a maximum τ_{eff} of 1.86 ms (S_{eff} < 4.02 cm s^{-1}) was recorded at Q_{eff} of 1.4 x 10^{12} q cm^{-2}. This was achieved using a corona discharge time of 30 s. Migrating more Cs^+ ions to the interface results in a decrease in τ_{eff} to a low of 0.55 ms at Q_{eff} = 3.75 x 10^{12} q cm^{-2}.

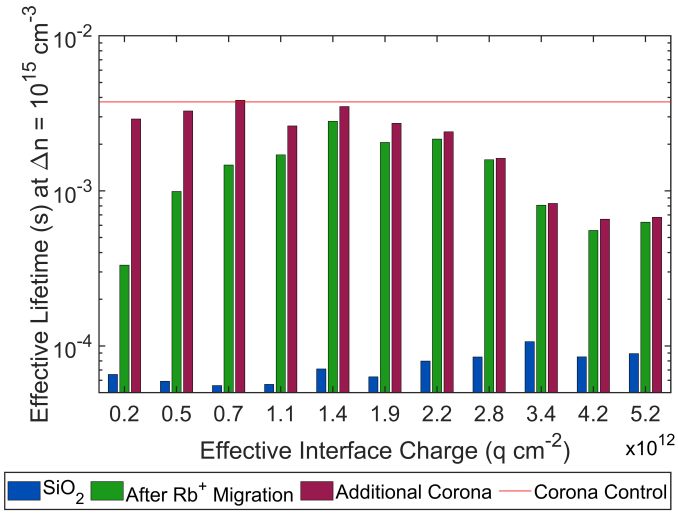

(a)

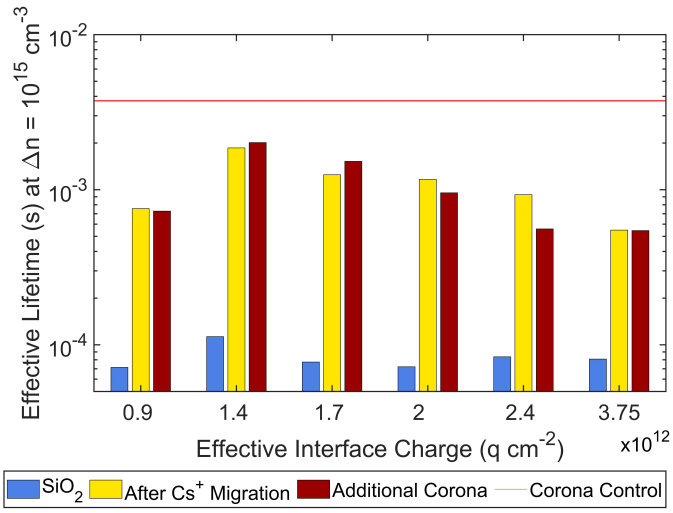

(b)

Figure 5.2: The dependence of effective lifetime on (a) Rb^+ and (b) Cs^+ interface charge concentration. The corona control represents the effective lifetime of an as-received oxidised wafer after 60 s corona charge deposition. Corona charge was deposited at a tip voltage of +30 kV.

The maximum τ_{eff} of ion-charged specimens after annealing (prior to additional corona charging) is plotted in Figure 5.3a as a function of excess carrier concentration (Δn). This is shown in comparison to the carrier-dependent lifetimes of a standard untreated oxidised control, an oxidised control after corona charging, and the intrinsic lifetime of the specimen. For the corona-charged and ion-charged specimens, at low injection conditions, τ_{eff} is maximised as surface SRH recombination is minimised through field effect. At high injection conditions, τ_{eff} reduces as Auger recombination dominates. Figure 5.3b shows the equivalent S_{eff} of the ion-charged specimens and corona-charged control. Across all injection conditions, the passivation performance of the corona-charged control outperforms that of the ion-charged specimens. It is possible that the maximum τ_{eff} (minimum S_{eff}) of ion-charged specimens is limited due to the generation of defects by excess ions at the Si-SiO_2 interface. The lower maximum τ_{eff}, and higher S_{eff}, of Cs^+ charged specimens may also be explained by the generation of defects in response to lattice strain. This is discussed in Section 5.2.

Figure 5.4 demonstrates the reproducibility of the maximum achievable τ_{eff} for films charged with K^+, Rb^+, and Cs^+ ions. Figure 5.4a compares the reproducibility of the maximum τ_{eff} for samples that had KCl solution evaporated onto the oxide surface and samples that had KCl solution spin coated prior to ion migration. Five 5 cm x 5 cm oxidised wafers had KCl thermally evaporated on both surfaces, and another five wafers had KCl spin coated on both sides. Subsequently, all specimens followed the same procedure of corona charging for 30 seconds on both faces, and annealing at 300 °C for 3 minutes to provide the optimal Q_{eff} $\sim$1.5 x 10^{12} q cm^{-2} determined from Figure 5.1. Of the five samples that had KCl evaporated, the mean maximum τ_{eff} was 2.30 ms with a standard deviation of 0.09 ms. The lowest recorded value was 2.21 ms and the highest was 2.40 ms. For spin coated specimens, the mean maximum τ_{eff} was 2.18 ms with a standard deviation of 0.22 ms. The lowest value was 1.86 ms and the highest was 2.42 ms. Despite the very similar means, the evaporated samples had better reproducibility in comparison to those that were spin coated. Figure 4.4 in Chapter 4 demonstrated that

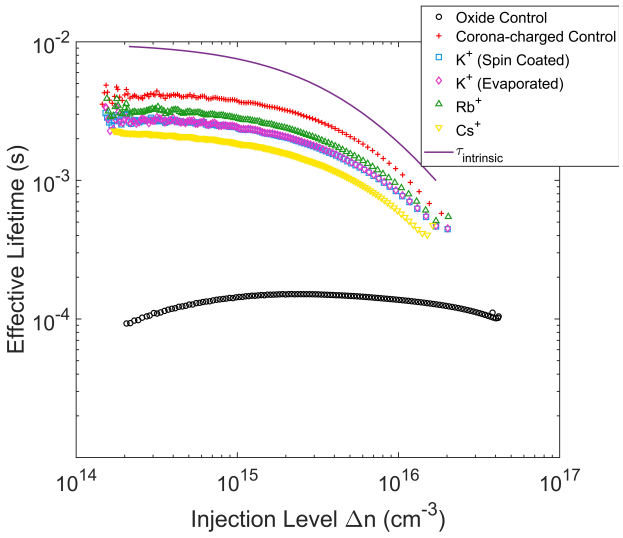

(a)

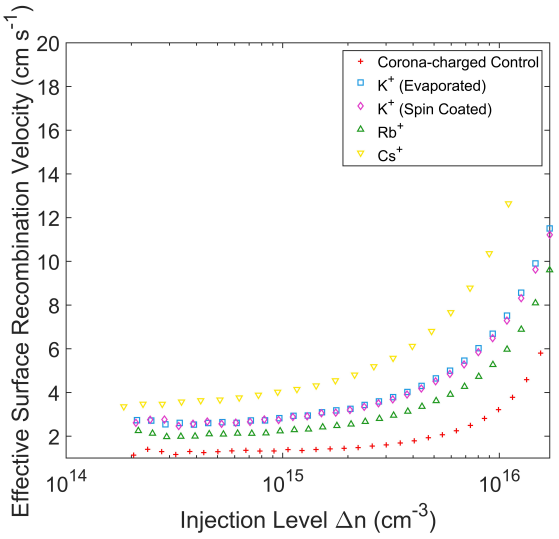

(b)

Figure 5.3: Plotted as a function of excess carrier concentration (a) maximum effective lifetimes of ion-charged specimens in comparison to an oxidised untreated control and an oxidised corona charged control (b) effective surface recombination velocity of the highest lifetime ion-charged specimens and corona-charged control.

evaporated samples had better charge uniformity at the Si-SiO_2 interface, possibly due to the minimisation of contaminants within the clean room and vacuum environment. Given the smaller fluctuations in dielectric charge within evaporated specimen, it follows that the passivation performance is more reliable. Nonetheless, both techniques

demonstrate excellent reproducibility. The standard deviation in maximum τ_{eff} of spin coated specimens falls within 10 % of the mean, and as such spin coating is a suitable and compatible technique.

Figure 5.4b demonstrates the reproducibility of the maximum τ_{eff} for Rb^+ and Cs^+ charged oxides across 5 samples. Rb^+ samples had 50 seconds of corona charge deposited on both oxide faces followed by annealing at 450 °C for 5 minutes. Cs^+ samples were corona charged for 30 s on both sides followed by a 60 s anneal at 600 °C. The maximum τ_{eff} for Rb^+ charged specimens ranged between 1.88 ms and 2.81, with a mean of 2.19 ms and a standard deviation of 0.37 ms. Although Rb^+ charged specimens demonstrated the highest overall maximum τ_{eff}, the mean value is very similar to that of K^+ charged specimens. The mean maximum τ_{eff} for Cs^+ charged specimens was 1.51 ms with a standard deviation of 0.21 ms. The lowest value was 1.34 ms and the highest was 1.86 ms.

Out of the specimens that were spin coated, it was observed that the Rb^+ samples had lowest reproducibility. Figure 4.5 in Chapter 4 showed that the fluctuation in Q_{eff} within a sample is greater for Rb^+ charged specimens than Cs^+, which explains the greater variation in maximum τ_{eff}. It is possible that the migration parameters for Rb^+ ions have not yet been fully optimised, and that if Rb^+ specimens were annealed at temperatures above 450 °C, the greater injection probability at the air-oxide interface would lead to greater uniformity in both Q_{eff} and τ_{eff}. A study of Rb^+ ion migration at temperatures >450 °C was not performed in this thesis, and should be studied in future work.

5.2 Electrical Properties of the Si-SiO_2 Interface in the Presence of Alkali Ions

In the previous section, it was demonstrated that the best surface passivation produced by ion-charged oxides occurs at Q_{eff} ~1.5 x 10^{12} q cm^{-2}. For all three ions, increasing

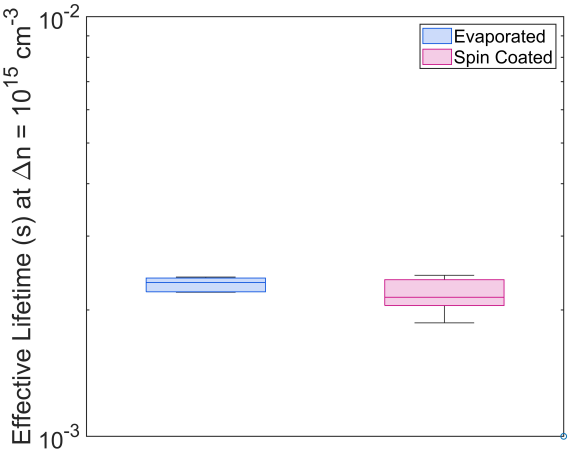

(a)

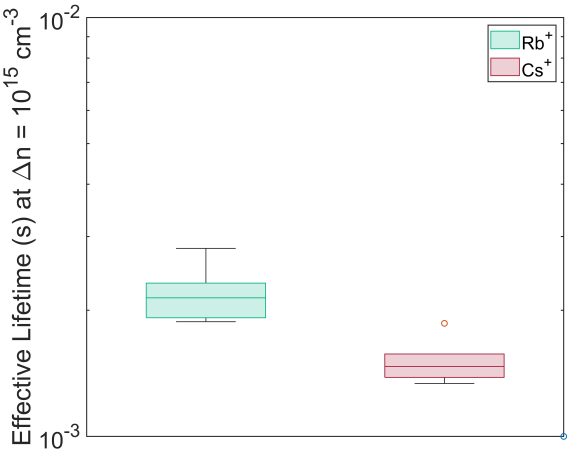

(b)

Figure 5.4: Reproducibility of maximum τ_{eff} across 5 samples for (a) evaporated and spin coated K^+ specimens and (b) spin coated Rb^+ and Cs^+ specimens.

the ionic charge beyond this optimal concentration results in a lower τ_{eff}. This is most likely due to the creation of interface defects arising from distortion and strain of the oxide matrix by excess charge [17, 191, 223]. Additionally, it was demonstrated that at the optimal Q_{eff}, the maximum τ_{eff} of Cs^+ charged specimens was lower than that of K^+ and Rb^+ charged specimens. Given that Cs^+ has the largest radius of the three ions, it is plausible that that the matrix distortion is amplified. To confirm these hypotheses, an

investigation into the interface properties of ion-charged oxides is presented here.

Figure 5.5 plots measured CV curves after migrating different concentrations of ionic charge. The experimental CV data was fit using the Terman method, as described in Section 2.8.3. D_{it} is used as a parameter to find the best fit between experimental and theoretical relations to determine the influence of K^+, Rb^+, and Cs^+ interface charge on defect density. Multiple specimens were created by migrating different amounts of ionic charge to the Si-SiO_2 interface. Additionally, a control specimen (blue curves) was produced that had no ions introduced but was corona charged for 60 s. Aluminium contacts were deposited on the front and rear of the samples and high frequency (1 MHz) CV measurements were taken. The results for K^+ ion-charged specimens are shown in Figure 5.5a. The annealed control was found to have a D_{it} of 2 x 10^{11} cm^{-2} eV^{-1}. Introducing 2 x 10^{12} q cm^{-2} of K^+ ions to the interface did not demonstrate an increase in D_{it}. At Q_{eff} = 5.9 x 10^{12} q cm^{-2} the D_{it} increases slightly to 3 x 10^{11} cm^{-2} eV^{-1}. The addition of more ionic charge further degrades the interface as the D_{it} increases to 8 x 10^{11} cm^{-2} eV^{-1} in the presence of 10^{13} q cm^{-2}. These results show that the passivation of K^+ ion-charged oxides is limited by defect generation at Q_{eff} > 2 x 10^{12} q cm^{-2}.

A similar trend exists in Figure 5.5b for Rb^+ ion-charged specimens. The introduction of 1.6 x 10^{12} q cm^{-2} increases the D_{it} from 2 x 10^{11} cm^{-2} eV^{-1} to 3 x 10^{11} cm^{-2} eV^{-1}. Increasing Q_{eff} further to 4.1 x 10^{12} q cm^{-2} results in a greater D_{it} of 6 x 10^{11} cm^{-2} eV^{-1}. The D_{it} was found to increase to 10^{12} cm^{-2} eV^{-1} at the greatest Q_{eff} of 6.1 x 10^{12} q cm^{-2}. The results for Cs^+ ion specimens are shown in Figure 5.5c. Similar to K^+ and Rb^+ ions, more defects are created as more charge is migrated to the interface. The passivation is limited by defect generation from Q_{eff} > 1 x 10^{12} q cm^{-2}. At the maximum Q_{eff} of 4.1 x 10^{12} q cm^{-2}, it was found that the D_{it} increased to 2 x 10^{12} q cm^{-2}. The generation of interface defects by Cs^+ ions is significantly greater than for K^+ and Rb^+ charged specimens at similar values of Q_{eff}. These results confirm that the ionic radius plays an important role in the interface properties. The correlation between Q_{eff} and D_{it} observed in Figures 5.5a, 5.5b, and 5.5c confirms that excess ionic charge leads to the

creation of interface states, which explains the decrease in τ_{eff} beyond the optimal Q_{eff}. The relationship between Q_{eff} and D_{it} for each ion is summarised in Figure 5.6.

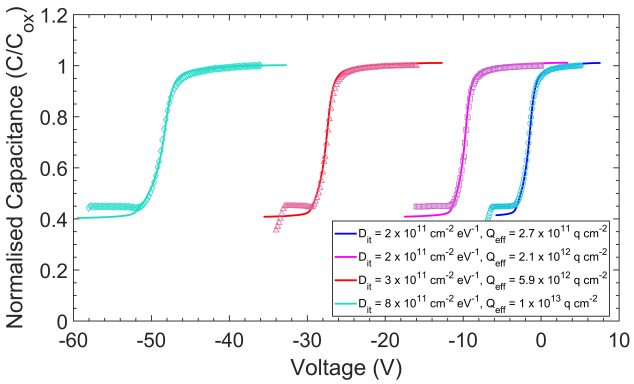

(a)

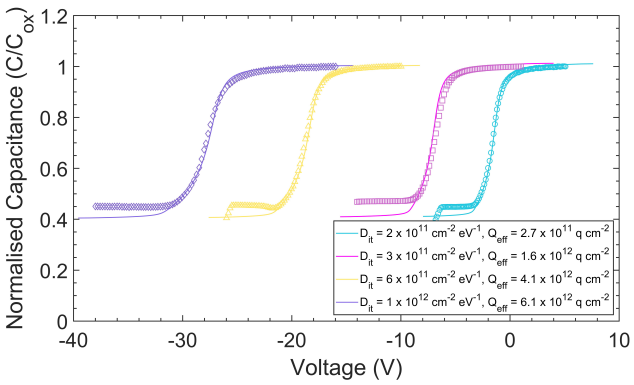

(b)

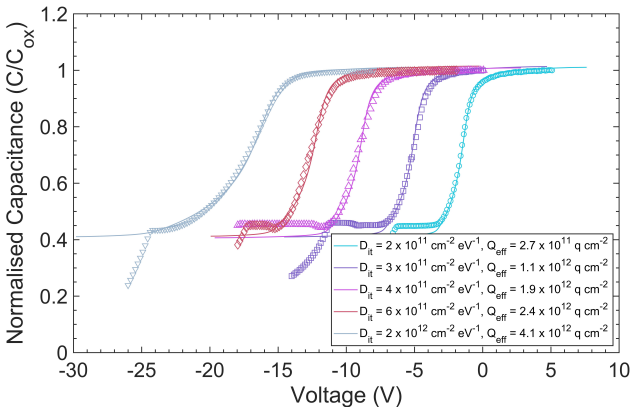

(c)

Figure 5.5: CV measurements demonstrating the influence of increasing amounts of (a) K^+ (b) Rb^+ and (c) Cs^+ ion interface charge on D_{it}. Solid lines are model fittings. Blue curves on the far right represent the control.

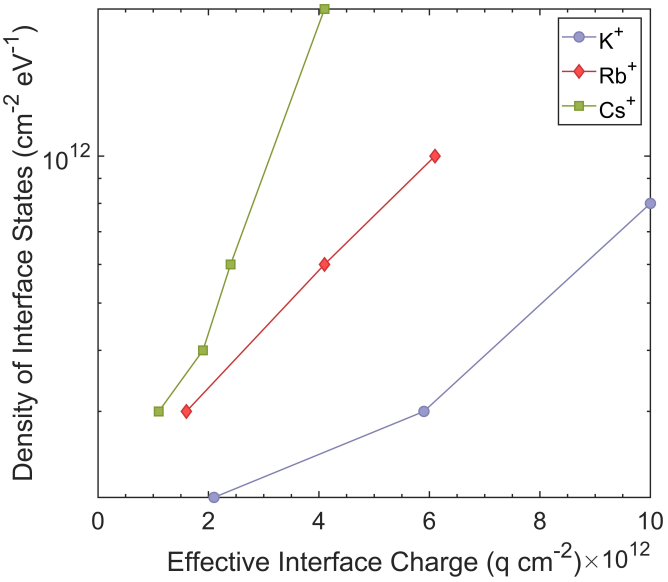

Figure 5.6: Summary of the ion-dependent relationship between Q_{eff} and D_{it}.

5.2.1 Discussion

Section 5.1 and 5.2 explored the use of K^+, Rb^+, and Cs^+ ion-charged dielectrics in silicon surface passivation. From Figure 5.1, a maximum τ_{eff} of 2.40 ms and 2.42 ms was determined for K^+ ion-charged dielectrics, where thermal evaporation and spin coating deposition was used respectively. Both these values are equivalent to S_{eff} < 2.80 cm s^{-1}. This is superior to the previously reported work on K^+ ion-charged dielectrics that demonstrated S_{eff} < 3.3 cm s^{-1} on the same type silicon [67]. In this thesis, the maximum lifetime was achieved at Q_{eff} of 1.5 - 1.7 x 10^{12} q cm^{-2}. This optimal Q_{eff} is consistent with findings by Collett et al. that the incorporation of 1-2 x 10^{12} q cm^{-2} of K^+ ions provides superior passivation during *alnealing* [68]. Nevertheless, the best recorded τ_{eff} was 1.32 ms lower than the maximum τ_{eff} achieved by the corona-charged control. Compensating the electric field with a greater concentration of K^+ ions, instead of additional corona charge, resulted in a degradation of the passivation quality as evidenced by the reduction in τ_{eff}. As shown in Figure 5.2, a similar trend was observed in Rb^+ and Cs^+ charged specimens. A maximum τ_{eff} of 2.81 ms and 1.86 ms was

recorded for Rb^+ and Cs^+ specimens, respectively. Similarly to K^+ charged specimens, the optimal Q_{eff} occurred at 1.4 x 10^{12} q cm^{-2}. The relatively low concentration of ions required for maximum passivation means that a low concentration of corona charge is required to produce the necessary surface field. This is beneficial considering reports that excessive corona charges absorbed into the dielectric can generate defects at the interface with silicon [66, 224, 225].

The mean τ_{eff} of Cs^+ charged specimens was 1.51 ms. This is 0.68 - 0.79 ms lower than the mean maximum τ_{eff} of both K^+ and Rb^+ specimens. It was demonstrated in Figure 5.6 that for a given interface charge concentration, the defect density increases as the ionic radius increases. Additionally, it was shown that for all three ions, the incorporation of ionic charge beyond the optimal value of Q_{eff} resulted in greater defect creation. The generation of defect states is attributed to the distortion and strain of the SiO_2 matrix in response to both the excess ionic interface charge and ionic size [17, 191, 223]. As shown by the corona-charged control, a maximum τ_{eff} of 3.75 ms can be produced by a non-invasive field effect. Therefore, a possible method to improve the passivation of ion-charged oxides is to control the proximity of the ions to the interface so as to avoid damage to the silicon surface. Recently reported simulations of PERC structures demonstrated that the efficiency is maximised where the dielectric charge is greater than 2 x 10^{12} q cm^{-2} [214]. This study did not account for defect generation at the Si-SiO_2 interface, and provides an indication of the superior performance that can be achieved if defect generation is mitigated. One method of defect mitigation is the deposition of a SiN_x capping layer. It has previously been postulated that the presence of hydrogen in SiN_x films can passivate interface defects, including those generated by ions [18, 75, 226]. This is expected to result in a significant increase in the maximum attainable τ_{eff} of ion-charged specimens. Nitride deposition was not available in this work, however, this should certainly be explored in the future.

5.3 Passivation Stability of Ion-Charged Oxides

Electronic devices often function at elevated temperatures and under operational voltages [112, 176, 227]. Ion-charged dielectrics are therefore susceptible to heat and bias stress conditions [112, 176, 227]. Additionally, PV modules are exposed to UV radiation due to their placement outdoors. Accelerated ageing experiments were carried out to determine how K^+, Rb^+, and Cs^+ ions at the Si-SiO_2 interface respond to such conditions, and how the passivation performance provided by ion-charged oxides is affected.

Firstly, the stability of the passivation performance was studied. Figure 5.7 demonstrates how τ_{eff} of ion-charged specimens is affected by elevated temperatures and UV radiation. Here, in separate specimens, the optimal concentration of K^+, Rb^+, and Cs^+ ions were migrated to the interface to produce approximately the highest τ_{eff}. Three specimens, each containing either K^+, Rb^+, or Cs^+ ions were placed in a box furnace at 120 °C for 500 hours. Another three specimens were placed in a UV radiation chamber at room temperature for the same amount of time. The UV illumination intensity was 5 mW cm^{-2}. It should be noted that for all specimens, ions were migrated to the Si-SiO_2 interface at both the front and rear of the substrate, however, within the chamber only one face could be exposed to the UV radiation. The exposed face was kept constant throughout. At intervals, the specimens were removed from the box furnace and the UV radiation chamber to measure τ_{eff} on the Sinton Lifetime Tester. Figure 5.7a demonstrates the changes in τ_{eff} as a result of elevated temperature. Within the first 24 hours at 120 °C, τ_{eff} decreased by 0.14 ms, 0.42 ms, and 0.2 ms for K^+, Rb^+, and Cs^+ ion specimens, respectively. A slower rate of decline was recorded in subsequent measurements. By 500 hours, the initial τ_{eff} of each specimen had dropped by 0.72 ms, 0.91 ms, and 0.50 ms. Figure 5.7b shows the results for the three specimens exposed to UV radiation. Within the first 24 hours, there was a decrease in τ_{eff} by 1.15 ms, 0.66 ms, and 0.42 ms for K^+, Rb^+, and Cs^+ ion specimens, respectively. The passivation continued to deteriorate for all three ions. For the Cs^+ charged specimen, the τ_{eff} remained at $\sim$0.8 ms between 120 hours and

250 hours. This temporary plateau is most likely due to shading of the specimen within the chamber. By 500 hours, the initial τ_{eff} had dropped by 1.81 ms, 1.28 ms, and 0.94 ms.

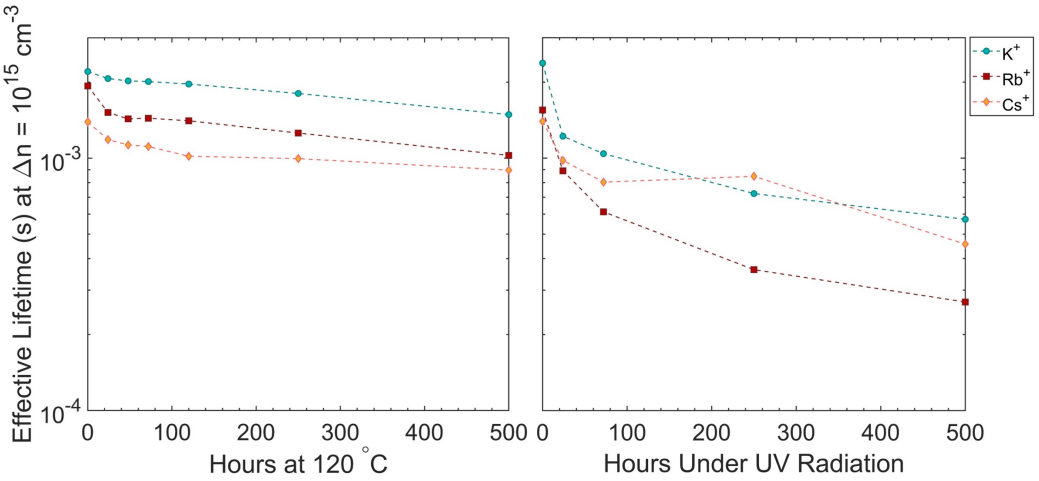

(a) (b)

Figure 5.7: Influence of (a) 120 °C heat and (b) UV radiation on τ_{eff} of K^+, Rb^+, and Cs^+ charged specimens over the course of 500 hours. Dashed lines are a guide to the eye.

It was hypothesised that the decline in surface passivation may be due to the migration of ionic charge away from the interface, or due to the creation of interface defects in response to heat and UV radiation. To determine the cause, fresh specimens were prepared. Additionally, two control specimens were prepared by spin coating pure DI water and IPA solvents on the SiO_2 surface prior to corona charging and annealing at 300 °C. MOS structures were created out of the specimens so that CV measurements could be performed to evaluate changes in Q_{eff} and D_{it}. Three of the MOS structures embedded with either K^+, Rb^+, or Cs^+ ions along with one control specimen were placed in the box furnace at 120 °C for 500 hours. Another three ion-charged MOS structures and the second control were placed in the UV radiation chamber.

Figure 5.8a shows the charge stability of K^+, Rb^+, and Cs^+ ions at the Si-SiO_2 interface over the course of 500 hours at 120 °C. The prepared MOS structures allowed for intermittent CV measurements to determine the stability of the interface charge

concentration over time. An average of 5 randomly selected locations demonstrated a charge retention of >98 % after 120 hours for all three ions. The charge retention remained >98 % after 500 hours for K^+ and Rb^+ ions, whist Cs^+ ions demonstrated 96 % charge retention. The control sample lost an average of 55 % after 120 hours. After 500 hours, there was an increase in the average Q_{eff} of the control sample as well as an increase in the fluctuation in charge. This can be attributed to the high mobility of contaminants such as Na^+ that respond to internal concentration gradients at low temperatures giving rise to variable charge distributions within the oxide. Given the negligible Na^+ $Q_{eff} \leq 10^{11}$ q cm^{-2}, these fluctuations do not have a significant impact on the measured Q_{eff} of the ion-charged specimens.

Figure 5.8b demonstrates the charge stability of all three ions under UV radiation over 500 hours. As UV radiation cannot pass through the aluminium dots on the surface, each time the samples were removed for testing, new dots were thermally evaporated next to the previous ones. After 120 hours, an average of 94 % and 87 % charge retention was found for K^+ and Rb^+ ions respectively. Of the three ions, Cs^+ ions demonstrated the best charge retention of 100 %. After 500 hours, the charge retention of K^+ and Rb^+ samples lowered to 90 % and 84 %, respectively. Cs^+ showed the highest charge retention of 95 % after 500 hours. Given the requirement for creating a new MOS structure before each CV measurement, it is possible that the decrease in measured charge after each time interval is due to small variation of ionic charge across the SiO_2 film.

As shown in Figure 5.9, the CV curves of MOS structures before and after heat ageing were subsequently modelled according to the Terman method to evaluate changes in D_{it}. Figure 5.9a plots the results for the K^+ charged specimen and the control. From the fitted curve of the K^+ specimens, a small increase in D_{it} from 2 x 10^{11} cm^{-2} eV^{-1} to 3 x 10^{11} cm^{-2} eV^{-1} was determined. The control specimen showed the same absolute increase of 1 x 10^{11} q cm^{-2} after 500 hours, thus indicating that the increase in D_{it} may not be related to the ionic charge but is thermally generated. Figure 5.9b shows the changes in D_{it} for Rb^+ and Cs^+ charged specimens. After 500 hours, the D_{it} of the Rb^+ charged specimen

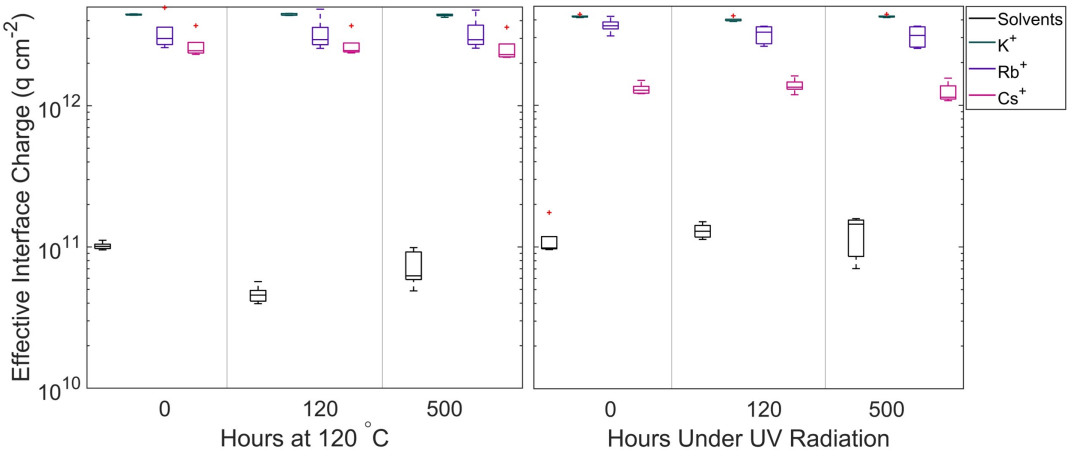

(a) (b)

Figure 5.8: Stability of K^+, Rb^+ and Cs^+ ions at the Si-SiO_2 interface over the course of 500 hours at (a) 120 °C and (b) under UV radiation.

increased from 8 x 10^{11} cm^{-2} eV^{-1} to 9 x 10^{11} cm^{-2} eV^{-1}. The Cs^+ specimen exhibited the same absolute increase in D_{it} from 3 x 10^{11} cm^{-2} eV^{-1} to 4 x 10^{11} cm^{-2} eV^{-1}. The results in Figure 5.9 confirm that at elevated temperatures, a small amount of defects are generated in response to heat, which affects all specimens equally.

A similar study was carried out on the MOS structures before and after 500 hours of exposure to to UV radiation. The results are shown in Figure 5.10. As before, due to the lack of UV transmittance through aluminium, CV measurements were performed on fresh MOS samples. Figure 5.10a shows the results for the K^+ charged specimen and the control. For the K^+ specimen, the D_{it} was found to increase from 2 x 10^{11} cm^{-2} eV^{-1} to 5 x 10^{11} cm^{-2} eV^{-1}. For the control, there was a smaller increase from 1 x 10^{11} cm^{-2} eV^{-1} to 2 x 10^{11} cm^{-2} eV^{-1}. Figure 5.10b shows the results for the Rb^+ and Cs^+ charged specimens. Here an increase in D_{it} from 7 x 10^{11} cm^{-2} eV^{-1} to 1.5 x 10^{12} cm^{-2} eV^{-1} was determined for the Rb^+ specimen. For the Cs^+ specimen, the D_{it} increased from 5 x 10^{11} q cm^{-2} to 6 x 10^{11} cm^{-2} eV^{-1}.

Further tests were carried out to determine how K^+, Rb^+, and Cs^+ ions at the Si-SiO_2 interface respond to reverse biases at elevated temperatures. Ions were migrated to the

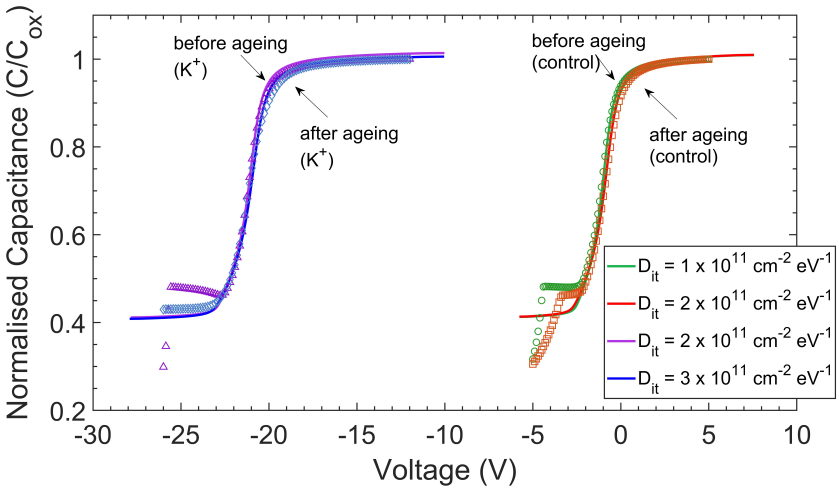

(a)

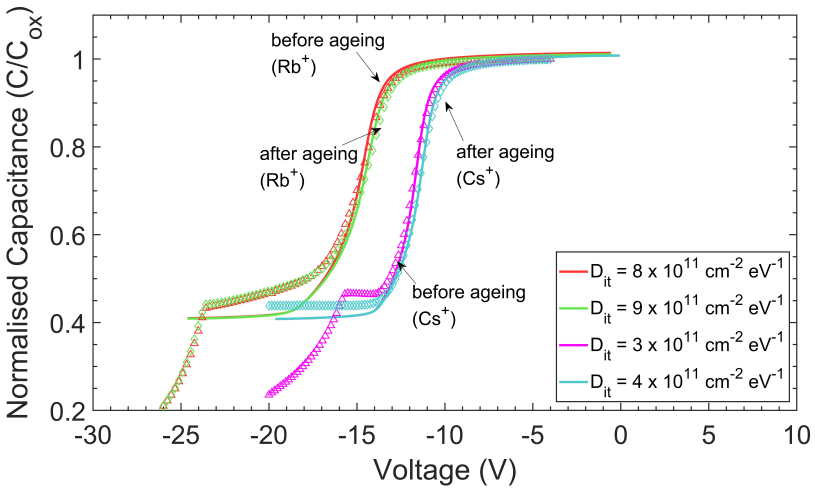

(b)

Figure 5.9: CV measurements demonstrating the change in D_{it} after 500 hours at 120 °C for (a) control and K^+ charged specimens (b) Rb^+ and Cs^+ charged specimens.

$Si\text{-}SiO_2$ interface following corona charging and annealing. MOS structures were subsequently produced and the samples heated to 200 °C. A reverse bias of -1 V, -5 V and -10 V was applied separately to three samples for a total of 60 minutes. As shown in Figure 5.11, CV measurements were taken every 10 minutes over the course of 1 hour to record changes in Q_{eff}. Figure 5.11a compares the charge retention of all three ions held at a reverse bias of -1 V, equivalent to a field of -10^5 V cm^{-1}. Rb^+ and Cs^+ ions show

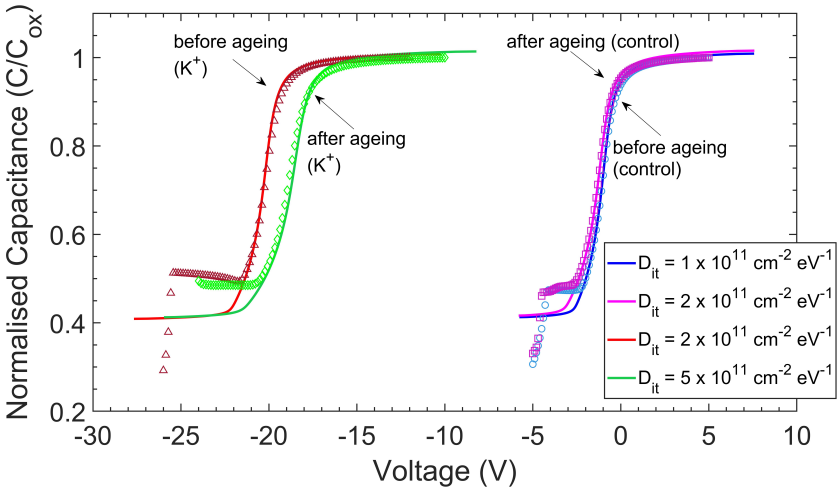

(a)

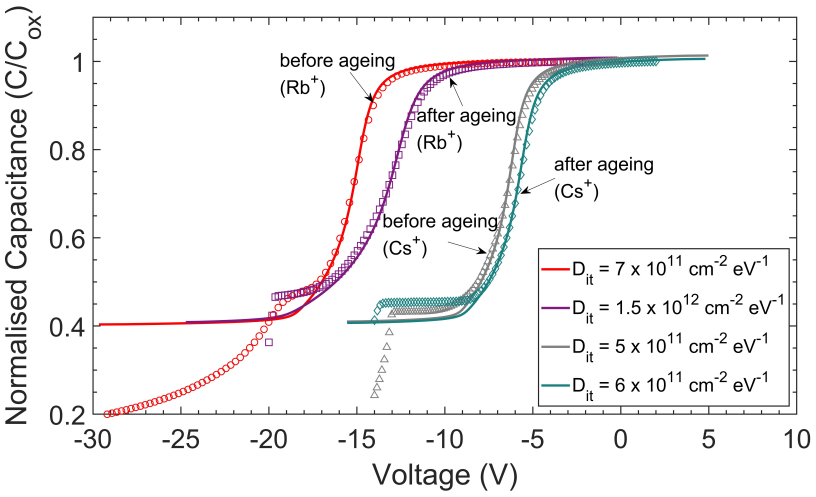

(b)

Figure 5.10: CV measurements demonstrating the change in D_{it} after 500 hours under UV radiation (a) control and K^+ charged specimens (b) Rb^+ and Cs^+ charged specimens.

negligible change over the course of 60 minutes. On the other hand, K^+ ions show a 13 % loss in Q_{eff} after the first 10 minutes and 42 % loss after 60 minutes. In Figure 5.11b, a stronger reverse bias of -5 V, equivalent to a field of -5 x 10^5 V cm^{-1}, was applied. Approximately 75 % of K^+ charge is lost after the first 10 minutes, followed by $\sim$90 % depletion after 60 minutes. The Rb^+ ion concentration falls by 12 % in the first 10 minutes and by 29 % after 60 minutes. Cs^+ ions demonstrate excellent stability, losing

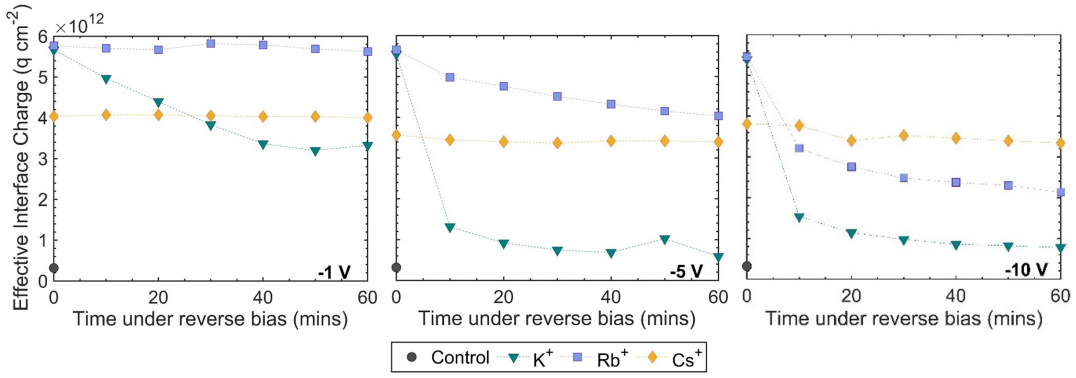

(a) (b) (c)

Figure 5.11: Stability of K^+, Rb^+, and Cs^+ ions at the Si-SiO_2 interface under a reverse bias of (a) -1 V (b) -5 V and (c) -10 V at 200 °C over 60 minutes. Dashed lines are a guide to the eye.

just ∼5 % of its initial Q_{eff} after a total of 60 minutes. The results after applying a bias of -10 V, equivalent to a field of -10^6 V cm^{-1}, are shown in Figure 5.11c. The decline of K^+ charge at the interface follows a similar to trend to the results in Figure 5.11b. The final value of 7.8 x 10^{11} q cm^{-2} is comparable to the control's interface charge of 3.2 x 10^{11} q cm^{-2}. This indicates that the Si-SiO_2 interface is almost entirely depleted of ions. The Rb^+ sample lost 41 % of its Q_{eff} within the first 10 minutes and a further 20 % by the end of 60 minutes. The Cs^+ sample showed the most gradual degradation, losing 12 % of its initial Q_{eff} after 60 minutes.

5.3.1 Discussion

This section demonstrated the influence of heat and UV radiation on passivation performance through accelerated ageing experiments. The endurance of ionic charge is critical in the operation of charged dielectric devices. The reported endurance of K^+ ion-charged oxide films under vacuum at room temperature is 400 years, however, at a temperature of 65 °C under vacuum the lifespan drops to 8 years [112]. It is expected that under harsh atmospheric conditions, this lifespan would be even lower. Studies of the longevity of the surface passivation provided by K^+ ions under indoor ambient conditions demonstrated that after an initial drop in τ_{eff} of 10 % within the first 10 days,

the passivation is stable for up to 4 years [93].

Figure 5.7 demonstrated the reduction in τ_{eff} for K^+, Rb^+, and Cs^+ charged specimens during exposure to a temperature of 120 °C and, separately, UV radiation. It was determined that after 500 hours at 120 °C, the initial τ_{eff} had fallen by 0.72 ms, 0.91 ms, and 0.50 ms for K^+, Rb^+, and Cs^+ charged specimens, respectively. An examination of the interface properties was carried out to determine the predominant mechanism for the loss in passivation following exposure to elevated temperature. CV measurements in Figure 5.8a demonstrated that K^+, Rb^+, and Cs^+ ions all have excellent physical stability at the interface at 120 °C. A charge retention >96 % was determined for all three ions after 500 hours. The exposure to elevated temperature produced a small increase in D_{it} of 1 x 10^{11} q cm^{-2} for all three ions. The same difference in D_{it} was recorded for the control specimen after 500 hours at 120 °C. Therefore the generation of defects is attributed to thermal activation, and not to the presence of ionic charge. This explains why the relative loss in τ_{eff} was similar for K^+ and Cs^+ charged specimens. The Rb^+ specimen demonstrated a slightly greater loss in passivation. Although the specimens were individually wrapped in aluminium foil before being placed in the box furnace to prevent damage or dust settling on the surface, the Rb^+ specimen may nonetheless have been mishandled, thus resulting in faster lifetime decay.

The ion-charged specimens exposed to UV radiation on one side demonstrated a more significant loss in τ_{eff}. After 500 hours, initial τ_{eff} fell by 1.81 ms, 1.28 ms, an 0.94 ms for K^+, Rb^+, and Cs^+ charged specimens, respectively. It is assumed that if both faces were exposed equally to UV radiation, the lifetimes would have been reduced even further. Tests conducted to determine the charge stability of the ions at the Si-SiO_2 interface under UV radiation demonstrated 84 - 95 % charge retention after 500 hours. Following reports that UV radiation can produce defects within the oxide film at the interface and within the oxide bulk itself, it is possible that the trapped electron density partially shields the electric field produced by the ions, thus limiting the FEP and recorded Q_{eff} [226, 228]. Given the relatively high Q_{eff} detected by CV, it is not possible to attribute such severe reduction in

τ_{eff} to either a significant physical loss of ionic charge at the interface nor shielding of the electric field. Changes in the chemical passivation of the interface were therefore studied. In this work, it was found that the increase in D_{it} after 500 hours was 3 x 10^{11} cm^{-2} eV^{-1} and 4.5 x 10^{11} cm^{-2} eV^{-1} for K^+ and Rb^+ charged specimens, respectively. The D_{it} of the Cs^+ charged specimen and the control both only increased by 1 x 10^{11} cm^{-2} eV^{-1}. The latter results are supported by prior work by Hezel et al. that showed that the presence of Cs^+ ions at the Si-SiO_2 interface did not influence the D_{it} generation under UV radiation [78, 226]. It is not clear why K^+ and Rb^+ charged specimens produce a greater defect density under UV radiation. Although defect generation is certainly a contributor to the deterioration in surface passivation, it is unlikely to be the sole cause, especially for Cs^+ specimens that demonstrated little change in D_{it}. Further work is required to understand the various mechanisms of UV degradation, and their weighted contributions. Despite the lower maximum τ_{eff}, Cs^+ charged specimens show better resistance to defect formation, which may make them the more practical choice for long-term passivation.

Figure 5.11 demonstrated the reduction in Q_{eff} of all three ions in response to a reverse bias of -1 V, -5 V, and -10 V at 200 °C. Of the three ions, K^+ ions demonstrated the poorest endurance. Cs^+ ions demonstrated the best endurance; at the strongest bias of -10 V, equivalent to an electric field of -10^6 V cm^{-1}, the Q_{eff} of Cs^+ ions only lowered by 12.4 % after a total of 60 minutes. Resistance to reverse bias is important in the long-term operation of PV modules. The short circuit current (J_{sc}) of solar cells connected in series within a module is limited by the lowest current produced by an individual cell. Under ideal uniform illumination, all cells are expected to produce an equal J_{sc}. In reality, there may exist a mismatch in J_{sc} between individual cells due to shading as a result of cloud cover, trees, debris, or other environmental obstacles. Shaded cells tend to produce a smaller J_{sc} in comparison to the fully illuminated cells. Instead of passing through an external load, the surplus current produced by illuminated cells is dissipated within the shaded cell [229–231]. The shaded cell as a result operates under reverse bias, which could affect the stability of ionic charge at the interface.

Additionally, the power produced under reverse bias can lead to excessive heat dissipation, which is reported to be detrimental to cell performance [229–231]. Although K^+ ions demonstrated excellent surface passivation, their stability at the Si-SiO_2 interface under bias stress conditions was poor. It is possible that under operational voltages and elevated temperatures, K^+ ion dielectrics may not be suitable for commercial purpose. Rb^+ and Cs^+ charged oxides may therefore present a more stable alternative.

It is expected that the use of a SiN_x capping layer will improve the passivation stability of the ion-charged oxides. It has been reported that SiN_x acts as a highly effective protective layer against UV radiation damage at the Si-SiO_2 [226, 232]. By optimising the SiN_x film deposition parameters, Lauinger et al. reported no detrimental influence of UV radiation on oxidised interfaces, leading to stable cell efficiencies exceeding 10 years [232]. It is postulated in this work that the presence of fixed positive charge in SiN_x could also help stabilise the alkali ions at the Si-SiO_2 interface through electrostatic force. This may result in improved endurance of all three ions under reverse bias conditions. As SiN_x deposition was not available for much of this thesis, such experiments could not be performed. The exploitation of SiN_x as a protective layer should be explored in future work.

5.4 Summary

A maximum τ_{eff} of 2.42 ms, 2.81 ms and 1.86 ms was determined for K^+, Rb^+, and Cs^+ charged specimens, respectively. The optimal Q_{eff} for all three ions was found to be $\sim$1.5 x 10^{12} q cm^{-2}. Further improvements in FEP were found to be limited by the generation of interface defects due to over-saturation of ions at the interface, resulting in distortion of the oxide matrix. Excellent reproducibility of the maximum τ_{eff} was demonstrated for both evaporated and spin coated K^+ specimens, and for Rb^+ and Cs^+ specimens. Accelerated ageing experiments at elevated temperature and UV radiation demonstrated that the all three ions are physically very stable within the SiO_2 film. Nevertheless, the exposure to such conditions resulted in a decrease in surface

passivation quality as demonstrated by the loss in τ_{eff} over time and the generation of interface defects. Under reverse bias, the larger alkali ions demonstrated significantly better stability than K^+ ions. Rb^+ ions were observed to withstand an electric field of -10^5 V cm^{-1} whilst Cs^+ ions presented excellent stability up to a field strength of -10^6 V cm^{-1} at 200 °C. Overall, these results demonstrate the advantages of ion-charged dielectrics as a promising material for surface passivation. The versatility of ion-charged dielectrics allows for exploitation in numerous applications, and opens possibilities for new device architectures where field effect can be used successfully.

6 | Field Induced Chemical Passivation of the Si-SiO_2 Interface

The growth of dry thermal SiO_2 on silicon is reported to provide the best chemical interface passivation amongst dielectrics, with D_{it} as low as 10^9 - 10^{10} cm^{-2} eV^{-1} reported after growth and post-processing [18, 233–235]. The deposition of an additional SiN_x capping layer is often used to enhance the chemical passivation of the Si-SiO_2 interface further through hydrogenation of interface defects [18, 236]. The hydrogenation of the interface typically takes places during a high temperature anneal, relying on the diffusion of hydrogen desorbed from SiN_x to migrate towards the silicon surface [18, 236, 237]. Hydrogen has also been reported to migrate across the silicon-dielectric interface and into the silicon bulk. Within the bulk, hydrogen can also passivate defects [30, 238], and is considered critical in the regeneration of light-induced defects in both n and p-type silicon as reported in references [239–241]. However, it is also responsible for the unwanted electrical de-activation of dopant atoms, which can result in a significant increase in resistivity [242, 243]. Similarly, at the Si-SiO_2 interface, hydrogen can re-activate previously passivated defects [244, 245]. Therefore, the ability to carefully control hydrogen within the dielectric-silicon system would be advantageous to better exploit its passivation properties, and minimise its harmful effects. Hydrogen-containing dielectrics have been utilised to produce record breaking solar cells with >26 % efficiency [124, 246]. The earlier chapters of this thesis demonstrated that embedding alkali ions at the Si-SiO_2 interface can provide long-lasting field effect passivation. By maximising the chemical passivation through controlled hydrogenation, and profiting from the superior FEP of ion-charged dielectrics, it may be possible for higher efficiency solar cells to be produced.

In this chapter, surface electric fields during a post-deposition anneal are used to tailor the chemical passivation provided by SiO_2 + SiN_x dielectric stacks. It is demonstrated here that an electric field present in the dielectric not only modifies the surface carrier concentration via field effect, but can also induce a chemical change in the interface properties upon annealing. By tailoring the surface electric field in the dielectric stack prior to annealing, it is shown that the capture rates and density of interface states at the Si-SiO_2 interface can be modified depending on the field polarity and magnitude. It is hypothesised that the observed changes in the chemical properties of the interface are due to the response that charged hydrogen atoms can have depending on the surface electric fields. Different Si-SiO_2-SiN_x sample structures are tested here. It is shown that the changes in chemical passivation depend strongly upon the dielectric properties and silicon type, with factors such as SiN_x refractive index and SiO_2 properties playing a role in the observations. This chapter discusses the various mechanisms by which these field-dependent changes in chemical passivation can be explained.

6.1 Literature Review of Hydrogen Dynamics at the Si-SiO_2 Interface

Section 1.3.2 described how hydrogen can be introduced to dielectric films during synthesis for beneficial passivation effects. Hydrogen desorbed from the dielectric can exist as dimers (H_2), or atomic form. Furthermore, atomic hydrogen is reported to be amphoteric, meaning it can exist in the positive (H^+), negative (H^-), or neutral (H^0) charge state [239, 247, 248]. The predominance of one charge state over the other depends upon the position of the Fermi level of the dielectric or semiconductor relative to the acceptor and donor levels of atomic hydrogen [247]. Numerous reports exist concerning the role of hydrogen in silicon surface passivation, however, the mechanism by which hydrogen passivates interface defects is still under debate [41, 239, 249–251]. The general observations in the field indicate that dangling bonds at the Si-SiO_2 interface

can be passivated by both molecular and atomic forms of hydrogen [224, 252–254]. Atomic hydrogen is reported to passivate dangling bonds (D) following the reaction in Equation 6.1a [252, 255]. Conversely, atomic hydrogen can also be responsible for the de-passivation of dangling bonds, following the reaction in Equation 6.1b.

$$D + H \rightarrow D\text{–}H \tag{6.1a}$$

$$D\text{–}H + H \rightarrow D + H_2 \tag{6.1b}$$

The passivation and de-passivation mechanisms above are reported to occur spontaneously with a very small non-zero energy barrier [255]. Although the energy barrier has not been quantified, Stathis reports that there is a greater probability of the passivation mechanism occurring compared to the de-passivaton mechanism [255].

It is widely reported that H^+ is the predominant charge state within SiO_2 [245, 252, 256, 257]. It has been proposed that H^+ is generated within the oxide though a reaction between holes and hydrogen [245, 252, 257]. The positive charge state is highly stable owing to the considerably higher energy level of H^+ compared to the conduction band of silicon, which minimises the probability of neutralisation by electron injection [245, 252, 256]. In addition to H^+, neutral H^0 has also been reported to remain stable and passivate defects at the Si-SiO_2 interface [255, 258]. Experimental studies in the literature show that dimers can also passivate silicon dangling bonds at the Si-SiO_2 interface via the reaction in Equation 6.2a [249, 253, 254, 259, 260]. At temperatures >500 °C, hydrogenated dangling bonds can be thermally dissociated according to Equation 6.2b, thus de-passivating the defect [249, 260]. The defect can also be de-passivated by atomic hydrogen as described by Equation 6.1b.

$$D + H_2 \rightarrow D\text{–}H + H \tag{6.2a}$$

$$D\text{–}H \rightarrow D + H \tag{6.2b}$$

The activation energies associated with the passivation and de-passivation mechanisms above are reported to have little dependency on interface orientation [254, 261]. In the case of a textured (111) Si-SiO_2 interface, passivation by H_2 can be defined by a single activation energy of 1.66 eV [249, 254, 261]. At a planar (100) face, the passivation activation energy is reported to range between 1.51 eV and 1.6 eV [254, 262, 263]. The activation energy of the de-passivation mechanism is $\sim$2.6 eV for both (111) and (100) orientations [255, 264]. Therefore the behaviour of hydrogen is not expected to significantly depend upon the interface orientation. The primary difference between the two orientations is the density of electrically active defects present and the intrinsic positive interface charge. At the (100) Si-SiO_2 interface, there are significantly fewer defects created than at the (111) interface [234, 265], resulting in a lower concentration of trapped positive charge composed of holes [234]. In a study by Reed et al. [234], it was determined that the annealing of traps by hydrogen was slower at the (111) Si-SiO_2 interface compared to the (100) interface due to the greater accumulation of trapped positive interface charge electrostatically limiting the migration of H^+ towards the interface.

Within SiN_x, the desorption of hydrogen is due to the dissociation of N–H and Si–H bonds [266, 267]. The amount of desorbed hydrogen is dependent upon the density of the film, and the primary binding site of hydrogen. Studies have shown that in response to the same thermal stress, greater hydrogen desorption is measured in lower density, silicon-rich films [266, 267]. In low density films, where the refractive index (n) is approximately 2.1 or above, hydrogen has been reported to be released from temperatures as low as 400 °C with maximum desorption occurring $\geq$600 °C [236]. In high density films (n < 2.1), maximum desorption occurs at temperatures >800 °C,

reportedly due to the greater dissociation energy of N–H bonds (∼4.1 eV) in comparison to S–H bonds (∼3.1 eV) [236]. High density films have a greater tendency to release atomic hydrogen while in low density films, the hydrogen released tends to form dimers [72, 159, 236]. The interaction of dimers with defects is yet not well-established. While there are numerous studies that demonstrate that H_2 is capable of passivating defects at the silicon interface [248, 249, 261, 264, 268], it is also reported that H_2 generated in SiN_x evaporates from the dielectric, and therefore should not be considered to play a significant role in surface passivation [72, 268]. Although still under debate, it has been proposed that charged hydrogen atoms within dielectrics may respond to surface electric fields [257, 269]. A study on SiO_2 films subjected to a forming gas anneal (FGA) showed, via CV measurements of Q_{eff}, that suspected H^+ could be cycled back and forth from the Si-SiO_2 interface in response to an electric field [269]. A computational study by Pantelides et al. based on density functional theory proposed that excess H^+ atoms that do not interact with the Si-SiO_2 interface can be drifted into the silicon bulk, and subsequently withdrawn under a reverse field [256]. Experimental and theoretical studies show that many mechanisms are in play during hydrogen release and passivation, most of which are still being studied. Conclusions drawn in relation to hydrogen are therefore carefully considered here.

6.2 Interface Passivation Quality after Firing in the Presence of Surface Electric Fields

In this chapter, both planar Set A (n-type 1 Ωcm FZ) and textured Set C (n-type 5-10 Ωcm CZ) wafers were used to investigate the effects of surface fields on chemical passivation. Set A wafers had 100 nm thermal SiO_2 grown on both sides, followed by a forming gas anneal (FGA) in a tube furnace at 425 °C for 30 minutes. Both oxidation and FGA were carried out at Fraunhofer ISE. At the Begbroke clean room, University of the Oxford, a single layer of 65 nm SiN_x was deposited on both oxide surfaces via PECVD using the

parameters listed in Table 2.2 in Chapter 2. The refractive index of the SiN_x film was 1.9, as confirmed by ellipsometry. These substrates are referred to as Type A. Prior to further processing the full size 4 inch substrates were cleaved into quarters so that each Type A specimen was approximately 5 cm x 5 cm in size. Set C wafers had 5 nm thermal SiO_2 grown on both sides at Trina Solar facilities. Oxidised wafers with no further processing are identified as Type C–Ox. On a subset of oxidised samples, referred to here as Type C–Ox–Ni1, 65 nm SiN_x was deposited on both oxide surfaces. The deposition parameters were varied to produce films with a refractive index of 1.95, 2.1, or 2.4. This was intended to vary the native concentration of H in the film, as reported in the literature [159]. On another subset of oxidised Set C wafers, a double layer SiN_x was deposited. These are referred to as Type C–Ox–Ni2. The first SiN_x layer was 5 nm in thickness with a refractive index of 2.2, and the second layer was 60 nm in thickness with a refractive index of 1.95. For all Type C specimens, both oxidation and nitride deposition were performed at Trina Solar facilities under a proprietary process. Further processing and testing were carried out on full size 6 inch substrates. A summary of the four types of substrates used in this chapter is provided in Table 6.1.

IDENTIFIER	SILICON TYPE	SiO_2 THICKNESS	SiN_X THICKNESS	REFRACTIVE INDEX
Type A	planar 1 Ωcm FZ	100 nm	65 nm	1.9
Type C–Ox	textured 5-10 Ωcm CZ	5 nm	-	-
Type C–Ox–Ni1	textured 5-10 Ωcm CZ	5 nm	60 nm	1.95, 2.1, 2.4
Type C–Ox–Ni2	textured 5-10 Ωcm CZ	5 nm	5 nm [a)] 60 nm [b)]	2.2 [a)] 1.95 [b)]

[a)]first SiN_x layer [b)]second SiN_x layer

Table 6.1: Summary of substrates used in Chapter 6.

Firstly, the effective lifetime was monitored on Type A specimens subjected to an annealing process under the presence of a positive or negative surface field. The electric surface field was applied by depositing a controlled concentration of corona discharge. The charge concentration was monitored via Kelvin Probe to ensure that it remains on the surface during the time that it takes to measure the specimens, or transport them across different steps. The results are shown in Figure 6.1. The blue bars represent the τ_{eff} of the substrates following oxidation and nitride deposition, at approximately 0.35 ms. The red bars represent τ_{eff} after 10 - 40 seconds of positive or negative corona discharge was applied to both surfaces of the SiO_2 + SiN_x dielectric stack, immediately followed by annealing at 450 °C for 20 seconds. The yellow bars represent τ_{eff} after a second identical corona-anneal was performed to evaluate the maximum passivation that can be achieved by annealing in the presence of a surface field. It can be seen in Figure 6.1a that all samples treated with positive charge demonstrated improvements in τ_{eff}. A maximum τ_{eff} of 6.4 ms was recorded, which is equivalent to an S_{eff} < 0.24 cm s^{-1}. In contrast, the results in Figure 6.1b demonstrate that applying negative corona charge to the dielectric surfaces prior to annealing resulted in τ_{eff} of $\sim$0.3 ms, well below that obtained by a positive corona anneal.

Since surface passivation can be both chemical and field effect in origin, the results in Figure 6.1 could imply that the hydrogen, which is suspected to exist in the dielectric in H^+ form, is drifted towards the interface under a positive surface electric field. Once at the interface, H^+ may chemically passivate interface defects. Following this hypothesis, negative surface electric fields would retract existing H^+ from the interface, thus de-passivating defects and increasing the interface recombination. Alternatively, any charge remaining after the anneal, as a product of corona ions or charged states, can vary the dielectric charge concentration, which for positive (negative) charge would lead to lower (higher) recombination. The exact mechanism behind the change in τ_{eff} is explored in more detail in Section 6.3.

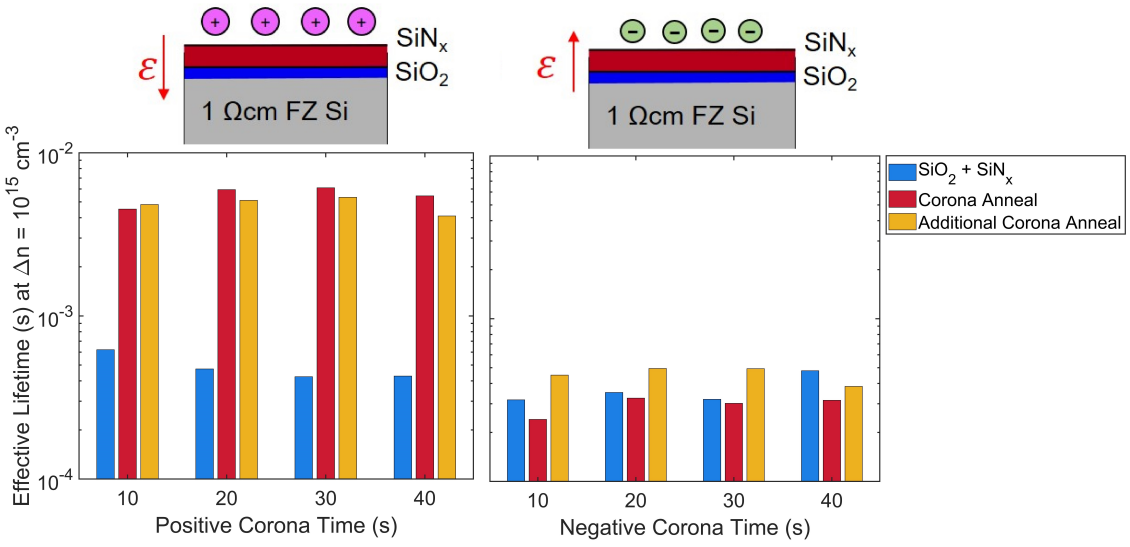

(a) (b)

Figure 6.1: Effective lifetimes of Type A specimens before and after corona annealing using increasing concentrations of (a) positive and (b) negative corona charge. The additional corona anneal performed on each specimen was identical to the first. The corona charge was deposited at a tip voltage of ±30 kV.

A similar experiment was performed on Type C–Ox–Ni2 samples. The changes in τ_{eff} after both corona charging and annealing are presented in Figure 6.2. Here 30 or 60 seconds of positive or negative corona charge applied to both surfaces followed by a 2 minute anneal at 450 °C. In Figure 6.2a, it can be seen that annealing in the presence of a positive surface field results in only a small improvement in τ_{eff} compared to that of the untreated dielectric stack. Unexpectedly, annealing in the presence of a negative surface field also resulted in a small improvement in τ_{eff}. The effective lifetime increased from 2.69 ms to 3.21 ms after depositing 30 s of negative corona charge, equivalent to $Q_{surf} \sim$ -1.6 x 10^{12} q cm^{-2}, followed by annealing. It is clear from the different results in Figure 6.1 and Figure 6.2 that the surface polarisation during an anneal produces different results depending on the type of silicon in addition to the oxide and nitride synthesis methods. To determine how the surface electric field influences surface passivation, a study of the interface electrical characterisation was performed, as discussed next.

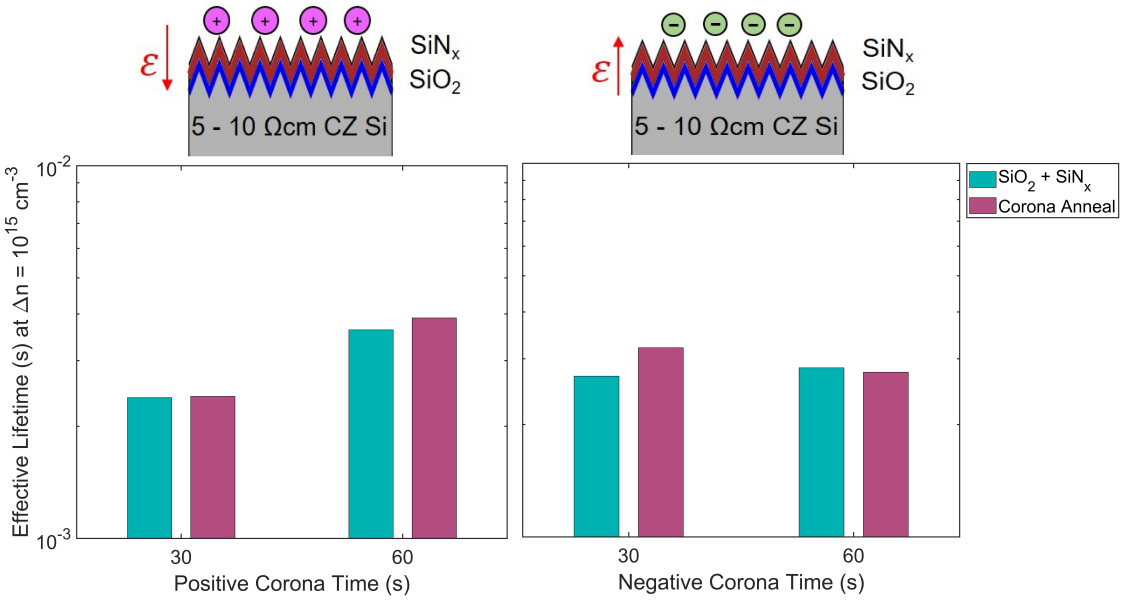

(a) (b)

Figure 6.2: Effective lifetimes of Type C–Ox–Ni2 specimens before and after corona annealing using increasing concentrations of (a) positive and (b) negative corona charge. The corona charge was deposited at a tip voltage of $\pm$30 kV.

6.3 Interface Recombination Parameters after Firing in the Presence of Surface Electric Fields

To determine the interface recombination parameters for Type A and Type C–Ox–Ni2 specimens after corona charging and annealing, surface recombination at the Si-SiO_2 interface was varied by regulating the surface carrier densities, n_s and p_s. As described in Section 2.8.2, a thin layer of PEDOT:PSS was applied to the dielectric surfaces of planar (Type A) specimens to serve as a transparent gate electrode. The use of a transparent gate allowed for the temporary and controllable biasing of the dielectric, while simultaneously permitting the photo-generation of charge carriers. By taking effective lifetime measurements on the Sinton tester, the carrier-dependent surface recombination can be determined as a function of surface bias. As PEDOT:PSS does not apply well to the textured surface of Type C–Ox–Ni2 specimens, increasing amounts of

corona charge were deposited to bias the dielectric surface, and regulate the surface carrier densities.

An analytical model was used to fit the experimental data, and to quantify the interface recombination parameters. The model was adapted from Girisch and Aberle's iterative formalism to calculate the density of carriers at the surface [167, 233]. Once n_s and p_s are known, the effective surface recombination velocity (S_{eff}) can be calculated from the surface recombination rate (U_s), as defined by Equations 1.18 and 1.19 in Section 1.2.4. This formalism is described in detail in Appendix A.2. Following reference [214], this thesis takes into account the influence of fluctuations in dielectric charge on the surface recombination by introducing a Gaussian distribution of fluctuations with standard deviation, σ_q. The surface recombination velocity can therefore be calculated as [214]:

$$S = \int_{-\infty}^{\infty} S(D_{it}, \sigma_n, \sigma_p, Q_f, \Psi_s) * \frac{1}{\sigma_q \sqrt{2\pi}} \exp\left(\frac{(Q_f - Q_{f0})^2}{2\sigma_q^2}\right) \quad dQ_f \tag{6.3}$$

The results for Type A specimens are presented in Figure 6.3. Four types of samples were produced. The control had no processing performed after deposition of SiO_2 and SiN_x. A separate control specimen was produced that was annealed for 20 seconds at 450 °C after dielectric deposition. A third sample was created that had 30 s of positive corona charge applied to both surfaces followed by the same 20 s anneal at 450 °C. The fourth sample had 30 seconds of negative corona charge applied to both surface followed by the same anneal. After the application of PEDOT:PSS to the dielectric surface of all four samples, the gate bias was varied between +4 V and -8 V to control the silicon surface from deep accumulation to deep inversion, while τ_{eff} was measured throughout. Maximum recombination occurs when $n_s\sigma_n$ = $p_s\sigma_p$. This state occurs approximately when the dielectric charge is compensated by an equal but opposite bias gate voltage. Therefore, the x-axis co-ordinate of the minimum point of each plotted curve is an indicative measure of Q_f.

The differences in the minimum τ_{eff} observed for each of the four specimens allows a

comparison of the chemical interface passivation quality when the field effect component is nullified by the counter-bias applied on the dielectric surface. Under zero field effect, surface recombination is wholly attributable to the chemical properties of the Si-SiO_2 interface of each specimen, as given by the electron and holes capture velocities, S_{n0} and S_{p0}, in Equation 1.18. The lowest minimum τ_{eff} of 0.07 ms was recorded for the specimen annealed in the presence of a negative surface field. The sample annealed in the presence of a positive surface field had a higher minimum τ_{eff} of 0.33 ms, thus indicating that the polarity of the surface field prior to the anneal influences the chemical passivation. The solid lines in Figure 6.3 indicate the model used to explain the observed behaviour. The values for the fitting parameters are given in Table 6.2. It was found that for Type A specimens, annealing under a positive electric field only increased the built-in charge (Q_f) and its inhomogeneity (σ_q) in the dielectric stack. No substantial reduction in S_{n0} and S_{p0} could be attributed in comparison to the two control specimens. On the other hand, applying a negative field on the surface was seen to have a strong effect on the passivation quality after annealing, with a 1 order of magnitude increase in D_{it} from 10^{10} to 10^{11} cm^{-2} eV^{-1} and an increase in S_{n0} and S_{p0} by two and fourfold, respectively. These results on Type A specimens confirm that the surface electric field does influence the chemical passivation of the interface. Given the hypothesis that these field dependent changes are related to hydrogen, these results support recent findings that atomic hydrogen exists in the positive charge state at the Si-SiO_2 interface [245], and would be in agreement with the originally stated hypothesis.

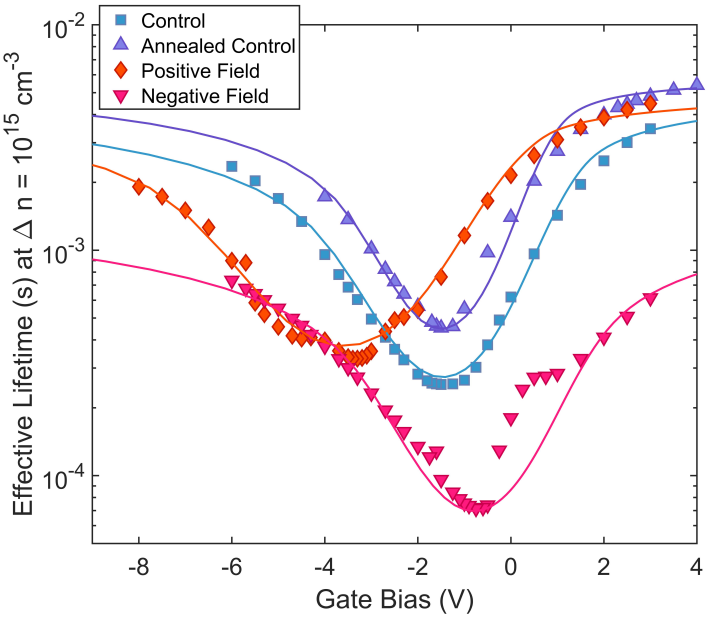

Figure 6.3: Effective lifetime as a function of gate bias as measured on planar Type A specimens using a PEDOT:PSS transparent gate.

	CONTROL	ANNEALED CONTROL	POSITIVE FIELD	NEGATIVE FIELD
τ_{eff}	Richter's Parametrisation [25]			
EOT (nm)	137.3			
Q_f (10^{11} q cm^{-2})	2.4	2.4	5.6	1.6
σ_q (10^{11} q cm^{-2})	1.4	1.2	2	1.3
S_{n0} (cm s^{-1})	305	172	293	607
S_{p0} (cm s^{-1})	34	17	29	137
$D_{it,mg}$ (10^{10} cm^{-2}eV^{-1})	1	1	1	10
$D_{it,VB}$, $D_{it,CB}$ (10^{15} cm^{-2}eV^{-1})	1, 3	1, 1	1, 3	2.5, 8

Table 6.2: Summary of modelling parameters used to fit effective lifetime as a function of gate bias in Figure 6.3. *EOT* is the equivalent oxide thickness.

To determine if similar trends are observed in other Si-SiO_2-SiN_x structures, a similar experiment was performed on Type C–Ox–Ni2 substrates. It should be noted that due to specimen and equipment availability, these experiments were performed on a different silicon surface and on a dielectric stack with different properties. Here corona discharge was used to regulate n_s and p_s since these specimens had a textured surface. The results are shown in Figure 6.4. The same four types of specimens were produced as above. An additional specimen was created that had 60 s of negative corona charge applied to both surfaces followed by annealing at 450 °C. This specimen is labelled as "stronger negative field". After processing of each specimen was completed, both dielectric surfaces of each specimen were biased with incremental additions of negative corona charge while τ_{eff} was recorded on the Sinton tester. Although the Kelvin Probe can be used to measure the surface charge on a full size 6 inch substrate, the dimensions of the instrument make it difficult to fit it under the probe. To prevent damage to the sample, one Kelvin Probe measurement was taken prior to depositing negative charge to determine the initial surface charge. A calibration was used to calculate the incremental increases in charge after each corona deposition. Corona charge was only added in 5 s and 10 s increments. As described in Appendix A.3, calibration samples were produced to determine the charge deposition rate. Effective lifetime measurements were taken immediately following corona deposition. The cycle of corona charging and Sinton testing was performed continuously to prevent the dissipation of corona charge. The whole experiment was completed within 90 minutes.

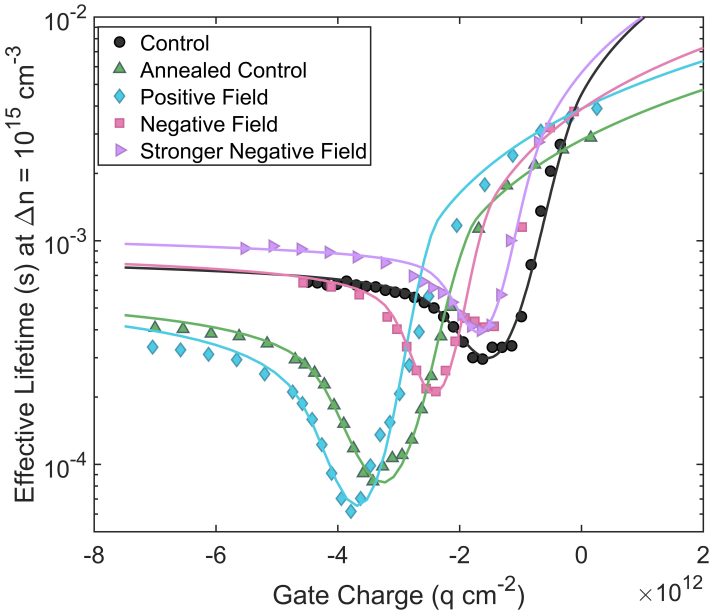

Figure 6.4: Effective lifetime as a function of charge on textured Type C–Ox–Ni2 specimens using increasing concentrations corona charge to bias the dielectric surface, following a corona-anneal process. The corona charge was deposited at a tip voltage of -30 kV.

The fitting parameters for Type C–Ox–Ni2 specimens are provided in Table 6.3. Annealing the SiO_2 + SiN_x stack without the presence of an extrinsic field resulted in degradation of the chemical passivation. Relative to the control, D_{it} increased from 2 x 10^{10} to 8 x 10^{10} cm^{-2} eV^{-1}, and the S_{n0} and S_{p0} values increased by approximately four times. Annealing the dielectric stack in the presence of an extrinsic positive field resulted in similarly poor levels of chemical passivation. However, applying negative surface fields resulted in high levels of interface passivation similar to the SiO_2 + SiN_x control. Strengthening the negative field pre-anneal resulted in the best quality interface out of all 5 specimen types. Relative to the control, the D_{it} decreased from 2 x 10^{10} to 1 x 10^{10} cm^{-2} eV^{-1}, and S_{n0} lowered by 50 %.

	CONTROL	ANNEALED CONTROL	POSITIVE FIELD	NEGATIVE FIELD	STRONGER NEGATIVE FIELD
τ_{eff}			Richter's Parametrisation [25]		
EOT (nm)			38.8		
Q_f (10^{11} q cm^{-2})	13	31	5	23	16
σ_q (10^{11} q cm^{-2})	4.1	4.3	3.6	2.8	3.0
S_{n0} (cm s^{-1})	687	2565	3664	779	343
S_{p0} (cm s^{-1})	60	366	275	124	69
$D_{it,mg}$ (10^{10} cm^{-2}eV^{-1})	2	8	8	2	1
$D_{it,VB}$, $D_{it,CB}$ (10^{15} cm^{-2}eV^{-1})	8, 7	8, 2.5	8, 2	6, 2	6, 0.9

Table 6.3: Summary of modelling parameters used to fit effective lifetime as a function of charge in Figure 6.4. *EOT* is the equivalent oxide thickness.

Bredemeier et al. reported that the in-diffusion and out-diffusion of hydrogen at the silicon interface is predominantly influenced the SiN_x film properties closest to the interface [159]. Therefore the behaviour of hydrogen within Type C–Ox–Ni2 specimens is primarily influenced by the first SiN_x layer of refractive index 2.2. High refractive index (low density) films have a greater tendency to release dimers rather than atomic hydrogen [72, 159]. Therefore, Type C–Ox–Ni2 substrates were polarised and annealed at a higher temperature of 600 °C to increase the likelihood that atomic hydrogen is desorbed. Additionally, to determine the dependency of the observations on surface electric field strength, both sides of the dielectric stack were subjected to positive or negative corona discharge for 30 s, 60 s, or 120 s prior to the anneal. The results of the surface biased lifetime experiment are shown in Figure 6.5. The fitting parameters used to model the interface properties are provided in Table 6.4. Figure 6.5a compares the results of the as-received control and a control annealed at 600 °C with no extrinsic electric present. Similarly to results performed at 450 °C, the chemical passivation worsened following the anneal under no added corona charge, with S_{n0} and S_{p0}

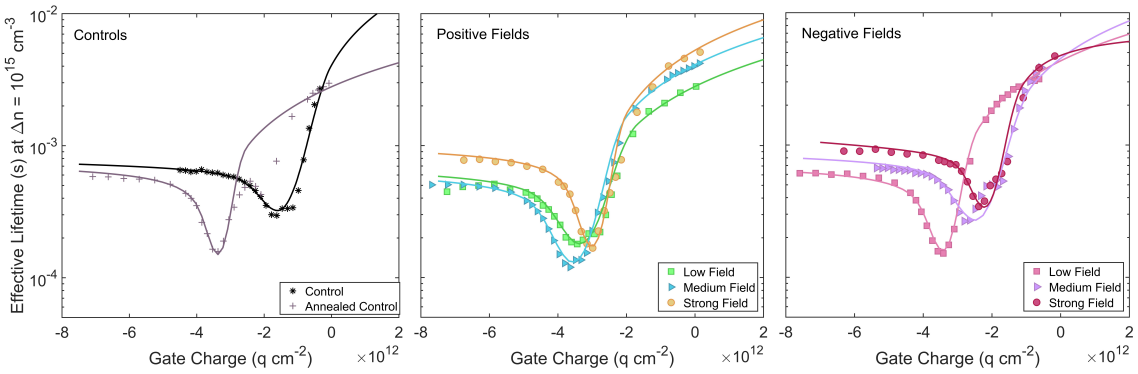

Figure 6.5: Effective lifetime as a function of charge as measured on textured Type C–Ox–Ni2 specimens annealed at 600 °C (a) control specimens (b) specimens annealed with a positive surface field (c) specimens annealed with a negative surface field. The corona charge was deposited at a tip voltage of -30 kV.

increasing by 47 % and 83 %, respectively. Figure 6.5b compares the specimens that were positively corona charged prior to annealing. Compared to the control, the sample annealed in the presence of a low positive surface electric field did not demonstrate an increase in D_{it}. However, S_{n0} and S_{p0} increased by approximately double. Annealing in the presence of a medium field strength, resulted in an increase in D_{it} of 1 x 10^{10} cm^{-2} eV^{-1}, and S_{n0} and S_{p0} increased by approximately two and fourfold, respectively. In the case of strong positive fields, the D_{it} remained unchanged compared to the control, and S_{n0} increased by 33 % and S_{p0} by 300 %. Figure 6.5c shows the results for specimens annealed in the presence of negative surface electric fields. A clear trend was observed where the chemical passivation improved with increasing negative field strength. Under a strong negative field, D_{it} decreased from 2 x 10^{10} cm^{-2} eV^{-1} to 1 x 10^{10} cm^{-2} eV^{-1}, and S_{n0} decreased by 37 %, relative to the control.

The results of Type A and Type C–Ox–Ni2 both demonstrate that the surface electric field influences the chemical passivation of the interface. However, the mechanisms by which the interface properties are changed in Type–C–Ox–Ni2 specimens appear to be different than in Type A specimens. In Type A, the negative electric field during annealing degrades the interface passivation. In contrast, for Type C–Ox–Ni2 specimens, negative

	Controls		Positive Fields			Negative Fields		
	Control	Annealed	Low	Medium	Strong	Low	Medium	Strong
τ_{eff}	Richter's Parametrisation [25]							
EOT (nm)	38.8							
Q_f (10^{11} q cm^{-2})	13	33	32	34	29	33	23	21
σ_q (10^{11} q cm^{-2})	4.1	2.3	4.6	4.3	2.8	2.8	4.5	3.8
S_{n0} (cm s^{-1})	687	1008	1374	1580	916	1008	824	435
S_{p0} (cm s^{-1})	60	110	128	275	183	137	103	73
$D_{it,mg}$ (10^{10} cm^{-2}eV^{-1})	2	2	2	3	2	2	1.5	1
$D_{it,VB}$, $D_{it,CB}$ (10^{15} cm^{-2}eV^{-1})	8, 7	8, 2	8, 3	8, 3	7, 2	8, 3	7, 2	6, 2

Table 6.4: Summary of modelling parameters used to fit effective lifetime as a function of gate charge in Figure 6.5. *EOT* is the equivalent oxide thickness.

surface fields during annealing showed improvements in the chemical passivation of the interface. A key difference between the two types of specimens is the properties of the SiN_x dielectric. The refractive index, and therefore the density, of the SiN_x film influences the desorption of hydrogen and its mobility [72, 159, 236]. To determine whether the nitride properties explain the difference in the observations made between the Type A and Type C–Ox–Ni2, the effect of surface electric fields on the chemical properties was studied on films with three different refractive indices.

For the following experiments, Type C–Ox–Ni1 substrates were used. The density of the single layer SiN_x film was varied to produce refractive indices of 1.95, 2.1, and 2.4. The refractive index is known to vary due to stoichiometry, and increases with greater silicon density [270]. As described in Section 1.3.2.2, the intrinsic charge concentration also depends upon film composition, and increases with increased nitrogen content due to the formation of K-centres. For each refractive index, 3 types of specimens were produced: a control with no further processing, a substrate that was annealed at 600 °C in the presence of a positive surface field, and a substrate that was annealed at 600 °C in the presence of a negative surface field. The results of the surface biased lifetime experiment are shown in Figure 6.6. The interface recombination modelling parameters are given in Table 6.5. Figure 6.6a compares the results for the three specimen types where the SiN_x refractive index was 1.95. Annealing in the presence of a positive surface field resulted in a significant reduction in chemical passivation, as the D_{it} increased from 2 x 10^{10} cm^{-2} eV^{-1} to 5.5 x 10^{10} cm^{-2} eV^{-1}, and the S_{n0} and S_{p0} values increased by approximately three to fourfold. In contrast, annealing in the presence of a negative surface field resulted in an improvement to the interface. Relative to the control the D_{it} lowered from 2 x 10^{10} cm^{-2} eV^{-1} to 1 x 10^{10} cm^{-2}, and S_{n0} and S_{p0} were reduced by 54 % and 73 % respectively. Figure 6.6b shows the results for a refractive index of 2.1. A similar pattern was observed as in Figure 6.6a, however, here the degradation due to positive surface fields was less stark. The positively charged sample showed a smaller increase in D_{it} from 2 x 10^{10} cm^{-2} eV^{-1} to 3 x 10^{10} cm^{-2} eV^{-1}. The value of S_{p0} increased by twofold

while S_{n0} remained constant. Annealing in the presence of a negative surface field showed a reduction in D_{it} from 2 x 10^{10} cm^{-2} to 1 x 10^{10} cm^{-2} eV^{-1}. S_{n0} and S_{p0} reduced by 60 % and 44 %, respectively. Figure 6.6c shows the results for the highest refractive index of 2.4. Here the D_{it} and the electron and hole capture rates did not vary substantially for the positively charged sample, compared to the control. The sample that was negatively charged again showed an improvement in the chemical passivation. The D_{it} lowered from 3.5 x 10^{10} cm^{-2} eV^{-1} to 1 x 10^{10} cm^{-2} eV^{-1}, and S_{n0} and S_{p0} lowered by 77 % and 75%, respectively.

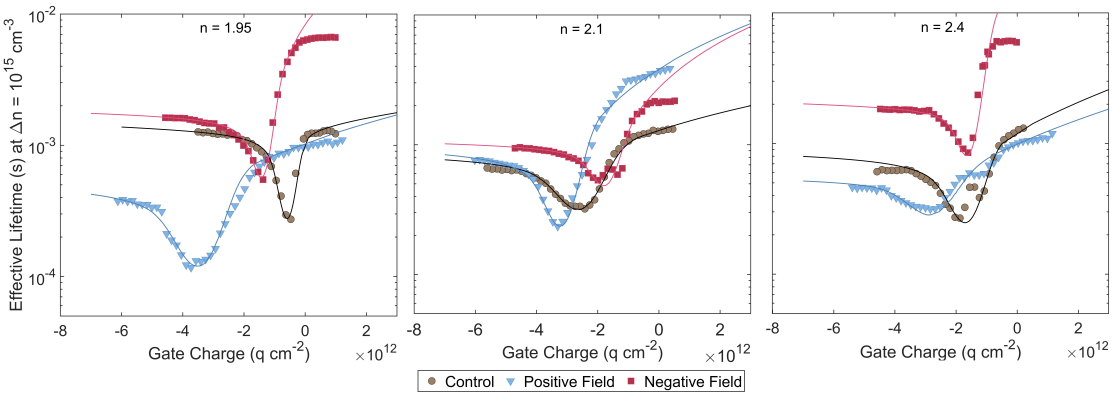

(a) (b) (c)

Figure 6.6: The influence of refractive index on the relationship between effective lifetime and charge on Type C–Ox–Ni1 specimens for (a) n = 1.95 (b) n = 2.1 and (c) n = 2.45. All specimens were annealed at 600 °C, excluding the controls. The corona charge was deposited at a tip voltage of -30 kV.

These results show that the refractive index affects the mechanism by which surface polarisation changes the chemical interface properties. This is particularly evident for samples annealed in the presence of a positive surface field. The detrimental effect of the positive polarisation is minimised as the refractive index increases. In all cases, annealing in the presence of a negative surface field improves the interface passivation. The results in Figure 6.6 do not provide an explanation of the contrasting observations on Type A specimens where the refractive index of the SiN_x film was 1.9. It is therefore hypothesised that the passivation/depassivation mechanism is not solely related to the

dielectric density. A discussion of various possible passivation mechanisms is presented next.

6.4 Explaining Changes in Interface Properties through Hydrogen Passivation

Previous work by Jin et al. used a comparable experimental approach and revealed analogous surface biased lifetime dependencies of hydrogenated Si-SiO_2 structures [271]. They reported interface degradation under both low positive and negative surface field conditions, which they attributed to both the depassivation of silicon dangling bonds, and the generation of new defects by atomic hydrogen [271]. Contrary to the observations of Jin et al., there is no evidence of interface degradation for positive surface fields on Type A specimens. Additionally, it was found that the passivation performance is improved in the case of Type C–Ox–Ni1 and Type C–Ox–Ni2 specimens when they are negatively charged before annealing. It is conjectured in this work that hydrogen is likely to be responsible for the observed changes in chemical passivation.

In the case of Type A specimens, a relatively low D_{it} of 10^{10} cm^{-2} eV^{-1} exists at the as-deposited Si-SiO_2 interface due to the low defect density in (100) surface. Additionally, the oxide film was subjected to a forming gas anneal, which is well-reported to introduce significant quantities of hydrogen [40, 64, 272]. It is proposed that the Si-SiO_2 interface was very well passivated by the hydrogen introduced during the FGA. The hypothesised mechanism under positive surface fields is illustrated in Figure 6.7a. Here it is proposed that H^+ is drifted towards the interface under positive fields. Neutral atomic and molecular forms may also diffuse under high temperature towards the interface. However, due to the excellent pre-existing passivation the hydrogen doesn't make a further impact on passivation. The accumulated H^+ at the interface may contribute to the increased Q_f determined after annealing under positive fields. The hypothesised mechanism under negative surface electric fields is shown in

	n = 1.95			n = 2.1			n = 2.4		
	Control	Positive Field	Negative Field	Control	Positive Field	Negative Field	Control	Positive Field	Negative Field
τ_{eff}				Richter's Parametrisation [25]					
EOT (nm)				38.8					
Q_f (10^{11} q cm^{-2})	5.3	33	9	24	31	14	15	26	14
σ_q (10^{11} q cm^{-2})	2	5.5	2.5	5.5	3.7	1.5	4.0	6.0	2.5
S_{n0} (cm s^{-1})	458	2204	252	824	824	332	801	618	183
S_{p0} (cm s^{-1})	87	220	23	41	96	23	72	62	18
$D_{it,mg}$ (10^{10} cm^{-2}eV^{-1})	2	5.5	1	2	3	1	3.5	3	1
$D_{it,VB}, D_{it,CB}$ (10^{15} cm^{-2}eV^{-1})	4, 8	9, 2	7, 1	10, 4.5	9, 0.9	8, 1	10, 1	10, 1	6, 0.8

Table 6.5: Summary of modelling parameters used to fit effective lifetime as a function of gate charge in Figure 6.6. *EOT* is the equivalent oxide thickness.

Figure 6.7b. After annealing under negative surface electric fields, it is possible that the pre-existing hydrogen is thermally dissociated from the defect sites, and retracted as H^+ from the interface by coulombic attraction. Upon retraction from the interface, the passivation is lost. This proposed mechanism may explain the changes in D_{it} and carrier capture rates following annealing of the polarised dielectric surface of Type A specimens.

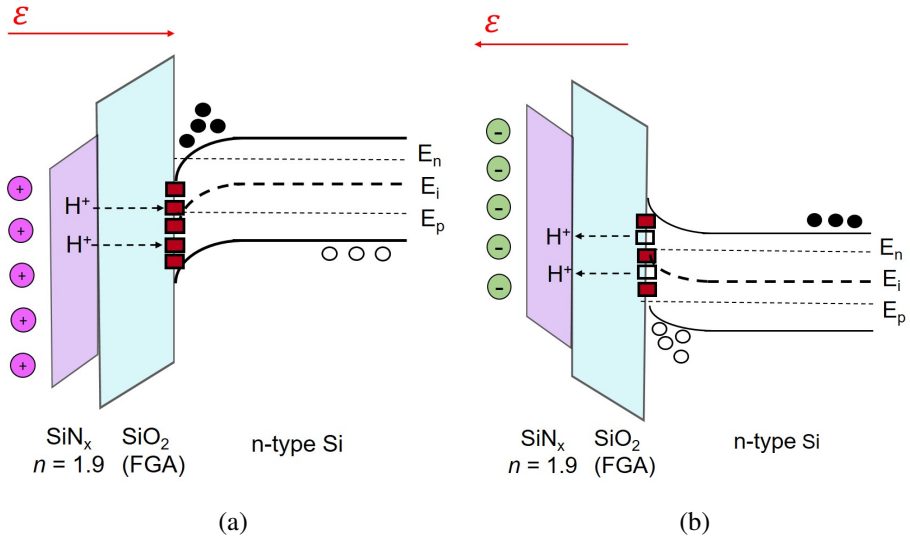

Figure 6.7: Proposed mechanism for the observed changes in interface passivation of Type A specimens annealed under (a) positive surface electric fields and (b) negative surface electric fields. Filled red squares represent passivated interface defects, and blank squares represent de-passivated defects.

In Type C–Ox–Ni2 specimens, a contradictory trend was observed. At annealing temperatures of both 450 °C and 600 °C, positive surface fields resulted in degradation of the chemical properties, and negative surface fields resulted in improvements. It is evident that surface electric fields influence the chemical passivation properties of the interface, however, the mechanism is clearly different to that observed in Type A specimens. The hypothesis for the de-passivaion of the interface under positive surface fields is schematically represented in Figure 6.8a, and can be described by a three step process. Firstly, under positive electric fields, the hydrogen is drifted to the interface. However, the drift is limited by the significant fixed positive interface charge arising

from trapped holes that is reported to exist at the (111) Si-SiO_2 interface [234]. Therefore, H^0 or H_2, which are decoupled from the electric field, may reach the interface first and passivate defects. Secondly, under the strength of the positive field, electrons are injected from the silicon into the SiO_2. The third step is the depassivation of weakly bonded Si–H bonds by hot electrons, thus re-activating defects. The role of electron injection in de-hydrogenation of the interface is reported in references [244, 245, 273, 274]. Additionally, studies have shown that neutral hydrogen forms weaker bonds at the interface compared to H^+ [258]. This may explain why hot electron injection was not observed to cause degradation in Type A specimens where H^+ was presumed to be the primary agent.

Figure 6.8b exhibits the proposed mechanism under negative surface electric fields. Here, H^+ generated within SiN_x would be attracted towards the negatively charged dielectric surface. However, as before, H^0 or H_2 could still diffuse towards the silicon surface and passivate defects. In the absence of electron accumulation at the silicon surface, the detrimental effect of hot electron injection does not occur, thus de-passivation is minimised. Electrons within the dielectric drifted by the negative corona charge can release the holes trapped at the (111) Si-SiO_2 interface [275]. The greater the negative field strength, the greater the hole de-trapping, which was observed in this work to result in a reduced dielectric positive charge. Once de-trapped, the holes may react with bound hydrogen within the oxide to release substantial concentrations of atomic hydrogen, as reported in [276]. The released atomic hydrogen is in close proximity to the interface and is expected to readily passivate defects.

To consolidate the proposed mechanisms, an additional experiment was performed. Here, a fresh Type C–Ox–Ni2 specimen had 60 s of negative corona charge deposited on the dielectric surfaces followed by annealing at 600 °C for 2 minutes. Immediately after, the same specimen had 60 s positive corona charge applied followed by the same anneal. The results of the subsequent surface-biased lifetime experiment are shown in Figure 6.9. The purple and blue curves are reproduced from Figure 6.5, and represent

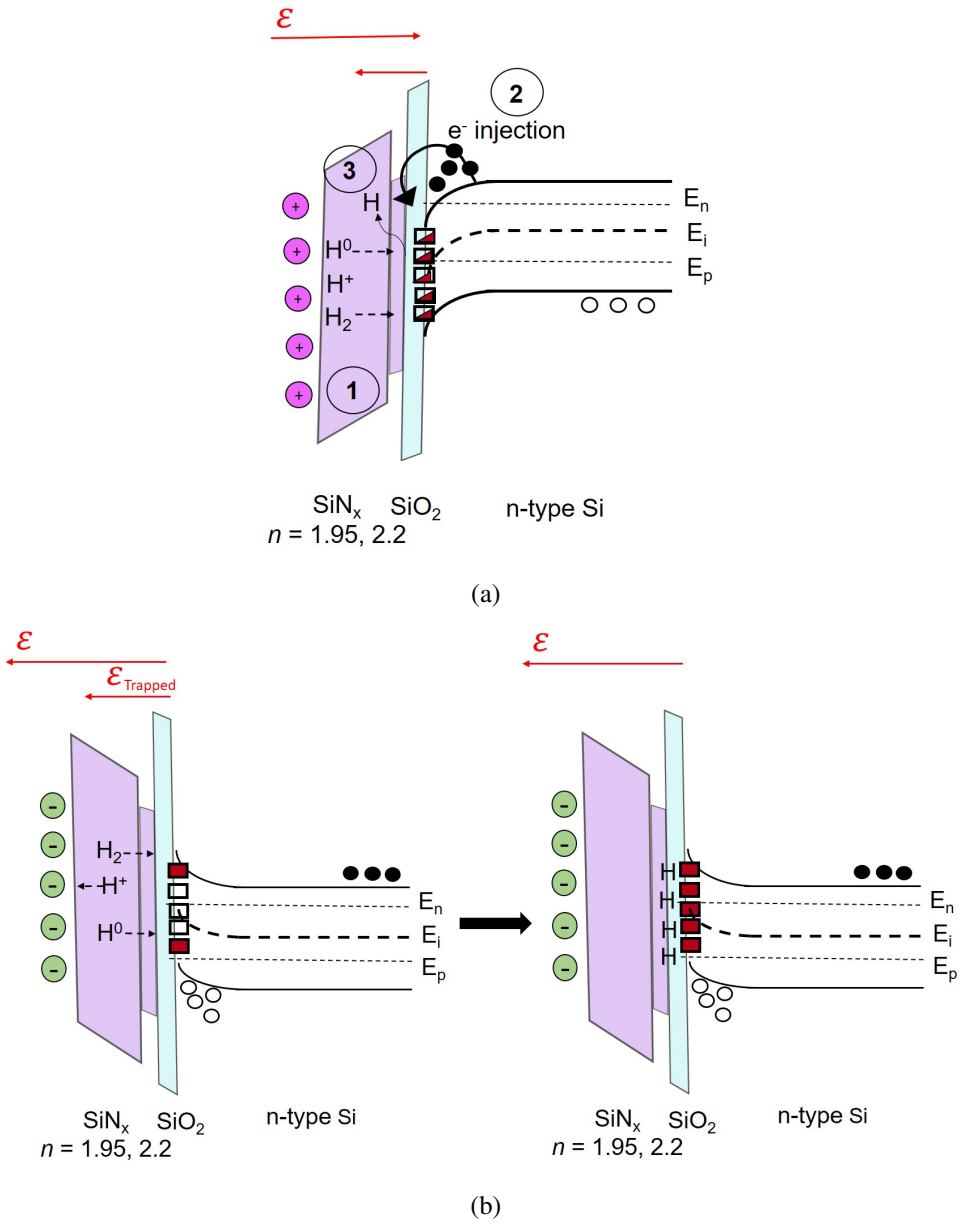

Figure 6.8: Proposed mechanism for the observed changes in interface passivation of Type C–Ox–Ni2 specimens annealed under (a) positive surface electric fields and (b) negative surface electric fields. Filled red squares represent passivated interface defects, and blank squares represent de-passivated defects.

specimens that separately had 60 s of positive or negative corona charge deposited before annealing at 600 °C for 2 minutes. The τ_{eff} of the specimen that was annealed twice under opposing polarities has a similar dependency on charge as the sample that was

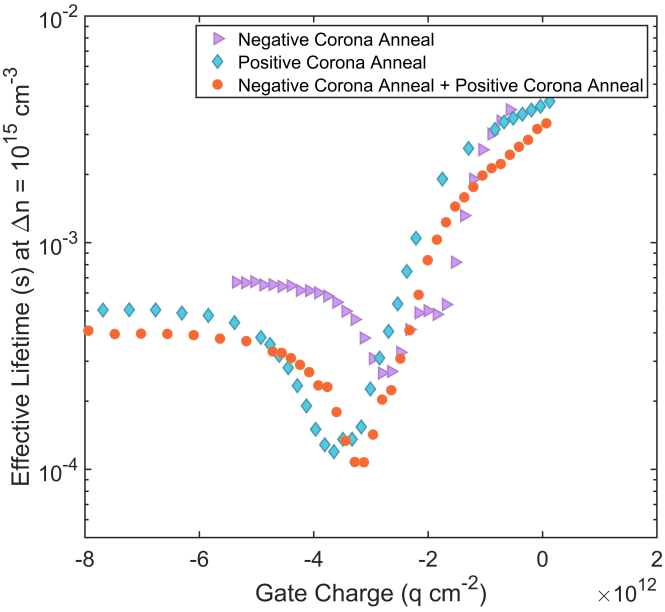

Figure 6.9: Surface biased lifetime experiment of Type C–Ox–Ni2 specimen that underwent a negative corona anneal followed by a positive corona anneal. The corona charge was deposited at a tip voltage of ±30 kV. The blue and purple curves are reproduced from Figure 6.5.

annealed once under a positive surface field. Firstly, these results demonstrate that the field-induced mechanism is reversible. Secondly, they provide a substantiation of the proposed mechanisms. The Si-SiO_2 interface passivation is well passivated by hydrogen under negative surface electric fields. When the same specimen is annealed under positive surface fields, electron injection from the silicon into the SiO_2 de-passivates the hydrogenated defects.

Type C–Ox–Ni1 specimens demonstrated a clear trend based on the refractive index of the SiN_x film. Here it was demonstrated that with increasing refractive index, the detrimental effect of positive surface fields during annealing was minimised. At the highest refractive index of 2.4, there was negligible difference between the chemical passivation of the interface for the control specimen and the positively charged specimen. It is well-reported that hydrogen content within SiN_x increases with increasing refractive index [159, 236]. Bredemeier et al. report that the maximum hydrogen concentration is desorbed in films where n = 2.4 [159]. It is hypothesised here that under positive surface

electric fields, hydrogen is either drifted or diffused to the silicon surface where it passivates dangling bonds. For the Type C–Ox-Ni1 specimens with the lowest n of 1.95, hydrogen-terminated dangling bonds are de-passivated by electron injection, similarly to the mechanism presented in Figure 6.8a. With increasing refractive index, the substantially higher concentration of available hydrogen is able to swiftly passivate previously de-passivated dangling bonds, thus overriding the de-passivation mechanism by electron injection. This effect is most evident in specimens with refractive index of 2.4, which are believed to have the greatest hydrogen concentration.

It was shown that irrespective of film density, annealing Type C–Ox–Ni1 specimens in the presence of negative surface fields provided improvements in chemical passivation. It is hypothesised that the mechanism is similar to that presented in Figure 6.8b. Hydrogen is generated within the oxide due to hole de-trapping at the (111) Si-SiO_2 interface, which is not dependent upon the properties of the SiN_x film. As before, since electrons are prevented from accumulating at the silicon surface under negative electric fields, the de-passivation effects are not observed. Therefore the density of the SiN_x film is mainly of consequence when annealing under positive surface electric fields.

In this work, it has been hypothesised that hydrogen is introduced to the Si-SiO_2 interface following desorption from the SiN_x layer. To confirm that the SiN_x film is necessary for the observed changes in interface passivation, a test was conducted on Type C–Ox substrates that had only a 5 nm SiO_2 dielectric on both surfaces following the same experimental procedure. The oxide surfaces were positively or negatively charged followed by annealing at 450 °C for 2 minutes. The results of the subsequent surface biased lifetime experiment on these samples are provided in Figure 6.10a. The interface recombination parameters used to fit the data to a theoretical model are given in Table 6.6. The as-oxidised interface of the control is highly recombination active. The modelled S_{n0} and S_{p0} were 26.3 x 10^3 cm s^{-1} and 9.16 x 10^3 cm s^{-1}, respectively. Annealing a control specimen without any extrinsic electric field present did not significantly alter the interface properties. Annealing the control in the presence of a

positive surface electric field resulted in an unexpected improvement to the interface properties as the D_{it} lowered by 60 %, and S_{n0} and S_{p0} by 36 % and 63 %, respectively. Additionally, a small increase in the dielectric's positive charge was detected. Annealing in the presence of negative surface electric fields also demonstrated improvements in the chemical passivation. The D_{it} decreased by 40 %, and S_{n0} and S_{p0} by 35 % and 55 %, respectively. Another unexpected finding was a sixfold increase in positive charge within the oxide film when it had been annealed after negative corona deposition. To ensure these results are reproducible and indicative of a trend, fresh specimens were produced that underwent identical positive and negative surface charging prior to annealing. The repeated surface biased lifetime results are plotted in Figure 6.10b. Similar dependencies on surface charge were demonstrated for both specimens, thus proving these findings are dependable and accurate. Here, the negatively charged sample had a greater positive oxide charge, as evidenced by the greater shift along the negative x axis. The results in Figure 6.10 lead to two key questions. Firstly, why is there is a difference in the interface properties upon annealing in the presence of positive and negative surface electric fields? And secondly, why does annealing the oxide in the presence of a negative surface lead to increases in positive dielectric charge?

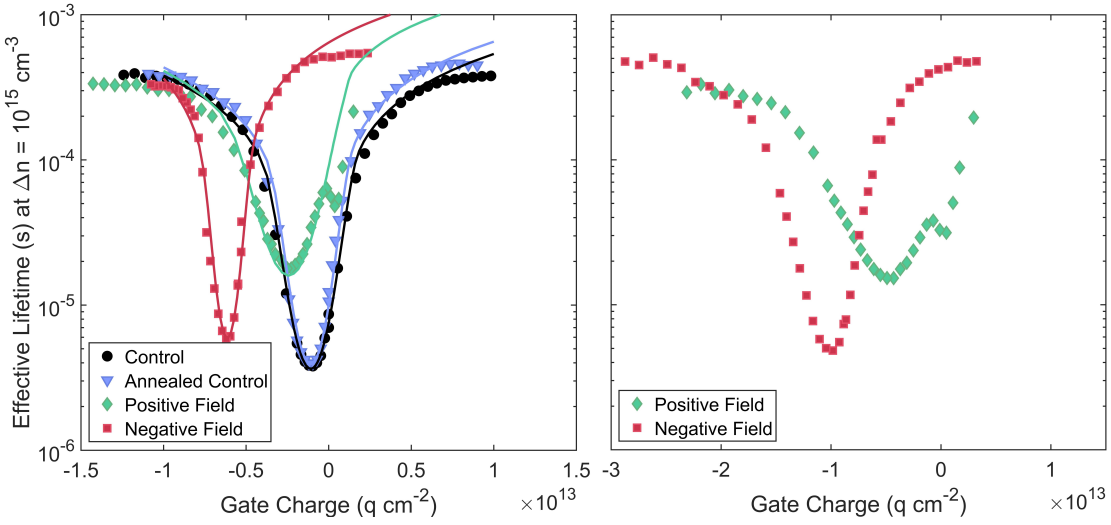

Figure 6.10: (a) Effective lifetime as a function of charge as measured on textured Type C–Ox specimens annealed at 450 °C under positive and negative surface electric fields (b) repeated results for specimens annealed under positive and negative electric fields. The corona charge was deposited at a tip voltage of ±30 kV.

	CONTROL	ANNEALED CONTROL	POSITIVE FIELD	NEGATIVE FIELD
τ_{eff}	Richter's Parametrisation [25]			
SiO_2 Thickness (nm)	5			
Q_f (10^{11} q cm^{-2})	10	11	21	58
σ_q (10^{11} q cm^{-2})	8	7	11	4.5
S_{n0} (cm s^{-1})	26334	22900	16946	17175
S_{p0} (cm s^{-1})	9160	7327	3389	4122
$D_{it,mg}$ (10^{10} cm^{-2}eV^{-1})	100	100	40	60
$D_{it,VB}$, $D_{it,CB}$ (10^{15} cm^{-2}eV^{-1})	8, 20	8, 20	10, 20	5, 20

Table 6.6: Summary of modelling parameters used to fit effective lifetime as a function of gate bias in Figure 6.10a.

With regards to the first question, it is known that hydrogen can be introduced to SiO_2 by water molecules present within the film [64, 277], and also through ions generated by corona discharge [271]. It is therefore not possible to assume zero presence of hydrogen within the system by eliminating the SiN_x capping layer. It is possible that the hydrogen content within Type C–Ox samples responds to surface electric fields. However, the mechanism by which hydrogen passivates the interface is clearly different in Type C–Ox specimens compared to Type C–Ox–Ni specimens, and therefore the inclusion of a SiN_x layer is critical to the observations. It is assumed that without the SiN_x layer, the hydrogen content generated in the SiO_2 layer by corona charges and residual water molecules is much lower. The lack of hydrogen explains the high defect density at the Si-SiO_2 interface of Type C–Ox specimens. The observed improvements in chemical passivation under positive electric fields can be explained by the capturing of the residual hydrogen by defects. The small improvement in chemical passivation observed under negative surface electric fields could be related to the diffusion of neutral hydrogen species to the Si-SiO_2 at elevated temperature.

Concerning the second question, the accumulation of positive dielectric charge after depositing negative corona charge on SiO_2 has been previously reported in [278–280]. It is believed that the positive charge arises from hole trapping at the interface [278–280]. Hole traps are neutral when empty and positively charged when occupied by a hole. These traps are reported to exist in high concentrations at the Si-SiO_2 interface, and are predominantly attributed to strained interfacial bonds [281, 282]. Hole trapping can occur through three primary mechanisms. The first mechanism, portrayed in Figure 6.11a, is through the emission of an electron from a neutral state to the conduction band of SiO_2, which leaves behind a hole [279]. Electron emission from such traps is reported to be the predominant mechanism of creating trapped holes [154]. The second mechanism, shown in Figure 6.11b, is via hot hole injection from the silicon to the SiO_2 [283, 284]. This mechanism becomes more likely with increasing negative field strength to overcome the valence band offset between silicon and SiO_2. The last mechanism,

shown in Figure 6.11c is the direct tunnelling of an electron from a neutral centre to the conduction band of silicon, which leaves behind a positively charged hole trap [279]. This mechanism is dependent upon the alignment of the energy levels, and is restricted to trap centres in very close proximity to the interface [279]. The hole trap generation is reversed once the electric field is removed, and for this reason is discounted as a viable mechanism since the positive dielectric charge exists after the negative corona charge has decayed after annealing.

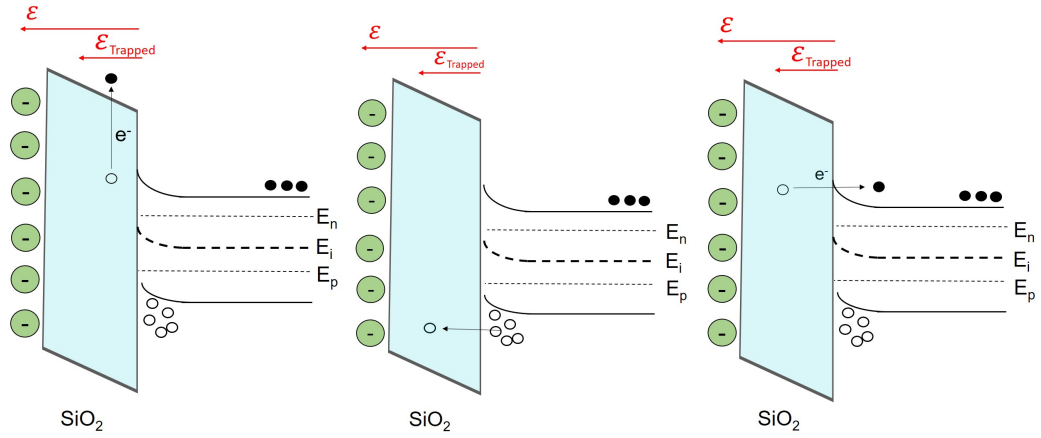

Figure 6.11: Reported mechanisms by which hole traps are generated within SiO_2 under negative surface electric fields (a) electron emission leaving behind a hole trap (b) hole tunelling into SiO_2 following impact ionisation and (c) electron tunneling into the silicon conduction band leaving behind a hole trap.

6.5 Discussion

This chapter demonstrated that the chemical passivation of the Si-SiO_2 interface can be strongly influenced by the polarisation of the dielectric prior to annealing. These findings are of consequence to the processing of industrial solar cells. The ability to modulate not only the surface carrier concentration but the chemical properties of the interface through extrinsic dielectric biasing opens the door to new methods of interface passivation. The unexpected demonstration that surface electric fields can impact the chemical passivation

of an oxide film, without the presence of SiN_x, is also of key importance. These results indicate that any extrinsic charging method must take into account the effect on the interface chemical properties, irrespective of the dielectric in question.

While tailoring the field induced chemical passivation of the Si-SiO_2 interface, it is important to ensure that FEP is not compromised. For Type C–Ox–Ni specimens, annealing under negative surface fields showed clear improvements in the chemical passivation, however, the dielectric charge density decreased. Thus the FEP provided by SiN_x is diminished. Therefore, to maximise both the chemical and field effect passivation, it may be advisable to anneal the SiO_2 surface in the presence of positive surface fields prior to the deposition of SiN_x. Corona charging has been demonstrated in this work to provide a metal-free method of imposing a temporary surface field. As reported in the literature, corona charging cannot be considered a non-invasive technique due to the absorption of corona-generated hydrogenated ions by the dielectric [228, 271]. It is therefore important to clarify in future studies the impact of corona charging on the interface passivation, and whether it can serve as a dependable technique to provide not just charge, but also hydrogen into surface dielectrics.

The use of both single and double layer SiN_x films was also explored in this work. Double layer SiN_x films are widely reported to provide superior passivation by allowing the best optical and chemical properties to be exploited without compromising the synthesis parameters [270, 285–287]. It is reported that high refractive index films provide better chemical passivation due to the greater hydrogen content [159, 270, 288]. Therefore the first layer deposited on the oxide surface is typically silicon-rich [270]. The optical properties of the topmost layer can be optimised independently to produce a highly effective anti-reflective coating [270, 285, 286]. It has been reported in the literature that double layer nitride coatings contain a greater concentration of hydrogen owing to the prevention of out-diffusion by the topmost layer [285, 286]. As a result, more hydrogen is retained close to the silicon surface, and may also diffuse into the silicon bulk [285]. The in-diffusion of hydrogen from SiO_2 into silicon has been reported

to be highly dependent on SiO_2 thickness, where greater hydrogen flux is observed at the interface with thinner oxides [289]. In the case of Type A specimens that had 100 nm thermal oxide capped by a single layer SiN_x film of refractive index 1.9, it is thought that the hydrogen is limited to the Si-SiO_2 interface and does not enter the silicon. As a result, hydrogen effectively passivates silicon dangling bonds under positive surface electric fields [270, 285]. In comparison, a subset of Type C–Ox–Ni1 substrates had a 5 nm SiO_2 film capped by a single layer SiN_x film of refractive index 1.95. Despite the similar SiN_x refractive indices of Type A and Type C–Ox–Ni1, the latter specimens showed degradation in response to positive surface electric fields. Further to the hypothesis that electron injection de-passivates Si–H bonds, it is possible that the oxide properties assist the migration of free hydrogen into bulk under positive surface fields, leaving less hydrogen available to passivate interface defects. Further work is required to understand the dependency of the observed changes in interface passivation on SiN_x and SiO_2 film properties, and silicon surface orientation.

6.6 Summary

This chapter demonstrated that a surface electric field can induce changes in the interface properties of SiO_2 + SiN_x dielectric stack, and that such changes could be related to the hydrogen content of the films. Additionally, it was demonstrated that the observed changes in interface passivation under surface electric fields differ depending on the dielectric properties. The results show that for Type A specimens the presence of positive surface fields during annealing does not affect the density of interface states nor their capture velocities. It only increases the film charge density, at the cost of inhomogeneity. Upon negative corona annealing, the hole capture rates increased fourfold, and the D_{it} by one order of magnitude. For Type C–Ox–Ni2 specimens, the opposite trend was observed where negative surface electric fields resulted in improvements to the chemical passivation of the interface upon annealing, and positive

surface electric fields resulted in degradation. In the case of Type C–Ox–Ni1 specimens, it was observed that the detrimental effect of positive surface fields is minimised in higher refractive (lower density) films, possibly due to greater hydrogen content.

It was also demonstrated that on Si-SiO_2 structures without any SiN_x-related hydrogenation process, the chemical passivation of the interface was also influenced by surface electric fields. It is hypothesised that this is due to the response of hydrogen generated by residual water molecules and corona charges. Further work on this topic should be pursued to provide clarity on the passivation mechanisms at play at the Si-SiO_2 interface, as well the optimal processing of oxidised silicon for the creation of well-passivated interfaces.

It is postulated that the silicon surface orientation and the dielectric film properties could play an important role in the dynamics of hydrogen at the Si-SiO_2 interface. The ability to control hydrogenation has become a key requirement in improving the passivation quality of silicon interfaces, and silicon bulk defects. Here it has been shown that it may be possible to use surface electric fields as a means of regulating hydrogen migration, yet careful attention must be put on the combination of surface orientation, passivating coatings, and charge conditions.

7 | Device Simulations for Integrating Extrinsic Surface Passivation

The prevalent silicon solar cell architecture in today's market is the *passivated emitter and rear cell* (PERC), with just over 50 % of the global market share [290]. The PERC has been extensively studied, and variations in the structure have been proposed to increase efficiency, including the bifacial cell design to increase light trapping, and the use of a selective emitter to reduce contact resistance [291, 292]. Nevertheless, the record efficiency of the PERC has not exceeded 25 % since 1999 [120, 121]. In light of the apparent plateau in PERC efficiency, novel contending architectures, such as *interdigitated back contact* (IBC) and *tunneling oxide passivated contact* (TOPCon), are gaining traction [290]. Despite the relatively recent advent of these technologies, record efficiencies $\geq$26 % have already exceeded that of the PERC [124, 126]. Such high efficiencies have been produced under laboratory conditions that use techniques that are too expensive or time-consuming to be compatible with industry. As a result, commercial cell efficiencies are reported to be $\sim$22 % for all three cell designs [293–297]. To increase the efficiency of mass-produced solar cells, low cost, rapid, and reproducible manufacturing techniques are required.

This thesis has demonstrated that outstanding improvements in surface passivation can be made following the embedding of ionic charge at the Si-SiO_2 interface. Due to the reduced recombination at the silicon surface, as evidenced by the marked reduction in S_{eff}, ion-charged dielectrics are expected to be advantageous to the development of high efficiency solar cells. The techniques used, such as spin coating, corona discharge, and annealing, are all commonplace within industry, and therefore ion-charged dielectrics can be readily integrated into a production line. Furthermore these techniques do not

require vacuum, plasmas, or temperatures above 600 °C. To consolidate the findings of this thesis and demonstrate their applicability, the effects of dielectric charge and interface state density on the performance of PERC, IBC, and TOPCon cells are quantified using the finite element simulation tool, Sentaurus TCAD. Sentaurus determines the electrostatic potential within the silicon from the Poisson equation, and the charge transfer of electrons and holes from the continuity equations [298]. The metrics most commonly used to evaluate the performance of a solar cell are efficiency (η), open circuit voltage (V_{oc}), and short circuit current (J_{sc}). Providing these metrics on their own does not indicate the limiting process or region of the cell. It is therefore important to provide context to demonstrate how improvements in η, V_{oc}, and J_{sc} are related to specific changes in cell design. This chapter studies the change in these metrics as a result of modulating the dielectric charge concentration, or changing the interface properties. In this way, improvements in cell performance can be directly attributed to the influence of field effect passivation of the silicon surface.

7.1 Passivation in Standard PERC Architectures

Studies have shown that it is critical to address the front surface losses within PERC in order to improve the efficiency [294, 299, 300]. Previous work, both experimental and theoretical, has focused on the optimisation of intrinsic dielectric properties and the fine tuning of emitter doping profiles to improve the surface passivation [236, 294, 301]. Via simulations in Sentaurus TCAD, Min et al. showed that the integration of a selective phosphorus emitter can increase solar cell efficiency by 0.71 % [294]. This is supported by experimental results that demonstrate 0.4 % - 0.7 % efficiency gain through the use of a lightly doped emitter with localised heavier doping under the front contacts [302, 303]. By tailoring the properties of the dielectrics at the front surface, the cell performance can be improved further. The use of a SiO_2 + SiN_x stack is essential for efficiencies >24 %, and is becoming more common in industry [53, 214, 294]. The second most

recombination active region is the rear of the cell [300]. The rear silicon surface in a standard PERC is p-type, and is hence passivated by an AlO_x + SiN_x stack that provides excellent chemical passivation through defect hydrogenation, as well as FEP due to the intrinsic negative charge within the AlO_x film [18, 80–82]. The properties of AlO_x are reported to be optimised by using PECVD, with a 0.5 % gain in efficiency reported compared to ALD [87]. To reduce resistivity at the metallised silicon surface, a local p^{++} aluminium back surface field is created to minimise the concentration of electrons [18, 294]. Optimisation of the BSF is reported to increase V_{oc} signficantly by 20 mV due to reduced reduced recombination at the metallised interface [294].

In this section, a detailed examination of how charge at the front and rear silicon surfaces influences device performance is presented. The effect of dielectric charge concentration on efficiency is studied for the front and rear interfaces with a range of defect densities. Figure 7.1 features the standard p-type PERC design and the unit domain modelled in this work. The simulation parameters are provided in Table 7.1, alongside supporting references. The full front finger width was set to 20 μm following recent reports showing that laser doping and electroplating can now produce such narrow fingers [304, 305]. The full rear finger width was set to 60 μm as is standard in the literature [294, 306]. Based on a typical front contact pitch of 1000 μm [294], the simulated domain was set to 500 μm. Figure 7.2 shows the modelled distribution of D_{it} within the band gap. D_{it} at the valence and conduction band was set to 10^{14} cm^{-2} eV^{-1} [307], and D_{it} at the mid-gap was varied between 10^{10} cm^{-2} eV^{-2} and 10^{12} cm^{-1} eV^{-1}.

Based on the given parameters, two PERC structures, termed PERC-1 and PERC-2, were modelled using different diffusion profiles. The set of profiles used in PERC-1 simulations are given in Figure 7.3. The phosphorus profiles used in the formation of the selective emitter are plotted in Figure 7.3a. The lightly doped emitter has a sheet resistance of 380 Ω/sq, and the more heavily doped diffusion under the front contact has a sheet resistance of 74 Ω/sq. At the rear contacts, a local heavily doped aluminium BSF was used, with a sheet resistance of 14 Ω/sq. The aluminium BSF is plotted in Figure

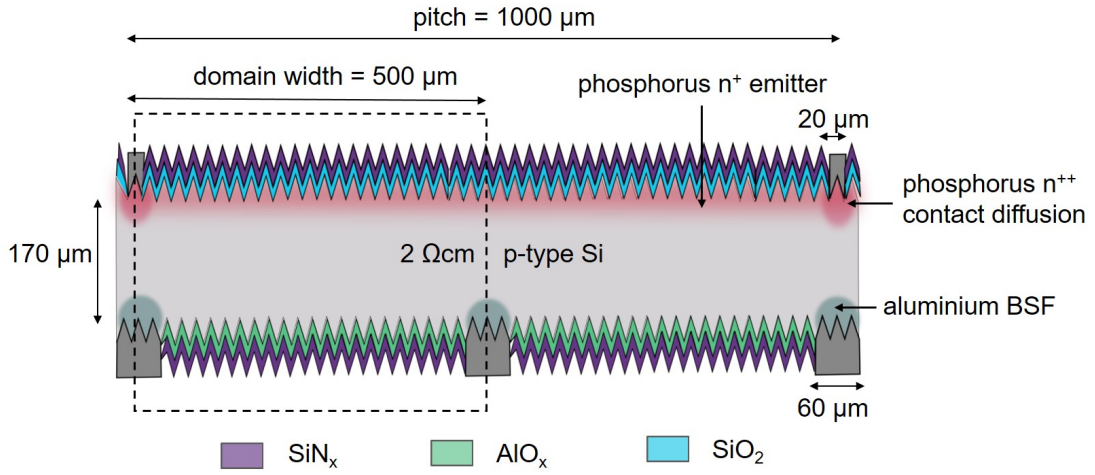

Figure 7.1: Simulation domain and modelled regions of the PERC.

Wafer Thickness	170 μm	-
Bulk Resistivity	2 Ω cm, p-type	[294, 306, 308]
Front Finger Half Width	10 μm	[304, 305]
Rear Finger Half Width	30 μm	[294, 306]
Domain Width	500 μm	[294]
Bulk Lifetime	2 ms	[294]
Front Contact Series Resistance	2 mΩ cm^{-2}	[294, 306]
Rear Contact Series Resistance	2.5 mΩ cm^{-2}	[294, 306]

Table 7.1: Parameters used in Sentaurus TCAD modelling of PERC solar cells, and supporting references.

7.3b. The three doping profiles were reported in reference [294] to contribute to a simulated PERC efficiency of 24.2 %. Such a high efficiency was attained by using optimised experimental data based on state-of-the-art technologies [294]. The sheet resistance of the phosphorus emitter is considerably higher than the average of ∼150 Ω/sq [309]. High sheet resistances are preferred to minimise Auger recombination. The BSF profile was developed from aluminium co-alloyed with <1 wt.% boron. Co-doping

is reported to reduce recombination in the contact region due to lower resistivity [310], but is not a widely used technique.

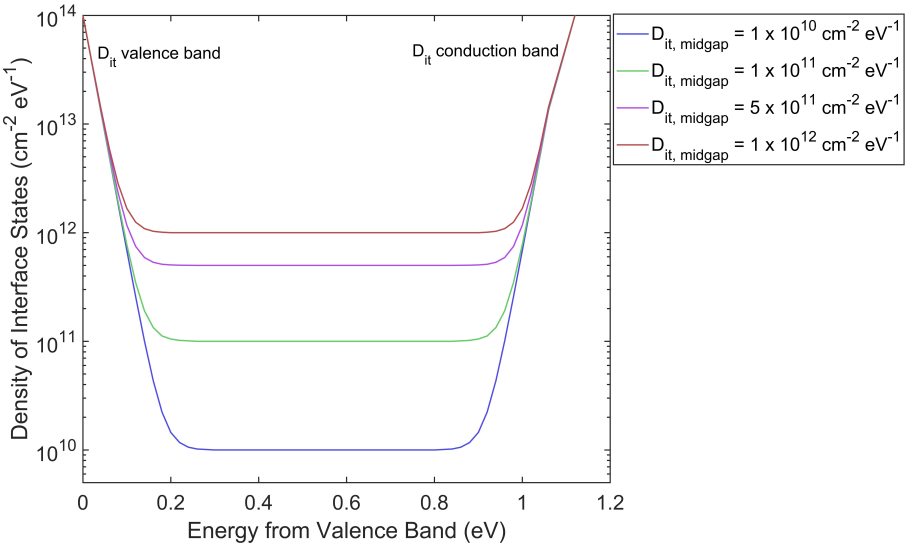

Figure 7.2: Density of interface states distribution at the Si-SiO_2 interface used in PERC simulations.

For the PERC-2 simulation, the rear contact BSF was kept the same, and only the phosphorus diffusions used in the emitter and front contact regions were changed. The diffusion profiles were chosen from the literature to represent those more typically seen within industry to compare the effect of dielectric charge on differently doped emitters. The phosphorus profiles are shown in Figure 7.4. The lightly doped emitter has a sheet resistance of 185 Ω/sq, which is considerately lower than that used in PERC-1 simulations, and closer to the industry average. The heavily doped contact diffusion has a sheet resistance of 70 Ω/sq. Both profiles are reproduced from reference [311], in which they contributed to an experimental cell efficiency of 22.12 %. The lightly-doped phosphorus emitter was produced through a selective etch-back process, which, despite its high cost, is gaining interest due to the absence of surface damage created by the more common laser-doping technique [311–313].

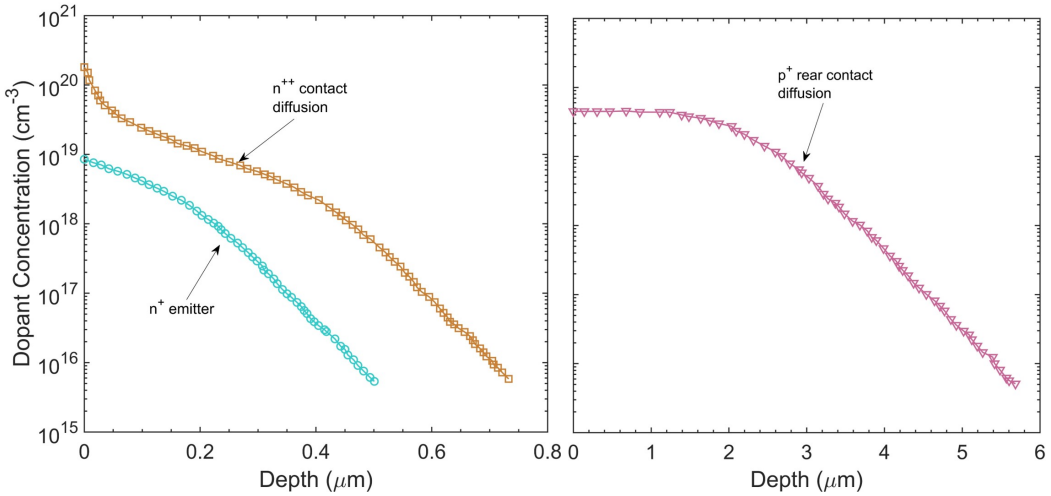

Figure 7.3: Profiles used in PERC-1 simulation (a) phosphorus emitter and front contact diffusion and (b) rear contact aluminium diffusion. Reproduced from [294].

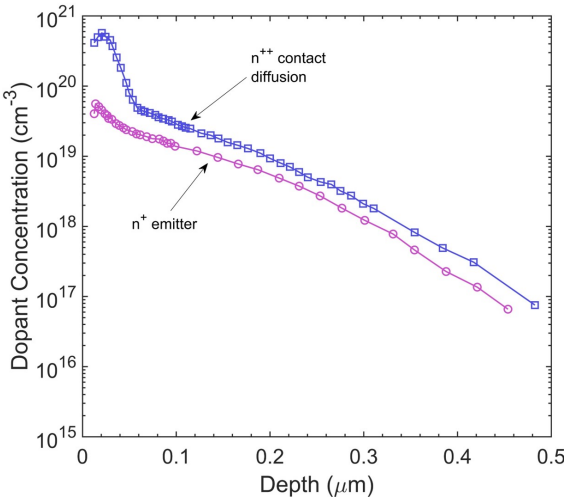

Figure 7.4: Profiles of the phosphorus emitter and front contact diffusion used in the PERC-2 simulation, reproduced from [311].

Figure 7.5 demonstrates the simulated performance of the PERC-1 structure as a function of front dielectric charge. The dielectric charge (Q_f) is positive to create a strong accumulation layer at the interface between SiO_2 and the lightly-doped phosphorus emitter. The rear dielectric has a fixed negative Q_f of -3 x 10^{12} q cm^{-2}, as representative of the typical charge within AlO_x [87, 314], and a standard D_{it} of 10^{11} cm^{-2} eV^{-1} [18, 87, 314]. Figure 7.5a demonstrates the simulated cell efficiency. It is shown that for a front surface with excellent chemical passivation (D_{it} = 10^{10} cm^{-2} eV^{-1}), the contribution from field effect is negligible. At higher defect densities, the requirement for dielectric charge becomes increasingly essential to produce high efficiencies. At the highest D_{it} of 10^{12} cm^{-2} eV^{-1}, the reduction in Q_f to 10^9 q cm^{-2} is responsible for a 0.7 % absolute loss in efficiency. When Q_f is maximised at 10^{13} q cm^{-2}, an efficiency exceeding 24.1 % is calculated for all values of D_{it}, with the highest efficiency of 24.20 % at D_{it} of 10^{10} q cm^{-2}. Such small variation in maximum efficiency demonstrates that the dielectric charge is highly effective at mitigating the recombination activity at interfaces with poor chemical passivation. Figure 7.5b and 7.5c plots the dependency of V_{oc} and J_{sc}. At $D_{it} \leq 10^{11}$ cm^{-2} eV^{-1}, the influence of dielectric charge is negligible. At the highest defect density, a maximum drop in V_{oc} of 11 mV is calculated when Q_f is minimised. J_{sc} is largely unaffected by the front defect density and changes in Q_f. A maximum drop of 0.02 mA cm^{-2} was calculated at D_{it} = 10^{12} cm^{-2} eV^{-1}.

Figure 7.6 plots the performance of the PERC-1 as a function of rear dielectric charge when both the chemical and field effect passivation at the front surface is maximised: D_{it} = 10^{10} cm^{-2} eV^{-1}, Q_f = 10^{13} q cm^{-2}. Here, the rear charge is negative to create an accumulation layer at the interface between AlO_x and the p-type silicon surface. The simulated results for η, V_{oc}, and J_{sc} are plotted Figure 7.6a, 7.6b, and 7.6c, respectively. It can be seen that the performance metrics are more sensitive to changes in Q_f and D_{it} at the rear of the cell than at the front. This indicates that in the absence of FEP, the recombination activity at the rear is higher. This is due to the lack of full coverage BSF, which results in little intrinsic FEP at the rear surface when Q_f is small. A maximum η,

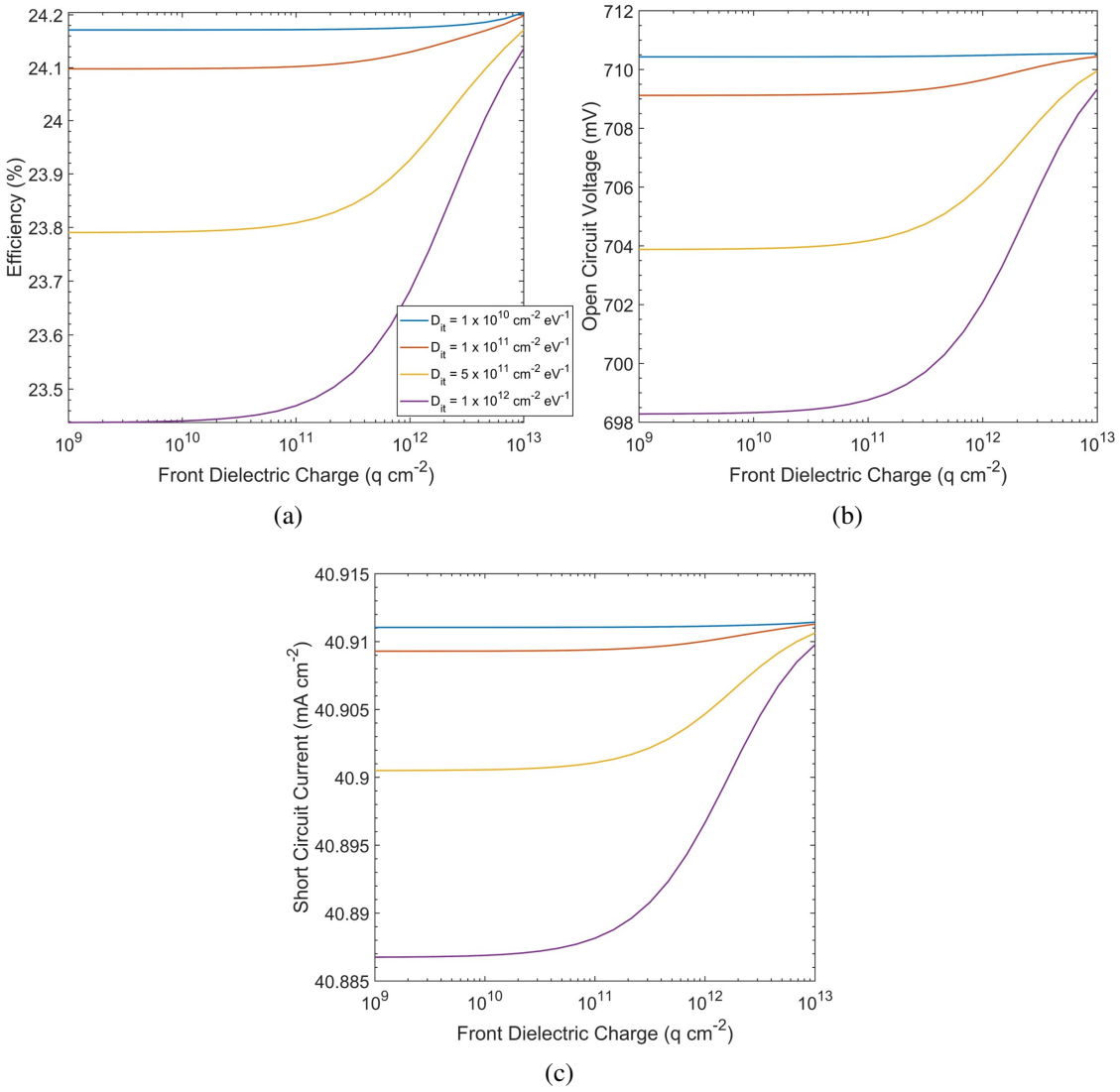

Figure 7.5: Simulated dependency (a) η (b) V_{oc} and (c) J_{sc} as a function of front positive dielectric charge and interface defect density for PERC-1.

V_{oc}, and J_{sc} of 24.25 %, 713 mV and 40.9 mA cm^{-2} were calculated when both chemical and field effect passivation are maximised. For D_{it} $\geq$5 x 10^{11} q cm^{-2}, a drop in η, V_{oc}, and J_{sc} of 6.5 %, 114 mV, and 4 mA cm^{-2} occurs when Q_f is reduced to -10^9 q cm^{-2}. A minimum Q_f $\sim$-10^{11} q cm^{-2} is required before the passivation provided by the electric field is able to counteract the recombination activity at the rear surface. Considering that AlO$_x$ has an intrinsic Q_f of $\sim$-3 x 10^{12} q cm^{-2} [87, 314], the rear interface should

not suffer from substantial recombination losses as the device operates within the high efficiency regime >24 %. Supplementing the charge extrinsically to produce Q_f = -10^{13} q cm^{-1} results in a gain in η and V_{oc} of 0.35 % and 7 mV absolute when D_{it} = 10^{12} cm^{-2} eV^{-1}. At $Q_f \geq -2$ x 10^{12} q cm^{-2}, J_{sc} is saturated at ~40.9 mA cm^{-2}, irrespective of D_{it}.

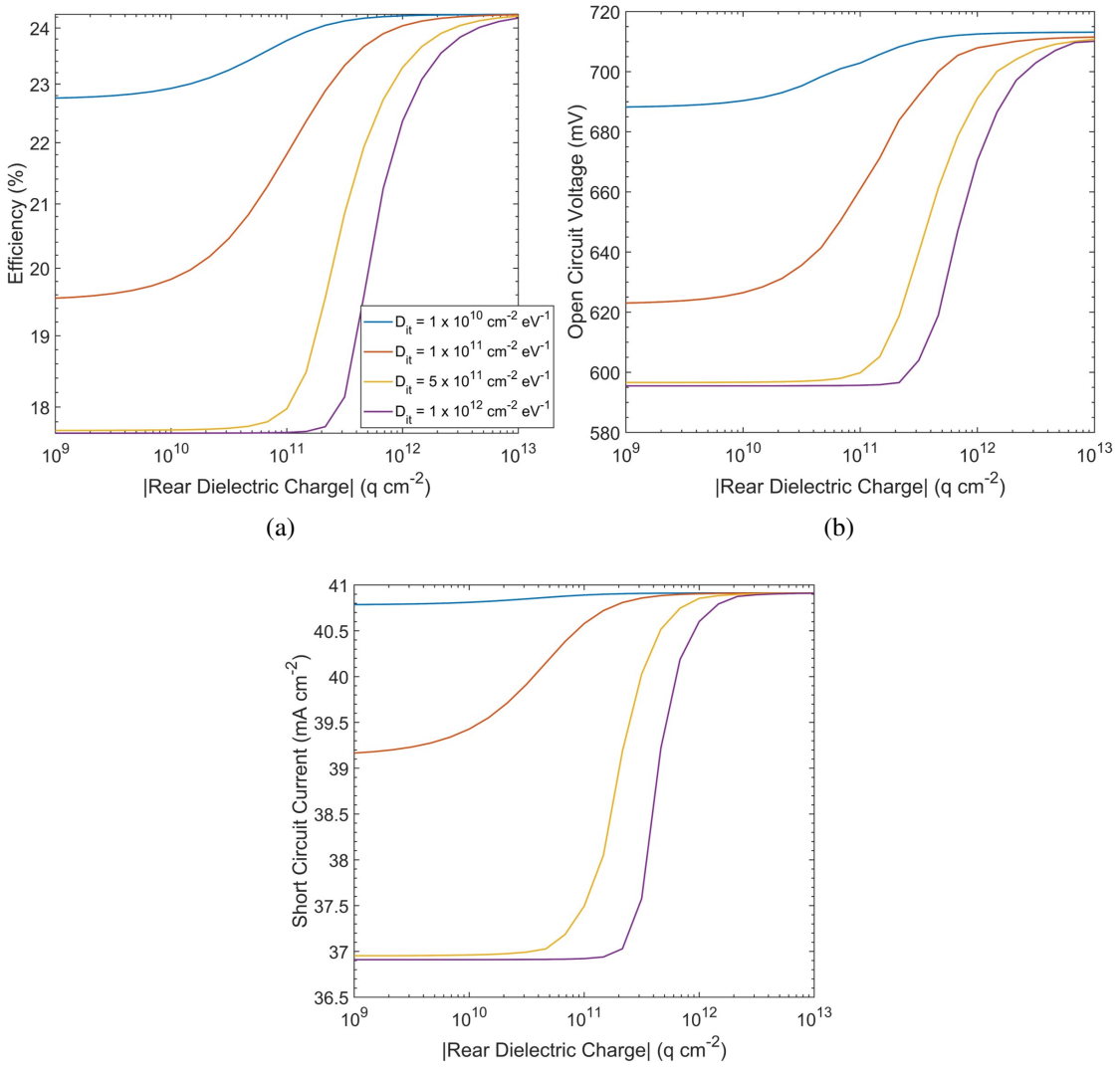

Figure 7.6: Simulated dependency of (a) η (b) V_{oc} and (c) J_{sc} as a function of rear negative dielectric charge and interface defect density for PERC-1.

The performance of the PERC-2 structure was similarly simulated. Figure 7.7 plots η, V_{oc}, and J_{sc} as function of positive front dielectric charge, and defect density. As before, the simulation accounted for a standard negative rear Q_f of -3 x 10^{12} q cm^{-2} and D_{it} of 10^{11} cm^{-2} eV^{-1}. Figure 7.7a plots the dependency of η. When the field effect is optimised at 10^{13} q cm^{-2}, cell efficiencies >24.2 % are achieved irrespective of D_{it}, with a maximum of 24.27 % when chemical passivation is also optimised. At the highest D_{it} of 10^{12} cm^{-2} eV^{-1}, a maximum absolute loss in η of 2.2 % was calculated as the Q_f was reduced to 10^9 q cm^{-2}. At the lowest D_{it}, η has a much smaller dependency on Q_f, as it decreased by a maximum of just 0.05 %. Figure 7.7b and 7.7c plot the dependency of V_{oc} and J_{sc}, respectively. For all values of D_{it}, a maximum of $\sim$710 mV and $\sim$40.9 mA cm^{-2} is predicted when Q_f = 10^{13} q cm^{-2}. As D_{it} becomes greater, the reduction in V_{oc} and J_{sc} becomes more significant as Q_f is reduced. At the highest D_{it} of 10^{12} cm^{-2} eV^{-1}, the V_{oc} drops by 47 mV when Q_f is minimised. At the same defect density, J_{sc} falls by 0.4 mA cm^{-2}.

Figure 7.8 shows the performance of the PERC-2 as a function of rear negative dielectric charge. The passivation of the front surface is fully optimised (D_{it} = 10^{10} cm^{-2} eV^{-1}, Q_f = 10^{13} q cm^{-2}) and the D_{it} at the rear Si-AlO_x interface is varied between 10^{10} cm^{-2} eV^{-1} and 10^{12} cm^{-2} eV^{-1}. Figure 7.8a plots the dependency of η of negative Q_f. When both the front and rear charge are maximised, the highest efficiency was 24.31 %. Similarly to what was observed in PERC-1 simulations, η is more sensitive to changes in Q_f at the rear interface compared to the front. At $D_{it} \geq$ 5 x 10^{11} cm^{-2} eV^{-1}, a significant drop in η of 6.4 % absolute occurs when Q_f is reduced from -10^{13} q cm^{-2} to $\sim$ -10^{11} q cm^{-2}. Decreasing the charge further results in little change. The dependency of η on Q_f reduces as the chemical passivation improves and, at the lowest D_{it}, η falls by a maximum of 1.4 % absolute. The dependency of V_{oc} and J_{sc} is shown in Figures 7.8b and 7.8c. A maximum of 710 mV and 40.9 mA cm^{-2} were calculated irrespective of D_{it}. At $D_{it} \geq$5 x 10^{11} cm^{-2} eV^{-1}, V_{oc} and J_{sc} fall sharply by 114 mV and 4.0 mA cm^{-2} when Q_f is reduced from -10^{13} q cm^{-2} to $\sim$ -10^{11} q cm^{-2}.

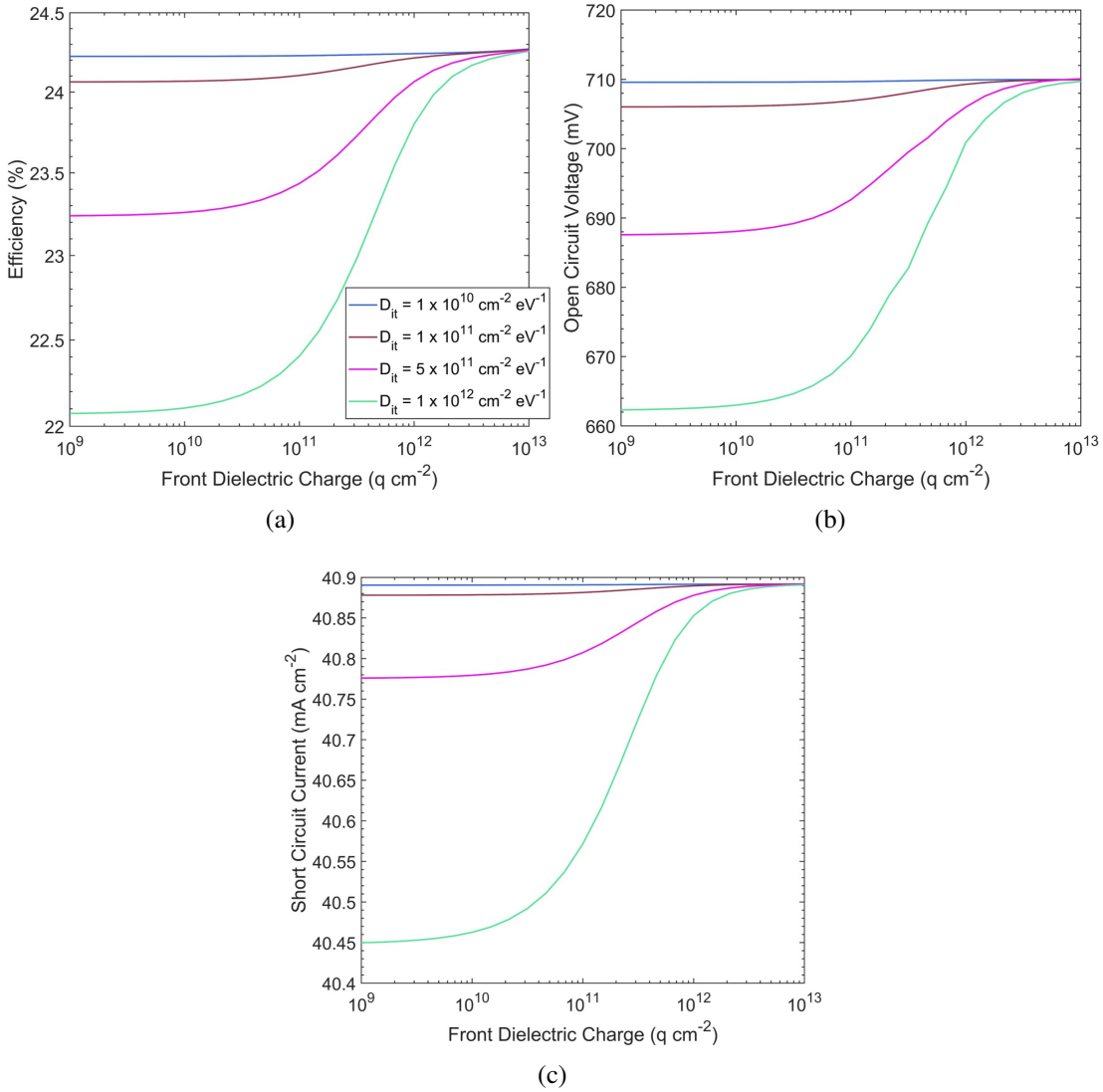

Figure 7.7: Simulated dependency of (a) η (b) V_{oc} and (c) J_{sc} as a function of front positive dielectric charge and interface defect density for PERC-2.

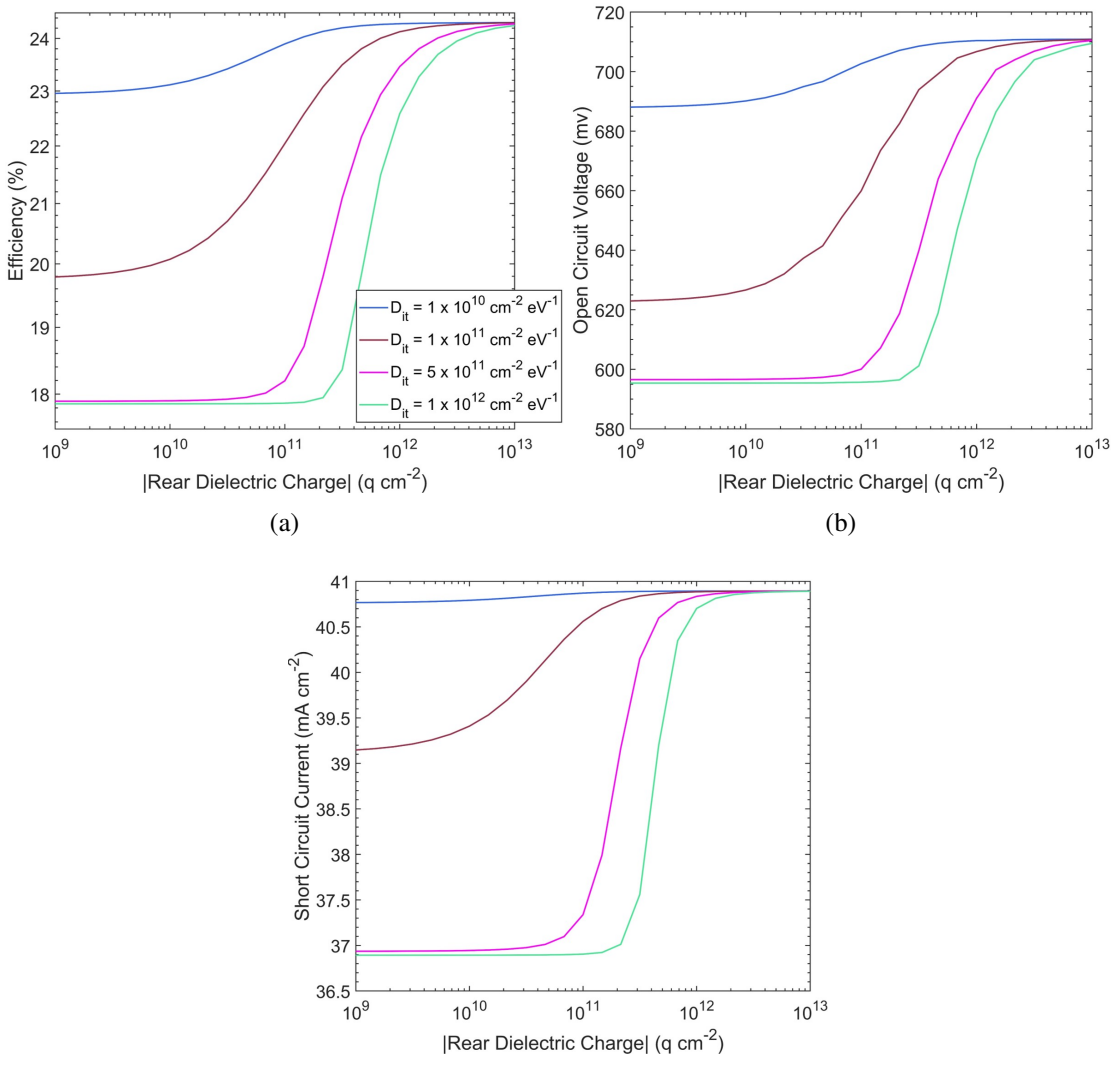

Figure 7.8: Simulated dependency of (a) η (b) V_{oc} and (c) J_{sc} as a function of rear negative dielectric charge and interface defect density for PERC-2.

7.1.1 Discussion

In this section, it was shown that the recombination activity of the front and rear surfaces can be largely mitigated by optimising the electric field within the dielectric. Two different PERC devices were simulated, which differed solely by the diffusion profiles used at the front surface. The profiles integrated into the PERC-1 simulation were state-of-the-art, and are not representative of current industry practice, but of potential future improvements. Such profiles were used to show the improvements that extrinsic FEP can make on surfaces that are already very well passivated. The peak concentration of the lightly doped emitter is 1 to 2 orders or magnitude lower than that of typical profiles published in the literature [301, 311, 315, 316]. The lower dopant density is ideal as it minimises Auger recombination [18, 50], and reduces the risk of an electrically inactive "dead layer" forming due to excess phosphorus, within which SRH recombination dominates [317, 318]. The incorporation of positive dielectric charge in the front dielectric removes the need for a highly doped emitter to create a strong accumulation region, and as such less recombination takes place within the emitter not only due to the modulation of charge carriers but also the absence of dopant-related defects.

The simulation of the PERC-2 used diffusion profiles that are typical within industry [301, 311, 315, 316]. The greater recombination activity within the emitter of the PERC-2 is clear by the lower V_{oc} of 663 mV when Q_f is minimised at D_{it} = 10^{12} cm^{-2} eV^{-1}, compared to 698 mV in the PERC-1. Additionally, J_{sc} of the PERC-2 showed considerably greater sensitivity to the front Q_f compared to the PERC-1. At the maximum defect density, J_{sc} of PERC-1 drops by only 0.02 mA cm^{-2} when Q_f was minimised. For the PERC-1, J_{sc} drops by 0.44 mA cm^{-2}. The greater loss in J_{sc} indicates that, in the absence of FEP, there is reduced conversion efficiency of blue light, which is primarily absorbed by the front of the wafer due to its short wavelength. The emitter peak concentration in the PERC-2 is $\sim$6 times higher than that of the emitter used in the PERC-1 simulation. The greater loss in

cell performance of the PERC-2, as a result of decreasing front Q_f, indicates that the more heavily doped emitter does not deliver as effective surface passivation as the more lightly doped emitter due to Auger and SRH recombination as well as optical losses. However, when the field effect is optimised, both PERC-1 and PERC-2 have very similar maximum cell efficiencies of 24.2 % and 24.3 %, respectively. These results show that extrinsic FEP is able to significantly reduce recombination within the emitter such that a more highly doped emitter can be used to produce high performance solar cells. The difference in 0.1 % efficiency between the two PERC devices can be explained by the finger spacing. Here a standard spacing of 1000 μm was used for both devices. Since the conductivity in the lightly doped emitter of the PERC-1 device is lower than industry standard, a narrower finger spacing may be required to improve the efficiency.

When the front surface passivation is optimised, and a standard Q_f = -3 x 10^{12} q cm^{-2} and D_{it} = 10^{11} cm^{-2} eV^{-1} exist at the rear Si-AlO_x interface [18, 87, 314], the maximum efficiency of PERC-1 and PERC-2 devices is 24.20 % and 24.27 %, respectively. Improving the chemical and field effect passivation at the rear beyond such conditions, does not result in a large increase in efficiency. When both the front and rear passivation is optimised, there is a gain of 0.05 % and 0.04 % for PERC-1 and PERC-2, respectively. These results indicate that the standard condition of the Si-AlO_x interface already provides excellent passivation, and that recombination at the front surface is the limiting factor in cell performance.

In Chapter 5, it was demonstrated that embedding ionic charge within a SiO_2 film significantly improved the surface passivation. The ideal charge concentration was determined to be $\sim$2 x 10^{12} q cm^{-2} since increasing concentration further resulted in an increase in D_{it} and a reduction in τ_{eff}. The results in this section show that even when the defect density at the Si-SiO_2 interface is as high as 10^{12} cm^{-2} eV^{-1}, the presence of dielectric charge is still advantageous to mitigate recombination at chemical defects. In all cases, an optimal Q_f of 10^{13} q cm^{-2} produces the best cell performance metrics. Rapid and low-cost experimental methods of achieving such high charge concentrations

were discussed in Chapters 3 and 4. This section has shown the potential improvements that can result from the incorporation of ionic charge in producing high efficiency PERC devices.

These results also demonstrate the requirement for negative extrinsic charging of the AlO_x film at the rear surface. This is an unexplored area and, to the author's knowledge, no reports exist concerning the extrinsic charging of AlO_x. On other dielectrics, namely SiO_2 and SiN_x, plasma charge injection has been used to embed negative charge in the form of electrons [319, 320]. Using this technique, concentrations of -10^{13} q cm^{-2} have been incorporated. However, it is reported that the passivation provided by a negatively charged SiO_2 + SiN_x stack is not as effective as an intrinsic AlO_x layer [320]. Based on the findings in this chapter, the exploration of extrinsic charging of AlO_x could present new passivation techniques and improved cell performances.

For both PERC-1 and PERC-2 simulations, it can be seen that when the chemical passivation is optimised, the dependency of the performance metrics on front and rear Q_f decreases. Chapter 6 demonstrated that the chemical passivation could be varied by surface electric fields, and it was hypothesised that these changes are due to the response of hydrogen in dielectric layers. Exploiting the intrinsic properties of hydrogenated dielectrics in this way could present new and industrially compatible techniques of reducing D_{it} to 10^{10} cm^{-2} eV^{-1}. It is particularly evident at the rear surface that, when the chemical passivation is maximised, a lower Q_f is required to attain top efficiencies. For example, in the case of the PERC-2 structure, for D_{it} = 10^{10} cm^{-2} eV^{-1} at the rear a minimum Q_f of -3 x 10^{11} q cm^{-2} is required for η > 24.2 %. At D_{it} = 10^{12} cm^{-2} eV^{-1}, the efficiency only exceeds 24.2 % when Q_f = -10^{13} q cm^{-2}. The response of hydrogen to surface electric fields at the Si-AlO_x interface should be explored in future work to optimise both chemical and field effect passivation.

7.2 Front Surface Passivation of IBC Solar Cells

The IBC cell design presents several advantages. Due to the placement of both electron and hole contacts at the rear of the cell, the front surface is fully exposed to incident light. This is reported to result in greater photo-generation, which improves J_{sc} and the output power [321, 322]. Long minority carrier diffusion lengths are essential and, as a result, n-type silicon is typically the base material of choice since it is intrinsically higher performing than p-type, and shows better resistance to impurities and temperature degradation [122, 129, 323, 324].

A standard IBC solar cell was simulated in Sentaurus TCAD to quantify the improvements made by optimising the electric field within the front dielectric. Minimising recombination at the front silicon surface is crucial since it is where the largest portion of minority carriers are generated. Excellent front surface passivation is required to maximise the minority carrier lifetimes for efficient collection at the rear contacts. Figure 7.9 illustrates the IBC design and simulated domain. The simulation parameters are listed in Table 7.2. A typical resistivity of 2 Ω cm was applied to the base silicon [325, 326]. The pitch was set to 600 μm. This is smaller than typically reported pitch sizes of $\sim$1000 μm [327]. Recent studies have shown that decreasing the pitch size leads to improved cell performance [325, 326, 328, 329]. Yang et al. demonstrated experimentally that J_{sc} can be improved by $\sim$21 % by decreasing the pitch size from 1000 μm to 100 μm. Such small pitch sizes of 100 μm can be made under laboratory conditions, however, to be implemented in industry pitch sizes $\sim$600 μm or above are more practical [328]. The widths of the phosphorus BSF and boron emitter were varied in the simulation to maximise the efficiency. An optimal full width of 100 μm and 250 μm was found for the BSF and emitter, respectively. A spacing of 125 μm was placed between the two doped regions. Typically, a smaller spacing between the BSF and emitter is desirable to minimise recombination when there is a high defect density at the rear interface. In this work, the rear silicon surface is optimised such that the D_{it} was

10^{10} cm^{-2} eV^{-1}, as has been reported for high quality passivation of SiO_2 + SiN_x dielectric stacks [18, 330].

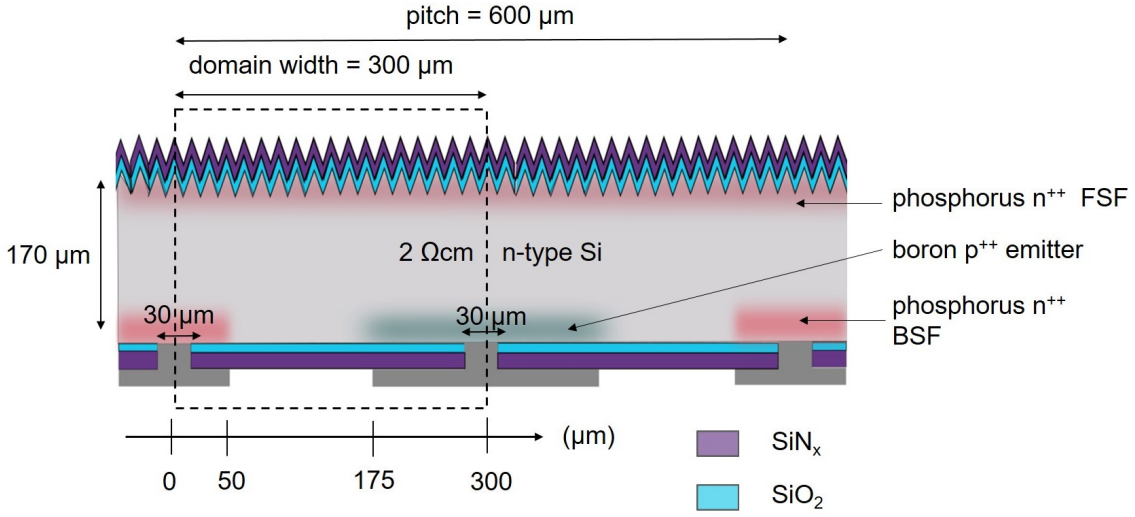

Figure 7.9: Simulation domain and modelled regions of the IBC cell.

Figure 7.10 plots the diffusion profiles used in the simulation of the IBC cell. The phosphorus diffusion used at the front and rear of the cell are shown in Figure 7.10a. A very shallow and lightly doped diffusion with a sheet resistance of 550 Ω/sq, reproduced from [337], was used as the front surface field. Due to the lack of series resistance in the absence of front metal contacts, a homogeneous lightly doped FSF is beneficial to provide good electrical conductivity, and low Auger and SRH recombination. A more concentrated phosphorus diffusion with a sheet resistance of 25 Ω/sq, reproduced from [334], was used as the BSF of the rear electron contact. The boron emitter profile, shown in Figure 7.10b, was reproduced from [338]. This diffusion produced a sheet resistance of 57 Ω/sq.

The distribution of D_{it} at the front Si-SiO_2 interface was the same as within the PERC simulation, shown in Figure 7.2. The rear surface passivation was optimised to have a D_{it} of 10^{10} cm^{-2} eV^{-1}, and Q_f of 10^{12} q cm^{-2}, as is typical in SiN_x films [18, 336]. By optimising the rear, the maximum efficiency of the cell could be calculated when the electrical losses at the front surface are minimal. Figure 7.11 plots the performance

Wafer Thickness	170 μm	-
Bulk Resistivity	2 Ω cm, n-type	[325, 326]
Electron/Hole Contact Half Width	15 μm	[326, 331, 332]
Domain Width	300 μm	[325, 328]
Bulk Lifetime	5 ms	[332, 333]
Electron Contact Series Resistance	2 mΩ cm^{-2}	[334]
Hole Contact Series Resistance	1 mΩ cm^{-2}	[334]
Rear BSF Half Width	50 μm	[335]
Rear Emitter Half Width	125 μm	[335]
SiN_x Charge Concentration	10^{12} q cm^{-2}	[18]
Density of Interface States at Rear Si-SiO_2 Interface	10^{10} cm^{-2} eV^{-1}	[18, 336]

Table 7.2: Parameters used in Sentaurus TCAD modelling of an IBC solar cell, and supporting references.

metrics of the IBC cell as a function of positive charge within the front dielectric. The dependency of η is shown in Figure 7.11a. A maximum η of 25.24 % is achieved at D_{it} = 10^{10} cm^{-2} eV^{-1}. At such high levels of chemical passivation, reducing Q_f negligibly influences η. At higher defect densities, the dependency of η on Q_f increases. A maximum loss of 2.53 % absolute is calculated when the charge is minimised at the highest D_{it}. When the field effect is maximised, the increase in D_{it} from 10^{10} cm^{-2} eV^{-1} to 10^{12} cm^{-2} eV^{-1} results in only a 0.06 % drop in efficiency. This demonstrates the outstanding effect Q_f can have on mitigating the recombination activity at defect-heavy interfaces. The dependency on V_{oc} and J_{sc} is shown in Figure 7.11b and 7.11c, respectively. When Q_f is optimised, a maximum of 715 V and 41.6 mA cm^{-2} is calculated for V_{oc} and J_{sc}, respectively. The maximum V_{oc} and J_{sc} drops by only 0.9 mV

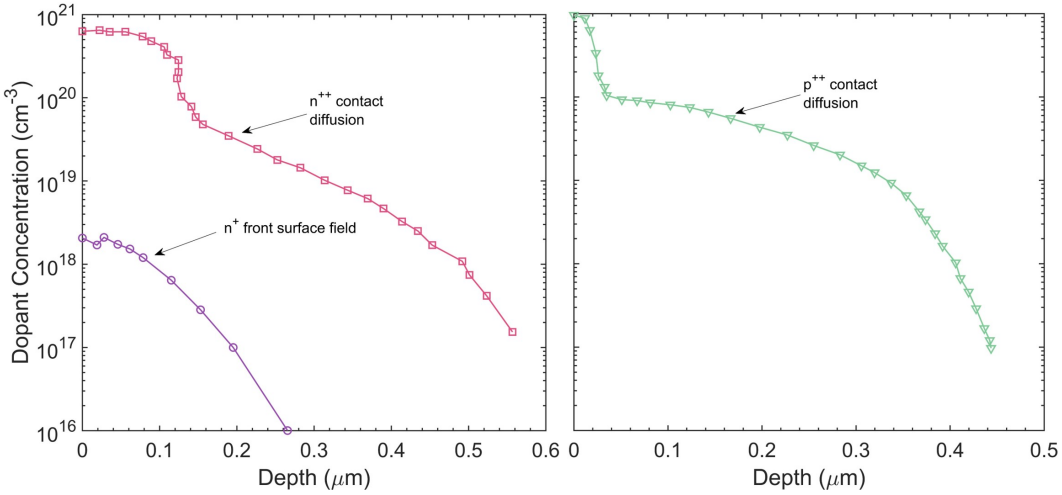

(a) (b)

Figure 7.10: Doping profiles of (a) phosphorus front surface field, reproduced from [337], and the phosphorus back surface field, reproduced from [334] and (b) boron emitter, reproduced from [338].

and 0.03 mA cm^{-2} when D_{it} is increased by two orders of magnitude. Such high values are indicative of very low recombination at the front surface in the presence of a strong positive electric field.

Figure 7.12 compares the cell performance as a function of dielectric charge with and without the presence of a front surface field when the chemical passivation is fully optimised. The dependency of η is shown in Figure 7.12a. When Q_f is maximised, a very similar maximum efficiency of 25.24 % and 25.25 % is achieved with and without the FSF, respectively. When Q_f is minimised, the efficiency drops by 1.54 % absolute in the absence of the FSF. In contrast, when the FSF is present, a decrease is η of just 0.02 % is calculated. The dependency of V_{oc} and J_{sc} are shown in Figures 7.12b and 7.12c, respectively. When the FSF is present, V_{oc} is maintained at ∼714 mV regardless of Q_f, and J_{sc} remains constant at 41.6 mA cm^{-2}. Without the FSF, V_{oc} drops by 8 mV, and J_{sc} by 1 mA cm^{-2} in the absence of strong FEP. These results show that when the dielectric charge is optimised, both devices operate with the high efficiency regime >25.2 %. The incorporation of extrinsic charge could therefore eliminate the requirement for an FSF.

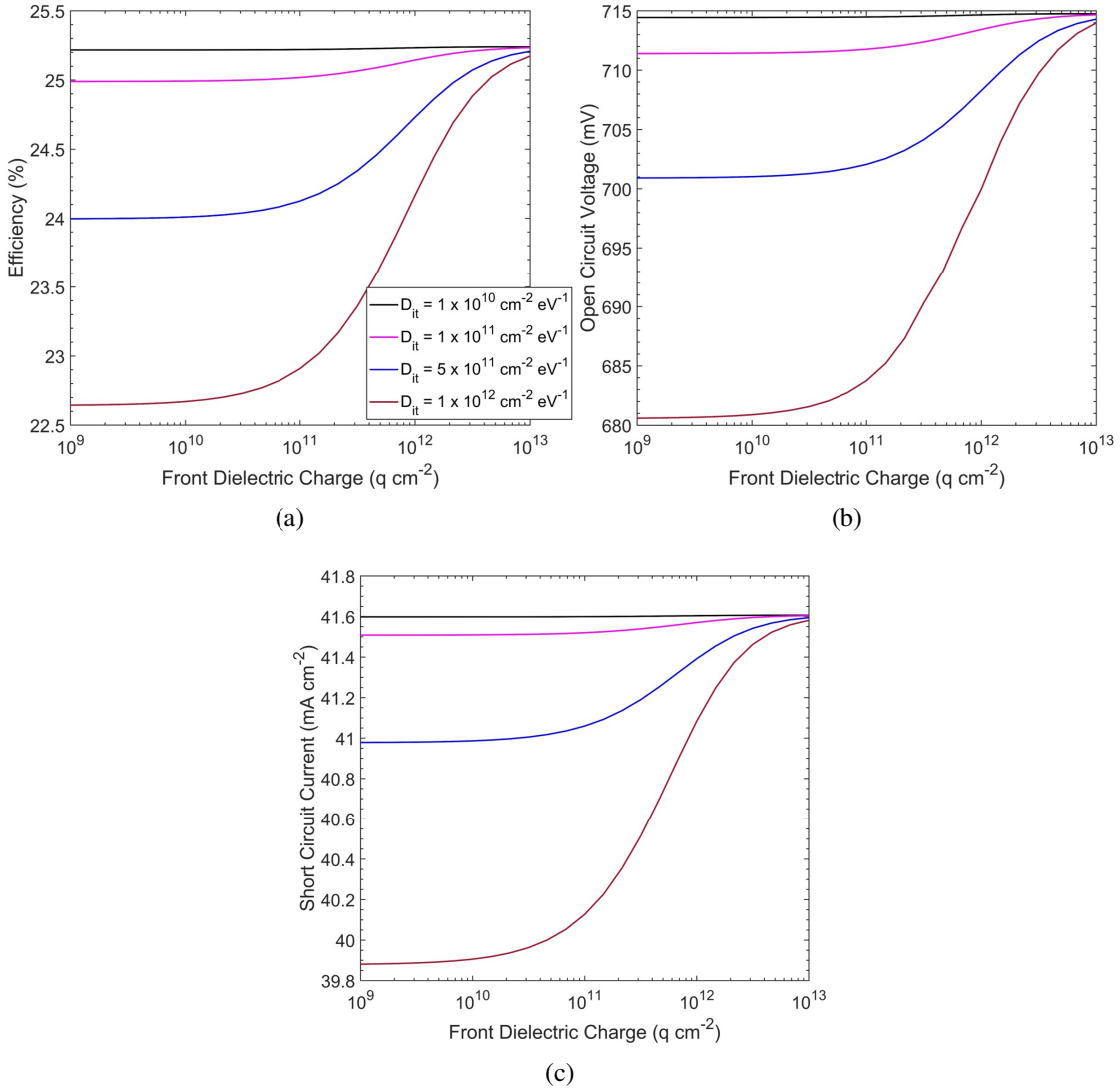

(a) (b)

(c)

Figure 7.11: Simulated dependency of (a) η (b) V_{oc} and (c) J_{sc} as a function of front positive dielectric charge and interface defect density in the IBC cell.

7.2.1 Discussion

The development of IBC cells is currently disadvantaged by their high manufacturing cost, predominantly due to the use of n-type silicon and the multiple photolithography steps required to produce the rear geometry [123, 326]. Therefore new low-cost initiatives to improve the performance of IBC cells are required. Previous experimental work has shown the benefits of applying an extrinsic electric field on the front surface of IBC cells

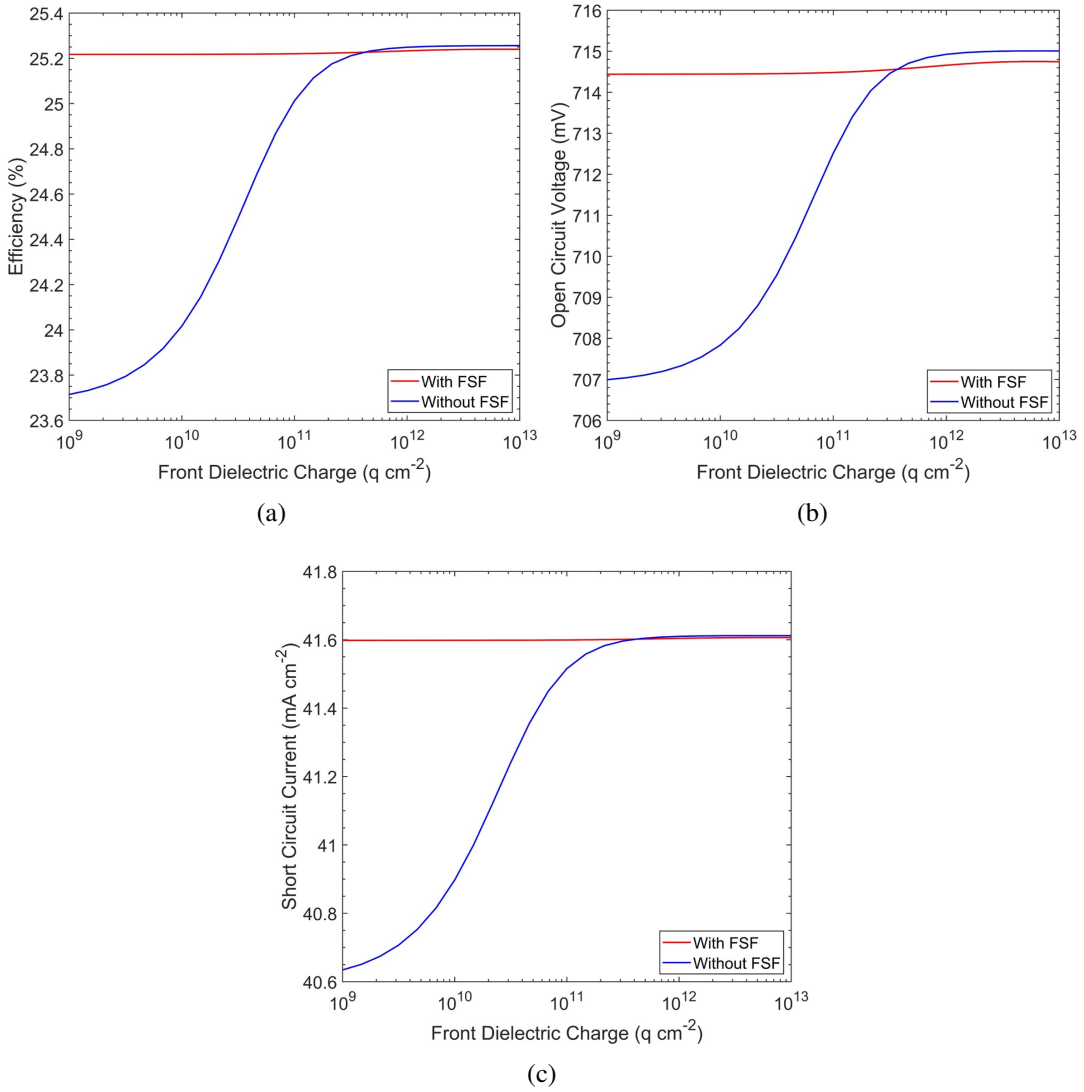

Figure 7.12: Comparison of (a) η (b) V_{oc} and (c) J_{sc} for IBC cells with and without a front surface field, for D_{it} = 10^{10} cm^{-2} eV^{-1}.

by depositing corona charge [94, 100]. Kho et al. demonstrated surface recombination currents as low as 2 fA cm^{-2} when a phosphorus FSF is used in combination with positive corona charging of the front dielectric [94]. Corona charging is unlikely to be integrated into commercial production lines due to instability [43, 101, 104]. Embedding ionic charge within the dielectric to provide a durable electric field could be an effective and practical alternative. The methods presented in this thesis of introducing K^+, Rb^+ and Cs^+

ions used low-cost, industrially compatible techniques, and as such could be exploited to produce high charge density dielectrics.

One of the most effective and low-cost improvements made to the standard IBC cell design is the integration of a heterojunction at the rear [44, 124]. The heterojunction is formed by a thin hydrogenated amorphous silicon layer, which provides very good passivation of the silicon surface. Additionally, the phosphorus and boron localised diffusions are replaced by segmented p-doped and n-doped amorphous silicon. The manufacturing of the heterojunction is highly compatible with pre-existing industry practices and uses relatively low processing temperatures of 200 °C, which is significantly lower than typical temperatures of ∼850 °C used to create traditional diffusions [44, 45, 47, 311, 328]. Due to reduced rear recombination, this cell design has led to the record efficiency of 26.7 %, and a V_{oc} and J_{sc} of 738 mV and 42.7 mA cm^{-2} [124, 125]. The simulation in this section did not incorporate a heterojunction, and therefore leads to lower top efficiencies. A maximum η, V_{oc}, and J_{sc} of ∼25.2 %, ∼714 mV, and ∼41.6 mA cm^{-2}, respectively, were predicted irrespective of interface defect density for the IBC cell simulated in this work. Combining the excellent passivation provided by the heterojunction rear with the extrinsic FEP of the front surface could lead to further improvements in efficiency. This should be explored in future work.

Compared to PERC-1 and PERC-2 devices, the performance of the IBC cell is superior. The maximum efficiency when chemical and field effect passivation are fully optimised is ∼1 % higher. The maximum V_{oc} of the IBC surpasses that of the PERC simulations by less that 4 mV. This indicates that the there is only small contribution to carrier collection in IBC cells when the passivation is optimised. The improved cell efficiency can be mostly attributed to the gain in maximum J_{sc} of 0.7 mA cm^{-2}. The higher J_{sc} of the IBC cell is due to the increase in photo-generated carriers in the absence of front contacts [321, 322, 339]. These results indicate that the improved performance of IBC cells is primarily due to the greater light exposure. The short circuit current of the IBC cell shows a greater dependency on front Q_f compared to PERC-1 and PERC-2. At the maximum defect

density, J_{sc} drops by 1.7 mA cm^{-2} compared to 0.02 mA cm s^{-2} for PERC-1 and 0.44 mA cm^{-2} for PERC-2. The greater loss in J_{sc} of IBC cells is due to the greater distance that charge carriers have to travel to arrive at the metal contacts, which means that the performance is more sensitive to carrier lifetimes.

It was shown that extrinsic FEP can serve very effectively as a replacement for the FSF. When Q_f is optimised, a very similar cell performance is predicted. As there are no metal contacts on the front surface, lateral conductivity at the front surface is not required. The accumulation layer provided by extrinsic charge is sufficient to minimise recombination at the front surface through modulation of the charge carrier concentrations. These results are particularly consequential to low-cost manufacturing. The replacement of a high temperature phosphorus diffusion with the lower temperature, rapid introduction of ionic charge could be highly desirable.

7.3 Front Surface Passivation of TOPCon Solar Cells

The TOPCon cell architecture is predicted to become a strong competitor to the mainstream PERC design in the upcoming years [43, 297, 340]. Similarly to IBC cells, the standard TOPCon design uses n-type base silicon. As of 2018, n-type silicon solar cells make up only 5 % of the PV market share, however, by 2030 the n-type share is forecast to be >40 % [309, 324]. The International Technology Roadmap for Photovoltaic (ITPRV) report predicts that this 40 % share will be dominated by TOPCon technology [309]. Due to the increasing use of n-type silicon, and the similarity to the PERC design, the TOPCon cell is well-suited to existing production lines.

The dominant loss in TOPCon cell performance is reported to occur in the emitter [341–343]. Simulation studies have shown that if recombination can be suppressed in the emitter, a gain in efficiency of 0.6 % can be achieved [341]. Extensive experimental studies of various boron diffusions within the emitter region have demonstrated that the V_{oc} is maximised for lightly doped diffusions with a deep junction depth $\geq$1 μm [342].

In this section, recombination within the emitter is reduced by incorporating negative charge within the front dielectric layer to create a hole-rich accumulation layer.

Figure 7.13 exhibits the TOPCon design and simulated domain. The simulation parameters and supporting references from the literature are given in Table 7.3. Due to the simulation set-up and the lack of data concerning the distribution of D_{it} at the rear interface, the capture velocity of electrons and holes (S_{n0} and S_{p0}) was used instead as the variable parameter to define the passivation quality. At the front surface, S_{n0} was varied between 10^2 cm s^{-1} and 10^5 cm s^{-1}. The value of S_{p0} was varied with S_{n0} at a factor of 10 difference [18]. At the rear Si-SiO_x interface, S_{n0} and S_{p0} were fixed at 7 x 10^3 cm s^{-2} and 7 x 10^2 cm s^{-2}, respectively, following [344, 345]. The charge in the rear dielectric was kept fixed at 10^{12} q cm^{-2}, as is typical in SiN_x films [18].

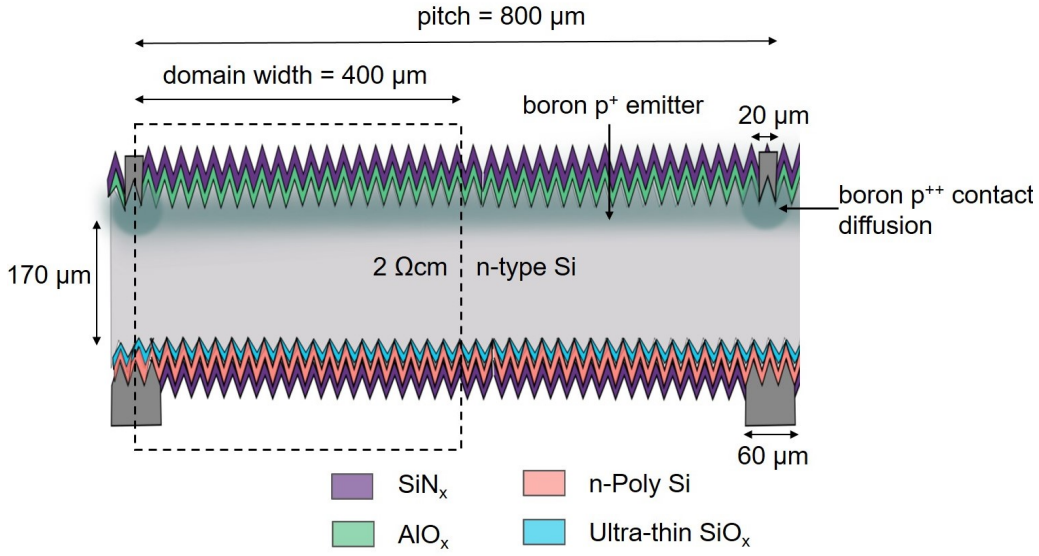

Figure 7.13: Simulation domain and modelled regions of the TOPCon cell.

The full rear surface is passivated by a 1 nm ultra-thin SiO_x layer. It is well-reported that electrons are able to tunnel through thin oxides $\sim$1 nm thick [350, 352, 353]. Tunnelling oxides have a low resistance to electrons due to the lower injection barrier of 3.1 eV compared to that of 4.5 eV for holes [351, 352, 354]. The transport of holes is further impeded by the highly conductive phosphorous doped poly-silicon layer on top of the

Wafer Thickness	170 μm	-
Bulk Resistivity	2 Ω cm, n-type	[346]
Front Finger Half Width	10 μm	[304, 305]
Rear Finger Half Width	30 μm	[294, 306]
Domain Width	400 μm	[347]
Bulk Lifetime	5 ms	[348]
Front Contact Series Resistance	1 mΩ cm^2	[342, 346]
Rear Contact Series Resistance	2 mΩ cm^2	[346]
Ultra-thin SiO_x Thickness	1 nm	[349, 350]
n-poly Si Thickness	30 nm	[349]
Electron/Hole Tunnelling Mass	0.5	[351]
S_{n0} Si-SiO_x Interface	7 x 10^3 cm s^{-1}	[344]
S_{p0} Si-SiO_x Interface	7 x 10^2 cm s^{-1}	[344, 345]
SiN_x Charge Concentration	10^{12} q cm^{-2}	[18]

Table 7.3: Parameters used in Sentaurus TCAD modelling of a TOPCon cell, and supporting references.

oxide. The doping profile of the n-poly silicon layer is shown in Figure 7.14a. The layer is 30 nm thick with a doping of 4.54 x 10^{20} cm^{-3} and a sheet resistance $\sim$170 Ω/sq. This profile was reported to produce a surface saturation current density (J_{0s}) of 6 fA cm^{-2} [349]. As is typically observed after high temperature doping, the phosphorus diffuses a small distance into the crystalline silicon wafer [349, 352]. The high concentration and sharp drop in doping results in strong band bending in very close proximity to the rear silicon surface. It has been calculated that such a high doping concentration >10^{19} cm^{-3} within the n-poly silicon layer is equivalent to a charge concentration >10^{12} q cm^{-2}

[351]. The strong electric field generated by the n-poly silicon layer is therefore highly effective at minimising carrier recombination at the rear through FEP. A selective emitter is applied at the front surface. Figure 7.14b plots the lightly doped boron diffusion used as the emitter, and the more heavily doped boron diffusion under the front contact. The lighter diffusion has a sheet resistance of 180 Ω/sq, and is reproduced from [346]. It was reported to produce an emitter saturation current density (J_{0e}) of ∼12 fA cm^{-2} [346]. The heavier doped contact diffusion has a sheet resistance of ∼72 Ω/sq, and is reproduced from [342]. This was reported to produce a J_{0e} in the metallised region of ∼40 fA cm^{-2} [342].

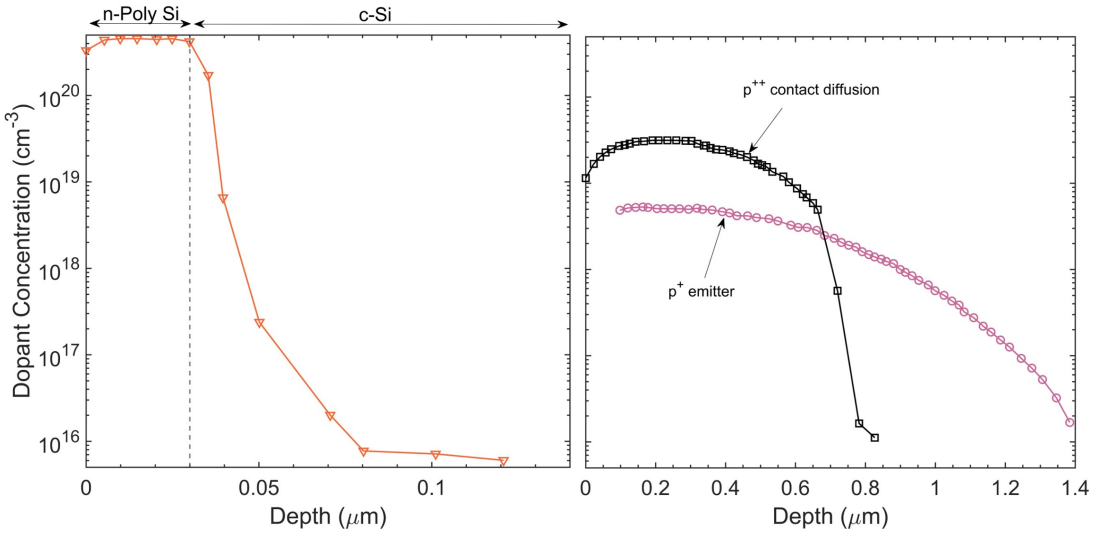

Figure 7.14: Profiles of (a) phosphorus diffusion extending from the n-poly silicon layer into the rear silicon bulk, reproduced from [349] and (b) boron emitter and local front contact diffusions, reproduced from [346] and [342], respectively.

Figure 7.15 plots the simulated cell performance metrics as a function of negative charge concentration within the front dielectric, where S_{n0} is varied between 10^2 cm s^{-1} and 10^5 cm s^{-1}. The dependency of η, V_{oc}, and J_{sc} are shown in Figures 7.15a, 7.15b, and 7.15c, respectively. It can be seen that the best performance is achieved when Q_f = -10^{13} q cm^{-2}. A maximum η, V_{oc}, and J_{sc} of 24.62 %, 723 mV and 40.0 mA are calculated when S_{n0} is minimised. At such low values of 10^2 cm s^{-1}, varying Q_f has negligible effect due to low

recombination at chemical defects. As S_{n0} increases, the requirement for FEP becomes more essential to produce high performance. Provided that $S_{n0} \leq 10^4$ cm s^{-1}, maximising Q_f leads to high cell efficiencies exceeding 24.1 %. At the highest S_{n0} of 10^5 cm s^{-1}, a significant reduction in cell performance occurs even when the electric field is maximised. For such conditions, the highest η, V_{oc}, and J_{sc} are 22.5 %, 681 mV, and 39.6 mA cm^{-2}, respectively. When Q_f is reduced to -10^9 q cm^{-2}, a minimum of 18.9 %, 629 mV, and 36.5 mA cm^{-2} are calculated.

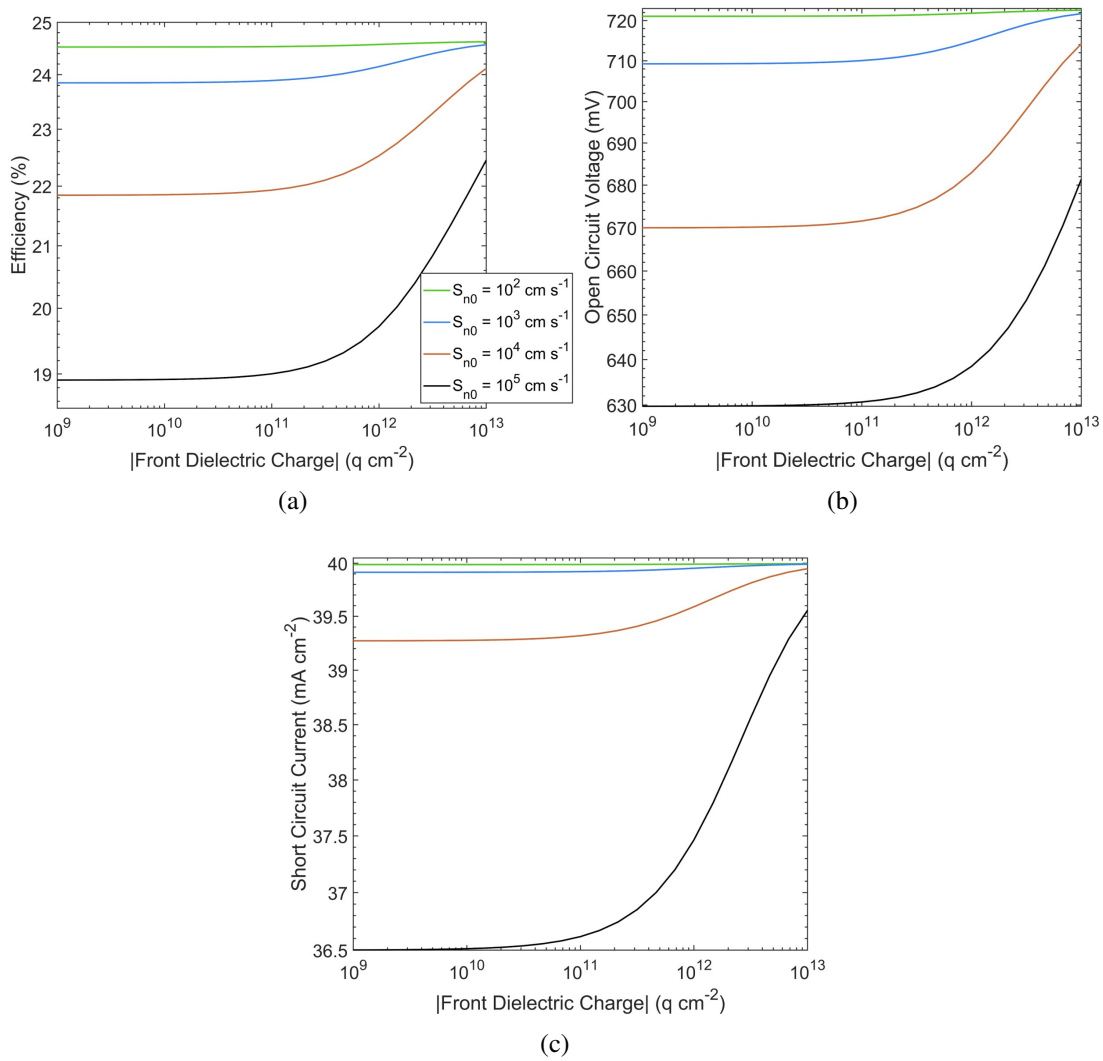

Figure 7.15: Simulated dependency of (a) η (b) V_{oc} and (c) J_{sc} as a function of front negative dielectric charge and interface defect density for the TOPCon cell.

7.3.1 Discussion

The industrial mass manufacturing of TOPcon cells has recently taken off [297]. Since 2019, the highest reported industrial efficiency has increased rapidly from 23.6 % to 25.25 % [297, 355]. A direct comparison between the results in this work and those within industry is not possible as data are often undisclosed. However, the simulated efficiencies >24 % in this work appear to be within the industrial-grade range. Within industry there is a strong incentive to improve the surface passivation through the use of lowly doped emitters [309, 342, 356]. Lowly doped emitters benefit from low Auger and SRH recombination but, due to the lower majority carrier concentration, the intrinsic FEP at the silicon surface is reduced. Currently, the average sheet resistance of a boron emitter is $\sim$100 Ω/sq [309]. Following predictions in [309], the sheet resistance is expected to increase over the coming years as selective emitters become more common and advances in metallisation techniques improve the contact formation [357]. This work used an emitter with a sheet resistance of 180 Ω/sq [346]. The results in this section demonstrate the need for extrinsic FEP to compensate the reduction in doping concentration that is projected in the future. In the absence of dielectric charge, the performance of the TOPCon cell is limited by the low intrinsic field effect of the boron emitter as the efficiency falls between 0.7 % and 3.5 % absolute for S_{n0} between 10^3 cm s^{-1} and 10^5 cm s^{-1}.

Typical capture velocities for AlO_x passivated boron emitters are reported to be on the order of 10^3 cm s^{-1} [345, 358–361]. Considering that AlO_x has an intrinsic Q_f $\sim$-3 x 10^{12} q cm^{-2}, when Q_f is supplemented extrinsically to reach the optimal -10^{13} q cm^{-2}, an absolute gain in η of 0.1 % is predicted when S_{n0} = 10^3 cm s^{-1}. It is likely that industrial techniques will use lower quality passivation techniques for mass production, and as a result S_{n0} will be greater than 10^3 cm s^{-1}. In such a case, supplementing the intrinsic charge can improve η by 0.8 % and 1.6 % absolute when S_{n0} is 10^4 cm s^{-1} and 10^5 cm s^{-1}, respectively. This translates to an increase in V_{oc} of 16 mV and 28 mV. Similarly to

the discussion in Section 7.1.1, these predictions require the exploration of negative extrinsic charging techniques of dielectric films. As currently extrinsic charging techniques of AlO_x films have not been developed, control of the chemical passivation may present a more suitable method to improve performance. The use of surface electric fields to influence the chemical passivation of the front Si-AlO_x interface should be studied in further work, and could lead to new methods to control the effects of hydrogen. If the minority capture velocity can be sufficiently controlled, research-grade chemical passivation could become standard in industry practice.

7.4 Summary

This chapter explored the influence of dielectric charge on improving the performance of standard PERC, IBC, and TOPCon cells. For all cell architectures, it was demonstrated that the optimal performance is achieved when $Q_f = \pm 10^{13}$ q cm^{-2}. A maximum efficiency of 24.31 %, 25.24 %, and 24.62 % was achieved for PERC, IBC, and TOPCon cells, with maximum V_{oc} and J_{sc} exceeding 710 mV and 40 mA cm^{-2}. In the case of PERC and IBC cells, the incorporation of such concentrations was sufficient to offset the recombination at front and rear surfaces with poor chemical passivation, with little change in maximum efficiency between D_{it} of 10^{10} cm^{-2} eV^{-1} and 10^{12} cm^{-2} eV^{-1} when field effect was optimised. The TOPCon results demonstrated greater sensitivity to the chemical passivation as the maximum efficiencies varied between 0.06 % and 2.2 %, depending on the minority capture velocity, S_{n0}.

Extrinsic charging has thus far been neglected in industry due to the inability to stabilise the charge. The work in this thesis on extrinsic FEP demonstrated the significant improvement that ion-charged dielectrics can have on minority carrier lifetimes, as well as the industrial compatibility of the incorporation techniques. The simulation studies performed in this chapter consolidate this work by showing the advantageous impact that both positive and negative extrinsic charge can have on solar cell performance. The role

of extrinsic FEP is also increasingly relevant as emitter diffusions become lighter in the next few years, resulting in weaker accumulation regions at the silicon surface. Future work is necessary to deliver controllable and industrially feasible techniques of incorporating negative charge within dielectrics.

8 | SUMMARY AND FUTURE DIRECTIONS

8.1 Determining Alkali Ion Dynamics in SiO_2

In line with industrial initiatives, a low-cost, rapid, and versatile method of incorporating alkali ions into SiO_2 was used in this thesis. Following the deposition of ionic precursors, the ions on the SiO_2 surface were migrated during high temperature anneals to the Si-SiO_2 interface under a positive electric field provided by corona charge. Experimental results showed that the concentration of ions at the interface could be controlled by varying the strength of the corona-induced electric field, or the annealing duration and temperature. This work demonstrated for the first time that alkali ions larger than K^+ are mobile within SiO_2, and respond to such stimuli. A novel and comprehensive model was presented that accurately predicted the experimental findings by simulating the injection of ions at the air-SiO_2 interface, and their subsequent drift under a variable electric field. From this model, the activation energies of injection and diffusion for K^+, Rb^+, and Cs^+ ions could be determined. This is the first time that the activation energy of these ions has been modelled at a metal-free (air-SiO_2) interface, and the first time the activation energies of Rb^+ and Cs^+ ions have determined experimentally. It was concluded that the rate of ion injection is independent of the electric field strength, and that the variation in ion kinetics is due to the electrostatics governing the drift velocity.

The ability to control the charge concentration within a dielectric presents new avenues of exploration across the semiconductor industry. The built-in electric field of ion-charged dielectrics can be beneficial to the development of low power consumption devices that typically rely upon DC biasing to attain the same electrical conditions. As was demonstrated in this thesis, the electric field generated by ion-charged dielectrics

can be used to modulate the concentration of charge carriers at the silicon surface, and effectively prevent electron-hole recombination. The passivation performance of ion-charged dielectrics on silicon surfaces is summarised next.

8.2 The Importance of Extrinsic FEP in Surface Passivation

It was demonstrated that ion-charged dielectrics can provide very high quality surface passivation at the silicon surface. A maximum τ_{eff} of 2.42 ms, 2.81 ms, and 1.86 ms was recorded on silicon wafers passivated by K^+, Rb^+, and Cs^+ ion-charged oxide films, respectively. These lifetimes are equivalent to S_{eff} as low as 2.80 cm s^{-1}, 2.23 cm s^{-1}, and 4.02 cm s^{-1}. The optimal concentration of ions within the dielectric was determined to be $\sim$1.5 x 10^{12} q cm^{-2}. It was found that the passivation is limited by the generation of interface defects that are generated as a consequence of the ions themselves. A study of the defect density at the Si-SiO_2 interface in the presence of increasing ionic charge confirmed that the higher the concentration and the larger the ionic radius, the greater the generation of defects. It was postulated that defects are induced by strain and distortion of the interfacial oxide matrix in response to excess ions, and to ionic size.

In addition to high performance, an important metric for any passivation technique is durability. It was confirmed via CV measurements that the physical presence of K^+, Rb^+, and Cs^+ ions at the Si-SiO_2 interface was undisturbed by exposure to elevated temperatures and UV radiation. However, the passivation performance declined, as evidenced by a loss in τ_{eff} and an increase in interface defect density. In view of reports that SiN_x provides a highly effective barrier against radiation-induced defects, it is possible that the deposition of SiN_x may serve as a protective layer that helps to maintain the initial passivation. Due to equipment constraints, this could not be studied in this work, but should certainly be explored in the future.

A clear advantage of the use of larger alkali ions was demonstrated following the reverse biasing of ion-charged oxides at elevated temperatures. Of the three ions, K^+ demonstrated the poorest resistance, and was unable to withstand an electric field of -10^5 V cm^{-1}. Rb^+ ions were able to withstand a stronger electric field of -5×10^5 V cm^{-1} for a minimum of 60 minutes at 200 °C. Cs^+ ions demonstrated superior endurance by withstanding the strongest electric field of -10^6 V cm^{-1} at 200 °C. These findings indicate that despite the very high passivation provided by K^+ ion-charged dielectrics, they may not be suitable for solar cells under operational and field conditions. Rb^+ and Cs^+ ions may serve as a more suitable alternative to provide durable field effect passivation.

The importance of extrinsic charge in producing high efficiency solar cells was studied through simulations using Sentautus TCAD. It was demonstrated that charge concentrations of 10^{13} q cm^{-2} are optimal to maximise the efficiency of the PERC, IBC, and TOPCon cells. It was shown that at such high charge concentrations, the recombination activity at defect heavy interfaces is significantly reduced, and almost equivalent in cell performance to surfaces with D_{it} and S_{n0} as low as 10^{10} cm^{-2} eV^{-1} and 10^2 cm s^{-1}. The necessity for extrinsic FEP is likely to become more essential in order to supplement the loss in the intrinsic electric field as the average sheet resistance of emitters increases, as predicted, over the next few years. Additionally, in IBC cells, it was demonstrated that extrinsic FEP could serve as an effective replacement of the front surface field, which would minimise dopant-related recombination. The use of ionic charge to provide the necessary surface electric field could potentially serve as an industrially attractive technique to minimise cost and power-consumption relative to high temperature diffusions.

8.3 Influence of Surface Electric Fields on the Chemical Passivation of Si-SiO_2 Interfaces

The Si-SiO_2 interface is commonly improved via hydrogen passivation following the deposition of dielectrics such as SiN_x and AlO_x. It is also well-reported that hydrogen can induce defects at the silicon surface and within the bulk. Therefore, the ability to control hydrogen within the dielectric–silicon system would be advantageous to better exploit its passivation performance. In this work, it was demonstrated that the chemical passivation of the interface could be modulated depending on the polarity and strength of the bias applied to the dielectric surface during annealing. Due to ability of hydrogen to assume different charge states, it is hypothesised that the changes in chemical passivation are due to the response of charged hydrogen to the surface electric field. Different Si-SiO_2-SiN_x sample structures were tested where characteristics such as surface orientation and dielectric properties were changed. It was determined that observed changes in chemical passivation depend strongly on the specific structure. In planar (100) structures, positively polarising the dielectric surface during the anneal resulted in no change in chemical passivation, however, following negative polarisation, a significant increase in defect density and capture velocities was observed. In textured (111) structures, the opposite trend was seen where negative surface fields resulted in improvements to the chemical passivation, and positive fields resulted in degradation. A study of the dielectric film properties revealed that the refractive index of the SiN_x film is a significant factor to consider. It was observed that the harmful effects of positive charging were minimised in films with higher refractive indices. It is postulated that this may be due to the variation in hydrogen content that is reported to depend on the film's chemical composition.

An interesting and unexpected finding of this work was that in the absence of a hydrogenated dielectric, the chemical passivation of a Si-SiO_2 interface could still be

impacted by surface electric fields. It is hypothesised that this may be due to the response of residual hydrogen within the oxide film as well as hydrogen generated by corona charges. It was observed that the changes in chemical passivation due to the surface field differed depending on whether the same specimen was capped with a SiN_x layer or not. Further work should be carried out to clarify the source of hydrogen within dry thermal oxides, as well as the passivation mechanisms under electric fields. These findings may present new avenues of surface passivation, and may be indicative of the optimal processing procedure to fully exploit the benefits of extrinsic charging.

8.4 Future Work

This thesis has shown that high quality surface passivation can be achieved through the use of ion-charged dielectrics. Due to the demonstrated durability of ions at the Si-SiO_2 interface and the use of industrially prevalent techniques, ion-charged dielectrics are expected to be highly compatible with existing solar cell production lines. Additionally, this thesis explored how extrinsic charge can influence the chemical passivation of the Si-SiO_2 interface. The optimisation of both chemical and field effect passivation of the silicon surface could lead to further improvements in solar cell performance. Based on the findings presented in this work, nine key areas for future research are identified:

1. The model of alkali ion dynamics presented in the work demonstrated very good reproducibility of experimental results. Due to the lack of data available, the reported mobility of K^+ ions with SiO_2 was used for Rb^+, Cs^+ ions. To further improve the accuracy of the model, experimental values of mobility for ions larger than K^+ should be determined.

2. K^+, Rb^+, and Cs^+ ions showed excellent physical endurance at the Si-SiO_2 interface under elevated temperatures and UV radiation. Additionally, the larger ions demonstrated resistance to strong reverse biases. However, the passivation performance was not stable during accelerated ageing due to the generation of

defects. It is expected that SiN_x would serve effectively as a protective layer against the harmful effects of operational and field conditions. The passivation performance and durability of ion-charged oxides capped by SiN_x should be explored in further work.

3. Ionic precursors were delivered to the SiO_2 surface using thermal evaporation and spin coating techniques. Although thermal evaporation is common within the semiconductor industry at large, it is rarely used within the PV industry. Spin coating and spray coating are more prevalent. Due to the lack of available equipment, spray coating could not be performed. In the future, spray coating should be studied as an alternative deposition technique to determine if uniform ion-charged oxides can be produced with dependable passivation. Versatility is key for industry production, and the ability to deposit precursors using a range of techniques is advantageous.

4. The *in situ* delivery of Cs^+ ions during oxidation was shown to work successfully. Further optimisation of the precursor solution and process conditions is required to introduce controlled concentrations of ionic charge. Additionally, the high level of contamination is crucial to address before the surface passivation performance can be studied. It is strongly recommended that oxidation is performed under clean room conditions to minimise contamination.

5. Various hypothesised mechanisms were presented to explain the field-induced chemical passivisation changes observed in this work. It was demonstrated that both the dielectric properties and the surface orientation of the silicon surface influenced the chemical passivation. Due to equipment constraints, limited work could be performed on planar (100) specimens. To understand further the importance of surface orientation, parallel experiments should be performed on both planar and textured specimens to clarify how the different orientations combined with variations in the dielectric properties can influence the suspected

hydrogen behaviour.

6. Simulation studies of PERC and IBC cells showed that the cell performance is maximised when n-type silicon is passivated by a dielectric containing a charge of $+10^{13}$ q cm^{-2}. This thesis demonstrated that such concentrations can be achieved within SiO_2 by varying the corona charge concentration and annealing conditions, however, the generation of defects due to excess ions > 2 x 10^{12} cm^{-2} limited the surface passivation performance. It is therefore necessary for future research to focus on methods to mitigate defect generation. It is possible that capping ion-charged oxides with SiN_x may provide effective hydrogen passivation to de-activate defects. The combination of ion-charged dielectrics and hydrogenation should be explored in further work.

7. Simulations of PERC and TOPCon cells demonstrated that increasing the negative charge within surface dielectrics to concentrations of -10^{13} q cm^{-2} could lead to improvements in cell performance. Very little research has been conducted on extrinsic negative charging, and as such novel explorations of this concept would be of great interest to the PV industry.

8. To maximise the passivation of both p-type and n-type surfaces, the response of hydrogen within AlO_x films should be explored. The typical reported values of D_{it} at the Si-AlO_x interface are $\sim 10^{11}$ cm^{-2} eV^{-1}. Controlling the hydrogenation of the interface through surface fields could reduce the D_{it} further. Simulated PERC and TOPCon cells showed that when the chemical passivation is optimised, the efficiency is predicted to exceed 24.5 %, and that requirement for FEP is less critical to obtain such high performance.

9. It was demonstrated through simulation studies of IBC cells that the electric field provided by extrinsic charging of the front dielectric could serve as a highly effective replacement for the phosphorus doped front surface field. Methods of ion introduction are expected to be lower in cost and and energy consumption

compared to high temperature diffusions, and as such could be very attractive to industry production. The use of extrinsic FEP as an alternative to a front surface field should be explored in future work.

References

[1] Z. Li, L. Guo, Y. Sha, and K. Yang, "Knowledge Map and Global Trends in Extreme Weather Research from 1980 to 2019: A Bibliometric Analysis", *Environmental Science and Pollution Research*, pp. 1–19, 2021.

[2] IPCC Working Group III, "Climate Change 2014-Mitigation of Climate Change: Summary for Policymakers", 2014.

[3] I. Global, "Energy Transformation: A Roadmap to 2050", 2018.

[4] N. N. C. for Environmental Information, "State of the Climate: Global Climate Report for Annual 2020", 2020.

[5] M. Davis and S. Clemmer, "How Climate Change Puts Our Electricity at Risk", *Union of Concerned Scientists: Cambridge, MA, USA*, 2014.

[6] BP Global, "BP Statistical Review of World Energy June 2017", 2017.

[7] "Fraunhofer ISE: Photovoltaics Report", 2019, updated: 14 March 2019.

[8] IEA, "Renewables 2019", 2019. [Online]. Available: `https://www.iea.org/reports/renewables-2019`.

[9] IRENA, "Future of Solar Photovoltaic: Deployment, Investment, Technology, Grid Integration and Socio-Economic Aspects", *International Renewable Energy Agency, Abu Dhabi*, 2019.

[10] IEA, "Global Energy Review 2020", 2020. [Online]. Available: `https://www.iea.org/reports/global-energy-Review-2020`.

[11] REN21, "Renewables 2019 Global Status report", 2019.

[12] A. Jäger-Waldau, "Snapshot of Photovoltaics - February 2019", *Energies*, vol. 12, no. 5, p. 769, 2019.

[13] A. Jäger-Waldau *et al.*, "PV Status Report 2019", *Publications Office of the European Union: Luxembourg*, 2019.

[14] S. A. Mann, M. J. de Wild-Scholten, V. M. Fthenakis, W. G. van Sark, and W. C. Sinke, "The Energy Payback Time of Advanced Crystalline Silicon PV Modules in 2020: A Prospective Study", *Progress in Photovoltaics: Research and Applications*, vol. 22, no. 11, pp. 1180–1194, 2014.

[15] S. Rühle, "Tabulated Values of the Shockley-Queisser Limit for Single Junction Solar Cells", *Solar Energy*, vol. 130, pp. 139–147, 2016.

[16] J. Nelson, *The Physics of Solar Cells*. World Scientific Publishing Company, 2003.

[17] M. A. Green, "Silicon Solar Cells Advanced Principles & Practice, Centre for Photovoltaic Devices and Systems university of New South Wales Sydney", *NSW*, vol. 2052, 1995.

[18] A. G. Aberle, *Crystalline Silicon Solar Cells: Advanced Surface Passivation and Analysis*. Centre for Photovoltaic Engineering. University of New South Wales, 1999.

[19] H. Schlangenotto, H. Maeder, and W. Gerlach, "Temperature Dependence of the Radiative Recombination Coefficient in Silicon", *physica status solidi (a)*, vol. 21, no. 1, pp. 357–367, 1974.

[20] J. Dziewior and W. Schmid, "Auger Coefficients for Highly Doped and Highly Excited Silicon", *Applied Physics Letters*, vol. 31, no. 5, pp. 346–348, 1977.

[21] J. Schmidt, M. Kerr, and P. P. Altermatt, "Coulomb-Enhanced Auger Recombination in Crystalline Silicon at Intermediate and High Injection Densities", *Journal of Applied Physics*, vol. 88, no. 3, pp. 1494–1497, 2000.

[22] E. Yablonovitch and T. Gmitter, "Auger Recombination in Silicon at Low Carrier Densities", *Applied Physics Letters*, vol. 49, no. 10, pp. 587–589, 1986.

[23] A. Hangleiter and R. Häcker, "Enhancement of Band-to-Band Auger Recombination by Electron-Hole Correlations", *Physical Review Letters*, vol. 65, no. 2, p. 215, 1990.

[24] P. P. Altermatt, J. Schmidt, G. Heiser, and A. G. Aberle, "Assessment and Parameterisation of Coulomb-Enhanced Auger Recombination Coefficients in Lowly Injected Crystalline Silicon", *Journal of Applied Physics*, vol. 82, no. 10, pp. 4938–4944, 1997.

[25] A. Richter, S. W. Glunz, F. Werner, J. Schmidt, and A. Cuevas, "Improved Quantitative Description of Auger Recombination in Crystalline Silicon", *Physical Review B*, vol. 86, no. 16, p. 165 202, 2012.

[26] W. Shockley and W. Read, "Statistics of the Recombination of Electrons and Holes", *Physical Review*, vol. 87, pp. 835–842, 1952.

[27] R. N. Hall, "Electron-Hole Recombination in Germanium", *Physical Review*, vol. 87, no. 2, p. 387, 1952.

[28] S. S. Li, *Semiconductor Physical Electronics*. Springer Science & Business Media, 2012.

[29] J. Li, L. Song, X. Yu, and D. Yang, "Effects of Iron Contamination and Hydrogen Passivation on the Electrical Properties of Oxygen Precipitates in CZ-Si", *Journal of Electronic Materials*, vol. 47, no. 9, pp. 5039–5044, 2018.

[30] B. Hallam, C. Chan, M. Abbott, and S. Wenham, "Hydrogen Passivation of Defect-Rich N-Type Czochralski Silicon and Oxygen Precipitates", *Solar Energy Materials and Solar Cells*, vol. 141, pp. 125–131, 2015.

[31] L. Chen, X. Yu, P. Chen, P. Wang, X. Gu, J. Lu, and D. Yang, "Effect of Oxygen Precipitation on the Performance of Czochralski Silicon Solar Cells", *Solar Energy Materials and Solar Cells*, vol. 95, no. 11, pp. 3148–3151, 2011.

[32] R. J. Falster, M. Cornara, D. Gambaro, M. Olmo, and M. Pagani, "Effect of High Temperature Pre-Anneal on Oxygen Precipitates Nucleation Kinetics in Si", in *Solid State Phenomena*, Trans Tech Publ, vol. 57, 1997, pp. 123–128.

[33] B. J. Hallam, P. G. Hamer, S. R. Wenham, M. D. Abbott, A. Sugianto, A. M. Wenham, C. E. Chan, G. Xu, J. Kraiem, J. Degoulange, *et al.*, "Advanced Bulk Defect Passivation for Silicon Solar Cells", *IEEE Journal of Photovoltaics*, vol. 4, no. 1, pp. 88–95, 2013.

[34] T. Niewelt, J. Schön, W. Warta, S. W. Glunz, and M. C. Schubert, "Degradation of Crystalline Silicon Due to Boron–Oxygen Defects", *IEEE Journal of Photovoltaics*, vol. 7, no. 1, pp. 383–398, 2016.

[35] A. G. Aberle, "Surface Passivation of Crystalline Silicon Solar Cells: A Review", *Progress in Photovoltaics: Research and Applications*, vol. 8, no. 5, pp. 473–487, 2000.

[36] J. I. Pankove and N. M. Johnson, *Hydrogen in Semiconductors*. Academic Press, 1991, pp. 35–47.

[37] K. L. Luke and L.-J. Cheng, "Analysis of the Interaction of a Laser Pulse with a Silicon Wafer: Determination of Bulk Lifetime and Surface Recombination Velocity", *Journal of Applied Physics*, vol. 61, no. 6, pp. 2282–2293, 1987.

[38] A. Sproul, "Dimensionless Solution of the Equation Describing the Effect of Surface Recombination on Carrier Decay in Semiconductors", *Journal of Applied Physics*, vol. 76, no. 5, pp. 2851–2854, 1994.

[39] K. R. McIntosh and L. E. Black, "On Effective Surface Recombination Parameters", *Journal of Applied Physics*, vol. 116, no. 1, p. 014 503, 2014.

[40] R. S. Bonilla, B. Hoex, P. Hamer, and P. R. Wilshaw, "Dielectric Surface Passivation for Silicon Solar Cells: A Review", *physica status solidi (a)*, vol. 214, no. 7, p. 1 700 293, 2017.

[41] J. Schmidt, M. Kerr, and A. Cuevas, "Surface Passivation of Silicon Solar Cells using Plasma-Enhanced Chemical-Vapour-Deposited SiN Films and Thin Thermal SiO_2/Plasma SiN Stacks", *Semiconductor Science and Technology*, vol. 16, no. 3, p. 164, 2001.

[42] H. Wagner, A. Dastgheib-Shirazi, B. Min, A. E. Morishige, M. Steyer, G. Hahn, C. del Cañizo, T. Buonassisi, and P. P. Altermatt, "Optimizing Phosphorus Diffusion for Photovoltaic Applications: Peak Doping, Inactive Phosphorus, Gettering, and Contact Formation", *Journal of Applied Physics*, vol. 119, no. 18, p. 185 704, 2016.

[43] G. M. Wilson, M. Al-Jassim, W. K. Metzger, S. W. Glunz, P. Verlinden, G. Xiong, L. M. Mansfield, B. J. Stanbery, K. Zhu, Y. Yan, *et al.*, "The 2020 Photovoltaic Technologies Roadmap", *Journal of Physics D: Applied Physics*, vol. 53, no. 49, p. 493 001, 2020.

[44] A. Louwen, W. Van Sark, R. Schropp, and A. Faaij, "A Cost Roadmap for Silicon Heterojunction Solar Cells", *Solar Energy Materials and Solar Cells*, vol. 147, pp. 295–314, 2016.

[45] J. Mandelkorn and J. H. Lamneck Jr, "A New Electric Field Effect in Silicon Solar Cells", *Journal of Applied Physics*, vol. 44, no. 10, pp. 4785–4787, 1973.

[46] A. Kaminski, B. Vandelle, A. Fave, J. Boyeaux, R. Monna, D. Sarti, A. Laugier, *et al.*, "Aluminium BSF in Silicon Solar Cells", *Solar Energy Materials and Solar Cells*, vol. 72, no. 1-4, pp. 373–379, 2002.

[47] C. Duran, T. Buck, R. Kopecek, J. Libal, and F. Traverso, "Bifacial Solar Cells with Boron Back Surface Field", in *25th European Photovoltaic Solar Energy Conference and Exhibition, Valencia*, 2010.

[48] M. Li, B. Hoex, F.-J. Ma, K. Devappa Shetty, A. Aberle, and S. Ganesh, "Modelling and Characterisation of BBr_3 Boron Diffusion Process for N-Type Si Wafer Solar Cells", in *31st European Photovoltaic Solar Energy Conference and Exhibition*, 2015.

[49] H. Ghembaza, A. Zerga, R. Saım, and M. Pasquinelli, "Optimization of Phosphorus Emitter Formation from $POCl_3$ Diffusion for P-Type Silicon Solar Cells Processing", *Silicon*, vol. 10, no. 2, pp. 377–386, 2018.

[50] J. G. Fossum, F. A. Lindholm, and M. A. Shibib, "The Importance of Surface Recombination and Energy-Bandgap Narrowing in pn-Junction Silicon Solar Cells", *IEEE Transactions on Electron Devices*, vol. 26, no. 9, pp. 1294–1298, 1979.

[51] A. G. Aberle, "Overview on sin Surface Passivation of Crystalline Silicon Solar Cells", *Solar Energy Materials and Solar Cells*, vol. 65, no. 1-4, pp. 239–248, 2001.

[52] S. Zhang, Y. Yao, D. Hu, W. Lian, H. Qian, J. Jie, Q. Wei, Z. Ni, X. Zhang, and L. Xie, "Application of Silicon oxide on High Efficiency Monocrystalline Silicon PERC Solar Cells", *Energies*, vol. 12, no. 6, p. 1168, 2019.

[53] S. W. Glunz and F. Feldmann, "SiO_2 Surface Passivation Layers - A Key Technology for Silicon Solar Cells", *Solar Energy Materials and Solar Cells*, vol. 185, pp. 260–269, 2018.

[54] G. Thareja, "Surface Passivation and Junction Engineering in Silicon/Germanium Metal-Oxide-Semiconductor Field-Effect-Transistors for High Performance Application", PhD thesis, Stanford University, 2011.

[55] S. Bae, R. Hillard, C. Olsen, M. Benjamin, S. Thirupapuliyur, N. Ho, and P. Kraus, "Interface Trap Characterization of Alternate Gate Dielectrics with Elastic Gate MOS Metrology", in *AIP Conference Proceedings*, American Institute of Physics, vol. 788, 2005, pp. 191–193.

[56] H. Mueller and M. Schulz, "Individual Interface Traps at the Si—SiO_2 Interface", *Journal of Materials Science: Materials in Electronics*, vol. 6, no. 2, pp. 65–74, 1995.

[57] S. Franssila, *Introduction to Microfabrication*. John Wiley & Sons, 2010.

[58] K. L. Kishore and V. Prabhakar, *VLSI design*. IK International Pvt Ltd, 2013.

[59] S. M. Sze and K. K. Ng, *Physics of Semiconductor Devices*. John Wiley & Sons, 2006.

[60] P. Balk, in *Electrochemical Society Meeting*, 1965.

[61] B. E. Deal, "Measurement and Control of Dielectric Film Properties During Semiconductor Device Processing", *Silicon Device Processing*, pp. 36–50, 1970.

[62] J. Schmidt, A. Merkle, R. Brendel, B. Hoex, M. v. de Sanden, and W. Kessels, "Surface Passivation of High-Efficiency Silicon Solar Cells by Atomic-Layer-Deposited Al_2O_3", *Progress in Photovoltaics: Research and Applications*, vol. 16, no. 6, pp. 461–466, 2008.

[63] J. Zhao, A. Wang, P. P. Altermatt, S. R. Wenham, and M. A. Green, "24% Efficient PERL Silicon Solar Cell: Recent Improvements in High Efficiency Silicon Cell Research", *Solar Energy Materials and Solar Cells*, vol. 41, pp. 87–99, 1996.

[64] L. Do Thanh and P. Balk, "Elimination and Generation of Si-SiO_2 Interface Traps by Low Temperature Hydrogen Annealing", *Journal of The Electrochemical Society*, vol. 135, no. 7, p. 1797, 1988.

[65] M. J. Kerr and A. Cuevas, "Very Low Bulk and Surface Recombination in Oxidized Silicon Wafers", *Semiconductor Science and Technology*, vol. 17, no. 1, p. 35, 2001.

[66] T. C. Kho, S. C. Baker-Finch, and K. R. McIntosh, "The Study of Thermal Silicon Dioxide Electrets Formed by Corona Discharge and Rapid-Thermal Annealing", *Journal of Applied Physics*, vol. 109, no. 5, p. 053 108, 2011.

[67] K. A. Collett, S. Du, G. Bourret-Sicotte, Z. Luo, P. Hamer, B. Hallam, R. S. Bonilla, and P. R. Wilshaw, "Scalable Techniques for Producing Field-Effect Passivation in High-Efficiency Silicon Solar Cells", *IEEE Journal of Photovoltaics*, vol. 9, no. 1, pp. 26–33, 2018.

[68] K. A. Collett, R. S. Bonilla, P. Hamer, G. Bourret-Sicotte, R. Lobo, T. Kho, and P. R. Wilshaw, "An Enhanced Alneal Process to Produce SRV< 1 cm/s in 1 Ω cm N-Type Si", *Solar Energy Materials and Solar Cells*, vol. 173, pp. 50–58, 2017.

[69] M. Lipiñski *et al.*, "Silicon Nitride for Photovoltaic Application", *Archives of Materials Science and Engineering*, vol. 46, no. 2, pp. 69–87, 2010.

[70] S. Duttagupta, F. Ma, B. Hoex, T. Mueller, and A. G. Aberle, "Optimised Antireflection Coatings Using Silicon Nitride on Textured Silicon Surfaces Based on Measurements and Multidimensional Modelling", *Energy Procedia*, vol. 15, pp. 78–83, 2012.

[71] W. Soppe, H. Rieffe, and A. Weeber, "Bulk and Surface Passivation of Silicon Solar Cells Accomplished by Silicon Nitride Deposited on Industrial Scale by Microwave PECVD", *Progress in Photovoltaics: Research and Applications*, vol. 13, no. 7, pp. 551–569, 2005.

[72] A. Weeber, H. Rieffe, W. Sinke, and W. Soppe, "Structural and Passivating Properties of SiN_x:H Deposited Using Different Precursor Gases", in *Proceedings of the 19th European Photovoltaic Solar Energy Conference*, vol. 1005, 2004, pp. 7–11.

[73] Y. Wan, K. R. McIntosh, and A. F. Thomson, "Characterisation and Optimisation of PECVD SiN_x as an Antireflection Coating and Passivation Layer for Silicon Solar Cells", *AIP Advances*, vol. 3, no. 3, p. 032 113, 2013.

[74] T. Lauinger, J. Moschner, A. G. Aberle, and R. Hezel, "Optimization and characterization of Remote Plasma-Enhanced ChemicalVapor Deposition Silicon Nitride for the Passivation of P-Type Crystalline Silicon Surfaces", *Journal of Vacuum Science & Technology A: Vacuum, Surfaces, and Films*, vol. 16, no. 2, pp. 530–543, 1998.

[75] J. Schmidt, F. Werner, B. Veith, D. Zielke, S. Steingrube, P. P. Altermatt, S. Gatz, T. Dullweber, and R. Brendel, "Advances in the Surface Passivation of Silicon Solar Cells", *Energy Procedia*, vol. 15, pp. 30–39, 2012.

[76] G. Dingemans, M. Mandoc, S. Bordihn, M. Van De Sanden, and W. Kessels, "Effective Passivation of Si Surfaces by Plasma Deposited SiO_x/a-SiN_x: H Stacks", *Applied Physics Letters*, vol. 98, no. 22, p. 222 102, 2011.

[77] B. Hoex, S. Heil, E. Langereis, M. Van de Sanden, and W. Kessels, "Ultralow Surface Recombination of c-si Substrates Passivated by Plasma-Assisted Atomic Layer Deposited Al_2O_3", *Applied Physics Letters*, vol. 89, no. 4, p. 042 112, 2006.

[78] R. Hezel and K. Jaeger, "Low-temperature Surface Passivation of Silicon for Solar Cells", *Journal of the Electrochemical Society*, vol. 136, no. 2, p. 518, 1989.

[79] K. Matsunaga, T. Tanaka, T. Yamamoto, and Y. Ikuhara, "First-Principles Calculations of Intrinsic Defects in Al_2O_3", *Physical Review B*, vol. 68, no. 8, p. 085 110, 2003.

[80] N. Terlinden, G. Dingemans, M. M. Van De Sanden, and W. Kessels, "Role of Field-Effect on c-Si Surface Passivation by Ultrathin (2–20 nm) Atomic Layer Deposited Al_2 O_3", *Applied Physics Letters*, vol. 96, no. 11, p. 112 101, 2010.

[81] R. S. Johnson, G. Lucovsky, and I. Baumvol, "Physical and Electrical Properties of Noncrystalline Al_2 O_3 Prepared by Remote Plasma Enhanced Chemical Vapor Deposition", *Journal of Vacuum Science & Technology A: Vacuum, Surfaces, and Films*, vol. 19, no. 4, pp. 1353–1360, 2001.

[82] D. Hoogeland, K. Jinesh, F. Roozeboom, W. Besling, M. Van De Sanden, and W. Kessels, "Plasma-Assisted Atomic Layer Deposition of TiN/Al_2O_3 Stacks for Metal-Oxide-Semiconductor Capacitor Applications", *Journal of Applied Physics*, vol. 106, no. 11, p. 114 107, 2009.

[83] G. Dingemans and W. Kessels, "Status and Prospects of Al_2O_3-Based Surface Passivation schemes for Silicon Solar Cells", *Journal of Vacuum Science & Technology A: Vacuum, Surfaces, and Films*, vol. 30, no. 4, p. 040 802, 2012.

[84] K. Arafune, S. Miki, R. Matsutani, J. Hamano, H. Yoshida, T. Tachibana, H. J. Lee, A. Ogura, Y. Ohshita, and S.-i. Satoh, "Surface Recombination of Crystalline Silicon Substrates Passivated by Atomic-Layer-Deposited AlO_x", *Japanese Journal of Applied Physics*, vol. 51, no. 4S, 04DP06, 2012.

[85] L. E. Black, *New Perspectives on Surface Passivation: Understanding the Si-Al_2O_3 Interface*. Springer, 2016.

[86] G. Dingemans, R. Seguin, P. Engelhart, M. v. d. Sanden, and W. Kessels, "Silicon Surface Passivation by Ultrathin Al_2O_3 Films Synthesized by Thermal and Plasma Atomic Layer Deposition", *physica status solidi (RRL)–Rapid Research Letters*, vol. 4, no. 1-2, pp. 10–12, 2010.

[87] B. Veith, T. Dullweber, M. Siebert, C. Kranz, F. Werner, N.-P. Harder, J. Schmidt, B. Roos, T. Dippell, and R. Brendel, "Comparison of ICP-AlO_x and ALD-Al_22o_3 Layers for the Rear Surface Passivation of c-Si Solar Cells", *Energy Procedia*, vol. 27, pp. 379–384, 2012.

[88] L. E. Black and K. R. McIntosh, "Surface Passivation of c-Si by Atmospheric Pressure Chemical Vapor Deposition of Al_2O_3", *Applied Physics Letters*, vol. 100, no. 20, p. 202 107, 2012.

[89] G. Dingemans, M. Van De Sanden, and W. Kessels, "Plasma-Enhanced Chemical Vapor Deposition of Aluminum Oxide using Ultrashort Precursor Injection Pulses", *Plasma Processes and Polymers*, vol. 9, no. 8, pp. 761–771, 2012.

[90] Z. Wang and M. Zhiming, "High Efficiency Solar Cells", *Physics, Materials, and Devices. Springer Series in Materials Science*, vol. 190, 2014.

[91] D. Hiller, J. Göttlicher, R. Steininger, T. Huthwelker, J. Julin, F. Munnik, M. Wahl, W. Bock, B. Schoenaers, A. Stesmans, *et al.*, "Structural Properties of Al-O Monolayers in SiO_2 on Silicon and the Maximization of their Negative Fixed Charge Density", *ACS Applied Materials & Interfaces*, vol. 10, no. 36, pp. 30 495–30 505, 2018.

[92] D. Hiller, P. M. Jordan, K. Ding, M. Pomaska, T. Mikolajick, and D. König, "Deactivation of Silicon Surface States by al-Induced Acceptor States from Al-O Monolayers in SiO_2", *Journal of Applied Physics*, vol. 125, no. 1, p. 015 301, 2019.

[93] R. S. Bonilla and P. R. Wilshaw, "Potassium Ions in SiO_2: Electrets for Silicon Surface Passivation", *Journal of Physics D: Applied Physics*, vol. 51, no. 2, p. 025 101, 2017.

[94] T. C. Kho, K. C. Fong, M. Stocks, K. McIntosh, E. Franklin, S. P. Phang, W. Liang, and A. Blakers, "Excellent ONO Passivation on Phosphorus and Boron Diffusion Demonstrating a 25% Efficient IBC Solar Cell", *Progress in Photovoltaics: Research and Applications*, vol. 28, no. 10, pp. 1034–1044, 2020.

[95] M. Schofthaler, R. Brendel, G. Langguth, and J. Werner, "High-Quality Surface Passivation by Corona-Charged Oxides for Semiconductor Surface Characterization", in *Proceedings of 1994 IEEE 1st World Conference on Photovoltaic Energy Conversion-WCPEC (A Joint Conference of PVSC, PVSEC and PSEC)*, IEEE, vol. 2, 1994, pp. 1509–1512.

[96] D. K. Schroder, "Contactless Surface Charge Semiconductor Characterization", *Materials Science and Engineering: B*, vol. 91, pp. 196–210, 2002.

[97] H. D. Goodfellow, *Industrial Ventilation Design Guidebook*. Elsevier, 2001.

[98] M. M. Shahin, "Mass-Spectrometric Studies of Corona Discharges in Air at Atmospheric Pressures", *The Journal of Chemical Physics*, vol. 45, no. 7, pp. 2600–2605, 1966.

[99] M. M. Shahin, "Nature of Charge Carriers in Negative Coronas", *Applied Optics*, vol. 8, no. 101, pp. 106–110, 1969.

[100] R. S. Bonilla, N. Jennison, D. Clayton-Warwick, K. A. Collett, L. Rands, and P. R. Wilshaw, "Corona Charge in SiO_2: Kinetics and Surface Passivation for High Efficiency Silicon Solar Cells", *Energy Procedia*, vol. 92, pp. 326–335, 2016.

[101] R. S. Bonilla, C. Reichel, M. Hermle, P. Hamer, and P. R. Wilshaw, "Long Term Stability of c-Si Surface Passivation Using Corona Charged SiO_2", *Applied Surface Science*, vol. 412, pp. 657–667, 2017.

[102] R. S. Bonilla, F. Woodcock, and P. R. Wilshaw, "Very Low Surface Recombination Velocity in N-Type c-Si Using Extrinsic Field Effect Passivation", *Journal of Applied Physics*, vol. 116, no. 5, p. 054 102, 2014.

[103] S. W. Glunz, D. Biro, S. Rein, and W. Warta, "Field-Effect Passivation of the SiO_2 Si Interface", *Journal of Applied Physics*, vol. 86, no. 1, pp. 683–691, 1999.

[104] A. Sprenkels, W. Olthuis, and P. Berveld, "The Application of Silicon Dioxide as an Electret Material", in *6th International Symposium on Electrets,(ISE 6) Proceedings.*, IEEE, 1988, pp. 165–169.

[105] V. Leonov, C. Van Hoof, M. Goedbloed, and R. Van Schaijk, "Charge Injection and Storage in Single-Layer and Multilayer Inorganic Electrets Based on SiO_2 and Si_3N_4", *IEEE Transactions on Dielectrics and Electrical Insulation*, vol. 19, no. 4, pp. 1253–1260, 2012.

[106] K. C. Kao, *Dielectric Phenomena in Solids*. Elsevier, 2004.

[107] M. Goel, "Electret Sensors, Filters and MEMS Devices: New Challenges in Materials Research", *Current Science*, vol. 85, no. 4, pp. 443–453, 2003.

[108] R. Kressmann, G. Sessler, and P. Gunther, "Space-Charge Electrets", *IEEE Transactions on Dielectrics and Electrical Insulation*, vol. 3, no. 5, pp. 607–623, 1996.

[109] K. Hagiwara, M. Goto, Y. Iguchi, Y. Yasuno, H. Kodama, K. Kidokoro, and T. Tajima, "Soft X-ray Charging Method for a Silicon Electret Condenser Microphone", *Applied Physics Express*, vol. 3, no. 9, p. 091 502, 2010.

[110] U. Mescheder, B. Müller, S. Baborie, and P. Urbanovic, "Properties of SiO_2 Electret Films Charged by Ion Implantation for MEMS-Based Energy Harvesting Systems", *Journal of Micromechanics and Microengineering*, vol. 19, no. 9, p. 094 003, 2009.

[111] T. Sugiyama, M. Aoyama, Y. Shibata, M. Suzuki, T. Konno, M. Ataka, H. Fujita, and G. Hashiguchi, "SiO_2 Electret Generated by Potassium Ions on a Comb-Drive Actuator", *Applied Physics Express*, vol. 4, no. 11, p. 114 103, 2011.

[112] K. Misawa, T. Sugiyama, G. Hashiguchi, and H. Toshiyoshi, "Reliability of Potassium Ion Electret in Silicon Oxide for Vibrational Energy Harvester Applications", *Japanese Journal of Applied Physics*, vol. 54, no. 6, p. 067 201, 2015.

[113] R. S. Bonilla, "Surface Passivation of Silicon Solar Cells", PhD thesis, University of Oxford, 2015.

[114] J. Eldridge and D. Kerr, "Sodium Ion Drift Through Phosphosilicate Glass-SiO_2 Films", *J. Electrochem. Soc.*, vol. 118, no. 6, p. 986, 1971.

[115] K. Collett, "Surface Passivation for Silicon Solar Cells using Stable Extrinsic Field Effect Passivation", PhD thesis, University of Oxford, 2018.

[116] Y. Larionova, V. Mertens, N.-P. Harder, and R. Brendel, "Surface Passivation of N-Type Czochralski Silicon Substrates by Thermal-SiO_2/Plasma-Enhanced Chemical Vapor Deposition SiN Stacks", *Applied Physics Letters*, vol. 96, no. 3, p. 032 105, 2010.

[117] H. Liu, Y. Wang, L. Dong, H. Wang, and Z. Zhang, "Improved al_2O_3/SiN_x and SiO_2/SiN_x Stack Passivation Layer Structure PERC sc-Silicon Solar Cells on Mass Production Line", *International Journal of Energy Research*, vol. 45, no. 4, pp. 5806–5814, 2021.

[118] E. Urrejola, R. Petres, J. Glatz-Reichenbach, K. Peter, E. Wefringhaus, H. Plagwitz, and G. Schubert, "High Efficiency Industrial PERC Solar Cells with All PECVD-Based Rear Surface Passivation", in *Proceedings of the 26th European Photovoltaic Solar Energy Conference and Exhibition*, 2011, p. 2233.

[119] "CPVT Confirms LONGi Produced First Bifacial Monocrystalline Silicon PERC Solar Cell Exceeding 24% on Commercial Wafer Size". [Online]. Available: `http://taiyangnews.info/technology/longi-24-06-efficiency-perc-cell-world-record/`.

[120] M. A. Green, "The Path to 25% Silicon Solar Cell Efficiency: History of Silicon Cell Evolution", *Progress in Photovoltaics: Research and Applications*, vol. 17, no. 3, pp. 183–189, 2009.

[121] J. Zhao, A. Wang, and M. A. Green, "24·5% Efficiency Silicon PERT Cells on MCZ Substrates and 24·7% Efficiency PERL Cells on FZ Substrates", *Progress in Photovoltaics: Research and Applications*, vol. 7, no. 6, pp. 471–474, 1999.

[122] S. H. Lee *et al.*, "Advancements in N-Type Base Crystalline Silicon Solar Cells and their Emergence in the Photovoltaic Industry", *The Scientific World Journal*, vol. 2013, 2013.

[123] B. Singha and C. S. Solanki, "N-Type Solar Cells: Advantages, Issues, and Current Scenarios", *Materials Research Express*, vol. 4, no. 7, p. 072 001, 2017.

[124] K. Yoshikawa, H. Kawasaki, W. Yoshida, T. Irie, K. Konishi, K. Nakano, T. Uto, D. Adachi, M. Kanematsu, H. Uzu, *et al.*, "Silicon Heterojunction Solar Cell with Interdigitated Back Contacts for a Photoconversion Efficiency Over 26%", *Nature Energy*, vol. 2, no. 5, pp. 1–8, 2017.

[125] M. A. Green, Y. Hishikawa, W. Warta, E. D. Dunlop, D. H. Levi, J. Hohl-Ebinger, and A. W. Ho-Baillie, "Solar Cell Efficiency Tables (Version 50)", *Progress in Photovoltaics: Research and Applications*, vol. 25, no. 7, pp. 668–676, 2017.

[126] A. Richter, R. Müller, J. Benick, F. Feldmann, B. Steinhauser, C. Reichel, A. Fell, M. Bivour, M. Hermle, and S. W. Glunz, "Design Rules for High-Efficiency Both-Sides-Contacted Silicon Solar Cells with Balanced Charge Carrier Transport and Recombination Losses", *Nature Energy*, vol. 6, no. 4, pp. 429–438, 2021.

[127] B. Kafle, B. S. Goraya, S. Mack, F. Feldmann, S. Nold, and J. Rentsch, "TOPCon–Technology Options for Cost Efficient Industrial Manufacturing", *Solar Energy Materials and Solar Cells*, vol. 227, p. 111 100, 2021.

[128] J. Cotter, J. Guo, P. Cousins, M. Abbott, F. Chen, and K. Fisher, "P-Type versus N-Type Silicon Wafers: Prospects for High-Efficiency Commercial Silicon Solar Cells", *IEEE Transactions on Electron Devices*, vol. 53, no. 8, pp. 1893–1901, 2006.

[129] L. C. Andreani, A. Bozzola, P. Kowalczewski, M. Liscidini, and L. Redorici, "Silicon Solar Cells: Toward the Efficiency Limits", *Advances in Physics: X*, vol. 4, no. 1, p. 1 548 305, 2019.

[130] W. Zulehner, "Czochralski Growth of Silicon", *Journal of Crystal Growth*, vol. 65, no. 1-3, pp. 189–213, 1983.

[131] W. Dietze, W. Keller, and A. Mühlbauer, "Float-zone Grown Silicon", in *Silicon*, Springer, 1981, pp. 1–42.

[132] J. Vedde, T. Clausen, and L. Jensen, "Float-Zone Silicon for High Volume Production of Solar Cells", in *3rd World Conference onPhotovoltaic Energy Conversion, 2003. Proceedings of*, IEEE, vol. 1, 2003, pp. 943–946.

[133] K. Sumino and I. Yonenaga, "Difference in the Mechanical Strengths of Dislocation-Free Crystals of Czochralski Silicon and Float-Zone Silicon", *Japanese Journal of Applied Physics*, vol. 20, no. 9, p. L685, 1981.

[134] K. Hoshikawa, H. Kohda, H. Hirata, and H. Nakanishi, "Low Oxygen Content Czochralski Silicon Crystal Growth", *Japanese Journal of Applied Physics*, vol. 19, no. 1, p. L33, 1980.

[135] C. Londos, M. Potsidi, and V. Emtsev, "Effect of Carbon on Oxygen Precipitation in Czochralski Silicon", *physica status solidi (c)*, vol. 2, no. 6, pp. 1963–1967, 2005.

[136] W. Chen, Y. Liu, L. Yang, J. Wu, Q. Chen, Y. Zhao, Y. Wang, and X. Du, "Difference in Anisotropic Etching Characteristics of Alkaline and Copper Based Acid Solutions for Single-Crystalline Si", *Scientific Reports*, vol. 8, no. 1, pp. 1–8, 2018.

[137] W. Y. Ou, Y. Zhang, H. L. Li, L. Zhao, C. L. Zhou, H. W. Diao, M. Liu, W. M. Lu, J. Zhang, and W. J. Wang, "Effects of IPA on Texturing Process for Mono-Crystalline Silicon Solar Cell in TMAH Solution", in *Materials Science Forum*, Trans Tech Publ, vol. 685, 2011, pp. 31–37.

[138] M. Moynihan, C. O'Connor, B. Barr, S. Tiffany, W. Braun, G. Allardyce, J. Rentsch, and K. Birmann, "In-Line and Vertical Texturing of Mono-Crystalline Solar Cells", in *2010 35th IEEE Photovoltaic Specialists Conference*, IEEE, 2010, pp. 001 028–001 033.

[139] M. Ju, N. Balaji, C. Park, H. T. T. Nguyen, J. Cui, D. Oh, M. Jeon, J. Kang, G. Shim, and J. Yi, "The Effect of Small Pyramid Texturing on the Enhanced Passivation and Efficiency of Single c-Si Solar Cells", *RSC Advances*, vol. 6, no. 55, pp. 49 831–49 838, 2016.

[140] I. Zubel and M. Kramkowska, "The Effect of Isopropyl Alcohol on Etching Rate and Roughness of (100) Si Surface Etched in KOH and TMAH Solutions", *Sensors and Actuators A: Physical*, vol. 93, no. 2, pp. 138–147, 2001.

[141] P. Singh, R. Kumar, M. Lal, S. Singh, and B. Das, "Effectiveness of Anisotropic Etching of Silicon in Aqueous Alkaline Solutions", *Solar Energy Materials and Solar Cells*, vol. 70, no. 1, pp. 103–113, 2001.

[142] G. Jellison Jr, "Optical Functions of Silicon Determined by Two-Channel Polarization Modulation Ellipsometry", *Optical Materials*, vol. 1, no. 1, pp. 41–47, 1992.

[143] E. D. Palik, *Handbook of Optical Constants of Solids*. Academic press, 1998, vol. 3.

[144] C. Cushman, N. Smith, M. Kaykhaii, N. Podraza, and M. Linford, "An Introduction to Modeling in Spectroscopic Ellipsometry, Focusing on Models for Transparent Materials: The Cauchy and Sellmeier Models", *Vacuum Technology & Coating*, 2016.

[145] R. Pascu and M. Dinescu, "Spectroscopic Ellipsometry", *Romanian Reports in Physics*, vol. 64, no. 1, pp. 135–142, 2012.

[146] R. S. Bonilla and P. R. Wilshaw, "A Technique for Field Effect Surface Passivation for Silicon Solar Cells", *Applied Physics Letters*, vol. 104, no. 23, p. 232 903, 2014.

[147] D. Meyerhofer, "Characteristics of Resist Films Produced by Spinning", *Journal of Applied Physics*, vol. 49, no. 7, pp. 3993–3997, 1978.

[148] W. Daughton and F. Givens, "An Investigation of the Thickness Variation of Spun-on Thin Films Commonly Associated with the Semiconductor Industry", *Journal of The Electrochemical Society*, vol. 129, no. 1, p. 173, 1982.

[149] C. M. Hansen, "The Three Dimensional Solubility Parameter", *Danish Technical: Copenhagen*, vol. 14, 1967.

[150] W. Mu, T. Lin, Y. Hu, Y. Sun, Z. Du, J. Jin, D. Zhang, and Z. Cui, "Double Layer Printed High Performance OLED Based on PEDOT: PSS/Ir (bt) 2acac: CDBP", *AIP Advances*, vol. 8, no. 11, p. 115 112, 2018.

[151] Y. Vaynzof, "The Future of Perovskite Photovoltaics—Thermal Evaporation or Solution Processing?", *Advanced Energy Materials*, vol. 10, no. 48, p. 2 003 073, 2020.

[152] V. Scholtz, J. Julák, V. Krıha, and J. Mosinger, "Decontamination Effects of Low-Temperature Plasma Generated by Corona Discharge. Part I: An Overview", *Prague Med Rep*, vol. 108, no. 2, pp. 115–27, 2007.

[153] B. L. Henson, "A Derivation of Warburg's Law for Point to Plane Coronas", *Journal of Applied Physics*, vol. 52, no. 6, pp. 3921–3923, 1981.

[154] F. Woodcock, "Passivation of Semiconductor Surfaces for High-Efficiency Solar Cells", University of Oxford, 2014.

[155] R. S. Bonilla, "Controlling Surface Carrier Density via a PEDOT: PSS Gate: An Application to the Study of Silicon-Dielectric Interface Recombination", *Solar RRL*, vol. 2, no. 10, p. 1 800 172, 2018.

[156] F. Qian, D. Kai, L. Yu-Kun, S. Peng, and F. Qing, "Effect of Annealing on Performance of PEDOT: PSS/n-GaN Schottky Solar Cells", *Chinese Physics B*, vol. 23, no. 7, p. 077 303, 2014.

[157] B. Friedel, P. E. Keivanidis, T. J. Brenner, A. Abrusci, C. R. McNeill, R. H. Friend, and N. C. Greenham, "Effects of Layer Thickness and Annealing of PEDOT: PSS Layers in Organic Photodetectors", *Macromolecules*, vol. 42, no. 17, pp. 6741–6747, 2009.

[158] M. Boudry and J. Stagg, "The Kinetic Behavior of Mobile Ions in the Al-SiO_2-Si System", *Journal of Applied Physics*, vol. 50, no. 2, pp. 942–950, 1979.

[159] D. Bredemeier, D. C. Walter, R. Heller, and J. Schmidt, "Impact of Hydrogen-Rich Silicon Nitride Material Properties on Light-Induced Lifetime Degradation in Multicrystalline Silicon", *physica status solidi (RRL)–Rapid Research Letters*, vol. 13, no. 8, p. 1 900 201, 2019.

[160] L. Helmich, D. C. Walter, D. Bredemeier, and J. Schmidt, "Atomic-Layer-Deposited Al_2O_3 as effective Barrier against the Diffusion of Hydrogen from SiN_x: H Layers into Crystalline Silicon during Rapid Thermal Annealing", *physica status solidi (RRL)–Rapid Research Letters*, vol. 14, no. 12, p. 2 000 367, 2020.

[161] D. K. Schroder, *Semiconductor Material and Device Characterization*. John Wiley & Sons, 2015.

[162] E. H. Nicollian, J. R. Brews, and E. H. Nicollian, *MOS (Metal Oxide Semiconductor) Physics and Technology*. Wiley New York, 1982, vol. 1987.

[163] W. D. Eades and R. M. Swanson, "Improvements in the Determination of Interface State Density Using Deep Level Transient Spectroscopy", *Journal of Applied Physics*, vol. 56, no. 6, pp. 1744–1751, 1984.

[164] L. M. Terman, "An Investigation of Surface States at a Silicon/Silicon Oxide Interface Employing Metal-Oxide-Silicon Diodes", *Solid-State Electronics*, vol. 5, no. 5, pp. 285–299, 1962.

[165] D. A. Deen and J. G. Champlain, "High Frequency Capacitance-Voltage Technique for the Extraction of Interface Trap Density of the Heterojunction Capacitor: Terman's Method Revised", *Applied Physics Letters*, vol. 99, no. 5, p. 053 501, 2011.

[166] I. Baikie, S. Mackenzie, P. Estrup, and J. Meyer, "Noise and the Kelvin Method", *Review of Scientific Instruments*, vol. 62, no. 5, pp. 1326–1332, 1991.

[167] R. Girisch, R. Mertens, and R. Dekeersmaecker, "Determination of si-SiO_2 Interface Recombination Parameters Using a Gate-Controlled Point-Junction Diode under Illumination", *IEEE Transactions on Electron Devices*, vol. 35, no. 2, pp. 203–222, 1988.

[168] H. Mitsuya, H. Ashizawa, T. Sugiyama, M. Kumemura, M. Ataka, H. Fujita, and G. Hashiguchi, "Electret-Based Low Power Resonator for Robust Pressure Sensor", in *2014 IEEE 27th International Conference on Micro Electro Mechanical Systems (MEMS)*, IEEE, 2014, pp. 717–720.

[169] L. Guo and R. Hezel, "Studies on Evaporated Cesium Incorporation in MIS Inversion Layer Solar Cells", *Solid-State Electronics*, vol. 37, no. 9, pp. 1659–1662, 1994.

[170] R. Hezel, K. Blumenstock, and R. Schörner, "Interface States and Fixed Charges in MNOS Structures with APCVD and Plasma Silicon Nitride", *Journal of the Electrochemical Society*, vol. 131, no. 7, pp. 1679–1683, 1984.

[171] W. Bauch, K. Jäger, and R. Hezel, "Effect of Cs Contamination on the Interface State Density of MNOS Capacitors", *Applied Surface Science*, vol. 39, no. 1-4, pp. 356–363, 1989.

[172] G. Sixt and A. Goetzberger, "Control of Positive Surface Charge in Si–SiO_2 Interfaces by Use of Implanted Cs Ions", *Applied Physics Letters*, vol. 19, no. 11, pp. 478–479, 1971.

[173] G. Sixt, M. Schulz, and A. Goetzberger, "Determination of Cesium Distributions in Oxides of MOS structures by Photoinjection Studies", *Applied Physics*, vol. 4, no. 3, pp. 217–223, 1974.

[174] G. Greeuw and J. Verwey, "The Mobility of Na^+, Li^+, and K^+ Ions in Thermally Grown SiO_2 Films", *Journal of Applied Physics*, vol. 56, no. 8, pp. 2218–2224, 1984.

[175] B. E. Deal, "The Current Understanding of Charges in the Thermally Oxidized Silicon Structure", *Journal of the Electrochemical Society*, vol. 121, no. 6, p. 198C, 1974.

[176] W. Luo, Y. S. Khoo, P. Hacke, V. Naumann, D. Lausch, S. P. Harvey, J. P. Singh, J. Chai, Y. Wang, A. G. Aberle, *et al.*, "Potential-Induced Degradation in Photovoltaic Modules: A Critical Review", *Energy & Environmental Science*, vol. 10, no. 1, pp. 43–68, 2017.

[177] Y. Suzuki, "Recent Progress in MEMS Electret Generator for Energy Harvesting", *IEEJ Transactions on Electrical and Electronic Engineering*, vol. 6, no. 2, pp. 101–111, 2011.

[178] G. Hashiguchi, D. Nakasone, T. Sugiyama, M. Ataka, and H. Toshiyoshi, "Charging Mechanism of Electret Film Made of Potassium-Ion-Doped SiO_2", *AIP Advances*, vol. 6, no. 3, p. 035 004, 2016.

[179] C. Sano, M. Ataka, G. Hashiguchi, and H. Toshiyoshi, "An Electret-Augmented Low-Voltage MEMS Electrostatic Out-of-Plane Actuator for Acoustic Transducer Applications", *Micromachines*, vol. 11, no. 3, p. 267, 2020.

[180] M. Yamin, "Charge Storage Effects in Silicon dioxide Films", *IEEE Trans. Electron Devices*, vol. 12, no. 3, pp. 88–96, 1965.

[181] E. Snow, A. Grove, B. Deal, and C. Sah, "Ion Transport Phenomena in Insulating Films", *Journal of Applied Physics*, vol. 36, no. 5, pp. 1664–1673, 1965.

[182] P. Nauta and M. Hillen, "Investigation of Mobile Ions in MOS Structures Using the TSIC Method", *Journal of Applied Physics*, vol. 49, no. 5, pp. 2862–2865, 1978.

[183] J. Stagg, "Drift Mobilities of Na^+ and K^+ Ions in SiO_2 Films", *Applied Physics Letters*, vol. 31, no. 8, pp. 532–533, 1977.

[184] M. Hillen, G. Greeuw, and J. Verweij, "On the Mobility of Potassium Ions in SiO_2", *Journal of Applied Physics*, vol. 50, no. 7, pp. 4834–4837, 1979.

[185] T. Hickmott, "Thermally Stimulated Ionic Conductivity of Sodium in Thermal SiO_2", *Journal of Applied Physics*, vol. 46, no. 6, pp. 2583–2598, 1975.

[186] D. Kerr, "A Review of Instability Mechanisms in Passivation Films", in *8th Reliability Physics Symposium*, IEEE, 1970, pp. 1–8.

[187] J. Piprek, "Numerical Analysis of TVS Ionic Current Applied to the Na^+ Motion in Implanted MOS Oxide Layers", *physica status solidi (a)*, vol. 112, no. 2, pp. 551–560, 1989.

[188] S. R. Hofstein, "An Investigation of Instability and Charge Motion in Metal-Silicon Oxide-Silicon Structures", *IEEE Transactions on Electron Devices*, no. 2, pp. 222–237, 1966.

[189] K. Kajihara, T. Miura, H. Kamioka, M. Hirano, L. Skuja, and H. Hosono, "Spontaneous Oxygen Loading into SiO_2 Glass by Thermal Anneal", *Journal of Non-Crystalline solids*, vol. 349, pp. 205–208, 2004.

[190] T. Hickmott, "Dipole Layers at the Metal-SiO_2 Interface", *Journal of Applied Physics*, vol. 51, no. 8, pp. 4269–4281, 1980.

[191] O. Anderson and D. Stuart, "Calculation of Activation Energy of Ionic Conductivity in Silica Glasses by Classical Methods", *Journal of the American Ceramic Society*, vol. 37, no. 12, pp. 573–580, 1954.

[192] B. Biswas, S. Chatterjee, S. Mukherjee, and S. Pal, "A Discussion on Euler Method: A Review", *Electronic Journal of Mathematical Analysis and Applications*, vol. 1, no. 2, pp. 2090–2792, 2013.

[193] P. Wesseling, "Von Neumann Stability Conditions for the Convection-Diffusion Equation", *IMA journal of Numerical Analysis*, vol. 16, no. 4, pp. 583–598, 1996.

[194] B. J. Fishbein and J. D. Plummer, "Characterization of Cesium Diffusion in Silicon Dioxide Films using Backscattering Spectrometry", *Applied Physics Letters*, vol. 50, no. 17, pp. 1200–1202, 1987.

[195] G. Derbenwick, "Mobile Ions in SiO_2: Potassium", *Journal of Applied Physics*, vol. 48, no. 3, pp. 1127–1130, 1977.

[196] H. Toshiyoshi, "MEMS Vibrational Energy Harvester for IoT Wireless Sensors", in *2020 IEEE International Electron Devices Meeting (IEDM)*, IEEE, 2020, pp. 37–3.

[197] S. Krivec, M. Buchmayr, T. Detzel, T. Froemling, J. Fleig, and H. Hutter, "The Effect of Bias-Temperature Stress on Na^+ Incorporation into Thin Insulating Films", *Analytical and Bioanalytical Chemistry*, vol. 400, no. 3, pp. 649–657, 2011.

[198] F.-C. Chiu, "A Review on Conduction Mechanisms in Dielectric Films", *Advances in Materials Science and Engineering*, vol. 2014, 2014.

[199] Y. Shibata, T. Sugiyama, H. Mimura, and G. Hashiguchi, "In Situ Measurement of Charging Process in Electret-Based Comb-Drive Actuator and High-Voltage Charging", *Journal of Microelectromechanical Systems*, vol. 24, no. 4, pp. 1052–1060, 2014.

[200] H. Koga, H. Mitsuya, H. Honma, H. Fujita, H. Toshiyoshi, and G. Hashiguchi, "Development of a Cantilever-Type Electrostatic Energy Harvester and its Charging Characteristics on a Highway Viaduct", *Micromachines*, vol. 8, no. 10, p. 293, 2017.

[201] E. Yon, W. Ko, and A. Kuper, "Sodium Distribution in Thermal Oxide on Silicon by radiochemical and MOS Analysis", *IEEE Transactions on Electron Devices*, no. 2, pp. 276–280, 1966.

[202] I. Constant, F. Tardif, and J. Derrien, "Deposition and Removal of Sodium Contamination on Silicon Wafers", *Semiconductor Science and Technology*, vol. 15, no. 1, p. 61, 2000.

[203] M. Kuhn and D. Silversmith, "Ionic Contamination and Transport of Mobile Ions in MOS Structures", *Journal of the Electrochemical Society*, vol. 118, no. 6, p. 966, 1971.

[204] S. P. Harvey, J. A. Aguiar, P. Hacke, H. Guthrey, S. Johnston, and M. Al-Jassim, "Sodium Accumulation at Potential-Induced Degradation Shunted Areas in Polycrystalline Silicon Modules", *IEEE Journal of Photovoltaics*, vol. 6, no. 6, pp. 1440–1445, 2016.

[205] J. Oh, S. Bowden, and G. TamizhMani, "Potential-Induced Degradation (PID): Incomplete Recovery of Shunt Resistance and Quantum Efficiency Losses", *IEEE Journal of Photovoltaics*, vol. 5, no. 6, pp. 1540–1548, 2015.

[206] P. Günther, "SiO_2 Electrets for Electric-Field Generation in Sensors and Actuators", *Sens. Actuator A Phys.*, vol. 32, no. 1-3, pp. 357–360, 1992.

[207] K. Hagiwara, M. Goto, Y. Iguchi, T. Tajima, Y. Yasuno, H. Kodama, K. Kidokoro, and Y. Suzuki, "Electret Charging Method Based on Soft X-Ray Photoionization for MEMS Transducers", *IEEE Transactions on Dielectrics and Electrical Insulation*, vol. 19, no. 4, pp. 1291–1298, 2012.

[208] N. Yuan and J. Li, "SiO_2 Film Electret with High Surface Potential Stability", *Applied Surface Science*, vol. 252, no. 2, pp. 455–460, 2005.

[209] F. Bonacci, A. Di Michele, S. Caponi, F. Cottone, and M. Mattarelli, "High Charge Density Silica Micro-Electrets Fabricated by Electron Beam", *Smart Mater. Struct.*, vol. 27, no. 7, p. 075 052, 2018.

[210] H. C. Lai, P. Murphy, and M. Latour, "Improved Silicon Dioxide Electret for Silicon-Based Integrated Microphones", in *Proceedings of 8th International Symposium on Electrets (ISE 8)*, IEEE, 1994, pp. 949–954.

[211] A. Metz, M. Fischer, and J. Trube, *Recent Results of the International Technology Roadmap for Photovoltaics (ITRPV)*, 2017.

[212] P. Węgierek, J. Pastuszak, K. Dziadosz, and M. Turek, "Influence of Substrate Type and Dose of Implanted Ions on the Electrical Parameters of Silicon in Terms of Improving the Efficiency of Photovoltaic Cells", *Energies*, vol. 13, no. 24, p. 6708, 2020.

[213] A. Lanterne, T. Desrues, C. Lorfeuvre, M. Coig, F. Torregrosa, F. Milési, L. Roux, and S. Dubois, "Plasma-Immersion Ion Implantation: A Path to Lower the Annealing Temperature of Implanted Boron Emitters and Simplify PERT Solar Cell Processing", *Progress in Photovoltaics: Research and Applications*, vol. 27, no. 12, pp. 1081–1091, 2019.

[214] R. S. Bonilla, I. Al-Dhahir, M. Yu, P. Hamer, and P. P. Altermatt, "Charge Fluctuations at the Si–SiO_2 Interface and its Effect on Surface Recombination in Solar Cells", *Solar Energy Materials and Solar Cells*, vol. 215, p. 110 649, 2020.

[215] F. Degreve and P. Ged, "SIMS Study of the SiO_2/Si Interface and of the Si+O_2 System", *Surface and Interface Analysis*, vol. 5, no. 2, pp. 83–86, 1983.

[216] K. Wittmaack, "The Use of Secondary Ion Mass Spectrometry for Studies of Oxygen Adsorption and Oxidation", *Surface Science*, vol. 68, pp. 118–129, 1977.

[217] B. E. Deal and A. Grove, "General Relationship for the Thermal Oxidation of Silicon", *Journal of Applied Physics*, vol. 36, no. 12, pp. 3770–3778, 1965.

[218] N. Sahu, B. Parija, and S. Panigrahi, "Fundamental Understanding and Modeling of Spin Coating Process: A Review", *Indian Journal of Physics*, vol. 83, no. 4, pp. 493–502, 2009.

[219] S. Wang, X. Li, J. Wu, W. Wen, and Y. Qi, "Fabrication of Efficient Metal Halide Perovskite Solar Cells by Vacuum Thermal Evaporation: A Progress Review", *Current Opinion in Electrochemistry*, vol. 11, pp. 130–140, 2018.

[220] G. Chen, Y. Xu, X. Chen, and H. Xiao, "A Charging Method for Electrets Based on Interfacial Polarization", *IEEE Transactions on Dielectrics and Electrical Insulation*, vol. 25, no. 3, pp. 797–802, 2018.

[221] H. Von Seggern, "Improved Surface Voltage Uniformity on Electrets Obtained by Modified Corona Charging Method", *IEEE transactions on industry applications*, no. 6, pp. 1623–1626, 1984.

[222] R. Thakur, D. Das, and A. Das, "Electret Air Filters", *Separation & Purification Reviews*, vol. 42, no. 2, pp. 87–129, 2013.

[223] G. Kovačević and B. Pivac, "Structure, Defects, and Strain in Silicon-Silicon Oxide Interfaces", *Journal of Applied Physics*, vol. 115, no. 4, p. 043 531, 2014.

[224] A. Stesmans and V. Afanas' ev, "Invasive Nature of Corona Charging on Thermal Si/SiO_2 Structures with Nanometer-Thick Oxides Revealed by Electron Spin Resonance", *Applied Physics Letters*, vol. 82, no. 17, pp. 2835–2837, 2003.

[225] A. Stesmans and V. Afanas' ev, "Corona Charging Damage on Thermal Si/SiO_2 Structures with nm-Thick Oxides Revealed by Electron Spin Resonance", *Microelectronic Engineering*, vol. 72, no. 1-4, pp. 55–60, 2004.

[226] R. Hezel, "UV Radiation Hardness of Silicon Inversion Layer Solar Cells", in *IEEE Conference on Photovoltaic Specialists*, IEEE, 1990, pp. 239–244.

[227] A. Mirtchev, T. Mouselinos, S. Syrigos, and E. Tatakis, "Behavioral Analysis of Potential Induced Degradation on Photovoltaic Cells, Regeneration and Artificial Creation", *Energies*, vol. 14, no. 13, p. 3899, 2021.

[228] V. Afanas' ev, J. De Nijs, P. Balk, and A. Stesmans, "Degradation of the Thermal Oxide of the Si/Sio_2/Al System Due to Vacuum Ultraviolet Irradiation", *Journal of Applied Physics*, vol. 78, no. 11, pp. 6481–6490, 1995.

[229] M. Alonso-Garcia, J. Ruiz, and F. Chenlo, "Experimental Study of Mismatch and Shading Effects in the I–V Characteristic of a Photovoltaic Module", *Solar Energy Materials and Solar Cells*, vol. 90, no. 3, pp. 329–340, 2006.

[230] K. Al Abdullah, F. Al Alloush, A. Jaafar, and C. Salame, "Study of the Effects Related to the Electric Reverse Stress Currents on the Mono-Si Solar Cell Electrical Parameters", *Energy Procedia*, vol. 36, pp. 104–113, 2013.

[231] R. Ramaprabha and B. Mathur, "Impact of Partial Shading on Solar PV Module Containing Series Connected Cells", *International Journal of Recent Trends in Engineering*, vol. 2, no. 7, p. 56, 2009.

[232] T. Lauinger, J. Moschner, A. G. Aberle, and R. Hezel, "UV Stability of Highest-Quality Plasma Silicon Nitride Passivation of Silicon Solar Cells", in *Conference Record of the Twenty Fifth IEEE Photovoltaic Specialists Conference-1996*, IEEE, 1996, pp. 417–420.

[233] A. G. Aberle, S. Glunz, and W. Warta, "Impact of Illumination Level and Oxide Parameters on Shockley-Read-Hall Recombination at the Si-SiO_2 Interface", *Journal of Applied Physics*, vol. 71, no. 9, pp. 4422–4431, 1992.

[234] M. L. Reed and J. D. Plummer, "Chemistry of Si-SiO_2 Interface Trap Annealing", *Journal of Applied Physics*, vol. 63, no. 12, pp. 5776–5793, 1988.

[235] A. Aberle, S. Glunz, A. Stephens, and M. Green, "High-Efficiency Silicon Solar Cells: Si/SiO_2 Interface Parameters and Their Impact on Device Performance", *Progress in Photovoltaics: Research and Applications*, vol. 2, no. 4, pp. 265–273, 1994.

[236] J.-F. Lelièvre, E. Fourmond, A. Kaminski, O. Palais, D. Ballutaud, and M. Lemiti, "Study of the Composition of Hydrogenated Silicon Nitride SiN_x:H for Efficient Surface and Bulk Passivation of Silicon", *Solar Energy Materials and Solar Cells*, vol. 93, no. 8, pp. 1281–1289, 2009.

[237] F. Jiang, M. Stavola, A. Rohatgi, D. Kim, J. Holt, H. Atwater, and J. Kalejs, "Hydrogenation of Si from SiN_x (H) Films: Characterization of H Introduced into the Si", *Applied Physics Letters*, vol. 83, no. 5, pp. 931–933, 2003.

[238] P. Manshanden and P. C. Bronsveld, "Investigation of Hydrogenation in N-Type Wafers with Ring-and Disc-Shaped Defect Zones", *Energy Procedia*, vol. 92, pp. 857–866, 2016.

[239] B. J. Hallam, P. G. Hamer, A. M. Ciesla née Wenham, C. E. Chan, B. Vicari Stefani, and S. Wenham, "Development of Advanced Hydrogenation Processes for Silicon Solar Cells via an Improved Understanding of the Behaviour of Hydrogen in Silicon", *Progress in Photovoltaics: Research and Applications*, vol. 28, no. 12, pp. 1217–1238, 2020.

[240] G. Krugel, W. Wolke, J. Geilker, S. Rein, and R. Preu, "Impact of Hydrogen Concentration on the Regeneration of Light Induced Degradation", *Energy Procedia*, vol. 8, pp. 47–51, 2011.

[241] B. Hallam, A. Herguth, P. Hamer, N. Nampalli, S. Wilking, M. Abbott, S. Wenham, and G. Hahn, "Eliminating Light-Induced Degradation in

Commercial P-Type Czochralski Silicon Solar Cells", *Applied Sciences*, vol. 8, no. 1, p. 10, 2018.

[242] D. Chen, P. G. Hamer, M. Kim, T. H. Fung, G. Bourret-Sicotte, S. Liu, C. E. Chan, A. Ciesla, R. Chen, M. D. Abbott, *et al.*, "Hydrogen Induced Degradation: A Possible Mechanism for Light-and Elevated Temperature-Induced Degradation in N-Type Silicon", *Solar Energy Materials and Solar Cells*, vol. 185, pp. 174–182, 2018.

[243] D. Madi and D. E. Belfennache, "A Discussion About Hydrogen Diffusion in n+ pp+ Polysilicon Solar Cells Following Analysis of Both Dopant Deactivation and Defects Passivation", in *Advances in Green Energies and Materials Technology*, Springer, 2021, pp. 159–165.

[244] C. G. Van de Walle, "Hydrogen in Silicon: Fundamental Properties and Consequences for Devices", *Journal of Vacuum Science & Technology A: Vacuum, Surfaces, and Films*, vol. 16, no. 3, pp. 1767–1771, 1998.

[245] S. Rashkeev, D. Fleetwood, R. Schrimpf, and S. Pantelides, "Defect Generation by Hydrogen at the Si-SiO_2 Interface", *Physical Review letters*, vol. 87, no. 16, p. 165 506, 2001.

[246] F. Haase, C. Hollemann, S. Schäfer, A. Merkle, M. Rienäcker, J. Krügener, R. Brendel, and R. Peibst, "Laser Contact Openings for Local Poly-Si-Metal Contacts Enabling 26.1%-Efficient POLO-IBC Solar Cells", *Solar Energy Materials and Solar Cells*, vol. 186, pp. 184–193, 2018.

[247] C. G. Van de Walle and J. Neugebauer, "Universal Alignment of Hydrogen Levels in Semiconductors, Insulators and Solutions", *Nature*, vol. 423, no. 6940, p. 626, 2003.

[248] C. G. Van de Walle and B. R. Tuttle, "Microscopic Theory of Hydrogen in Silicon Devices", *IEEE Transactions on Electron Devices*, vol. 47, no. 10, pp. 1779–1786, 2000.

[249] K. Brower, "Kinetics of H_2 Passivation of P_b Centers at the (111) Si-SiO_2 Interface", *Physical Review B*, vol. 38, no. 14, p. 9657, 1988.

[250] P. Balk *et al.*, "Effects of Hydrogen Annealing on Silicon Surfaces", in *Electrochemical Society Spring Meeting*, vol. 14, 1965, pp. 237–240.

[251] T. Mueller, S. Schwertheim, and W. R. Fahrner, "Application of Wide-Bandgap Hydrogenated Amorphous Silicon Oxide Layers to Heterojunction Solar Cells for High Quality Passivation", in *2008 33rd IEEE Photovoltaic Specialists Conference*, IEEE, 2008, pp. 1–6.

[252] S. Pantelides, S. Rashkeev, R. Buczko, D. Fleetwood, and R. Schrimpf, "Reactions of Hydrogen with Si-SiO_2 Interfaces", *IEEE Transactions on Nuclear Science*, vol. 47, no. 6, pp. 2262–2268, 2000.

[253] E. Cartier, J. Stathis, and D. Buchanan, "Passivation and Depassivation of Silicon Dangling Bonds at the Si/SiO_2 Interface by Atomic Hydrogen", *Applied Physics Letters*, vol. 63, no. 11, pp. 1510–1512, 1993.

[254] A. Stesmans, "Passivation of Pb0 and Pb1 Interface Defects in Thermal (100) Si/SiO_2 with Molecular Hydrogen", *Applied Physics Letters*, vol. 68, no. 15, pp. 2076–2078, 1996.

[255] J. Stathis, "Dissociation Kinetics of Hydrogen-Passivated (100) Si/SiO_2 Interface Defects", *Journal of Applied Physics*, vol. 77, no. 12, pp. 6205–6207, 1995.

[256] S. T. Pantelides, L. Tsetseris, S. Rashkeev, X. Zhou, D. M. Fleetwood, and R. D. Schrimpf, "Hydrogen in MOSFETs–A Primary Agent of Reliability Issues", *Microelectronics Reliability*, vol. 47, no. 6, pp. 903–911, 2007.

[257] D. Brown and N. Saks, "Time Dependence of Radiation-Induced Interface Trap Formation in Metal-Oxide-Semiconductor Devices as a Function of Oxide Thickness and Applied Field", *Journal of Applied Physics*, vol. 70, no. 7, pp. 3734–3747, 1991.

[258] J. De Nijs, K. Druijf, V. Afanas' ev, E. Van der Drift, and P. Balk, "Hydrogen Induced Donor-Type Si/SiO_2 Interface States", *Applied Physics Letters*, vol. 65, no. 19, pp. 2428–2430, 1994.

[259] N. Thoan, K. Keunen, V. Afanas' ev, and A. Stesmans, "Interface state Energy Distribution and Pb Defects at Si (110)/SiO_2 Interfaces: Comparison to (111) and (100) Silicon Orientations", *Journal of Applied Physics*, vol. 109, no. 1, p. 013 710, 2011.

[260] K. L. Brower and S. Myers, "Chemical Kinetics of Hydrogen and (111) Si-SiO_2 Interface Defects", *Applied Physics Letters*, vol. 57, no. 2, pp. 162–164, 1990.

[261] A. Stesmans, "Revision of H_2 Passivation of P_b Interface Defects in Standard (111)Si/SiO_2", *Applied Physics Letters*, vol. 68, no. 19, pp. 2723–2725, 1996.

[262] L.-Å. Ragnarsson and P. Lundgren, "Electrical Characterization of Pb Centers in (100) Si–SiO_2 Structures: The Influence of Surface Potential on Passivation During Post Metallization anneal", *Journal of Applied Physics*, vol. 88, no. 2, pp. 938–942, 2000.

[263] A. Stesmans, "Comparative Analysis of the H_2 Passivation of Interface Defects at the (100) Si-SiO_2 Interface Using Electron Spin Resonance", *Solid State Communications*, vol. 97, no. 4, pp. 255–259, 1996.

[264] K. Brower, "Dissociation Kinetics of Hydrogen-Passivated (111) Si-SiO_2 Interface Defects", *Physical Review B*, vol. 42, no. 6, p. 3444, 1990.

[265] A. Stesmans and V. Afanas' ev, "Thermally Induced Interface Degradation in (100) and (111) Si/SiO_2 Analyzed by Electron Spin Resonance", *Journal of Vacuum Science & Technology B: Microelectronics and Nanometer Structures Processing, Measurement, and Phenomena*, vol. 16, no. 6, pp. 3108–3111, 1998.

[266] D. Benoit, J. Regolini, and P. Morin, "Hydrogen Desorption and Diffusion in PECVD Silicon Nitride. Application to Passivation of CMOS Active Pixel Sensors", *Microelectronic Engineering*, vol. 84, no. 9-10, pp. 2169–2172, 2007.

[267] D. Benoit, P. Morin, and J. Regolini, "Determination of Silicon Nitride Film Chemical Composition to Study Hydrogen Desorption Mechanisms", *Thin Solid Films*, vol. 519, no. 19, pp. 6550–6553, 2011.

[268] H. Dekkers, G. Beaucarne, M. Hiller, H. Charifi, and A. Slaoui, "Molecular Hydrogen Formation in Hydrogenated Silicon Nitride", *Applied Physics Letters*, vol. 89, no. 21, p. 211 914, 2006.

[269] K. Vanheusden, W. Warren, R. Devine, D. Fleetwood, J. Schwank, M. Shaneyfelt, P. Winokur, and Z. Lemnios, "Non-Volatile Memory Device Based on Mobile Protons in SiO_2 Thin Films", *Nature*, vol. 386, no. 6625, pp. 587–589, 1997.

[270] J. Hofstetter, C. Del Canizo, S. Ponce-Alcantara, and A. Luque, "Optimisation of SiN_x: H Anti-Reflection Coatings for Silicon Solar Cells", in *2007 Spanish Conference on Electron Devices*, IEEE, 2007, pp. 131–134.

[271] H. Jin, K. Weber, N. Dang, and W. Jellett, "Defect Generation at the Si–SiO_2 Interface Following Corona Charging", *Applied Physics Letters*, vol. 90, no. 26, p. 262 109, 2007.

[272] B. Sopori, X. Deng, J. Benner, A. Rohatgi, P. Sana, S. Estreicher, Y. Park, and M. Roberson, "Hydrogen in Silicon: A Discussion of Diffusion and Passivation Mechanisms", *Solar Energy Materials and Solar Cells*, vol. 41, pp. 159–169, 1996.

[273] B. R. Tuttle, W. McMahon, and K. Hess, "Hydrogen and Hot Electron Defect Creation at the Si (100)/SiO_2 Interface of Metal-Oxide-Semiconductor Field Effect Transistors", *Superlattices and Microstructures*, vol. 27, no. 2-3, pp. 229–233, 2000.

[274] M. Houssa, J. Autran, M. Heyns, and A. Stesmans, "Model for Defect Generation at the (100) Si/SiO_2 Interface During Electron Injection in MOS Structures", *Applied Surface Science*, vol. 212, pp. 749–752, 2003.

[275] S. Chang, J. Wu, and S. A. Lyon, "Amphoteric Defects at the Si-SiO_2 Interface", *Applied Physics Letters*, vol. 48, no. 10, pp. 662–664, 1986.

[276] V. Afanas'ev and A. Stesmans, "Hydrogen Release Related to Hole Injection into SiO_2 Layers on Si", *Materials Science in Semiconductor Processing*, vol. 4, no. 1-3, pp. 149–151, 2001.

[277] F. Feigl, D. Young, D. DiMaria, S. Lai, and J. Calise, "The Effects of water on oxide and Interface Trapped Charge Generation in Thermal SiO_2 Films", *Journal of Applied Physics*, vol. 52, no. 9, pp. 5665–5682, 1981.

[278] Z. Weinberg, "Hole Injection and Transport in SiO_2 Films on Si", *Applied Physics Letters*, vol. 27, no. 8, pp. 437–439, 1975.

[279] M. H. Woods and R. Williams, "Hole Traps in Silicon Dioxide", *Journal of Applied Physics*, vol. 47, no. 3, pp. 1082–1089, 1976.

[280] Z. Weinberg, W. Johnson, and M. Lampert, "High-field Transport in SiO_2 on Silicon Induced by Corona Charging of the Unmetallized Surface", *Journal of Applied Physics*, vol. 47, no. 1, pp. 248–255, 1976.

[281] V. Afanas' ev, M. Depas, J. De Nijs, and P. Balk, "Simultaneous Elimination of Electrically Active Defects in Si/SiO_2 Structures by Implanted Fluorine", *Microelectronic Engineering*, vol. 22, no. 1-4, pp. 93–96, 1993.

[282] R. Stahlbush, A. Edwards, D. Griscom, and B. Mrstik, "Post-Irradiation Cracking of H_2 and Formation of Interface States in Irradiated Metal-Oxide-Semiconductor Field-Effect Transistors", *Journal of Applied Physics*, vol. 73, no. 2, pp. 658–667, 1993.

[283] Q. D. M. Khosru, N. Yasuda, K. Taniguchi, and C. Hamaguchi, "Spatial Distribution of Trapped Holes in SiO_2", *Journal of Applied Physics*, vol. 76, no. 8, pp. 4738–4742, 1994.

[284] J. F. Chen, K.-S. Tian, S.-Y. Chen, K.-M. Wu, J. Shih, and K. Wu, "An Investigation on Anomalous Hot-Carrier-Induced On-Resistance Reduction in N-Type LDMOS Transistors", *IEEE Transactions on Device and Materials Reliability*, vol. 9, no. 3, pp. 459–464, 2009.

[285] J. Ko, D. Gong, K. Pillai, K.-S. Lee, M. Ju, P. Choi, K.-R. Kim, J. Yi, and B. Choi, "Double Layer SiN_x: H Films For Passivation and Anti-Reflection Coating of c-Si Solar Cells", *Thin Solid Films*, vol. 519, no. 20, pp. 6887–6891, 2011.

[286] D. Gong, Y.-J. Lee, M. Ju, J. Ko, D. Yang, Y. Lee, G. Choi, S. Kim, J. Yoo, B. Choi, *et al.*, "SiN_x Double Layer Antireflection Coating by Plasma-Enhanced Chemical Vapor Deposition for Single Crystalline Silicon Solar Cells", *Japanese Journal of Applied Physics*, vol. 50, no. 8S2, 08KE01, 2011.

[287] D. N. Wright, E. S. Marstein, and A. Holt, "Double Layer Anti-Reflective Coatings for Silicon Solar Cells", in *Conference Record of the Thirty-first IEEE Photovoltaic Specialists Conference, 2005.*, IEEE, 2005, pp. 1237–1240.

[288] A. Dastgheib-Shirazi, F. Book, H. Haverkamp, B. Raabe, and G. Hahn, "Investigations of High Refractive Silicon Nitride Layers for Etched Back Emitters: Enhanced Surface Passivation for Selective Emitter Concept (SECT)", in *24th European Photovoltaic Solar Energy Conference*, 2009, pp. 1600–1604.

[289] N. Nickel, "Hydrogen Diffusion Through Silicon/Silicon Dioxide Interfaces", *Journal of Vacuum Science & Technology B: Microelectronics and Nanometer Structures Processing, Measurement, and Phenomena*, vol. 18, no. 3, pp. 1770–1772, 2000.

[290] S. Kashyap, J. Madan, R. Pandey, and R. Sharma, "Comprehensive Study on the Recent Development of PERC Solar Cell", in *2020 47th IEEE Photovoltaic Specialists Conference (PVSC)*, IEEE, 2020, pp. 2542–2546.

[291] T. Dullweber, "High-Efficiency Industrial PERC Solar Cells for Monofacial and Bifacial Applications", in *High-Efficient Low-Cost Photovoltaics*, Springer, 2020, pp. 65–94.

[292] T. Lauermann, B. Fröhlich, G. Hahn, and B. Terheiden, "Design Considerations for Industrial Rear Passivated Solar Cells", in *2012 38th IEEE Photovoltaic Specialists Conference*, IEEE, 2012, pp. 001 710–001 715.

[293] M. Müller, G. Fischer, B. Bitnar, S. Steckemetz, R. Schiepe, M. Mühlbauer, R. Köhler, P. Richter, C. Kusterer, A. Oehlke, *et al.*, "Loss Analysis of 22% Efficient Industrial PERC Solar Cells", *Energy Procedia*, vol. 124, pp. 131–137, 2017.

[294] B. Min, M. Müller, H. Wagner, G. Fischer, R. Brendel, P. P. Altermatt, and H. Neuhaus, "A Roadmap Toward 24% Efficient PERC Solar Cells in Industrial Mass Production", *IEEE Journal of Photovoltaics*, vol. 7, no. 6, pp. 1541–1550, 2017.

[295] A. Halm, V. D. Mihailetchi, G. Galbiati, L. J. Koduvelikulathu, R. Roescu, C. Comparotto, R. Kopecek, K. Peter, and J. Libal, "The Zebra Cell Concept-Large Area N-Type Interdigitated Back Contact Solar Cells and One-Cell Modules Fabricated Using Standard Industrial Processing Equipment", *27nd EU-PVSEC, Frankfurt, Germany*, 2012.

[296] F. Haase, C. Hollemann, S. Schafer, J. Krügener, R. Brendel, and R. Peibst, "Transferring the Record P-Type Si POLO-IBC Cell Technology Towards an Industrial Level", in *2019 IEEE 46th Photovoltaic Specialists Conference (PVSC)*, IEEE, 2019, pp. 2200–2206.

[297] Y. Chen, D. Chen, C. Liu, Z. Wang, Y. Zou, Y. He, Y. Wang, L. Yuan, J. Gong, W. Lin, *et al.*, "Mass Production of Industrial Tunnel Oxide Passivated Contacts (i-TOPCon) Silicon Solar Cells with Average Efficiency over 23% and Modules over 345 W", *Progress in Photovoltaics: Research and Applications*, vol. 27, no. 10, pp. 827–834, 2019.

[298] C. Lee, H. Efstathiadis, J. E. Raynolds, and P. Haldar, "Two-Dimensional Computer Modeling of Single Junction a-Si: H Solar Cells", in *2009 34th IEEE Photovoltaic Specialists Conference (PVSC)*, IEEE, 2009, pp. 001 118–001 122.

[299] B. Min, H. Wagner, M. Müller, H. Neuhaus, R. Brendel, and P. Altermatt, "Incremental Efficiency Improvements of Mass-Produced PERC Cells up to 24%, Predicted Solely with Continuous Development of Existing Technologies and Wafer Materials", in *31st European Photovoltaic Solar Energy Conference and Exhibition*, 2015, pp. 473–476.

[300] P. Saint-Cast, S. Werner, J. Greulich, U. Jäger, E. Lohmüller, H. Höffler, and R. Preu, "Analysis of the Losses of Industrial-Type PERC Solar Cells", *physica status solidi (a)*, vol. 214, no. 3, p. 1 600 708, 2017.

[301] T. Dullweber, H. Hannebauer, S. Dorn, S. Schimanke, A. Merkle, C. Hampe, and R. Brendel, "Emitter Saturation Current Densities of 22 fA/cm^2 Applied to Industrial PERC Solar Cells Approaching 22% Conversion Efficiency", *Progress in Photovoltaics: Research and Applications*, vol. 25, no. 7, pp. 509–514, 2017.

[302] B. Hallam, A. Urueña, R. Russell, M. Aleman, M. Abbott, C. Dang, S. Wenham, L. Tous, and J. Poortmans, "Efficiency Enhancement of i-PERC Solar Cells by Implementation of a Laser Doped Selective Emitter", *Solar Energy Materials and Solar Cells*, vol. 134, pp. 89–98, 2015.

[303] W. Wu, Z. Zhang, F. Zheng, W. Lin, Z. Liang, and H. Shen, "Efficiency Enhancement of Bifacial PERC Solar Cells with Laser Doped Selective Emitter and Double-Screen-Printed Al Grid", *Progress in Photovoltaics: Research and Applications*, vol. 26, no. 9, pp. 752–760, 2018.

[304] M. Aleem, R. Vishnuraj, B. Krishnan, and B. Pullithadathil, "Realization of Micropatterned, Narrow Line-Width Ni–Cu–Sn Front Contact Grid Pattern Using Maskless Direct-Write Lithography for Industrial Silicon Solar Cells", *ACS Applied Energy Materials*, 2021.

[305] R. S. Davidsen, H. Li, A. To, X. Wang, A. Han, J. An, J. Colwell, C. Chan, A. Wenham, M. S. Schmidt, *et al.*, "Black Silicon Laser-Doped Selective Emitter Solar Cell with 18.1% Efficiency", *Solar Energy Materials and Solar Cells*, vol. 144, pp. 740–747, 2016.

[306] A. Fell and P. P. Altermatt, "A Detailed Full-Cell Model of a 2018 Commercial PERC Solar Cell in Quokka3", *IEEE Journal of Photovoltaics*, vol. 8, no. 6, pp. 1443–1448, 2018.

[307] M. Yu, S. McNab, I. Al-Dhahir, C. E. Patrick, P. P. Altermatt, and R. S. Bonilla, "Extracting Band-Tail Interface State Densities from Measurements and Modelling of Space Charge Layer Resistance", *Solar Energy Materials and Solar Cells*, vol. 231, p. 111 307, 2021.

[308] Y. Lv, Y. Zhuang, W. Wang, W. Wei, J. Sheng, S. Zhang, and W. Shen, "Towards High-Efficiency Industrial P-Type Mono-Like Si PERC Solar Cells", *Solar Energy Materials and Solar Cells*, vol. 204, p. 110 202, 2020.

[309] V. P. Equipment, *International Technology Roadmap for Photovoltaic (ITRPV)*, 2018.

[310] M. Rauer, C. Schmiga, M. Glatthaar, and S. W. Glunz, "Alloying from Screen-Printed Aluminum Pastes Containing Boron Additives", *IEEE Journal of Photovoltaics*, vol. 3, no. 1, pp. 206–211, 2012.

[311] F. Ye, Y. Li, X. Jia, H. Guo, X. Wang, J. Ding, N. Yuan, and Z. Feng, "Optimization of Phosphorus Dopant Profile of Industrial P-Type Mono PERC Solar Cells", *Solar Energy Materials and Solar Cells*, vol. 190, pp. 30–36, 2019.

[312] T. Dullweber, M. Stöhr, C. Kruse, F. Haase, M. Rudolph, B. Beier, P. Jäger, V. Mertens, R. Peibst, and R. Brendel, "Evolutionary PERC+ Solar Cell Efficiency Projection Towards 24% Evaluating Shadow-Mask-Deposited Poly-Si Fingers Below the Ag Front Contact as Next Improvement Step", *Solar Energy Materials and Solar Cells*, vol. 212, p. 110 586, 2020.

[313] S. Song, C. Sheng, R. Cao, T. Song, and Q. Wang, "The Study on Low Laser Damage Technology of SE Solar Cell", in *International Symposium on Intelligence Computation and Applications*, Springer, 2019, pp. 689–698.

[314] F. Werner, B. Veith, D. Zielke, L. Kühnemund, C. Tegenkamp, M. Seibt, R. Brendel, and J. Schmidt, "Electronic and Chemical Properties of the c-Si/Al_2O_3 Interface", *Journal of Applied Physics*, vol. 109, no. 11, p. 113 701, 2011.

[315] P.-C. Hsiao, N. Song, X. Wang, X. Shen, B. Phua, J. Colwell, U. Römer, B. Johnston, S. Lim, Y. Shengzhao, *et al.*, "266-nm ps Laser Ablation for Copper-Plated P-Type Selective Emitter PERC Silicon Solar Cells", *IEEE Journal of Photovoltaics*, vol. 8, no. 4, pp. 952–959, 2018.

[316] D. Suh, "Efficient Implementation of Multiple Drive-In Steps in Thermal Diffusion of Phosphorus for PERC Solar Cells", *Current Applied Physics*, vol. 18, no. 2, pp. 178–182, 2018.

[317] H. Li, F.-J. Ma, Z. Hameiri, S. Wenham, and M. Abbott, "On Elimination of Inactive Phosphorus in Industrial $POCl_3$ Diffused Emitters for High Efficiency Silicon Solar Cells", *Solar Energy Materials and Solar Cells*, vol. 171, pp. 213–221, 2017.

[318] B. Min, H. Wagner, A. Dastgheib-Shirazi, and P. P. Altermatt, "Limitation of Industrial Phosphorus-Diffused Emitters by SRH Recombination", *Energy Procedia*, vol. 55, pp. 115–120, 2014.

[319] E. Cho, Y.-W. Ok, J. Hwang, A. Jain, V. D. Upadhyaya, J. K. Tate, and A. Rohatgi, "Field-Effect Passivation by Negative Charge on Boron Emitter and Boron-Doped Surfaces by a Novel Low-Cost Plasma Charge Injection", in *2017 IEEE 44th Photovoltaic Specialist Conference (PVSC)*, IEEE, 2017, pp. 333–336.

[320] J.-M. Hwang, C. Chen, Y.-W. Ok, W. Choi, A. Upadhyaya, V. Upadhyaya, B. Rounsaville, and A. Rohatgi, "Investigation on Light Stability of Injected Charge in α-SiN x: H by Plasma Charge Injection Technology", in *2021 IEEE 48th Photovoltaic Specialists Conference (PVSC)*, IEEE, 2021, pp. 2119–2123.

[321] A. El-Shaer, M. Tadros, and M. Khalifa, "Effect of Light Intensity and Temperature on Crystalline Silicon Solar Modules Parameters", *International Journal of Emerging Technology and Advanced Engineering*, vol. 4, no. 8, pp. 311–318, 2014.

[322] T. Watahiki, Y. Kobayashi, T. Morioka, S. Nishimura, D. Niinobe, K. Nishimura, H. Tokioka, and M. Yamamuka, "Analysis of Short Circuit Current Loss in Rear Emitter Crystalline Si Solar Cell", *Journal of Applied Physics*, vol. 119, no. 20, p. 204 501, 2016.

[323] F. Colville, "N-Type Solar Cell Production to Exceed 5GW in 2018 with 135% Growth Since 2013", *PV Tech*, 2018.

[324] H. Park, S. Chang, S. Park, and W. K. Kim, "Outdoor Performance Test of Bifacial N-Type Silicon Photovoltaic Modules", *Sustainability*, vol. 11, no. 22, p. 6234, 2019.

[325] D. S. Kim, V. Meemongkolkiat, A. Ebong, B. Rounsaville, V. Upadhyaya, A. Das, and A. Rohatgi, "2D-Modeling and Development of Interdigitated Back Contact Solar Cells on Low-Cost Substrates", in *2006 IEEE 4th World Conference on Photovoltaic Energy Conference*, IEEE, vol. 2, 2006, pp. 1417–1420.

[326] E. Franklin, K. Fong, K. McIntosh, A. Fell, A. Blakers, T. Kho, D. Walter, D. Wang, N. Zin, M. Stocks, *et al.*, "Design, Fabrication and Characterisation of a 24.4% Efficient Interdigitated Back Contact Solar Cell", *Progress in Photovoltaics: Research and Applications*, vol. 24, no. 4, pp. 411–427, 2016.

[327] F. Haase, B. Min, C. Hollemann, J. Krügener, R. Brendel, and R. Peibst, "Fully Screen-Printed Silicon Solar Cells with Local Al-p^+ and N-Type POLO Interdigitated Back Contacts with a VOC of 716 mV and an Efficiency of 23%", *Progress in Photovoltaics: Research and Applications*, vol. 29, no. 5, pp. 516–523, 2021.

[328] Y. Chen, Y. Yang, G. Xu, J. K. Marmon, Z. Feng, and H. Shen, "Optimization of Micron Size Passivated Contact and Doping Level for High Efficiency Interdigitated Back Contact Solar Cells", *Solar Energy*, vol. 178, pp. 308–313, 2019.

[329] Z. Yang, H. Lin, J. Sheng, X. Yang, W. Wang, K. W. Chee, P. Gao, and J. Ye, "Design Principles of Silicon Heterojunction Solar Cells with Dopant-Free Interdigitated Back Contacts", *Solar RRL*, vol. 3, no. 11, p. 1 900 230, 2019.

[330] S. Dauwe, J. Schmidt, A. Metz, and R. Hezel, "Fixed Charge Density in Silicon Nitride Films on Crystalline Silicon Surfaces under Illumination", in *Conference Record of the Twenty-Ninth IEEE Photovoltaic Specialists Conference, 2002.*, IEEE, 2002, pp. 162–165.

[331] C. Chan, "Novel Laser Doping Technology for Silicon Solar Cell", *PhD, SPREE, University of New South Wales*, 2014.

[332] T. Rahman, A. To, M. E. Pollard, N. E. Grant, J. Colwell, D. N. Payne, J. D. Murphy, D. M. Bagnall, B. Hoex, and S. A. Boden, "Minimising Bulk Lifetime Degradation During the Processing of Interdigitated Back Contact Silicon Solar Cells", *Progress in Photovoltaics: Research and Applications*, vol. 26, no. 1, pp. 38–47, 2018.

[333] T. Sugiura, S. Matsumoto, and N. Nakano, "Optimization of Front Diffusion Profile in Bifacial Interdigitated Back Contact Solar Cell", *IEEE Journal of Photovoltaics*, vol. 10, no. 6, pp. 1582–1590, 2020.

[334] Y. Chen, Y. Yang, J. K. Marmon, X. Zhang, Z. Feng, P. J. Verlinden, and H. Shen, "Independent Al_2O_3/SiN_x:H and SiO_2/SiN_x:H Passivation of p^+ and n_+ Silicon Surfaces for High-Performance Interdigitated Back Contact Solar Cells", *IEEE Journal of Photovoltaics*, vol. 7, no. 1, pp. 51–57, 2016.

[335] J. Renshaw and A. Rohatgi, "Device Optimization for Screen Printed Interdigitated Back Contact Solar Cells", in *2011 37th IEEE Photovoltaic Specialists Conference*, IEEE, 2011, pp. 002 924–002 927.

[336] G. Declerck, R. Van Overstraeten, and G. Broux, "Measurement of Low Densities of Surface States at the Si–SiO_2 Interface", *Solid-State Electronics*, vol. 16, no. 12, pp. 1451–1460, 1973.

[337] A. Ingenito, O. Isabella, and M. Zeman, "Simplified Process for High Efficiency, Self-Aligned IBC c-Si Solar Cells Combining Ion Implantation and Epitaxial Growth: Design and Fabrication", *Solar Energy Materials and Solar Cells*, vol. 157, pp. 354–365, 2016.

[338] J. D. Huyeng, S. F. Lang, R. Efinger, S. Schmidt, A. Spribille, D. Bruge, A. Wolf, R. Keding, O. Doll, and F. Clement, "Advancements in the Utilization of Screen-Printed Boron Doping Paste for High Efficiency Back-Contact Back-Junction Silicon Solar Cells", in *2018 IEEE 7th World Conference on Photovoltaic Energy Conversion (WCPEC)(A Joint Conference of 45th IEEE PVSC, 28th PVSEC & 34th EU PVSEC)*, IEEE, 2018, pp. 1544–1549.

[339] N. Tebal, "Photo-Generation Profiles in Deeply-Etched, Two-Dimensional Patterns in Interdigitated Back Contact Solar Cells", *Journal of Ovonic Research Vol*, vol. 17, no. 3, pp. 283–289, 2020.

[340] B. Steinhauser, F. Feldmann, D. Ourinson, H. Nagel, T. Fellmeth, and M. Hermle, "On the Influence of the SiN_x Composition on the Firing Stability of Poly-Si/SiN_2 Stacks", *physica status solidi (a)*, vol. 217, no. 21, p. 2 000 333, 2020.

[341] C. N. Kruse, S. Schäfer, F. Haase, V. Mertens, H. Schulte-Huxel, B. Lim, B. Min, T. Dullweber, R. Peibst, and R. Brendel, "Simulation-Based Roadmap for the Integration of Poly-Silicon on Oxide Contacts into Screen-Printed Crystalline Silicon Solar Cells", *Scientific Reports*, vol. 11, no. 1, pp. 1–14, 2021.

[342] Q. Wang, W. Wu, Y. Li, L. Yuan, S. Yang, Y. Sun, S. Yang, Q. Zhang, Y. Cao, H. Qu, *et al.*, "Impact of Boron Doping on Electrical Performance and Efficiency of n-TOPCon Solar Cell", *Solar Energy*, vol. 227, pp. 273–291, 2021.

[343] N. Anand and P. Kale, "Optimization of TOPCon Structured Solar Cell Using AFORS-HET", *Transactions on Electrical and Electronic Materials*, vol. 22, no. 2, pp. 160–166, 2021.

[344] S. McNab, M. Yu, I. Al-Dhahir, E. Khorani, T. Rahman, S. A. Boden, P. P. Altermatt, P. R. Wilshaw, and R. S. Bonilla, "Alternative Dielectrics for Hole Selective Passivating Contacts and the Influence of Nanolayer Built-in Charge", in *11th International Conference on Silicon Photovoltaics*, American Institute of Physics, 2021, In Press.

[345] T. Sugiura, S. Matsumoto, and N. Nakano, "Numerical Analysis of Tunnel Oxide Passivated Contact Solar Cell Performances for Dielectric Thin Film Materials and Bulk Properties", *Solar Energy*, vol. 214, pp. 205–213, 2021.

[346] Y.-Y. Huang, Y.-W. Ok, K. Madani, W. Choi, A. D. Upadhyaya, V. D. Upadhyaya, and A. Rohatgi, "Fully Screen-Printed Bifacial Large Area 22.6% N-Type Si Solar Cell with Lightly Doped Ion-Implanted Boron Emitter

andTunnel Oxide Passivated Rear Contact", *Solar Energy Materials and Solar Cells*, vol. 214, p. 110 585, 2020.

[347] S. Chowdhury, G. Chavan, S. Kim, D. Oh, Y. Kim, E. C. Cho, Y. Cho, and J. Yi, "Analysis of Passivation Property using Thin Al_2O_3 Layer and Simulation for Realization of High-Efficiency TOPCon Cell", *Infrared Physics & Technology*, vol. 110, p. 103 436, 2020.

[348] C. Liu, D. Chen, Y. Chen, Y. Ling, Y. Zou, Y. Wang, J. Gong, Z. Feng, P. P. Altermatt, and P. J. Verlinden, "Industrial TOPCon Solar Cells on N-Type Quasi-Mono Si Wafers with Efficiencies Above 23%", *Solar Energy Materials and Solar Cells*, vol. 215, p. 110 690, 2020.

[349] Z. Zhang, Y. Zeng, C.-S. Jiang, Y. Huang, M. Liao, H. Tong, M. Al-Jassim, P. Gao, C. Shou, X. Zhou, *et al.*, "Carrier Transport Through the Ultrathin Silicon-oxide Layer in Tunnel Oxide Passivated Contact (TOPCon) c-Si Solar Cells", *Solar Energy Materials and Solar Cells*, vol. 187, pp. 113–122, 2018.

[350] Q. Wang, W. Wu, N. Yuan, Y. Li, Y. Zhang, and J. Ding, "Influence of SiO_x Film Thickness on Electrical Performance and Efficiency of TOPCon Solar Cells", *Solar Energy Materials and Solar Cells*, vol. 208, p. 110 423, 2020.

[351] G. Janssen, M. Stodolny, I. Romijn, and L. Geerligs, *The Role of the Oxide in the Carrier Selectivity of Metal/Poly-Si/Oxide Contacts to Silicon Wafers*. Petten: ECN, 2017.

[352] D. Yan, A. Cuevas, J. Bullock, Y. Wan, and C. Samundsett, "Phosphorus-Diffused Polysilicon Contacts for Solar Cells", *Solar Energy Materials and Solar Cells*, vol. 142, pp. 75–82, 2015.

[353] H. Steinkemper, F. Feldmann, M. Bivour, and M. Hermle, "Numerical Simulation of Carrier-Selective Electron Contacts Featuring Tunnel Oxides", *IEEE Journal of Photovoltaics*, vol. 5, no. 5, pp. 1348–1356, 2015.

[354] Y. Tao, V. Upadhyaya, K. Jones, and A. Rohatgi, "Tunnel Oxide Passivated Rear Contact for Large Area N-Type Front Junction Silicon Solar Cells Providing Excellent Carrier Selectivity", *AIMS Materials Science*, vol. 3, no. 1, pp. 180–189, 2016.

[355] "JinkoSolar Improves Efficiency of N-Type Monocrystalline TOPCon Solar Cell by 0.35 %". [Online]. Available: `https://www.pv-magazine.com/2021/05/31/jinkosolar-improves-efficiency-of-n-type-monocrystalline-topcon-solar-cell-by-0-35/`.

[356] E. Lohmüller, M. Glatz, S. Lohmüller, U. Belledin, S. Mack, T. Fellmeth, R. Naber, and A. Wolf, "BBr_3 Diffusion: Process Optimization for High-Quality

Emitters with Industrial Cycle Times", in *Presented at the 37th European PV Solar Energy Conference and Exhibition*, vol. 7, 2020, p. 11.

[357] S. Bae, J.-W. Choi, C. Kim, S. H. Shin, H. Park, Y. Kang, H.-S. Lee, and D. Kim, "Effective Contact Formation Method on High-Sheet-Resistance Boron-Doped Emitter with Current Injection", *IEEE Journal of Photovoltaics*, vol. 9, no. 3, pp. 615–620, 2019.

[358] C.-W. Chen, M. Hermle, J. Benick, Y. Tao, Y.-W. Ok, A. Upadhyaya, A. M. Tam, and A. Rohatgi, "Modeling the Potential of Screen Printed Front Junction CZ Silicon Solar Cell with Tunnel Oxide Passivated Back Contact", *Progress in Photovoltaics: Research and Applications*, vol. 25, no. 1, pp. 49–57, 2017.

[359] A. Rohatgi, B. Rounsaville, Y.-W. Ok, A. M. Tam, F. Zimbardi, A. D. Upadhyaya, Y. Tao, K. Madani, A. Richter, J. Benick, *et al.*, "Fabrication and Modeling of High-Efficiency Front Junction N-Type Silicon Solar Cells with Tunnel Oxide Passivating Back Contact", *IEEE Journal of Photovoltaics*, vol. 7, no. 5, pp. 1236–1243, 2017.

[360] Y.-Y. Huang, Y.-W. Ok, K. Madani, W. Choi, A. Upadhyaya, V. Upadhyaya, B. Rounsaville, V. Chandrasekaran, and A. Rohatgi, "˜23% Rear Side Poly-Si/SiO_2 Passivated Silicon Solar Cell with Optimized Ion-Implanted Boron Emitter and Screen-Printed Contacts", *Solar Energy Materials and Solar Cells*, vol. 230, p. 111 183, 2021.

[361] P. Saint-Cast, A. Richter, E. Billot, M. Hofmann, J. Benick, J. Rentsch, R. Preu, and S. W. Glunz, "Very Low Surface Recombination Velocity of Boron Doped Emitter Passivated with Plasma-Enhanced Chemical-Vapor-Deposited AlO_x Layers", *Thin Solid Films*, vol. 522, pp. 336–339, 2012.

[362] W. Kern, "The Evolution of Silicon Wafer Cleaning Technology", *Journal of the Electrochemical Society*, vol. 137, no. 6, p. 1887, 1990.

[363] W. Kern, "Overview and Evolution of Silicon Wafer Cleaning Technology", in *Handbook of Silicon Wafer Cleaning Technology*, Elsevier, 2018, pp. 3–85.

[364] K. Reinhardt and W. Kern, *Handbook of Silicon Wafer Cleaning Technology*. William Andrew, 2018.

[365] G. Celler, D. Barr, and J. Rosamilia, "Etching of Silicon by the RCA Standard Clean 1", *Electrochemical and Solid State Letters*, vol. 3, no. 1, p. 47, 1999.

A | Appendix

A.1 RCA Cleaning

RCA cleaning is a technique used within the electronics industry to remove contaminants from the surface of silicon [362–364]. In this work, RCA cleaning was performed on Set B wafers before *in situ* Cs^+ ion delivery during oxidation discussed in Chapter 4. The RCA clean was performed on site at the University of Oxford. The procedure can be broken down into two steps: RCA 1 to remove organic impurities, and RCA 2 to remove metal and ionic contaminants. During the RCA 1 process, a solution of 7 parts DI water and 1 part hydrogen peroxide (30 %) is prepared and heated to 50 °C, at which point 1 part ammonia (30 %) is added. The alkaline solution is subsequently heated to 75 °C. When the target temperature is reached, the bare silicon wafer is immersed in the solution for 10 minutes. During this process the hydrogen peroxide oxidises the silicon surface thus consuming the organic impurities lying within. The ammonia works to dissolve the oxide and remove the impurities. These competing processes work together [363, 365]. Upon removal from the solution, a thin native oxide $\sim$1 nm thick remains on the silicon surface [362]. The wafer is rinsed thoroughly in pure DI water and the residual oxide is then etched off with hydrofluoric acid to reveal bare silicon. The RCA 2 process is performed immediately afterwards. Here, a fresh solution of 7 parts DI water and 1 part hydrogen peroxide (30 %) is heated to 50 °C before 1 part hydrochloric acid (32 %) is added. The acidic solution is heated to 75 °C, at which point the wafer is placed inside for 10 minutes. Analogous to the RCA 1 process, a continuous oxidation/dissolution process works to remove metal contaminants. At the end of 10 minutes, the wafer is extracted from the solution and the residual oxide once again removed with hydrofluoric acid.

A.2 Girisch and Aberle's Formulism

The Girisch and Aberle formulism is used in Chapter 5 to model the recombination rates at the Si-SiO_2 interface under non-equilibrium conditions [167, 233]. Figure A.1 provides a flowchart of the iterative algorithm. Following Equation A.1, the first step is the calculation of the carrier densities, n and p, located beyond the edge of the space charge region within the bulk of the silicon. The equilibrium carrier concentrations are known from the doping concentration of the wafer.

$$n = n_0 + \Delta n \tag{A.1a}$$

$$p = p_0 + \Delta p \tag{A.1b}$$

The equilibrium carrier concentrations, n_0 and p_0, are known from the doping concentration of the wafer. Once n and p are known, the quasi Fermi levels ($E_{F,n}, E_{F,p}$) at the edge of the SCR can be calculated from Equation A.2. The formulism assumes that the quasi Fermi levels are constant throughout the SCR, and that there is negligible generation or recombination occurring within this region [167, 233].

$$E_{(F,n)} = -\frac{kT}{q} ln\left(\frac{n}{n_i}\right) \tag{A.2a}$$

$$E_{(F,p)} = +\frac{kT}{q} ln\left(\frac{p}{n_i}\right) \tag{A.2b}$$

Given that the Fermi levels are assumed to lie flat, charge neutrality of the system must hold true. Therefore, charge within the silicon (Q_{Si}), the gate charge (Q_g), the dielectric charge (Q_f), and the interface trapped charge Q_{it} must all balance such that $Q_{Si} + Q_g + Q_f + Q_{it} = 0$. The dielectric charge, Q_f, can be determined experimentally from CV measurements. The other three charges are described by the following set of equations

[18, 167, 233]:

$$Q_{Si} = \pm\sqrt{\frac{2kTn_i\varepsilon_r}{q^2}e^{\beta(E_{F,p}-\Psi_s)} - e^{\beta E_{F,p}} + e^{\beta(\Psi_s - E_{F,n})} - e^{\beta E_{F,n}} + \beta\Psi_s\frac{(N_A - N_D)}{n_i}} \tag{A.3a}$$

$$Q_g = -\frac{1}{d}\left(\frac{Q_f d_f}{2} + \frac{\varepsilon_r}{q}(\Psi_s - V_g)\right) \tag{A.3b}$$

$$Q_{it} = -\int_{E_v}^{E_c} D_{it,a}(E)f_a(E) \quad dE + \int_{E_v}^{E_c} D_{it,d}(E)f_d(E) \quad dE \tag{A.3c}$$

$$f_a(E) = \frac{\sigma_n(E)n + \sigma_p(E)p_1}{\sigma_n(E)(n + n_1(E)) + \sigma_p(E)(p + p_1(E))} \tag{A.3d}$$

$$f_d(E) = \frac{\sigma_n(E)n_1 + \sigma_p(E)p}{\sigma_n(E)(n + n_1(E)) + \sigma_p(E)(p + p_1(E))} \tag{A.3e}$$

where d is the oxide thickness, d_f is the distance away from the interface Q_f is located. $D_{it,a}$ and $D_{it,d}$ are the density of acceptor and donor interface states, respectively, and $\beta = \frac{kT}{q}$.

The concentration of electrons and holes at the surface, n_s and p_s, are defined as:

$$n_s = ne^{\beta\Psi_s} \tag{A.4a}$$

$$p_s = pe^{\beta\Psi_s} \tag{A.4b}$$

In order to calculate n_s and p_s, the silicon surface potential, Ψ_s must be solved for numerically. Here, Ψ_s is iteratively varied until charge neutrality is achieved in the system. Once a solution to Ψ_s is found, the values of n_s and p_s can be inserted into the equation to calculate the SRH recombination rate, (U_s), and the surface recombination velocity (SRV) as given by Equations 1.18 and 1.19 in Chapter 1.

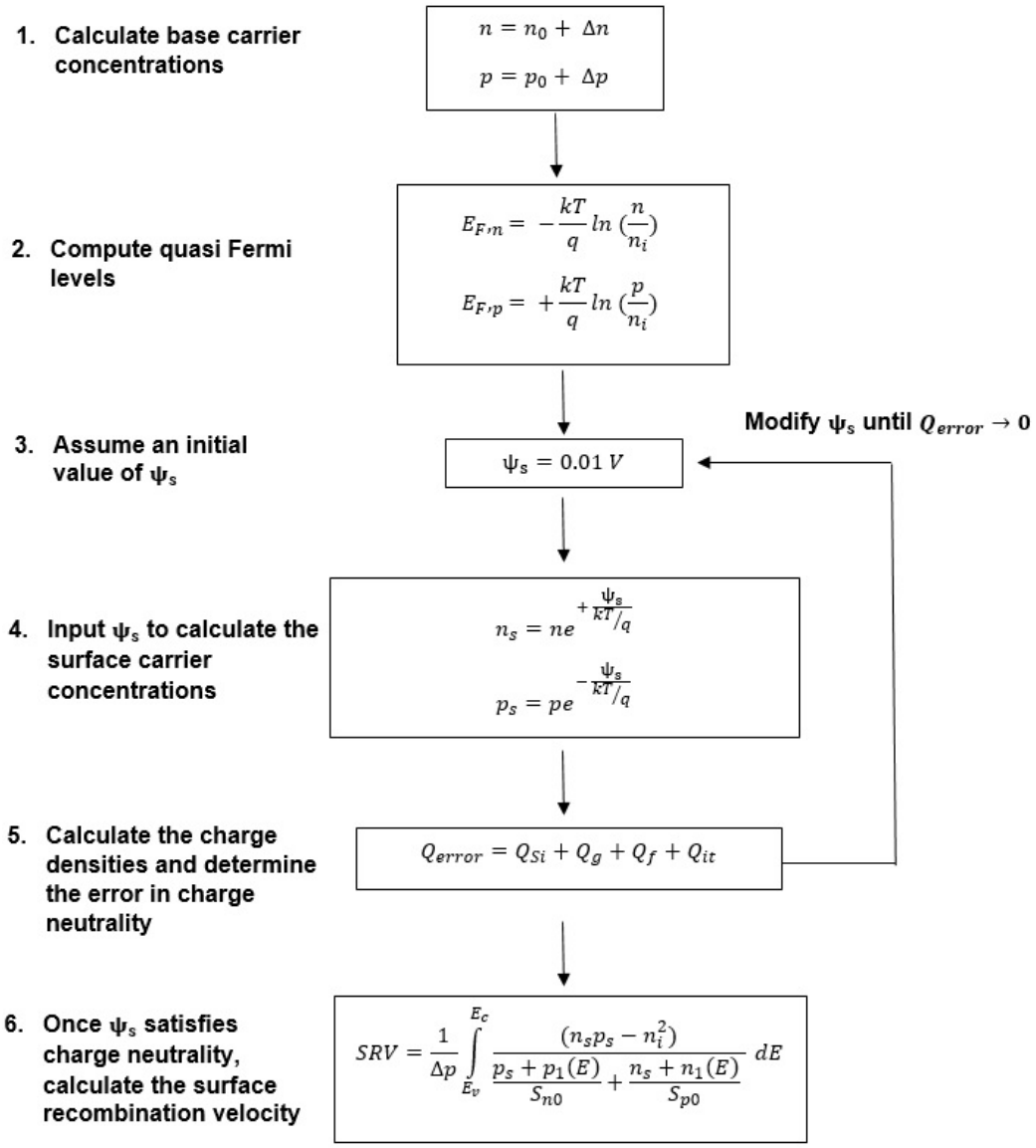

Figure A.1: Iterative algorithm used to determine the surface recombination parameters under the conditions of charge neutrality.

A.3 Corona Charge Calibration for Type C Specimens

Set C (n-type 5-10 Ωcm CZ) wafers were used to produce Type C–Ox–Ni1 and Type C–Ox–Ni2 specimens used in Chapter 6. Owing to their 6 inch dimension, great care had to be used to place them into the Kelvin Probe instrument. To prevent breakage or damage to the specimen, a calibration was produced to determine the surface charge concentration for positive and negative corona charge deposited in 5 s and 10 s increments. Different calibrations were required for each polarity since the drift of negative ions is faster than positive ions. Additionally, separate calibrations were required for each time interval since the concentration deposited is not linear with time within the first 3-4 seconds of discharge, as the voltage ramps up to ±30 kV. One full size 6 inch Type C–Ox–Ni2 substrate was cleaved into quarters. One quarter had 5 s of negative corona charge deposited 3 times consecutively. The absolute difference in charge between each deposition was averaged and used as the estimated concentration deposited per 5 s of negative discharge. A similar process was carried out on the remaining 3 pieces to produce calibrations for both polarities and discharge times. The calibrated values are provided in Table A.1.

	5 S AVERAGE CONCENTRATION (Q CM^{-2})	10 S AVERAGE CONCENTRATION (Q CM^{-2})
Positive	1.30 x 10^{11}	3.92 x 10^{11}
Negative	-1.60 x 10^{11}	-4.60 x 10^{11}

Table A.1: Calibrated charge values for 5 s and 10 s of positive and negative corona discharge.

To test the accuracy of this calibration, another quarter piece of a Type C–Ox–Ni2 substrate had real measurements taken within the Kelvin Probe. This test sample underwent identical charging to the full size experimental wafer that was used for lifetime testing. The charge on the test wafer was verified after every deposition using Kelvin Probe. Figure A.2 shows the comparison between the measured and estimated

charge concentrations. It can be seen that there is excellent agreement between the two, particularly at the location of the minimum point, which is the region of greatest interest for the determination of the interface recombination parameters. Such a comparison was only performed once given the small quantity of substrates received from Trina Solar.

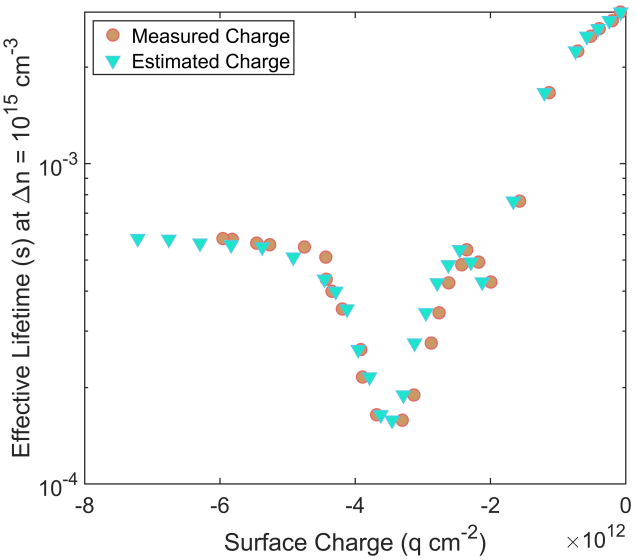

Figure A.2: Comparison of estimated corona charge concentration using a calibration and measured concentration.